University of Kentucky
UKnowledge

Theses and Dissertations--Chemical and Materials Engineering

Chemical and Materials Engineering

2014

# MIXED SURFACTANT SYSTEMS: THERMODYNAMICS AND APPLICATIONS IN METAL OXIDE IMPRINTING

Suvid Joshi
*University of Kentucky*, sjo222@l.uky.edu

Right click to open a feedback form in a new tab to let us know how this document benefits you.

## Recommended Citation

Joshi, Suvid, "MIXED SURFACTANT SYSTEMS: THERMODYNAMICS AND APPLICATIONS IN METAL OXIDE IMPRINTING" (2014). *Theses and Dissertations--Chemical and Materials Engineering*. 29.
https://uknowledge.uky.edu/cme_etds/29

This Doctoral Dissertation is brought to you for free and open access by the Chemical and Materials Engineering at UKnowledge. It has been accepted for inclusion in Theses and Dissertations--Chemical and Materials Engineering by an authorized administrator of UKnowledge. For more information, please contact UKnowledge@lsv.uky.edu.

STUDENT AGREEMENT:

I represent that my thesis or dissertation and abstract are my original work. Proper attribution has been given to all outside sources. I understand that I am solely responsible for obtaining any needed copyright permissions. I have obtained needed written permission statement(s) from the owner(s) of each third-party copyrighted matter to be included in my work, allowing electronic distribution (if such use is not permitted by the fair use doctrine) which will be submitted to UKnowledge as Additional File.

I hereby grant to The University of Kentucky and its agents the irrevocable, non-exclusive, and royalty-free license to archive and make accessible my work in whole or in part in all forms of media, now or hereafter known. I agree that the document mentioned above may be made available immediately for worldwide access unless an embargo applies.

I retain all other ownership rights to the copyright of my work. I also retain the right to use in future works (such as articles or books) all or part of my work. I understand that I am free to register the copyright to my work.

REVIEW, APPROVAL AND ACCEPTANCE

The document mentioned above has been reviewed and accepted by the student's advisor, on behalf of the advisory committee, and by the Director of Graduate Studies (DGS), on behalf of the program; we verify that this is the final, approved version of the student's thesis including all changes required by the advisory committee. The undersigned agree to abide by the statements above.

Suvid Joshi, Student

Dr Stephen Rankin, Major Professor

Dr Thomas Dziubla, Director of Graduate Studies

# MIXED SURFACTANT SYSTEMS: THERMODYNAMICS AND APPLICATIONS IN METAL OXIDE IMPRINTING

DISSERTATION

A dissertation submitted in partial fulfillment of the
requirements for the degree of Doctor of Philosophy in the
College of Engineering
at the University of Kentucky

By
Suvid Joshi

Lexington, Kentucky

Director: Dr. Stephen E Rankin, Professor of Chemical Engineering

Lexington, Kentucky

2014

Copyright © Suvid Joshi 2014

ABSTRACT OF DISSERTATION

# MIXED SURFACTANT SYSTEMS: THERMODYNAMICS AND APPLICATIONS IN METAL OXIDE IMPRINTING

In this work we study mixtures of cationic surfactant (CTAB) and sugar based surfactant(s) (octyl beta-D-glucopyranoside (C8G1), dodecyl maltoside (C12G2) and octyl beta-D-xylopyranoside (C8X1)) to understand the non-ideal thermodynamic behavior of the mixtures of cationic and non-ionic surfactants in water and synthesis of imprinted materials. The thermodynamics of micellization, mixing and dilution of these systems are studied using Isothermal Titration Calorimetry (ITC) and the experimental data obtained are modeled with a pseudo-phase separation model with non-ideal mixing described by regular solution theory. It is shown that a model accounting for enthalpy of demicellization and enthalpy of dilution based on McMillan-Mayer model is able to fit ITC data set for CTAB-C8G1 system with varying mole fractions.

In addition to measuring non-ideal mixing behavior, mixtures of cationic and saccharide-based surfactants are of interest for the molecular imprinting of oxide materials. Mixtures of CTAB and either C8G1 or C8X1 are utilized to prepare nonporous adsorbent materials which act as selective adsorbents towards the headgroup of the saccharide surfactant. The approach is based on the Stöber silica particle synthesis process in which surfactants are added to soft particles present at the onset of turbidity to imprint their surface. This approach is shown to yield particles displaying selective adsorption for sugars with different number of carbons, but also provide enantioselective adsorption of targeted saccharides. Enantioselectivity of D-glucose, D-xylose and D-maltose is demonstrated by imprinting with C8G1, C8X1 and C12G2, respectively. The imprinting technique provides the first example of selective adsorption based on non-covalent imprinting of silica for sugars.

The mixed surfactant are also used to synthesize templated porous materials incorporating titanium which are used for epoxidation catalysis. The porous materials obtained have high surface area, uniform pore sizes in the mesopore range, and provided high selectivity and activity towards epoxidation of styrene. Titanosilicate thin films are also synthesized using cationic and saccharide surfactant mixtures to understand the incorporation of the titanium into the porous material. It is demonstrated that large amounts of isolated, tetracoordinated titanium sites can be incorporated into mesoporous

silica-based materials via the complexation of the titanium precursor with a saccharide-based surfactant.

KEYWORDS: surfactants, silica, thermodynamics, adsorption, catalysis

Suvid Joshi

April 30, 2014

MIXED SURFACTANT SYSTEMS: THERMODYNAMICS AND APPLICATIONS IN METAL OXIDE IMPRINTING

By

Suvid Joshi

Dr Stephen Rankin
*Director of Dissertation*

Dr Thomas Dziubla

*Director of Graduate Studies*

*To, Late Dr. Shivram Dattatray Joshi*

## ACKNOWLEDGMENTS

*Gurur-Brahmaa Gurur-Vissnnur-Gururdevo Maheshvarah |*
*Guru sakshat Param Brahma Tasmai Shrii-Gurave Namah ||1||*

The Guru is Brahma, the Guru is Vishnu, the Guru Deva is Maheswara (Shiva). The Guru is Verily the Para-Brahman (Supreme Brahman); Salutations to that Guru. .The couplet summarizes all I have to say for my advisor Dr Stephen Rankin. I would like to express my deepest gratitudes to Dr Rankin for all the guidance he provided me throughout my PhD. Without him, the journey through my PhD would have been much harder. I would also like to thank Dr Barbara Knutson for encouragement she provided during my PhD. I would also like to thank my committee members Dr Paul Bummer and Dr Jeffrey Seay

I would like to thank all my past and present lab mates and people who worked on USDA grant, especially Dr Jyothirmai Ambati, Dan Schlipf, Suraj Nagpure, Ravinder Garlapalli, Saikat Das, Said Zahadul Islam, Dr Janet Mohandas and Srivenu Seelam for banter that helped me enjoy every second in the lab. Dr Gifty Osei-Prempeh for patiently teaching me to use my first instrument at the University of Kentucky.

I would like to thank CMEGSA (MACE) and all its members for amazingly entertaining meetings, tailgating and evenings at Pazzo's. I would like to thank all of the *Gazette Janata* for giving me a family away from India. My special thanks to Anwesha, Apurv and Sweta for listening to me the way only friends can and giving advice no one else could. I would also like to thank UKCC, and all the members of UKCC for keeping me engaged over the past 5 years playing cricket and providing regular breaks and enjoyment.

The acknowledgement would be incomplete without thanking my family who had my back every step of the way. I would like to thank my mother for standing by me through all the difficult times and my father for giving me confidence and guiding me to be a better person every time I faltered. I would also like to thank my brother Abhijat, who stood by me every time I needed support.

## TABLE OF CONTENTS

ACKNOWLEDGMENTS ..... iii
TABLE OF CONTENTS ..... v
LIST OF TABLES ..... viii
LIST OF FIGURES ..... ix
1. INTRODUCTION ..... 1
1.1 Research Hypothesis ..... 3
1.2 Research Contribution ..... 4
2. BACKGROUND ..... 6
2.1. Summary ..... 6
2.2 Introduction to saccharide surfactants ..... 7
2.3 Mixed micelles involving saccharide surfactants ..... 11
2.3.1 Thermodynamic models ..... 12
2.3.2 Mixtures with cationic, anionic and nonionic surfactants ..... 16
2.3.3 Adsorption of surfactant mixtures on solid surfaces ..... 18
2.4. Molecular imprinting ..... 20
2.5. Silica based materials ..... 24
2.5.1. Sol-gel process ..... 24
2.5.2. Templated porous silicates ..... 25
2.5.3. Metal oxide incorporation into the silica framework ..... 27
2.5.4. Nonporous silica particles ..... 29
2.6. Characterization techniques ..... 32
2.6.1 Isothermal Titration Calorimeter (ITC) ..... 32
2.6.2. Fourier Transform Infrared Spectroscopy (FTIR) ..... 34
2.6.3. X-ray diffraction (XRD) ..... 37
2.6.4. Scanning Electron Microscopy ..... 38
2.6.5 Nitrogen adsorption ..... 39
2.6.6 Dynamic Light Scattering (DLS) ..... 42
2.7. Conclusion ..... 44
3. MODELING THERMODYNAMIC BEHAVIOR OF NON-IDEAL MIXED SURFACTANTS: USE OF REGULAR SOLUTION THEORY FOR ISOTHERMAL TITRATION CALORIMETRY DATA ..... 50
3.1. Summary ..... 50

3.2. Introduction ..... 51
3.3. Experimental ..... 55
3.3.1. Materials ..... 55
3.3.2. Methods ..... 55
3.3.3. Surfactant pseudo-phase equilibrium model ..... 56
3.4. Thermodynamic model of micellization ..... 58
3.4.1 Fitting the model ..... 62
3.5. Results and Discussion ..... 62
3.6. Conclusion ..... 71
4. INTERFACIAL MOLECULAR IMPRINTING OF STÖBER PARTICLE SURFACES: A SIMPLE APPROACH TO TARGETED SACCHARIDE ADSORPTION ..... 84
4.1 Summary ..... 84
4.2 Introduction ..... 85
4.3 Experimental Section ..... 89
4.3.1 Materials ..... 89
4.3.2 Octyl-β-D-xylopyranoside synthesis (C8X1) ..... 89
4.3.3 Particle synthesis ..... 89
4.3.4 Particle characterization ..... 92
4.3.5 Saccharide Adsorption Measurements: ..... 92
4.3.6 Saccharide Analysis ..... 93
4.4. Results and Discussion ..... 93
4.5. Conclusions ..... 106
5. IMPRINTING OF STÖBER PARTICLES TO TARGET MONOSACCHARIDES AND DISACCHARIDES FOR APPLICATION IN CHIRAL SEPARATION ..... 120
5.1 Summary ..... 120
5.2 Introduction ..... 121
5.3 Materials and methods ..... 126
5.3.1 Materials ..... 126
5.3.2. Particle synthesis ..... 126
5.3.3. Particle characterization ..... 127
5.3.4. Saccharide Adsorption Measurements ..... 128
5.3.5. Saccharide Analysis ..... 128
5.4 Results and Discussion ..... 129
5.5 Conclusion ..... 136

6. INCORPORATION OF TITANIUM IN SILICA STRUCTURES USING SACCHARIDE SURFACTANTS TO STABILIZE AND LOCALIZE TITANIUM PRECURSORS ..... 146
6.1. Summary ..... 146
6.2. Introduction ..... 147
6.3 Experimental Section ..... 152
6.3.1 Materials ..... 152
6.3.2 Synthesis ..... 152
6.3.3 Catalytic testing ..... 156
6.3.4 Material characterization ..... 157
6.4. Results and discussion ..... 158
6.4.1 Titanosilicate thin films ..... 158
6.4.2 Titanosilicate bulk materials ..... 158
6.4.3. Titania incorporated Stöber particles ..... 162
6.5. Conclusion ..... 164
7. CONCLUSIONS AND FUTURE WORK ..... 176
7.1. Conclusions ..... 176
7.2. Future work ..... 183
APPENDIX A ..... 187
A.1. Visual basic code to estimate micellar mole fraction ..... 187
A.2 Supplemental information ..... 190
APPENDIX B ..... 196
B.1. Calibration curves for xylose and glucose ..... 196
B.2. Sugar adsorption ..... 198
APPENDIX C ..... 205
APPENDIX D ..... 209
REFERENCES ..... 211
VITA ..... 257

## LIST OF TABLES

**Table 2.1.** cmc's , free energies of micellization and enthalpies of micellization for some glucosidic surfactants with varying tail length, head group and anomeric center. ..... 49

**Table 3.1.** Properties obtained for single surfactant demicellization obtained from fitting the model to the data and from experiments. ..... 82

**Table 3.2.** Comparison of cmc of C8G1/CTAB mixtures calculated using best-fit parameters from the models, from the onset of micellization in the ITC curves, from differential analysis of the ITC data, and ideal values based on literature cmc values of C8G1 and CTAB..... 82

**Table 3.3.** Summary of dilution parameters providing best fits for Models 1 and 2. ..... 83

**Table 4.1.** Physical characteristics of particles synthesized with low-concentration ammonia with and without various surfactants, determined using nitrogen adsorption, SEM and DLS. ..... 117

**Table 4.2.** Langmuir isotherm parameters found by nonlinear regression for D-glucose and for D-xylose adsorbed to all silica samples. The curves corresponding to these parameters are shown in Figure 4.2.[a] ..... 118

**Table 4.3.** Synthesis conditions for particles prepared with fresh, saturated ammonia and varying ratios of surfactants, time of surfactant addition and temperature, and their physical characteristics determined using nitrogen adsorption, SEM and DLS. ..... 119

**Table 5.1.** Physical characteristics of particles prepared without surfactant, with a 1:1 mixture of CTAB and C8G1 and with a 1:1 mixture of CTAB and C12G2. ..... 145

**Table 6.1.** Textural and surface properties of titanosilicates..... 175

**Table 6.2.** Catalytic activity of titanosilicates with varying titanium content..... 175

## LIST OF FIGURES

**Figure 2.1** The figure shows the basic setup of an ITC instrument working on power compensation method and raw data obtained for a general case (From Freyer, M W and Lewis, E A, Methods in Cell Biology, 2008(*153*). Produced with permission. ..... 45

**Figure 2.2** Explanation of x-ray diffraction to obtain constructive interference. (Produced with permission from Smith, F. Industrial Applications of X-Ray Diffraction Smith, 1999, CRC Press (*158*)). ..... 46

**Figure 2.3** Schematic representation of perfect, imperfect crystals and amorphous materials. Adapted from Heiney et al(159)..... 47

**Figure 2.4.** Common classifications of the adsorption isotherm. Adapted from Sing et al(171). ..... 48

**Figure 3.1.** Representation of thermodynamic cycle used to represent demicellization of a non-ideal mixed micelle when the concentration of the system after injection of an aliquot is below the cmc of the mixture. ..... 74

**Figure 3.2.** Representation of thermodynamic cycle for demicallization of a non-ideal mixed micelle when the concentration in the ampoule is above cmc of the mixture. ..... 75

**Figure 3.3.** (a) Enthalpy vs. concentration diagram for (a) CTAB injected from a syringe containing 8 mM CTAB into an ampoule containing water and (b) C8G1injected from a syringe containing142 mM C8G1 into an ampoule containing water. ..... 76

**Figure 3.4.** Enthalpy vs. concentration diagrams for demicellization experiments measured using ITC for 0.25, 0.5, 0.75, 0.83 bulk mole fraction of C8G1 in C8G1/CTAB mixed surfactant solutions. The total concentrations of surfactants in the syringe used for these experiments were 12 mM, 8 mM, 60 mM and 80 mM, respectively. ..... 77

**Figure 3.5.** Experimental and best-fit enthalpy vs concentration diagrams obtained by fitting Model 1, in which enthalpy of dilution was modeled using all terms in equation 3.13. The plots are divided into (a) low concentration experiments with 8 mM CTAB, 12 mM 3:1 CTAB:C8G1 and 8 mM 1:1 CTAB:C8G1 and (b) high concentration experiments with 60 mM 1:3 CTAB:C8G1, 80 mM 1:5 CTAB:C8G1 and 142 mM C8G1. ..... 78

**Figure 3.6.** Experimental and best-fit enthalpy vs concentration diagrams obtained by fitting Model 2, in which enthalpy of dilution was modeled using all terms in equation 3.14. The plots are divided into (a) low concentration experiments with 8 mM CTAB, 12 mM 3:1 CTAB:C8G1 and 8 mM 1:1 CTAB:C8G1 and (b) high concentration experiments with 60 mM 1:3 CTAB:C8G1, 80 mM 1:5 CTAB:C8G1 and 142 mM C8G1. ..... 79

**Figure 3.7.** Critical micellar concentrations plotted against C8G1 mole fraction in the bulk mixture. The ideal/literature curve refers to cmc values obtained for pure surfactants

from literature along with an ideal model (β=0) for cmcs of mixed surfactants. Models 1 and 2 are curves plotted using the best-fit parameters from the two models. The points labeled "onset" are calculated based on the slope change in the ITC curve corresponding to the onset of micellization and the points labeled "differential" are calculated from the extremum in the derivative of heat with respect to concentration in the ITC curves. ..... 80

**Figure 3.8.** Calculated mole fraction of C8G1 in the micelle as a function of total bulk surfactant concentration for surfactant solutions at each injection step for mixtures containing 3:1, 1:1, 1:3 and 1:5 CTAB:C8G1. Curves are plotted using (a) best-fit Model 1 parameters and (b) best-fit Model 2 parameters. ..... 81

**Figure 4.1.** (A) High wavenumber and (B) low wavenumber regions of the FTIR spectra of imprinted Stöber particles, showing the presence of surfactant on the particles before washing and its removal upon washing. Spectra are shown for (a) sample 1, non-imprinted silica, (b) sample 2, prepared with CTAB, (c) sample 3, prepared with C8G1, (d) sample 4, prepared with a 1:1 CTAB / C8G1 mixture, (e) crystalline C8G1 and (f) crystalline CTAB. Spectra labeled with primes (a' through d') are the spectra of washed samples 1-4, respectively. ..... 108

**Figure 4.2.** Representative SEM micrograph of monodisperse nonporous silica particles synthesized using the Stöber process, with imprinting using a 1:1 mixture of CTAB and C8G1 by weight (sample **4**). SEM micrographs of all other samples are qualitatively similar, and included in the Supplemental Information. ..... 109

**Figure 4.3.** Comparison of adsorption isotherms for D-glucose and D-xylose adsorbing from aqueous solution onto (a) sample **1**, non-imprinted particles, (b) , sample **2**, prepared with CTAB, (c) sample **3**, prepared with C8G1, and (d) sample **4**, prepared with a 1:1 mixture of CTAB and C8G1. The vertical axis represents moles of saccharide adsorbed per $m^2$ of silica particle area, and the horizontal axis represents the final moles of sugar per liter of solution. Curves are best-fit Langmuir isotherms found by globally optimizing adsorption parameters for all adsorbents (see text for further explanation). 110

**Figure 4.4.** Adsorption isotherms for adsorption of glucose onto particles prepared with different ratios of surfactants (samples **5-8**), expressed as moles of glucose per $m^2$ of particle surface vs. moles of glucose remaining per liter of aqueous solution. ..... 111

**Figure 4.5.** FTIR absorbance curves for unwashed Stöber particles in KBr pellets. All samples (numbers **8-12**) were imprinted with a 1:1 mixture of CTAB and C8G1 by addition of the surfactant at the indicated times after addition of TEOS. The $CH_2$ stretching bands between 2800 and 3000 $cm^{-1}$ indicate surfactant incorporation in the particles. ..... 112

**Figure 4.6.** Moles of sugar adsorbed per area as a function of the time of addition of surfactant during the particle synthesis (for samples **8-12**). Results are shown for three different initial glucose concentrations, indicated in the legend. The rightmost set of points is for sample **5**, prepared without any surfactant added. ..... 113

**Figure 4.7** FTIR absorbance spectra for 1:1 CTAB / C8X1 imprinted Stöber particles (sample **13**) before and after washing to remove the template. The siloxane stretching band is visible between 1000 and 1300 $cm^{-1}$, and the $CH_2$ stretching band (indicating the presence of surfactants) is visible between 2800 and 3000 $cm^{-1}$ in the unwashed sample. ..... 114

**Figure 4.8.** Adsorption isotherms for xylose and glucose on comparable particles imprinted with a 1:1 mixture of C8X1 and CTAB (sample **13**) or prepared without surfactant (non-imprinted, sample **14**). ..... 115

**Figure 5.1.** Projections of the 3D geometry of the monosaccharides investigated in this study: (a) D-glucose, (b) D-galactose, (c) L-glucose and (d) D-mannose. The structures are all optimized using the Universal Force Field (UFF) as implemented in Avogadro, and the translucent surfaces are van der Waals surfaces colored by electrostatic potential. Hydrogen atoms were used for geometry optimization and to generate the surfaces, but are not depicted in the stick geometries shown. The circled atoms in (b) and (d) are the oxygen atoms with different chirality from D-glucose ..... 139

**Figure 5.2.** SEM images after washing and drying of particles made A) without addition of surfactants and B) particles prepared with addition of 1:1 mixture of CTAB and C8G1. ..... 140

**Figure 5.3.** FTIR spectra of Stöber particles in KBr pellets. (a) Washed non-imprinted Stöber particles, (a') As synthesized Stöber particles without surfactant addition, (b) Washed Stöber particles imprinted with 1:1 CTAB/C8G1 mixture, (b') As synthesized Stöber particles imprinted with 1:1 CTAB/C8G1 mixture by adding surfactant at 1 minute after TEOS addition. ..... 140

**Figure 5.4.** Comparison of the results of adsorption from aqueous solution of D-glucose and (A) L-glucose, (B) D-galactose and (C) D-mannose. The figures show that there is a higher preference for adsorption of D-glucose on C8G1 imprinted materials compared to other hexoses, while no significant difference is observed for adsorption of hexoses on non-imprinted Stöber particles. ..... 141

**Figure 5.5.** 3D structures of (a) cellobiose and (b) maltose obtained by starting with the experimental coordinates and performing geometry optimization with the UFF potential. The translucent surfaces are van der Waals surfaces colored by electrostatic potential using Avogadro. Note that the left glucopyranose units are oriented in roughly the same way in both molecules. ..... 142

**Figure 5.6.** SEM images of C) 1to1 CTAB and C12G2 imprinted nanoparticles. ..... 143

**Figure 5.7.** FTIR curves for particles imprinted with 1:1 mixture of CTAB and C12G2 before and after washing. $CH_2$ stretching bands can be seen between 3000 and 2800 $cm^{-1}$ before washing which are absent after washing. ..... 143

**Figure 5.8.** Adsorption of maltose and cellobiose on maltose imprinted Stöber particles and non-imprinted Stöber particles ..... 144

**Figure 6.1.** FTIR for titanosilicate thin films with increasing amount of titania incorporation from bottom to top. The figure shows increase in the intensity of the peak at 960 $cm^{-1}$ as the amount of incorporated titanium increases. ..... 166

**Figure 6.2.** Nitrogen adsorption isotherms for mesoporous titanosilicates..... 167

**Figure 6.3**. Pore size distribution for mesoporous titanosilicates estimated using the KJS method..... 168

**Figure 6.4.** Low angle X-ray diffraction pattern for mesoporous titanosilicates and pure mesoporous silica. ..... 169

**Figure 6.5.** FT-IR absorbance spectra of titano silicates with varying Ti content (a) TS-1 (Ti ~2.9 %) and mesoporous titanosilicates with Ti content corresponding to (b) no Ti (c) Ti ~7.4 % (d) Ti ~5.35 % (e) Ti ~3.29% and (f) Ti~1.14% ..... 170

**Figure 6.6.** Ratio of the integrated areas of the 960 and 800 $cm^{-1}$ IR bands with respect to the framework titanium content in different bulk titanosilicate powders. ..... 171

**Figure 6.7.** Diffuse reflectance UV-visible spectra of samples (a) $BaSO_4$ as background (b) $SiO_2$ (Ti~ 0 %) (c) TS1 (Ti ~2.9 %) (d) S-3 (Ti ~5.35%) (e) S-1 (Ti~1.14%) (f) S-2 (Ti ~3.29%) (g) S-4 (Ti ~7.4%) and (h) $TiO_2$ (Ti ~100%). ..... 172

**Figure 6.8.** Conversion and selectivity of various titanosilicate samples with respect to Ti content. With increasing mol percentage the samples go from S1 (1.29% titanium) to S4 (7.1 % titanium). ..... 173

**Figure 6.9.** Reflectance spectra of calcined and uncalcined titanosilicate Stöber particles collected using ATR. A) Spectra between 2600 and 3000 $cm^{-1}$ wavenumber, showing peaks between 2900 $cm^{-1}$ and 3000 $cm^{-1}$ associated with $CH_2$ stretching before calcination and disappearance of such peaks after calcination. B) Spectra between 700 and 1700 cm-1 shows siloxane stretching band with peak at 1050 cm-1 and a peak at at 960 cm-1 due to Si-O-Ti vibrations and Si-OH bond vibrations. After calcination the intensity at 960 cm-1 reduces due to removal of surface hydroxyl groups and residual intensity as a result of Si-O-Ti vibrations is observed. ..... 174

# CHAPTER ONE

## 1. INTRODUCTION

Surfactants from an important category of chemicals which find multiple applications in industry and the laboratory due to their amphiphilic nature. Saccharide surfactants represent an important class of amphiphiles due to their possible production from renewable resources and biodegradability. However, saccharide surfactants alone do not always confer the set of properties needed for a given application. Surfactant mixtures are often used in industrial applications instead of a single surfactant due to their superior properties compared to individual surfactants(*1-3*). Mixtures of non-ionic (such as sugar-based) and ionic surfactants often exhibit synergism which tends to lower the cmc of the surfactants and the surface tension of their solutions compared to ideal surfactant mixtures(*4*). In our lab templated porous materials have been synthesized using mixtures of cationic surfactants and saccharide surfactants(*5, 6*). The long-term goal of their use for materials synthesis is to utilize the saccharide headgroups to imprint the surface of the materials with selective adsorption and catalytic sites. Thus, understanding the behavior of mixtures of cationic and saccharide surfactant in micelles at low concentrations may help in screening surfactants for synthesis of templated materials.

Mixtures of cationic surfactants and saccharide surfactants have been studied experimentally using a variety of techniques in the past(*2*). From a theoretical point of view, modeling the mixing behavior of surfactants is a challenging problem that has been approached from a variety of directions(*7*). Significant models have been proposed by the Blakschtein group(*4, 8-10*) and by Nagarajan(*11*). Despite the availability of detailed models, experimental data are often not detailed enough to justify their use. Rubingh's

model,(*12*) which is based on regular solution theory (RST), is often used to model the effects on the critical micelle concentration (cmc) of nonideal mixing as represented with a single thermodynamic parameter (β) which can be used to compare the degree of non-ideality of various surfactant mixtures. RST assumes that the excess entropy of mixing is zero and the validity of the model has been questioned by Hoffman and Poessnecker(*13*). Despite its limitations, its widespread use in surfactant systems makes RST a reasonable starting point for the development of a nonideal surfactant thermodynamic mocel. In this dissertation, a model for isothermal titration calorimetry (ITC) has been developed using RST and applied to cationic / saccharide mixtures.

In addition to these fundamental studies, mixed surfactants are of particular interest to our group as novel metal oxide templating systems. Silica surface can be functionalized or imprinted to create sites complementary to the template molecule. It has been hypothesized that the polymerization of silica precursor around template molecules can be used to create molecular recognition sites specific to a particular molecule(*14*). In this regard, saccharide surfactants are of interest because the headgroup can create molecular recognition sites which are specific to a target saccharide and may lead to applications like sensing and separations. Molecular imprinting has been widely explored in the past using both organic and inorganic polymer matrices(*15-19*) for applications including catalysis, sensing and adsorption. In this dissertation, molecular imprinting will be explored on the surface of nonporous silica particles for preferential adsorption of targeted saccharide molecules.

In addition to bare surfaces, transition metals supported on silica are of significant interest due to their potential catalytic activity. Silica is an excellent support due to its

mechanical, chemical and thermal stability. Synthesis of templated materials, incorporating transition metals in the silica structure has been explored in the past(*20, 21*). The catalytic activity of the mixed metal oxides is high and arises from the variable oxidation and coordination states of transition metals. Saccharide surfactants during such a synthesis could play a dual role of reducing the reactivity of transition metal oxide precursors and acting as structure directing agents. Use of saccharide surfactants will be demonstrated in this work for synthesis of porous and nonporous titanosilicates.

## 1.1 Research Hypothesis

Three hypotheses will be tested in this dissertation. First, during modeling of the non-ideal mixing behavior of surfactants, it is hypothesized that a model for the thermodynamics of mixing based on RST can model the non-ideal mixing behavior of cationic and saccharide surfactants. Consistent application of RST to thermodynamic data obtained using Isothermal Titration Calorimetry (ITC) will be explored to model the broad micellization transitions observed for some non-ideal surfactant mixtures.

The second hypothesis tested is that Stöber(*22*) silica particle can be imprinted for a desired target molecule by adding a mixture of surfactants that includes an analogue of the target at a point just after the particles form. It is believed that such a process will be tunable for selectivity towards various saccharides through minor changes in the synthesis procedure and selection of the right surfactant mixture. Such nonporous imprinted materials are expected to be selective adsorbents with low diffusion resistance, and could be used for sensing applications as well. It is also hypothesized that such molecularly imprinted materials may demonstrate preferential adsorption based on chiral differences between the target saccharide and closely related compounds.

The third hypothesis is that it is possible to synthesize porous or nonporous metal-silicates with well distributed transition metal sites using complexation of saccharide surfactants with the transition metal oxide precursor. The complexation is expected both to reduce the hydrolysis rate of the transition metal precursor and to help distribute metal sites throughout the material.

## 1.2 Research Contribution

The work shown in the dissertation mainly contributes to the fields of material synthesis and thermodynamics of non-ideal surfactant mixing. Chapter 2 presents a literature survey of areas addressed, building a foundation for the work shown in the dissertation. Some of the experimental techniques used in the work are also discussed here in detail. In chapter 3, Isothermal Titration Calorimetry (ITC) is used to measure the demicellization thermodynamics for a surfactant system consisting of hexadecyltrimethylammonium bromide (CTAB) and n-octyl-β-D-glucopyranoside (C8G1). A model is developed for this non-ideal surfactant mixture through application of regular solution theory and applied to the CTAB / C8G1 system.

Chapter 4 demonstrates the use of CTAB and C8G1 to synthesize imprinted nonporous materials capable of preferential adsorption of D-glucose compared with D-xylose. The chapter also discusses experiments performed to support the hypothesis that early time of addition (around 1 minute after silica precursor addition) is the best time of addition to get maximum amount of surfactant onto the surface of particle as well as to show best enhancement of imprint molecule adsorption. Versatility of the method is shown through use of a different saccharide surfactant (n-octyl-β-D-xylopyranoside (C8X1)), to target D-xylose adsorption. Chapter 5 extends the use of the molecular imprinting technique described in Chapter 4 to study the difference in adsorption of

saccharides differing in chirality. Materials imprinted for D-glucose have prepared for comparison of the adsorption of D-glucose, D-mannose, D-galactose and L-glucose. Synthesis of materials imprinted with a combination of CTAB and n-dodecyl-β-D-maltopyranoside (C12G2) is also demonstrated. The synthesized materials are used to compare adsorption of D-maltose and D-cellobiose, which differ from each other only by the anomeric form of the 1,4 glucosidic linkage.

Chapter 6 will discuss a collection of work done on the synthesis of mesoporous thin films, bulk materials and nonporous materials incorporating titania within the silica framework. Thin films are synthesized first to demonstrate the incorporation of isolated tetracoordinated titanium sites through ligand assisted templating. Bulk titanosilicates are then synthesized and characterized for use as epoxidation catalysts to further demonstrate the presence and utility of tetracoordinated titanium sites. Finally, the possibility of incorporation of titania by surfactant complexation during the synthesis of nonporous particles is also demonstrated in this chapter. Chapter 7 provides a summary of the research presented in the dissertation and discusses potential future direction suggested by this research.

Copyright © Suvid Joshi 2014

# CHAPTER TWO

# 2. BACKGROUND

## 2.1. Summary

This chapter briefly reviews prior work relevant to remaining chapters of this dissertation. The first part discusses saccharide surfactants and their technological importance. This section also contains a discussion of the thermodynamic effects of surfactant headgroup, anomeric form and tail length. Adsorption of glucosidic surfactants on solid surfaces is also discussed. In the second part, mixtures of glucosidic surfactants with other surfactants are discussed, and the application of regular solution theory to mixture of surfactants studied in Chapter 3 is developed. Adsorption of mixtures of surfactants is also discussed with primary focus on cationic/non-ionic surfactant mixtures. The third part of chapter discusses molecular imprinting strategies with emphasis on imprinting of inorganic materials. The same section also discusses various routes that have been reported to synthesize imprinted materials and the use of surfactants to develop imprinted sites on inorganic materials. This is relevant to Chapters 4-5 of the dissertation. Synthetic methods of forming silica materials are then discussed with methods involved in both porous, nonporous and thin films synthesis. The porous materials are discussed in relation with strategies involved in pore templating and coassembly of surfactants and inorganic species to form networked structures. Incorporation of metal oxides in the silica structure is also discussed. Finally, the chapter includes an introduction to several of the techniques used in the course of completion of this work including isothermal titration calorimetry (ITC), x-ray diffraction (XRD),

Fourier transform infrared (FTIR) spectroscopy, scanning electron microscopy (SEM), nitrogen adsorption porosimetry, and dynamic light scattering (DLS).

## 2.2 Introduction to saccharide surfactants

Surfactants are amphiphilic molecules with polar headgroups and nonpolar tails. They tend to arrange themselves at interfaces in an orientation that leads to reduction in surface energy. Saccharide surfactant are generally nonionic surfactants, with hydrocarbon tails and nonionic polar headgroups which are derivatives of sugars. Saccharide surfactants include sorbitan esters, sucrose esters, alkyl polyglycosides and other categories such as methylglucosides and anionic alkyl polyglycosides(*23*). Out of these, (poly)glucoside surfactants and their derivatives are of particular interest due to the possibility of synthesis from renewable resources, high biocompatibility, high surface activity, solid surface adsorption affinity, and biodegradability.(*23*) Emil Fisher discovered the reaction of alcohols with glucose to form alkyl glucosides more than 100 years ago(*24*). Further developments led to processes for the reaction of glucose with various lengths of alkyl chains. The reaction product is a mix of glucosides polymerized to various degrees and attached to alkyl chains and hence industrially the mix is known as alkyl polyglucosides(*23*). Glycosidic formulations find applications in detergency(*25*), as antifoaming agents(*26*), in synthesis of templated materials(*27*), in cosmetic applications, biomimetic sciences(*28*) and biochemical separations(*29*).(*23*)

Like all surfactants, alkyl polyglycosides undergo aggregation at concentrations above the critical micelle concentration (cmc). At the cmc, a steep change in enthalpy is generally observed, which is similar to changes observed during type I transitions in thermodynamics (melting of solids)(*23*). Similarity to other phase transitions has led to

the pseudo phase separation approach, in which micellar aggregates are treated as a new phase at equilibrium with a homogeneous monomer solution(*30, 31*). Enthalpic data for glycosides with varying chain lengths and different headgroups have been reported by various groups and are listed in Table 1. With increase in tail length, the surfactants aggregate at lower concentrations due to unfavorable interactions of hydrophobic chain with water. As would be expected, Boyd et al. reported a decrease in cmc with increasing chain length for maltosides and glucosides(*32*). On the other hand, with increasing polymerization in the headgroup, hydration would be expected to increase due to the increase in polar hydroxyl groups, which would correlate with an increase in cmc, but such behavior is not observed for maltosides and glucosides(*33, 34*). The tail length tends to govern the cmc for glycosides.

Glycosides are classified based on the headgroup, the tail length and chirality of the headgroup (α vs. β anomer or L vs. D isomer(*35*)). A large variation in bulk and surface properties of these surfactants is observed based on isomerization of the headgroup. The change in structure of the surfactants has significant thermodynamic and physicochemical effects. Solution properties of glucoside surfactant micellization in water have been studied using techniques including light scattering, fluorescence techniques, surface tension, speed of sound measurements, densitometry and NMR. It has generally been reported that α anomers have lower cmc values compared to β anomers, suggesting that α anomers aggregate more easily due to higher hydrophobicity caused by the orientation of the headgroup(*36-38*). The anomeric form also tends to influence the type of self-assembled structure formed – for example, Foscher et al.(*39*) reported difference in self assembled structures formed by α-C8G1 which formed large non-spherical aggregates

and β-C8G1 formed spherical micelles. The difference in anomeric structure influences orientation of polar residue and in turn influencing packing of monomers. Table 1 provides list of the effects of chain length, headgroup and anomeric center on the cmc of the surfactants. The Krafft temperature of α anomers has also been reported to be higher than for β anomers, consistent with lower aqueous solubility of the α anomer(*40*).

Thermodynamic properties including the enthalpy, Gibbs free energy and entropy of micelle formation can be indirectly determined from cmc measurements using the van't Hoff relation(*41, 42*). Based on the pseudophase model, the Gibbs free energy of micellization for a nonionic surfactant can be determined from equation 2.1.

$$\Delta G_{mic}^{0} = RTln(cmc) \tag{2.1}$$

The van't Hoff equation then gives equation 2.2:

$$\Delta H_{mic}^{0} = \frac{\partial\left(\frac{\Delta G^{0}}{T}\right)}{\partial\left(\frac{1}{T}\right)} = -RT^{2}\frac{d}{dT}\ln(cmc) \tag{2.2}$$

The entropy of the system can then be determined as

$$\Delta S_{0}^{mic} = \frac{\Delta H_{0}^{mic} - \Delta G_{0}^{mic}}{T} \tag{2.3}$$

In addition to micellization, lyotropic liquid crystal behavior of glycoside surfactants has been studied to a significant extent. Nilsson et al. presented SAXS and NMR measurements regarding the liquid crystalline behavior of glucosides with varying carbon tail length from 8 to 10(*43, 44*). They observed similar behavior for 8 and 9 carbon chain where binary phase diagrams were dominated by large micellar regions and smaller

liquid crystal regions containing hexagonal region followed by bicontinous cubic phase and lamellar phase at high concentrations. They also observed that for C10G1 only two phases existed, either micellar or lamellar. Boyd et al. discussed the effect of maltosides in comparison to glucosides in lyotropic phase formation(*45*). They concluded that increasing degree of polymerization in headgroup had significantly increased surfactant solubility. Increasing chain lengths significantly impacted lyotropic phase behavior due to hydrophobic effects leading to phase separation at low concentrations. It was also observed that the anomeric configuration had large effects on lyotropic phases for shorter chain lengths, but the effects diminished for longer chains. Apart from these studies Boyd et al(*32*) and Platz et al(*46*) have also drawn similar conclusions about phase behavior of alkyl glucosides.

Adsorption of glycosidic surfactants on both hydrophilic and hydrophobic surfaces has been studied in the past. Zhang et al studied the adsorption of C12G2 on alumina and silica at pH 7 and 25 ˚C. It was observed that the adsorption of saccharide surfactants took place in three stages. Initially the surfactants form a monolayer on the solid surface in the first stage. In the second stage adsorption hemimicelles or solloids are formed due to chain-chain interactions and in the third stage a plateau region is observed. The region of change in slope between second and third stage is cmc of the surfactant associated with formation of micelles on the solid surface. Although in the study, alumina adsorbed surfactant strongly, on the silica surface the adsorption was negligible(*47*).

Adsorption on the alumina surface has also been reported based on changes in the surfactant headgroup, tail length, pH of the medium and addition of salt. It was reported that with a change in headgroup from maltose to glucose the amount of adsorbed

surfactant increased. Closer packing due to smaller headgroup was reported as the reason. With change in tail length the inflection point at the point of surface saturation varied based on the cmc of the surfactant(*23*). The S shaped adsorption isotherms indicated stronger surfactant-surfactant interactions compared to surfactant solid interactions(*48*). The S shaped curves indicate weak driving force for adsorption at low concentrations. Stronger interactions, like electrostatic forces would lead to higher driving force for adsorption and a slope of 1 at lower concentrations(*49*). Through change in pH it was observed that the adsorption of surfactants on alumina was not affected by the charge on the solid surface(*47, 50*).

Although adsorption has been studied on fully formed solid surfaces, the study in the thesis will talk about adsorption of surfactants during formation of silica particles when particles are still soft. The surfactant amount used is just enough to form a monolayer on the silica surface and no micelle formation at solid liquid interface is expected.

**2.3 Mixed micelles involving saccharide surfactants**

As mentioned earlier, due to biodegradability and potential synthesis from renewable resources, glycosidic surfactants are of significant current interest. Using mixtures of surfactants can extend their applications, especially when synergy arises in their interfacial properties due to favorable interactions between the components of the mixture. Mixtures that include sugar surfactants have been shown to reduce the amount of surfactant required for microemulsion stabilization(*51*), to provide better detergency in mixtures with cationic surfactants(*52*), to enhance micelle enahanced ultrafiltration,(*53, 54*) and for micellar catalysis(*23, 55*). A novel potential application of these mixtures would be in materials synthesis. In addition to the advantages of sugar-based surfactants found in other applications, their interactions with metal oxide precursors and organic

groups are of interest to our group for potential molecular imprinting to impart selectivity towards sugars. Mixtures of surfactants have been used as micellar templates for synthesis of ordered porous materials(*56, 57*) and sugar surfactants mixed with cationic surfactants have been shown to be applicable to materials formation in concentrated lyotropic liquid crystal-like solutions(*5, 6*). In this section, mixed surfactant micelle thermodynamics and studies of mixed sugar surfactant systems are discussed.

### 2.3.1 Thermodynamic models

Mixed surfactant systems have been well studied over the past few decades(*55*). Learning the solution behavior of surfactants and surfactant mixtures is important both for fundamental understanding of these systems and for developing their applications. Solution thermodynamics has been well studied and theoretical aspects of micellar thermodynamics have been summarized by Hines(*7*), and models proposed for micellization have been summarized by Nishikido(*58*). Various thermodynamic theories have been proposed to consistently explain micellization behavior and thermodynamics in mixtures by Nagrajan(*11*), Blankschtein and coworkers(*4, 9, 10, 59*), Maeda(*60*), Motomura(*61*), Clint(*62*), and Holland and Rubingh(*12*). The thermodynamic framework of Clint for ideal mixtures of surfactants and the regular solution theory model of Holland and Rubingh for non-ideal surfactant mixtures are here. Both models are based on pseudophase approximation approach. In the pseudophase approximation, micelles are assumed to act as a separate phase from the bulk monomeric phase, and thermodynamic equilibrium between the micellar phase and the monomeric phase is used to develop required relationships. Clint's(*62*) model utilizes the pseudo phase approximation to give a thermodynamic model for ideal mixture of surfactants. The model begins by defining

the chemical potential of surfactants in monomeric and micellar form. Assuming activity coefficients of one for monomers,

$$\mu_i = \mu_i^0 + RTln(C_i^m) \quad (2.4)$$

Where $\mu_i^0$ is the standard chemical potential and $C_i^m$ is the concentration of monomeric surfactant *i* in the bulk solution. For a mixed micelle the chemical potential of the i$^{th}$ component in a micelle with ideal mixing can be expressed in a pseudo-equilibrium framework as(*62*):

$$\mu_i^M = \mu_i^0 + RTln(C_i) + RTln(x_i) \quad (2.5)$$

where $C_i$is the cmc of the pure component $i$, $x_i$is the surfactant mole fraction of $i$ in the micelle. At equilibrium,$\mu_i = \mu_i^M$and so using equations **2.4** and **2.5** leads to:

$$C_i^M = x_i C_i = \alpha_i C^* \quad (2.6)$$

Where, $\alpha_i$is the mole fraction of i$^{th}$ component in the total mixed solute, and $C^*$is the cmc of the mixture. For an *n* component ideal mixture, the cmc of the mixture is calculated as:

For a binary surfactant mixture above cmc the mole fraction of surfactant 1 in the micelle ($x_1$) can be written as,

$$C^* = \sum_1^n \left(\frac{\alpha_i}{C_i}\right) \quad (2.7)$$

Based on phase separation approximation, applied to ideal micelles.

For a binary surfactant mixture above cmc the mole fraction of surfactant 1 in the micelle ($x_1$) can be written as,

$$x_1 = \frac{\alpha C - C_1^m}{C - C_2^m - C_1^m} \tag{2.8}$$

For the specific case of a binary mixture, equation 2.8 can be used to substitute *x* in equation 2.6 and written as a quadratic and solved to give the concentration of each monomer in solution as a function only of the cmcs of the pure components, overall mole fraction, and total surfactant concentration:

$$C_1^m = \frac{-(C - \Delta) \pm \sqrt{(C - \Delta)^2 + 4 * \alpha * C * \Delta}}{2 * [\frac{C_1}{C_2} - 1]} \tag{2.9}$$

$$\Delta = C_2 - C_1 \tag{2.10}$$

In equation 2.8 C is the bulk surfactant concentration.

Holland and Rubingh(*12*) extended this model to non-ideal surfactant mixtures to develop a predictive model of the cmc of nonideal mixed surfactants. When non-ideality is introduced the chemical potential expression in equation 2.10 can be written as:

$$\mu_i^M = \mu_i^0 + RTln(C_i) + RTln(f_i x_i) \tag{2.11}$$

where $f_i$is the activity coefficient of the $i^{th}$ component in the micelle. Note that it is still assumed that the monomeric surfactants are dilute and behave ideally. With this modification, the mixed micellar cmc is given by:

$$C^* = \sum_{1}^{n} \left( \frac{\alpha_i}{f_i C_i} \right) \tag{2.12}$$

For a binary system, based on the regular solution theory (RST) the activity coefficients are given by:

$$f_1 = e^{(\beta(1-x_1)^2)} \tag{2.13}$$

$$f_2 = e^{(\beta {x_1}^2)} \tag{2.14}$$

where β is the thermodynamic interaction parameter which relates to the difference in the enthalpic interactions between the two components compared to their interactions with like compounds. Although RST assumes that the excess entropy of mixing is zero, the approximation is adequate to predict nonideal cmc trends and is widely used in practice(*23*). To further expand the applicability of the theory, an equation for the concentration of monomers of each type can be developed following the derivation of Clint, which leads to the following nonideal monomer concentration expression:

$$C_1^m = \frac{-(C-\Delta) \pm \sqrt{(C-\Delta)^2 + 4 * \alpha * C * \Delta}}{2 * [\frac{f_1 C_1}{f_2 C_2} - 1]} \tag{2.15}$$

$$\Delta = f_2 C_2 - f_1 C_1 \tag{2.16}$$

A visual basic function is used in excel to solve for the value of $x_1$ and $x_2$ using Newton Raphson method. For non-ideal surfactant mixtures, equation 2.6 can be written as:

$$C_i^M = x_i * f_i * C_i \tag{2.17}$$

Similarly for non-ideal binary surfactant mixtures equation 2.8 for the mole fraction of surfactant 1 in micelle can be written as:

$$x_1 = \frac{\alpha_1 C - x_1 f_1 C_1}{C - x_1 f_1 C_1 - x_2 f_2 C_2} \tag{2.18}$$

Where $\alpha_1$ is the mole fraction of surfactant 1 in the bulk and $C$ is the overall concentration of the surfactant solution.

Using equation 2.18 and substituting for $f_1$ and $f_2$ using equations 2.13 and 2.14 respectively, a nonlinear equation with only $x_1$ as the unknown can be obtained.

$$x_1{}^2\left(e^{(\beta x_1{}^2)}C_2 - e^{(\beta(1-x_1)^2)}C_1\right) + x_1\left(C + e^{(\beta(1-x_1)^2)}C_1 - e^{(\beta x_1{}^2)}C_2\right) - \alpha_1 C \tag{2.19}$$

Equation 2.19 has been solved in the work shown in Chapter 3 using Newton Raphson method. A differential of equation 2.19 was taken for the solution and a guess value 10 times smaller than the bulk mole fraction of surfactant with higher cmc value was used to calculate $x_1$. As excel cycles thorugh possible nonlinear solutions, the values of cmcs of surfactant 1 and 2 in the binary mixture model get updated, thus landing on a final value of micellar mole fraction and concentrations of surfactant in micellar and monomeric form.

### 2.3.2 Mixtures with cationic, anionic and nonionic surfactants

Mixtures of alkyl polyglycosides have been studied with various ionic and nonionic surfactants for quite a while. The studies involved either water as the medium or salt

solutions to see the effect of presence of ions on micelle formation. Ruiz edited a book that discusses such mixtures in detail(*23*).

Anionic and nonionic mixtures of glucosides with varying chain length with sodium dodecylsulphate (SDS) have been reported. It has been widely reported that mixtures of various anionic surfactants with glycosidic surfactants tend to negatively deviate from ideality(*63-65*). Mixtures of anionic and saccharide surfactants have also been studied in the presence of salts, where no particular trend in non-ideal behavior could be observed (*64, 66*). The interaction parameter (β) is negative, which represents the tendency of the mixture to form micelles below the concentrations dictated by ideal surfactant mixing. It has been suggested that adding small amount of ionic surfactant leads to reduction in steric hindrance between nonionic surfactant headgroups leading to reduction in the cmc of the system(*67*).

The most commonly studied mixtures of cationic and saccharide surfactants consist of alkyltrimethylammonium bromides (ATAB) and alkyl glucosides (CNG1). It has been observed that for interaction of C8G1 with ATABs that with increasing alkyl length the micellar mixtures deviate farther from ideality leading to more negative interaction parameters, which may be result of increasing chain length causing higher hydrophobicity(*68, 69*). Higher hydrophobic effects force the surfactants to form micelles at lower concentration and synergistic mixing is promoted, which leads to more negative thermodynamic interaction parameter. Mixtures of glycosides with other cationic surfactants have been reported to consistently show negative deviation from ideality to varying degree(*70, 71*). The thermodynamics of these systems has been mostly studied through application of RST using Rubingh's model(*12*).

Mixtures of nonionic surfactants with other nonionic surfactants have also been studied. Unlike ionic and nonionic surfactant mixtures, saccharide surfactants mixed with other nonionic surfactants show ideal behavior in some cases(*67, 70, 72, 73*), but there are some mixtures with nonionic surfactants which show deviation from ideality in absence of salt(*67, 70*) as well as in presence of salt(*67, 73*). The non-ideal behavior shows negative deviation from ideality. Sierra and Svensson suggested that such behavior could be result of favorable packing leading to formation of micelles at lower concentrations than ideal behavior would suggest(*67*). Tsamaloukas et al.(*74*) applied Clint's(*62*) model to mixing of maltosides with varying chain lengths to ITC data. The behavior of maltosides in water is ideal in nature. It was found that it was possible to model the enthalpic curves of mixtures of maltosides based on Clint's model(*62*). Apart from matching the demicellization curves for maltosides the fitting also provided the enthalpy of demicellization and cmcs of the pure components.

### 2.3.3 Adsorption of surfactant mixtures on solid surfaces

Adsorption of mixtures of saccharide surfactants with anionic and cationic surfactants on both hydrophilic and hydrophobic surfaces is documented(*23*). Due to the application at hand, mixtures of cationic and saccharide surfactants will be discussed here.

In a surfactant mixture, the species that adsorbs is called the active species and the species that coadsorbs on the solid is called the passive species. Usually ionic surfactants only adsorb on the surface of oppositely charged solids, while the adsorption of sugar surfactants is not generally affected by the charge of the solids. The interactions can be described as follows,

1. Active nonionic + active ionic/nonionic surfactants: This kind of interaction occurs when both surfactants favor adsorption on the solid. In the pre-saturation region synergistic adsorption takes place, while in plateau region antagonistic interactions result due to competition. Due to electrostatic interactions ionic surfactants adsorb more in the plateau region. Such interaction has been reported for SDS/ octaethylene glycol mono-n-dodecyl ether (C12EO8) adsorption on kaolinite(*75*).
2. Active nonionic + passive ionic surfactants: On similarly charged solids ionic surfactants become passive. Ionic surfactants co-adsorb in such a case through chain-chain interactions with active sugar surfactant. Nonionic surfactants also reduce electrostatic repulsions in such a case. In the plateau region the adsorption of mixture is lower than adsorption of just sugar surfactant in such a case.
3. Passive nonionic + active ionic surfactants: In presence of ionic surfactant with opposite charge as solid surface, the adsorption of sugar surfactant is aided by ionic surfactant through synergism. Chain-chain interactions promote adsorption of sugar base surfactants in the plateau region as well as preplateau region. Many such examples are available in the literature where an increase of sugar surfactant adsorption was reported by orders of magnitude in presence of an active ionic surfactant(*76-78*).

It was observed by Zhang et al.(*79*) that on a fully formed silica at pH 9, C12G2 did not adsorb, while in presence of dodecyltrimethylammonium bromide (DTAB) adsorption of the mixture took place. It was also reported that the synergistic interactions led to higher adsorption of DTAB from solution in presence of sugar surfactant before a

plateau due to surface saturation and formation of hemimicelles was observed. The adsorption amount increase in C12G2 adsorption is a result of hydrophobic chain-chain interaction while adsorption of DTAB resulted from electrostatic interactions.

Although these interactions are reported on fully formed solid surfaces, such interactions are expected to be relevant to imprinted Stöber particle synthesis for mixtures of CTAB and C8G1 when used as an imprinting mixture. It is believed that better surfactant/ surface interaction are likely to results due to electrostatic interactions of CTAB with the precipitated liquid-like silica precursors, leading to better interaction of soft silica with C8G1.

## 2.4. Molecular imprinting

Molecular imprinting is the technique of creating molecular recognition sites in a polymer matrix through use of a template. Molecular imprinting was reported nearly 60 years ago(*19*) and vast amount of literature is available on the same topic(*15, 17-19, 80-84*). Polyakov(*85*) and his group in 1931 revealed that silica prepared by addition of toluene, xylene or benzene led to adsorption advantage to the molecule added to the silica gel during preparation(*16*). The property was attributed to changes in the silica structure based on the additive. Dickey in 1949 reported that adding methyl orange at the beginning of silica synthesis led to creation of molecular recognition sites which demonstrated selectivity for methyl orange(*14*). Haldeman and Emmett later verified the results for other alkyl orange dyes and showed that the entrapped dyes interfered with the results of the experiments(*86*). Curti et al in 1950's also demonstrated chiral selectivity using molecularly imprinted silica as stationary phases in chromatographic columns(*87*). Klotz extended the molecular imprinting for methyl orange using polymers instead of

silica(*88*) and Wulff et al demonstrated imprinting of polymers for resolution of racemates(*89*).

Imprinting involves three steps starting with template selection followed by incorporation of the template into a matrix and removal of the template, leaving behind recognition sites(*19*). Multiple techniques can be used to develop molecularly imprinted sites in a material. The techniques are briefly discussed here; reviews by Collinson(*80*) and Alexander et al(*16*) provide elaborate discussions of the techniques.

Covalent imprinting involves covalent bonding of the imprinting molecule with the polymerizable group(*16*). The covalent bonds between the template and polymers must be chosen so that they can be broken to leave behind the imprinted functionality. Selectivity can be obtained by re-establishing the covalent bond with the target molecules. Though the bond formation is very specific, only a limited number of groups can undergo such imprinting(*16*). The rebinding kinetics in covalent imprinting approach is also found to be very slow. The examples of such imprinting are for carboxylic acids(*90*), amino acids(*91*), aldehydes(*92*), ketones(*93*) and various saccharide derivatives(*94-96*).

Non-covalent approach involves use of weak forces like hydrogen bonding, van der Waals forces, ion-pairing and dipole interactions(*16*) for molecular recognition. This method is most commonly used for imprinting due to simplicity. Removal of templates is very simple in this approach and washing may be enough to remove templates(*80*). Though the technique is simpler, non-covalent approach gives the possibility of non-specific binding. Arshady and Mosbach described the use of such technique as host guest complex formation to accomplish non-covalent binding with easy removal of

template(*97*). Collinson and coworkers have also demonstrated the non-covalent imprinting approach for sol-gel silica materials(*98, 99*).

Other approaches to molecular imprinting are available.(*16*) In stoichiometric non-covalent imprinting(*100*), the equilibrium favors the complex formed between polymerizable species and the imprinting molecule. The semi-covalent approach involves template binding through covalent bond formation. After template removal the sites left behind show non-covalent binding with target molecules. This technique provides uniform site distribution for binding. Sometimes a spacer is added in this approach to reduce formation of sites close to each other(*101*). Metal ion imprinting approach involves property of transition metals to form complexes with compounds as the active imprinting agent(*83*).

Imprinted silica materials find a large number of applications in selective catalysis, separation, adsorption and sensing(*19, 102*). Silica is chemically and thermally stable and has the ability to incorporate heteroatoms in the structure linked by covalent bonds. Due to higher stability, removal of templates in silica based materials using harsher conditions becomes possible. Silica based materials also provide the ability to block the non-imprinted sites using silanol chemistry. Due to the mild condition involved in the synthesis of such materials using sol-gel method it is also possible to imprint the materials for biomolecular recognition(*80*). It is also possible to process the silica based materials in various forms like bulk porous/nonporous materials, thin films and membranes. These advantages make silica materials useful for molecular imprinting.

Chapter 4 and 5 discuss imprinted materials for saccharide separations. Some examples of molecularly imprinted silica are discussed here for various applications like

detection, catalysis, sensing and separation. Dai et al demonstrated the use of silica based molecularly imprinted materials for enhanced metal ion sorption using $UO_2(NO_3)_2.6H_2O$ as template. The prepared material gave enhanced selectivity for uranyl ion(*103*) compared to a non-imprinted gel. Makote and Collinson(*98*) made molecularly imprinted silica films which demonstrated molecular recognition of dopamine. An example of chromatographic separation using imprinted silica as stationary phase was demonstrated by Curti et al. which showed partial resolution of enantiomers(*87*).

Enzyme mimicking catalysis has also been demonstrated on silica based materials by incorporating a metal site. Morihara et al. reported such enantioselective catalysis for alumina incorporated silica material(*104*). Markowitz et al(*105-107*) reported the synthesis of silica nanoparticles in reverse microemulsion where the surfactant used to stabilize the emulsion also acted as the imprinting molecule. The resultant material was shown to show higher selectivity for D-arginine catalysis compared to L-arginine.

Chemical sensing applications of molecularly imprinted silica have also been reported in the literature. Xie et al reported imprinting of silica nanotubes for TNT, where acid-base interactions between TNT and 3-aminopropyltriethoxysilane (APTS) led to creation of molecular recognition sites. The material was suggested by authors to be ideal for biomolecule imprinting and detection(*108*). Dickert and Hayden(*109*) imprinted polymers as well as sol-gel materials for whole yeast cells and coated QCM sensors. The sensors demonstrated detection till 21 g/L of yeast cells in growth medium. Valdes and group(*110, 111*) also reported molecular imprinting on silica surface for detection of toxins using fluorescence.

In this work nonporous particles with selectivity which can be tuned to a specific saccharide will be demonstrated. The nonporous particles are tunable to different saccharides with use of different surfactants. Chapter 4 and Chapter 5 describe the work on these particles.

## 2.5. Silica based materials

Silica is abundant in nature and is utilized as such to manufacture glasses which can be tuned to have certain properties by doping the structure with various atoms. Silica has tetrahedral networked structure with each silica atom linked to four oxygen atoms. Through a reletiavely recent innovation, silica can also be synthesized from silicon alkoxides and other silicon precursors using sol-gel synthesis. These materials can be tuned to be porous, nonporous and provide similar physical characteristics as silica. Dopants can be added to these silica networks during synthesis for catalysis. Some of the sol-gel materials are discussed here with emphasis on mesoporous and nonporous silica materials and their applications. The sol-gel process provides the advantage of processing metal and semi-metal alkoxides at room temperatures instead of high temperatures usually required to form metal oxide networks. Processing at room temperature provides the advantage of using organic molecules, like surfactants, as templates and structure directing agents. Chapters 4,5 and 6 demonstrate the use of surfactants as imprinting molecules and structure directing agents in synthesis of mixed metal oxides.

### 2.5.1. Sol-gel process

Sols are defined dispersion of colloidal particles in liquids. A gel is a rigid network of such colloidal particles which ranges over more than a micrometer(*112*). Sol-gel process can be broken down in to seven steps as described by Hench and West(*112*). The first step involves hydrolysis of the alkoxide species in the silica precursor. The hydrolysis

process can either be catalyzed by a base or an acid. The hydrolyzed species form a network consisting of Si-O-Si units. The sol can then be given a shape in the casting step. During gelation the colloidal particles formed lead to formation of three dimensional networks. During aging which takes place over a long period of time polycondensation continues and gives rigidity to the structure. Aging is followed by drying which involves removal of the liquid from the materials. Control of drying step is important to prevent materials from developing cracks. Dehydration and chemical stabilization is then carried out to remove surface silanol groups to obtain a non-reactive porous structure. The materials can then be heated at temperatures higher than a 1000 ˚C for densification which leads to elimination of pores. Though seven steps have been described here, not all the steps are carried out all of the time. In basic medium when a lot of water is present during synthesis the sol agglomerates to form particles, while in acidic conditions and limited amounts of water condensation of sol in to networked structures takes place(*113*), which can be dried to form porous materials.

### 2.5.2. Templated porous silicates

To explain ordered structure formation in mesoporous silicates various mechanisms were suggested. Kuroda, Inagaki and co-workers suggested a layered to hexagonal transition mechanism(*114, 115*). Davis and co-workers suggested a silicate rod-assembly mechanism, where a few layers of silicates deposit on the micellar surface and then the silicate rods assemble in ordered fashion to give the final mesostructure(*116*).

Stuckey and co-workers proposed the most widely accepted mechanism for organic-inorganic assembly through a cooperative formation mechanism(*117*). The mechanism suggested that silicate polyanions interact with the surfactants through coulombic forces.

The final mesophase forms in the self-assembled configuration with the lowest energy state possible. Further evidence of this was obtained through NMR, SAXS and polarized light microscopy(*118, 119*). The mechanism suggested that silicates interact with surfactants in four possible ways. In basic medium silicate anions ($I^-$) interact with surfactant cations ($S^+$) through coulombic forces. In strongly acidic medium cationic silicates and cationic surfactants interact in presence of a strong anionic group for aseembly ($S^+X^-I^+$), where X- is a strong anionic group like halogen, nitrate or sulfate. Similar to this the other pathways could be $S^-I^+$ and $S^-X^+I^-$. Pinnavia and co-workers suggested a mechanism for synthesis in neutral medium through hydrogen bonding(*120, 121*).

Surfactant templated materials can be synthesized by the hydrothermal method(*122*). In this approach the surfactants are initially dissolved in a solvent to obtain homogenous solution. Silica precursor is then added which undergoes either acidic or basic hydrolysis. The hydrolyzed species interact with the surfactants forming gels. The treatment of the gels formed in reaction mixtures at temperatures ranging between 80 to 150 ˚C is called hydrothermal treatment. The gels are treated to promote solidification of the network structure. Generally very high temperatures are not used to avoid degradation of surfactants which would lead to disordered structure. Removal of templates leads to formation of mesoporous silicates. To remove surfactants treatments like calcination in air, ultraviolet irradiation, solvent extraction and microwave digestion can be used.

Another route to synthesize templated mesoporous materials is true liquid crystal templating. This method was first demonstrated by Attard et al(*123*). When the concentration of surfactants is raised above the cmc, at a certain point the concentrated

solution starts behaving like a liquid crystal, which has a defined crystal structure as well as flow properties like liquids. The liquid crystal templating approach utilizes the concentration of surfactants in the liquid crystal range followed by addition of silica precursor which can be hydrolyzed to create templated materials. This method provides the ability to predict the final crystalline structure of silicates, which follow the crystalline structure of the liquid crystals.

The third route to prepare templated silicates is called evaporation induced self-assembly (EISA). At the beginning, the surfactant concentration in the solution is very low (below cmc). A solvent with low boiling point is used for such syntheses. A sol containing the hydrolyzed precursor and surfactants is initially prepared. The dilute solution is then coated in a thin layer on a substrate and, as the solvent rapidly evaporates, organized self-assembly of surfactants and silica takes place leading to formation of templated materials. The first example of this method was reported by Ogawa et al using spin coating technique(*124*).

### 2.5.3. Metal oxide incorporation into the silica framework

Mesoporous silicates make very good supports for incorporation of transition metal atoms due to their high surface area, uniform and controllable pore size and high thermal stability. Various transition metals including Ti, V and Cr have been incorporated in the silica structure to create catalysts. The catalytic activity of these metallosilicates results from the variable oxidation state of the transition metal atoms. In addition to use as catalysts, these materials have also been used in electronic, magnetic and optical applications(*125*).

Titanium containing silica materials are perhaps the most widely studied mixed oxides. Titanium containing zeolites TS-1(*126*) and TS-2(*127*) were synthesized as oxidizing agents for small molecules. These materials require mild conditions for oxidation but are limited in application due to their small pore size. It is possible to incorporate Ti in mesoporous silicates to catalyze bulkier molecule oxidation. Corma et al(*128*) and Tanev et al(*20*) reported synthesis of titanium containing MCM-41 materials. It was demonstrated that larger accessible pores provide better catalytic activity for oxidation of large organic molecules(*129, 130*). Sugar surfactants tend to form complexes with transition metals. Use of saccharide surfactants has been demonstrated in Chapter 6 to synthesize porous titanosilicates. Saccharide surfactants help in reducing hydrolysis rate of titania precursor and also acts as a templating agent. The reduction of hydrolysis rate helps in homogenously distributing titania in the mesostructure.

Titanium can be present in zeolite framework or it can be present as extra framework titanium. Titania is incorporated directly in the framework by replacement of tetravalent silicon. The extraframework titanium can have multiple valence states as it is not restricted by bond formation. It is necessary to incorporate titania in the zeolite framework as the isolated tetra coordinated sites are thought to be responsible for oxidation.(*131, 132*).

Titanium incorporation in materials frameworks can be obtained through sol-gel synthesis, but due to high reactivity of titanium alkoxides, it is necessary to stabilize it. Various methods including substoichiometric water addition(*133*) to hydrolyze the silica precursor, ligand stabilization of the precursor,(*134*) and the non-hydrolytic method(*135*)

have been suggested. Ligand stabilization has been used in work presented here to synthesize silicates with isolated titanium sites.

### 2.5.4. Nonporous silica particles

Synthesis of dispersions of monodisperse nonporous silica particles were first described by Werner Stöber et al. in 1968(*22*). In this work various reaction mixtures containing different alcohols, alkyl silicates, water and ammonia either dissolved in alcohol or as ammonium hydroxide were used to make particles of different size. It was reported that ammonium hydroxide not only catalyzed the hydrolysis, but was also important for particle morphology. It was reported that in the absence of ammonia, non-spherical particles of large size distribution were obtained. Bogush et al(*136*) reported variation in particle size as a function of temperature at various TEOS concentrations. They found that at a particular TEOS concentration the size of particles decreased with increase in temperature of synthesis. They also reported that narrow size distribution particles between 20 to 800 nm could be synthesized. The effects of variation of water concentration was also studied at room temperature. It was found that keeping other reaction conditions the same the size of particles varied like a bell curve. At low concentrations of water the particle size was small and systematically increased till a maximum size was obtained. Increasing the water concentration further led to reduction in size of the particles. The final solids density was low in these synthesis methods. Wang et al(*137*) reported a method to synthesize Stöber particles in high concentration of TEOS. Branda et al(*138*) reported effect of mixing alkoxides (3-Aminopropyltriethoxysilane (APTS) and TEOS) on the size of particles; they reported

that mixing alkoxides led to formation of fewer but larger particles. The behavior was explained using an aggregation model.

Stöber particles have been used as supports in various imprinting applications. For example, Li et al.(*139*) used silica as support and imprinted the coated polymer layer for paclitaxel. They observed two types of binding sites with different dissociation constants on such particles. Wu et al(*140*) synthesized core-shell particles for chiral separation application in high performance liquid chromatography. Gao et al(*141*) used Stöber particles modified with acrylamide shell for high density TNT imprinting. Direct modification of Stöber particles has also been reported by incorporating. For example Ow et al(*142*) synthesized core shell fluorescent silica particles by incorporation of dye molecule in Stöber synthesis method. Luckarift et al(*143*) demonstrated encapsulation of lysozyme in silica particles with implications in development of anti-fouling materials. Although multiple applications have been studied, direct imprinting of Stöber particles has not yet been demonstrated. To design such a technique it is necessary to understand the formation of Stöber particles.

Stöber particle formation in the past has been explained either through controlled aggregation model or monomer addition model. LaMer and Dinegar(*144*) proposed that all the nuclei for particles formed within a short period of time and that after that the growth of the particles took place by addition of monomers. The particle growth was limited by diffusion such that the smaller particles grew faster and larger particles grew slower. Matsoukas and Gulari(*145*) used Raman spectroscopy and dynamic light scattering to find that rate of hydrolysis of TEOS is equivalent to rate of particle growth. Thus, hydrolysis of TEOS was rate limiting step. Based on these results, Matsoukas and

Gulari(*146*) presented a model which was similar to LaMer. Dinegar(*144*) suggested that monomer addition with self-sharpening growth of silica particles formed through ammonia catalyzed hydrolysis of silicon alkoxides. Aggregation model suggests that the growth of particles initially occurs through aggregation of colloidally unstable nuclei till a point where aggregation no longer occurs. The particle smoothening takes place later. This model was suggested by Feeney et al. for formation of colloidal latex particles(*147*). Hochberg et al(*148*) found proof for formation of such nuclei after polyacrylamide reached a certain molecular weight when it phase separated. Bogush and Zukoski(*149*) used NMR and conductivity measurements to determine the growth kinetics of Stöber particles. They concluded that unlike monomer addition the growth of particles was not size limited and that surface reaction limited aggregative growth was happening. Rate of loss of hydrolyzed silica species was also found to be different than the rate of particle growth. The aggregation model was further supported by Kim and Zukoski(*150*) who, using the theory of colloidal stability, demonstrated that nuclei below the size of 20 nm would not be stable and would aggregate. Tan and Rankin(*151*) studied the formation of porous silica particles in the presence of CTAB and found that such particles formed initially by nucleation of disordered clusters, followed by aggregation of clusters to form particles and finally assembly of surfactant micelles at particle surface. Through TEM imaging they found particles with rough edges at 50 s after TEOS addition similar to those observed by Bailey and Mecartney(*152*) for Stöber particles. They also found that turbidity occurred at 60 s and that particles of final size with surface aggregated micelles were visible at 70 s.

Based on the evidence a strategy to imprint external surface of silica particles by adding surfactant at the point of turbidity (60 s after TEOS addition). It is expected that addition of just enough surfactant at such a point of time when particles are soft enough for surfactant interaction and have achieved their final shape would be helpful for direct molecular imprinting of silica surface in Stöber synthesis method. The synthesis and process optimization has been shown in chapter 4. Chapter 4 also demonstrates the use of such particles in selective adsorption of glucose/xylose on like imprinted materials. Chapter 5 demonstrates the use of such particles for enantiomeric separation of hexose and maltose imprinted particles for separation of maltose and cellobiose.

## 2.6. Characterization techniques

### 2.6.1 Isothermal Titration Calorimeter (ITC)

In ITC, the heat associated with a chemical or physical process occurring in one cell is compared with a cell maintained at a constant temperature. There are three different ways to measure heat change: a) temperature change, b) power compensation (isothermal) and c) heat conduction(*153, 154*). It is necessary to understand the type of calorimeter to understand what the raw data means. A very good review of the three methods is given by Lewis and Freyer(*153*).

In a power compensation calorimeter (the approach used here) the temperature of the cell is maintained constant by using a temperature sensor and a heater/cooler assembly. As a reaction or thermodyhamic process occurs, the power supplied to the heater/cooler to bring the system back to isothermal state is measured. The raw signal in an isothermal calorimeter is the power needed to keep the system isothermal as a function of time. The other two types of calorimeters operate under similar principles except that temperature changes or heat conduction are measured over time.

A typical schematic of a power compensation calorimeter is shown in **Figure 1**. Two cells are employed: a reference cell which usually contains a liquid with similar thermal properties to the liquid in the sample cell and the sample cell itself. A syringe is employed to inject titrant into the sample cell which contains either another reactant or a solution of the titrant at a lower concentration. The cells are surrounded with a large isothermal bath, and the system is kept in an adiabatic jacket to prevent any effects associated with external stimuli. The injection process is either carried out stepwise in small aliquots or as a batch process where all of the titrant is injected into the ampoule (sample cell) at one time. In the TAM III ITC instrument (TA Instruments), the sample and reference cells are submerged in an oil bath at a constant temperature. Raw data can be processed to generate enthalpy vs. concentration diagrams by integrating the area under the curve for each of the peaks associated with heat evolved in each single injection step.

For ITC measurements, samples were prepared in the syringe with at least 5 times the concentration of the expected or known cmc of the surfactant mixture. Care was taken to avoid very high concentrations to prevent crystallization of dissolved surfactants. In case of samples where surfactant was not easily solubilized, samples were heated up to 40 ˚C during initial formation to promote solubilization. Reference cell was always filled with liquid, with similar physical properties or the solvent in the experimental cell. The syringe, ampoule and stirring assembly were washed multiple times with DIUF water and then flushed with dry air to avoid contamination. While filling the ampoules with DIUF water during experiments, care was taken to make sure that the total volume after injection of sample from syringe did not go above the mentioned ampoule capacity.

Vacuum grease was applied along the edge of ampoule cover to prevent leaks in case the ampoule was filled. Syringe was filled till the edge to avoid air bubbles. It was necessary to handle the stirrers with care so as to avoid bending of the stirring rods. Experimental cell assembly was carefully lowered into the isothermal chamber in three steps separated by five minutes to avoid sudden change in isothermal chambers temperature. At least three hours were provided before starting the experiment to attain equilibrium. Enough time was provided between the injection steps to avoid crossover of tails of data peaks to the next injection step.

### 2.6.2. Fourier Transform Infrared Spectroscopy (FTIR)

FTIR investigates vibrational features in the infrared range of wavelengths (2500 to 16000 nm). Atoms connected with a covalent bond can be thought of as balls connected to springs (associated with bond stretching, bond bending and bond torsion). Atoms which are lighter or which are weakly bound vibrate at higher frequencies while heavier atoms or strongly bound atoms have lower vibrational frequencies. As the atoms vibrate the change in intensity is observed as peaks in absorption spectra. The difference in the vibrational energy of the atoms is given by(*155*)

$$\Delta E = h\upsilon = \frac{hc}{\lambda} \qquad (2.20)$$

Where h is the Planck's constant, c is the velocity of light, υ is the frequency and λ is the wavelength.

Various types of vibrational modes possible are stretching (asymmetric and symmetric) and bending (scissoring, rocking, wagging and twisting). Depending on the molecule, the same subunit may give rise to multiple bands due to these different modes.

However, if the modes are identified and distinct bands associated with a particular molecule are isolated, quantitative information may be obtained. An additional FTIR sampling mode useful for strongly absorbing is attenuated total reflection (ATR) FTIR. In this technique, the IR beam passes through a faceted infrared-transparent crystal in which it is internally reflected. The sample (here, an aqueous solution) is dispersed at the surface of the crystal. The evanescent wave generated at the surface of the crystal is the basis for the spectral measurement, and gives a total path length on the order of microns. This allows interfacial sampling or examining solids and liquids with a high extinction coefficient. Upon exiting the crystal, the infrared beam is reflected back through a series of mirrors to the detector.

This method has been utilized frequently in this work for qualitative as well as quantitative analysis. Most of the qualitative analysis was carried out using KBr pellets to determine presence of certain vibrations indicative of the presence of organic and inorganic species. The pellets were analyzed using a Thermo Nicolet Nexus 470 FTIR with nitrogen purged chamber. A DTGS detector with KBr beam splitter was used to obtain spectra. At least 128 scans at a resolution of 8 $cm^{-1}$ or higher were collected. KBr pellets were uniformly pressed using a mechanical pellet press with approximately 1 wt% sample dispersed in dry KBr. Presence of titania in silica framework during synthesis of porous titanosilicates was carried out using FTIR. Characteristic peaks associated with Ti-O-Si vibrations at 960 $cm^{-1}$ were observed(*156*). Similarly the presence of surfactants on Stöber particles as well as removal based on presence/absence of $CH_2$ stretching bands were utilized to see incorporation and removal of surfactant after washing. The band at 2849 $cm^{-1}$ is associated with symmetric stretching and the band at 2919 $cm^{-1}$ is associated

with asymmetric stretching(*157*). For analysis of thin films, the films were dip coated onto 200 μm thick silicon wafers, it was found that thickness higher than 200 μm was not gave poor quality spectra. A liquid nitrogen cooled mercury cadium telluride (MCT) detector was used to detect spectra for thin films.

FTIR-ATR was used as a quantitative technique to analyze saccharide solutions for adsorption studies. For all spectra, the ATR spectrum of DIUF water was subtracted to remove the hydroxyl stretching bands between 3400 and 3800 $cm^{-1}$. The bands associated with glucose have been isolated from a collective peak usually observed between 900 to 1500 $cm^{-1}$. Generally for sugars, OH vibrational spectra is observed between 3876 to 3005 $cm^{-1}$, CH vibrations are seen up to 2061 $cm^{-1}$. The C=O stretching is observed between 1850 to 1634 $cm^{-1}$ and so on. The region between 900 and 1200 $cm^{-1}$ was used to obtain calibration curves in the study. This region has a combination of CO and CC stretching bands between 1191 and 995 $cm^{-1}$. Some CH bending is also observed till 900 $cm^{-1}$ and below. The low wavenumber region between 600 and 1500 $cm^{-1}$ has been shown to have differences based on sugar under study. Elimination of OH vibrational bands by subtraction of ATR spectra for water created a flat baseline except in the region between 600 to 1500 $cm^{-1}$. Despite this, integrating using the region from 900 to 1200 $cm^{-1}$ was found to give a highly linear calibration curve. ATR accessory for Nexus 470 with a ZnSe crystal was used for analysis of liquids. For measurement of sugar solution supernatant for adsorption isotherms, samples were carefully withdrawn to avoid contamination due to silica particles. In case turbidity was observed the samples were pushed through a 200 μm syringe filter to remove silica particles.

### 2.6.3. X-ray diffraction (XRD)

Atoms in well-defined spatial arrangements tend to scatter or diffract x-rays in specific directions related to their structure. It is possible to measure the angle and intensity of a diffracted beam relative to the source to determine the spatial arrangement. The diffraction is possible using x-rays because their wavelength is on the order of atomic spacing. In this work XRD has been used to find the ordering of pores in synthesized titanosilicates. As the pore sizes are in the range of 2 to 3 nm the diffraction patterns are usually obtained at low angles. Silica is amorphous in nature and hence no peaks are obtained at higher angles. It may be possible that titania crystallites may give diffraction patterns at higher angles, but for the purpose of the work done here higher angle diffraction patterns were not collected for these materials.

Constructive interference of diffracted X-rays leads to intense peaks at particular angles. The constructive interference of x-rays is governed by Bragg's law(*158*).

$$n\lambda = 2dsin(\theta) \qquad (2.21)$$

In the above equation $\lambda$ is the characteristic wavelength of x-rays, $d$ is the inter-planar spacing and $\theta$ is the angle of the detector relative to the source. **Figure 2.2** shows how constructive interference is obtained. As the x-rays hit planes 1, 2, and 3 they are diffracted to give vectors represented as 1', 2', and 3'. Constructive interference occurs when the distance between the planes is a function of n times the characteristic wavelength (λ). The extra distance travelled by x-rays hitting plane 2 in comparison to plane 1 is given by 2dsin(θ), which is equivalent to n times λ where n is an integer.

The width of the peak in an x-ray diffraction pattern can be used as a measure of degree of crystallanity of a solid. If the peaks are narrow and sharp, the diffraction pattern corresponds to highly crystalline materials, if the peaks are broad in a diffraction pattern the pattern corresponds to imperfect crystals and amorphous materials don't give any well-defined peaks. The difference is illustrated in Figure 2.3 adopted from Heiney et al(*159*).

XRD patterns were collected for the mesoporous materials between 1.5 to 8˚ angles. The diffraction patterns were observed due to the diffraction from the inorganic walls of the porous materials. The mesoporous silicates are amorphous in nature and hence no diffraction patterns were observed for larger angles (above 10˚). Mesoporous titanosilicates usually give broad peaks in the low angle range indicating imperfect mesocrystals. Even though the pores are ordered locally, they are based on liquid crystal-like structures, which contain many curved defects that give rise to the broad peaks observed. In case long range order is present for the pores, multiple diffraction peaks can be obtained. Long range order also helps in determining the crystallographic structure of the pores based on reciprocal d spacing. For example 2D hexagonal phase is identified by a reciprocal d spacing ratio of 1:√3: √4: √7: √9 corresponding to (100), (110), (200), (210), (300) planes in the material. Similarly, Ia3d cubic phase is identified by reciprocal d spacing ratios of √6: √10: √14: √16: √18: √20 indexed as (211), (220), (321), (400), (420), (332), (422), etc.

### 2.6.4. Scanning Electron Microscopy

Scanning electron microscopy involves the use of high velocity electrons to scan the surface of a material. An electron beam generated using an electron gun is accelerated

through a series of condenser lenses (electromagnets) until it hits the sample. Usually nonconductive samples are coated with a conductive coating to prevent accumulation of electric charge. As the electron beam hits the surface of material under analysis, Auger electron, secondary electrons, back scattered electrons and x-rays are emitted. Various detectors are employed to collect information from the various types of scattering phenomenon. Secondary electrons which are a result of inelastic scattering are used to create the image of a surface. The secondary electrons have low energy (<50 eV) and are emitted from the K shell of atoms(*160*). The secondary electrons are detected by an Everhart-Thornley detector(*161*). SEM can be used to image objects and has resolution to the order of nm. In this work SEM has been used to obtain images of particles ranging between 300 to 600 nm. The sample were prepared by grinding the particle clumps using a mortar and pestle. In some cases the particles were suspended in either ethanol or water through sonication and a few drops of solution were used to distribute sample on the carbon tape. The solvent was allowed to evaporate in a fume hood in presence of flowing air. This was done to form a thinner sample layer promoting better conductivity of electron beam. The particles were coated with gold / palladium to promote conductivity.

### 2.6.5 Nitrogen adsorption

Nitrogen adsorption is a technique which is used to characterize the surface area and pore size for a material. It is non-destructive and provides accurate data as long as a sufficient quantity of adsorbent is provided. Nitrogen adsorption is carried out at 77 K and the materials are degassed at temperatures above 100 ˚C to remove any adsorbed moisture from the pores. Here these experiments will be used to measure the surface area

and pore size distributions in titanosilicates, and to confirm the absence of pores in nonporous particles and to confirm particle size based on the surface area.

According to the IUPAC nitrogen adsorption isotherms can be broadly classified in to six different categories. A diagram of the six different types of isotherms has been presented in **Figure 2.5**. Type I isotherms are typically associate with micropores and the relative pressure at which adsorption takes place is less than 0.1 ($P/P_0$). Type II isotherms are associated with nonporous materials where monlayer formation is succeeded by multilayer formation at high relative pressure. Type III isotherms are associated with mixed micro and meso porosity. Type IV are a result of weak gas solid interaction and originate from nonporous or mesoporous solids, where complete filling of small capillaries takes place. Type V isotherms are associated with both micro and mesoporous materials. Type V isotherms are also associated with weak interaction of probe molecule and material. Type VI isotherms represent stepwise multilayer formation on uniform nonporous surfaces(*162, 163*).

The specific surface area of porous and nonporous materials will be evaluated using the Brauner Emmett and Teller (BET) multilayer adsorption model(*164*). The model assumes that the adsorbed molecules in a monolayer don't interact with molecules adsorbed on other sites in the same layer. The molecules in the first layer are part of the surface for deposition of the second molecular level(*165*). The BET method takes into account the monolayer capacity while calculating the surface area of a material. Experimental data from adsorption experiments is used to fit the linear form of BET to obtain the surface area. BET isotherm is not valid over the complete isotherm range but is accurate between 0.05 to 0.3 $P/P_0$. The linearized form of BET is shown in equation 2.18.

$$\frac{\frac{P}{P_0}}{v(1-\frac{P}{P_0})} = \frac{1}{v_m c} + (\frac{c-1}{v_m c})\frac{P}{P_0} \qquad (2.22)$$

In the above equation $v$ is the adsorption capacity of the material at a given relative pressure, $v_m$ is the monlayer capacity and $c$ is a constant which depends on the heat of adsorption in the first layer. From the linearized form of BET the monolayer capacity can be determined using slope and intercept of a graph between $\frac{\frac{P}{P_0}}{v(1-\frac{P}{P_0})}$ and $P/P_0$. Since it is assumed that nitrogen molecules cover the complete area of the material during monolayer formation, multiplying the monolayer capacity with surface area of nitrogen molecule yields the surface area of the material.

Pore size distributions will be estimated using the Barrett, Joyner and Halenda (BJH) method(*166*) with corrections based on statistical film thickness suggested by Kruk Jaroniec and Sayari (KJS)(*167*). Usually the adsorption branch is used to determine the pore size distribution because imperfections in pores and cavitation may lead to delayed capillary evaporation in materials with hysteresis(*168*). The statistical film thickness is calculated using the Harkins Jura equation. As the pores start filling up a meniscus is formed by the adsorbed gas on to the surface of the material. As multilayers of the adsorbate form the thickness of the adsorbed gas starts contributing to the determination of the pore size. The Kelvin equation helps in determining the radius of curvature of meniscus in the filled pores. The equation for the adsorption branch of the isotherm is shown here:

$$r_k = \frac{-\gamma V_l}{RT\ln\left(\frac{P}{P_0}\right)} \quad (2.23)$$

In the equation $r_k$ is the radius of curvature, γ is the surface tansion $V_l$ is the molar volume of the liquid adsorbate, R is the universal gas constant and T is the liquid nitrogen temperature. To obtain pore radius statistical film thickness is added to the radius of curvature and the correction suggested by Kruk et al is used. The equation for the radius of the pore is:

$$r = \frac{-\gamma V_l}{RT ln\left(\frac{P}{P_0}\right)} + t\left(\frac{P}{P_0}\right) + 0.3 \quad (2.24)$$

Equation 2.20 gives the radius of the pore in nanometers(*167*). The form of equation for statistical film thickness to be used is shown below(*167*):

$$t = 0.1\left[\frac{60.65}{0.03071 - \ln\left(P/P_0\right)}\right]^{0.3968} \quad (2.25)$$

### 2.6.6 Dynamic Light Scattering (DLS)

DLS uses photon correlation spectroscopy to provide an estimate of the velocity of particles in a liquid moving due to Brownian motion. Analysis of the intensity scattered light at time $t=t_0$ can be correlated with the intensity of scattered light at time $t= t_0+\delta$ using an autocorrelation function. The autocorrelation function is then used to calculate the value of decay rate (Γ) which is related to the mutual diffusion coefficient ($D_m$) and scattering vector (q) by equation 2.22:

$$\Gamma = D_m q^2 \tag{2.26}$$

$D_m$ is determined for use in Stokes Einstein equation which gives the hydrodynamic diameter of the particles and is shown in equation 2.23.

$$D_h = \frac{k_B T}{3\pi\eta(T) D_m} \tag{2.27}$$

In equation 2.23 $D_h$ is the hydrodynamic radius, $k_B$ is the Boltzmann constant, $\eta(T)$ is the viscosity at temperature T and $D_m$ is the mutual diffusion coefficient(*169*).

Certain units used to measure hydrodynamic radii can also be used to measure zeta potential of the suspended particles. Zeta potential is the potential difference between charged bi-layer of a particle and the bulk liquid in which particle is suspended. When an electrical potential is applied across a solution the charged particles start moving towards the oppositely charged electrode. The movement of the particles is governed by two forces acting opposite to each other. While electric forces tend to move particles towards the electrode the viscous forces inherent to the liquid tend to act in opposite direction. When the forces are balanced a constant velocity called electrophoretic mobility is obtained. The zeta potential can be determined using the Henry equation:

$$U_E = \frac{2\varepsilon Z f(ka)}{3\eta} \tag{2.28}$$

In equation 2.24 $U_E$ is the electrophoretic mobility, ε is the dielectric constant, Z is the zeta potential and η is the viscosity of the medium. The Smoluchowski approximation is

used to obtain the value of Henry's function [f(ka)]. For suspensions in water the value is usually approximated to 1.5(*170*).

## 2.7. Conclusion

In the next chapters, the use of the techniques discussed here will be shown with applications in quantitative and qualitative measurements. The background knowledge presented here will provide the framework for studying the thermodynamic behavior of mixed micelles based on data obtained using ITC. A model is based on what was discussed here is elaborated in Chapter 3 for the ITC data. The mixed surfactant system has also been used to develop imprinted nonporous materials demonstrating saccharide selectivity. The same technique has been extended to show preferential sites for D-xylose, D-glucose and D-maltose with minor process modifications. Chiral separation of hexoses and maltose and cellobiose has been demonstrated. Not only does chiral separation support the molecular imprinting principles, but also provides possibility of development of molecularly imprinted chiral separation phases with low diffusion resistance and uniform morphology. The use of surfactant mixtures has been further extended to synthesize epoxidation catalyst with high pore accessibility and higher activity compared to a zeolite. The mixed metal oxide porous materials have been processed in both thin film and bulk form. The incorporation of titania in the materials leads to catalytic sites and provides proof that the well dispersed Ti sites are tetracoordinated. Titania incorporating nonporous particles have been synthesized with possibility of applications in asymmetric catalysis and specific adsorption of saccharides.

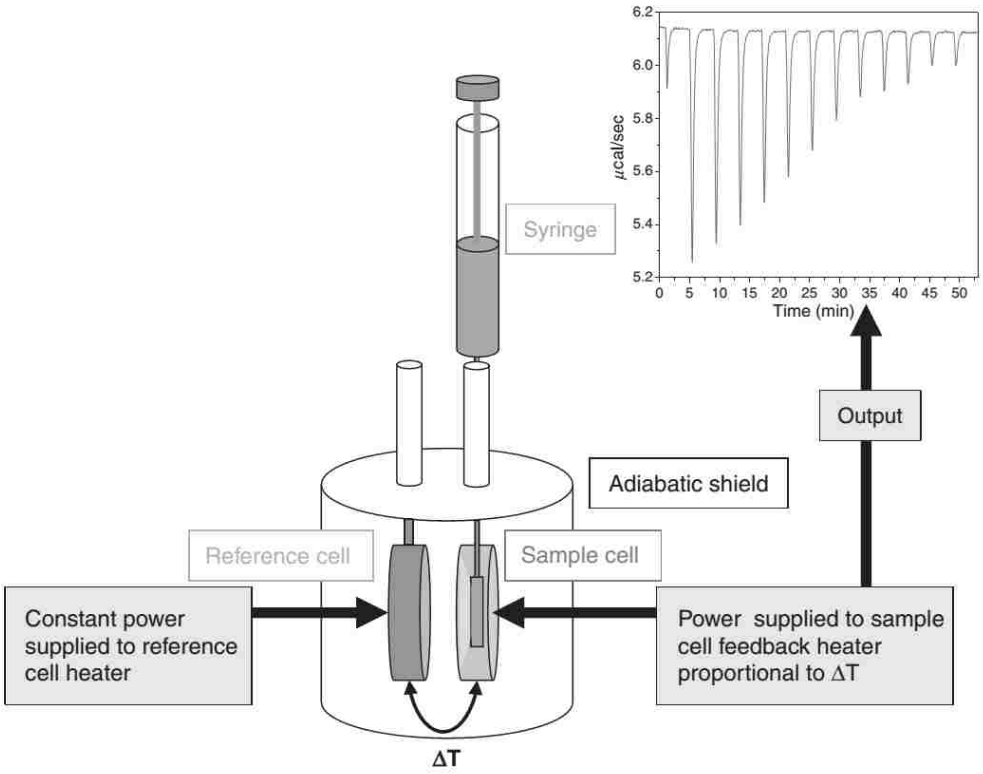


**Figure 2.1** The figure shows the basic setup of an ITC instrument working on power compensation method and raw data obtained for a general case (From Freyer, M W and Lewis, E A, Methods in Cell Biology, 2008(*153*). Produced with permission.

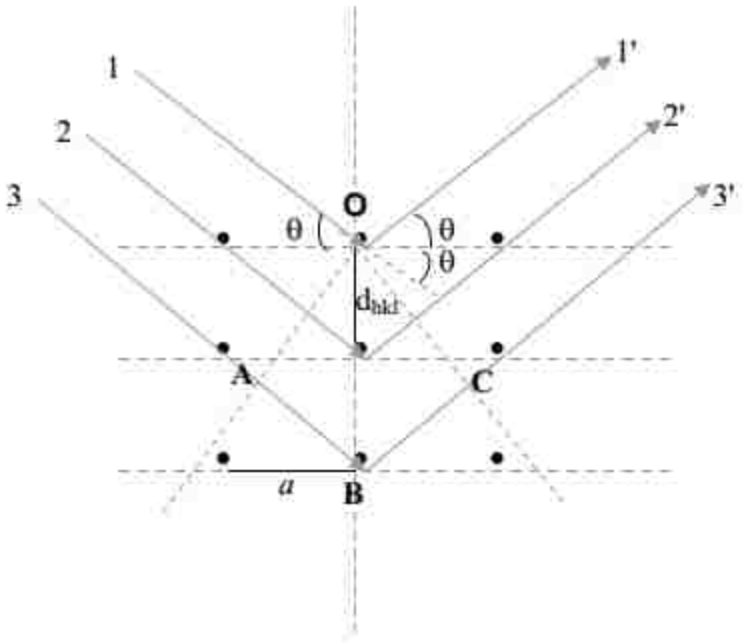


**Figure 2.2** Explanation of x-ray diffraction to obtain constructive interference. (Produced with permission from Smith, F. Industrial Applications of X-Ray Diffraction Smith, 1999, CRC Press (*158*)).

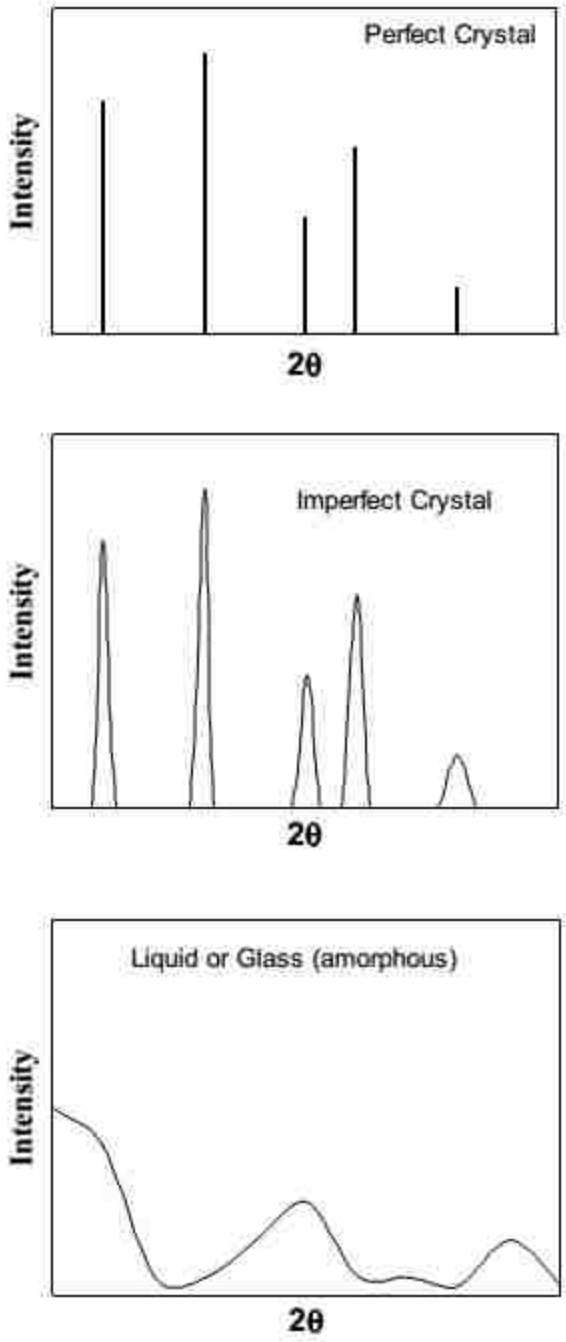


**Figure 2.3** Schematic representation of perfect, imperfect crystals and amorphous materials. Adapted from Heiney et al(159).

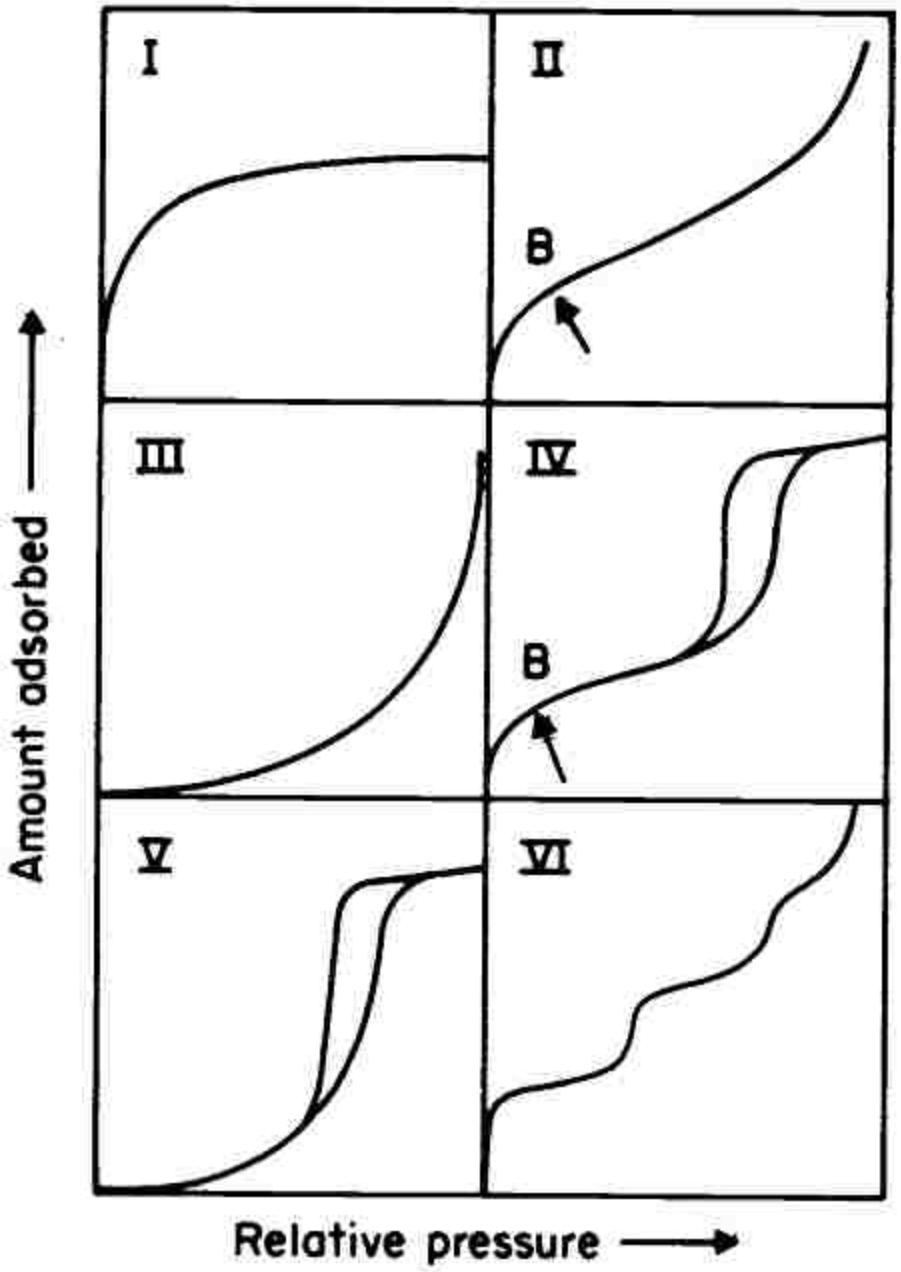


**Figure 2.4.** Common classifications of the adsorption isotherm. Adapted from Sing et al(171).

**Table 2.1.** cmc's , free energies of micellization and enthalpies of micellization for some glucosidic surfactants with varying tail length, head group and anomeric center.

| **Surfactant** | **CMC (mM)** | **$\Delta G_{mic}$ (kJ/mol)** | **$\Delta H_{mic}$ (kJ/mol)** |
|---|---|---|---|
| n-octyl-β-D-glucopyranoside (β-C8G1) | 18.3(*45*) | -19.9(*45*) | 7.01(*172*) |
| n-octyl-α-D-glucopyranoside (α-C8G1) | 12(*45*) | -21.0(*45*) | |
| n-nonyl-β-D-glucopyranoside (β-C9G1) | 6.9(*173*) | | -5(*174*) |
| n-decyl-β-D-glucopyranoside (β-C10G1) | 1.96(*45*) | -25.4(*45*) | -7.5(*35*) |
| n-decyl-α-D-glucopyranoside (α-C10G1) | 0.85(*37*) | | |
| n-dodecyl-β-D-glucopyranoside (β-C12G1) | 0.19 | | -10.1(*35*) |
| n-octyl-β-D-maltopyranoside (β-C8G2) | 19.1(*45*) | -19.8(*45*) | -8.4(*74*) |
| n-dodecyl-β-D-maltopyranoside (β-C12G2) | 0.13(*45*) | -32.1(*45*) | -0.9(*74*) |
| n-dodecyl-α-D-maltopyranoside (α-C12G2) | 0.12(*175*) | | |

Copyright © Suvid Joshi 2014

# CHAPTER THREE

# 3. MODELING THERMODYNAMIC BEHAVIOR OF NON-IDEAL MIXED SURFACTANTS: USE OF REGULAR SOLUTION THEORY FOR ISOTHERMAL TITRATION CALORIMETRY DATA

## 3.1. Summary

A model for non-ideal surfactant mixtures studied using isothermal titration calorimetry (ITC) is presented. Compared to common techniques used to measure characteristics of micellar systems like surface tension measurements, ITC provides the advantage of measuring enthalpy changes directly during an experiment. ITC has been used commonly in the past to measure protein ligand binding, but use of ITC for micellar thermodynamic measurements is still a developing area. In this work a non-ideal mixing model for ITC data has been developed through consistent application of regular solution theory (RST). Enthalpy of dilution was found to play a significant role in the full ITC curves, and non-ideal mixing is modeled based on an extension of the McMillan-Mayer model that includes terms for interactions of monomers and micelles with solvent and amongst each other. The model is applied to hexadecyltrimethylammonium bromide (CTAB) and n-octyl-β-D-glucopyranoside (C8G1), which form a non-ideal mixed surfactant pair. Nonlinear regression was used to fit the full model to the results of six ITC experiments with varying surfactant composition to determine the cmc values, enthalpies of demicellization, and thermodynamic interaction parameter (β) based on regular solution theory. The parameters associated with McMillan-Mayer model were also obtained as fitting parameters. The key feature that this new model was able to match in this type of ITC study, which does not arise in ideal micellization models, is the broad transition from monomeric solutions to micellar solutions for mixtures of CTAB and C8G1 with a high fraction of C8G1. This broad transition is the result of the continuous variation of micelle

composition with respect to the total surfactant concentration (even though the overall composition of the surfactants remains fixed during the experiment). The models described in this work provide the opportunity to determine micellar properties of both pure surfactants and their mixtures from a limited set of ITC data, and to begin to develop new experiments to better understand both the effects of molecular structure of the mixed surfactants and the nature of dilution enthalpy in mixed surfactant systems.

## 3.2. Introduction

Mixed surfactant systems are of widespread and growing interest for potential applications in industry(*176*). Much of this interest stems from synergy that arises from favorable interactions among surfactants and enhance their properties for various applications. Mixed surfactants also find application in emerging areas, such as in micellar templates for the synthesis of silicates for applications including catalysis and separation(*56, 57, 177-179*). In these applications, surfactant mixtures are used to modulate the micellar assembly process, or to provide specific sites for interactions with the materials precursors. Many of the novel features associated with mixed surfactant usage stem from the interactions between headgroups differing in charge and structure. For instance, favorable interactions among surfactants depress the critical micelle concentration (cmc) relative to ideal mixtures, which has distinct advantages for detergency applications. Hence, there is a persistent need to better characterize and model nonideal mixing behavior in surfactant systems, either to select the best surfactant mixture for a desired application, or to better utilize known mixtures.

Various methods have been used in the past to study interactions of surfactants with other surfactants, polymers and lipid vesicles(*1, 68, 74, 180*). While they each have their strengths, many of these techniques require many repeated experiments (for example,

varying mixed surfactant composition and temperature) to determine thermodynamic quantities such as enthalpy changes of micellization and of mixing within micelles. For example, the change in slope of a property (such as surface tension or conductivity) is most commonly used to assess the cmc, and hence only one "transition point" is indicated. The transition point creates an impression that micelle formation represents a step change in aggregation, while in reality (see below) micelle formation in mixed surfactant systems is a continuous and dynamic process. Beyond the cmc, which may be defined as the onset of micelle formation, the composition of the micelles keeps changing dynamically with increasing concentration. This is analogous to vapor-liquid phase transitions in mixtures where a continuous change in composition and phase quantity occurs along the pathway from bubble point to dew point (rather than a discontinuous change from vapor to liquid). To understand the process of micelle formation beyond the cmc, a technique is needed that can continuously monitor micelle formation in small steps before and after the onset of micellization.

Isothermal titration calorimetry (ITC) is such an alternative technique which can be used to directly obtain fundamental thermodynamic data associated with physical and chemical changes in solution. ITC has been used to study protein-ligand binding, surfactant-vesicle interactions, and drug binding to substrates(*181-187*). Over the past two decades, the use of titration calorimetry to study thermodynamics of micelle formation has gained momentum. Most reports use titration calorimetry to determine enthalpy, Gibbs free energy and entropy changes, along with the cmc of the system(*172, 188, 189*). ITC has also been used in recent years in attempts to interpret the enthalpy associated with dilution of micelles and dilution of monomers during an experiment(*190*).

ITC provides the distinct advantage over other techniques of directly measuring thermodynamic quantities (directly associated with heat) and the cmc of mixed micellar systems. Thermodynamic parameters can in principle be determined by ITC using a small set of experiments with very small amounts of surfactants.

In an ITC experiment, the enthalpy associated with going from micelles at a given concentration into a more dilute solution of the same overall composition is measured. A broader transition is observed than just a single "cmc", and it is necessary to establish where the cmc defined by other experiments should be located. For a sharp transition, the cmc can be estimated from the maximum in the first derivative of enthalpy with respect to concentration, which usually lies near the center of the transition region of the heat vs. concentration curve (which will be described in more detail below). However, in mixed micelles it is not unusual to see a broad transition region (which reflects the true nature of the demicellization process) and it becomes necessary to better model the gradually sloping heat curve that is obtained near the transition from micelle dissociation (at low concentrations) to micelle dilution (at higher concentration). This model is also needed because the high-concentration plateau usually observed for single surfactants (where a surfactant solution from the injection syringe is being added to a less concentrated but still micellar solution in the ampoule) is not easily observed because of the limited concentration range selected. Hence it is necessary to use a model for ITC experiments that does not rely on interpolation based on plateaus before and after the cmc to model both enthalpy of demicellization and cmc values.

Various models have been proposed to describe micellization in mixed surfactant systems(*10, 11, 59, 60*). Rubingh's model(*12, 191*) which uses the regular solution

activity coefficient model, is widely used to interpret mixed surfactant cmc data(*68, 192, 193*). This model is usually used to extract interaction parameters from cmc data collected as a function of composition in mixed systems, but it can also be used to infer thermodynamic parameters (such as enthalpy of mixing) from cmc data. While it would be possible to take this approach in ITC experiments, they provide more direct thermodynamic data on the heat evolved during a dynamic transition, so a model that accounts not just for the onset of micellization but also for the heat evolved during the entire ITC experiment is necessary. The model presented here is based on phase separation approximation as used by Clint,(*62*) which in its original formulation described ideal surfactant mixtures and was developed to predict the demicellization experiment end point for mixed surfactant system. Recently the model was applied to ITC measurements of mixtures of maltosides by Tsamaloukas et al (*74*) and some of the modeling equations have been adapted from their work.

A mixture of cationic and nonionic (saccharide-based) surfactants was selected for this work. Mixing in these types of systems has been investigated in some detail using traditional cmc measurements with analysis using Rubingh's model(*68*) In part, this is because nonionic surfactants help to increase the detergency of cationic surfactants(*23*). In particular, alkyl polyglucosides are very interesting due to their high detergency, biodegradability and possible synthesis from renewable resources(*194*). In our group, we are interested in using the polyfunctional saccharide headgroup for the design of mesoporous materials with specific adsorption and catalytic properties, and mixtures of cationic and sugar-based surfactants have used for predictive synthesis of mesoporous materials by lyotropic liquid crystal templating(*5, 6*). To provide further insights into

mixing in these systems, a model is proposed here to model heat evolved during ITC experiments of nonideal surfactant mixtures. For illustrative purposes, a binary surfactant system consisting of N-octyl-β-D-glucopyranoside (C8G1) and cetyltrimethylammonium bromide (CTAB) is used in the experiments. Regular solution theory is consistently applied to model the onset of micellization (which we will refer to as the cmc) and nonideal mixing in a phase separation model of micellization. By fitting the model to a set of ITC experiments with varying composition, we show that this model is able to capture the essential features of the ITC data, and to provide thermodynamic data consistent with micellization concentrations and heats for both single and mixed surfactants. The thermodynamic interaction parameter (β) found by this approach will be shown to be consistent with prior estimates and consistent with the excess enthalpy of mixing in the cationic / saccharide surfactant micelles.

## 3.3. Experimental

### 3.3.1. Materials

Deionized ultrafiltered (DIUF) water was obtained from Fisher Scientific. Hexadecyltrimethylammonium bromide (or cetyltrimethylammonium bromide, CTAB) was obtained from Fischer chemicals and was of 99% purity. N-octyl-β-d-glucopyranoside (C8G1, 99+% purity) was obtained from Affymetrix. All chemicals were used as received.

### 3.3.2. Methods

The calorimetry experiments were performed using a *TAM III* isothermal titration calorimeter manufactured by TA Instruments. For demicellization, the surfactant solutions of known concentration above the cmc were prepared for analysis and loaded into a 1 ml syringe. Care was taken to prevent any air bubbles from forming in the

syringe. The ampoule was loaded with up to 2.4 ml of DIUF water at the start of each experiment. The ampoule was slowly lowered into the calorimeter channel with pauses at three points to allow for thermal equilibration. All of the demicellization experiments were performed at 25 °C. Titrations were performed by adding 20 or 25 µl of the surfactant solution per injection from the syringe to the ampoule. Usually 5 to 7 minutes was provided between injections to allow time for thermal equilibration. The first injection is not considered for data analysis(*195*). The number of data points (the total volume of surfactant solution added) was varied depending on the experiment but were selected to give a range of concentrations such that there would be several data points below the cmc and many points above the cmc.

### 3.3.3. Surfactant pseudo-phase equilibrium model

For binary surfactant mixtures, the following equations can be developed based on regular solution theory to provide a consistent thermodynamic framework for modeling the ITC measurements. First, the pseudo-phase model for equilibrium between monomeric surfactant and surfactants in micelles gives(*12*):

$$C_m^i = x_i * f_i * C_i \tag{3.1}$$

In Eq. 3.1, $C_m^i$ stands for the monomeric concentration of the i$^{th}$ component. $x_i$ the mole fraction of component *i* in the micelle, $f_i$ the activity coefficient of component *i* in the micelle, and $C_i$ the cmc of pure component *i*.

For a binary surfactant mixture, a mole balance be used to derive an expression for the mole fraction of the component 1 in the micelle:

$$x_1 = \frac{\alpha_1 * C - C_1^m}{C - C_1^m - C_2^m} \tag{3.2}$$

In Eq. 3.2, $\alpha_1$ is the overall mole fraction of surfactant 1 and C is the overall concentration of the surfactant in solution. By using Eq. 3.1 to substitute for each monomer concentration in Eq. 3.2, we obtain:

$$x_1 = \frac{\alpha_1 C - x_1 f_1 C_1}{C - x_1 f_1 C_1 - x_2 f_2 C_2} \tag{3.3}$$

Eq. 3.3 can be used to obtain a non-linear equation for $x_1$ by utilizing the fact that in a binary mixture,

$$x_2 = 1 - x_1 \tag{3.4}$$

The following equation is obtained

$$x_1{}^2(f_2 C_2 - f_1 C_1) + x_1(C + f_1 C_1 - f_2 C_2) - \alpha_1 C = 0 \tag{3.5}$$

From regular solution theory (RST),

$$f_1 = e^{(\beta(1-x_1)^2)} \tag{3.6}$$

$$f_2 = e^{(\beta x_1{}^2)} \tag{3.7}$$

Substituting Eq. 3.6 in Eq. 3.7, we obtain a non-linear equation with $x_1$as the only unknown quantity once cmc values, β, the total surfacdtant concentration and bulk composition are specified:

$$x_1{}^2\left(e^{(\beta x_1{}^2)} C_2 - e^{(\beta(1-x_1)^2)} C_1\right) + x_1\left(C + e^{(\beta(1-x_1)^2)} C_1 - e^{(\beta x_1{}^2)} C_2\right) - \alpha_1 C = 0 \tag{3.8}$$

Eq. 3.8 can be solved numerically to calculate mole fraction of both the components in the micelles. Here, this was done by implementing the Newton-Raphson method using a VBA function in Excel starting from an initial guess of $x_1$ = 10% of the $\alpha_1$. The VBA code is provided as part of Appendix A.

Once the composition of the micelle at equilibrium with the bulk monomer solution is known, species concentrations can be determined. To calculate the amount of surfactant in monomeric form, a variant of Clint's phase separation model of micellar mixtures was used(*62*) that incorporates activity coefficients:(*196, 197*).

$$C_1^m = \frac{-(C-\Delta) \pm \sqrt{(C-\Delta)^2 + 4\alpha C\Delta}}{2[\frac{f_1 C_1}{f_2 C_2} - 1]} \tag{3.9}$$

where

$$\Delta = f_2 C_2 - f_1 C_1 \tag{3.10}$$

Once the monomeric concentrations are known, material balances can be used to determine the concentrations of each surfactant in micelles. To be consistent with RST, the excess enthalpy of mixing of surfactants in micelles is calculated using Eq. 3.11.

$$\Delta H_{mix} = \beta RT x_1(1-x_1) \tag{3.11}$$

**3.4. Thermodynamic model of micellization**

The complex process of redistribution of surfactants between monomeric and micellar form during an ITC experiment was broken down using a thermodynamic cycle so that mass and energy balance could be applied and well-defined thermodynamic quantities could be obtained. When the solution in the syringe is above the mixed micelle cmc but the concentration in the ampoule is below the cmc, demicellization is the only process that must be considered. As shown in Figure 3.1 the first step involves breaking of the mixed surfactant micelles into separate micelles of pure components. The heat of forming pure component micelles by demixing existing micelles is associated with the excess enthalpy of mixing (specifically, $-\Delta H_{mix}^{non-ideal}$). The second step requires the dissociation of the individual micelles into monomers of the pure components and is associated with the enthalpy of demicellization of each surfactant *i* ($\Delta H_{Si}^{m\rightarrow aq}$). It is

important to note that since the micelles are considered to be non-ideal, the enthalpy of mixing is non-zero and needs to be separated from enthalpy of demicellization. The overall process that results is the demicellization of a mixed micelle into monomers of constituent surfactants.

Figure 3.2 depicts the thermodynamic cycle that can be followed to estimate the heat of ITC experiments when the concentration in the ampoule is above the cmc. Above the cmc a dynamic equilibrium exists between the micelles and monomers already present in the ITC ampoule and the micelles and monomers which are being added from the syringe. The process is broken down into three thermodynamic steps. In the first step, the micelles existing in the ampoule inside the ITC undergo demixing and demicellization to form a solution containing only monomers of the surfactant mixture and the enthalpy of demixing/demicellization is calculated. Second, the new aliquot is added from the syringe in to the ampoule and is demixed/demicellized to form a monomeric mixture and the heat associated this process is calculated. Finally, the new aliquot is mixed with the existing contents of the ampoule, new overall concentrations are established and a new micelle/monomer equilibrium is established at a higher total surfactant concentration. The heat associated with the micellization process and mixing of surfactants in the micelles is calculated and used to estimate the overall heat associated with the injection following the cycle illustrated in Fig. 2. The net heat associated with this process is summarized in Eq. 3.12, where the overall heat ($Q$) is expected to be equivalent to what is measured by ITC.

$$Q = \Delta Q_{dil} + Q_{dil}^{syringe} + \frac{\left(\Delta C_{S1}^{aq}\right)_{demic}}{\Delta C_S}\Delta H_{S1}^{m\rightarrow aq} + \frac{\left(\Delta C_{S2}^{aq}\right)_{demic}}{\Delta C_S}\Delta H_{S2}^{m\rightarrow aq} + \frac{C_{mic}^{syringe}}{\Delta C_S}\Delta H_{S1}^{m\rightarrow aq,syringe} + \frac{C_{mic}^{syringe}}{\Delta C_S}\Delta H_{S2}^{m\rightarrow aq,syringe} - \frac{C_{mic}^{syringe}}{\Delta C_S}\Delta H_{mix}^{syringe} + \frac{C_{total,k}^{mic,ampoule}}{\Delta C_S}\Delta H_{mix}^{ampoule} - \frac{C_{total,k-1}^{mic,ampoule}}{\Delta C_S}\Delta H_{mix}^{ampoule} \quad (3.12)$$

In equation 3.12 $\Delta Q_{dil}$ stands for the change in enthalpy of dilution associated with change in concentration in the ampoule. $Q_{dil}^{syringe}$ is the enthalpy of dilution associated with the surfactant added to the ampoule from the syringe. $\frac{\left(\Delta C_{S1}^{aq}\right)_{demic}}{\Delta C_S}\Delta H_{S1}^{m\rightarrow aq}$ and $\frac{\left(\Delta C_{S2}^{aq}\right)_{demic}}{\Delta C_S}\Delta H_{S2}^{m\rightarrow aq}$ are the terms associated with demicellization of micelles present in the ampoule in step k-1 and reforming of micelles in step k for surfactants S1 and S2 respectively. $\frac{C_{mic}^{syringe}}{\Delta C_S}\Delta H_{S1}^{m\rightarrow aq,syringe}$ and $\frac{C_{mic}^{syringe}}{\Delta C_S}\Delta H_{S2}^{m\rightarrow aq,syringe}$ are the enthalpies associated with demicellization of surfactant present in micellar form at each injection step for surfactant 1 and surfactant 2 respectively from the syringe. $-\frac{C_{mic}^{syringe}}{\Delta C_S}\Delta H_{mix}^{syringe}$ is the enthalpy of demixing micelles in the syringe when aliquot is added to the ampoule. $-\frac{C_{total,k-1}^{mic,ampoule}}{\Delta C_S}\Delta H_{mix}^{ampoule}$ corresponds to the enthalpy of demixing whatever was present in micellar form in the ampoule at step k-1 and $\frac{C_{total,k}^{mic,ampoule}}{\Delta C_S}\Delta H_{mix}^{ampoule}$ is the enthalpy of mixing associated with reforming the micelles at a higher concentration in step k after the injected aliquot from the syringe.

In the model proposed by Tsamaloukas(*74*) an arbitrary constant value was used as the enthalpy of dilution for each ITC experiment, and the enthalpy of dilution and these values were independently varied during nonlinear regression. This did not provide

model results that were able to match the slopes of the ITC curves before and after the cmc accurately. Dilution in the case of non-ideal mixtures is more complex than this, and it is apparent from the raw ITC data that the heat of dilution follows a linear relationship with respect to concentration, and that the slopes vary above and below the *cmc*. These trends are poorly fit with a constant, arbitrary enthalpy of dilution. To address this, a dilution model is used that has a concentration dependence, and that can be used in conjunction with the thermodynamic cycles in Figs. 1 and 2 to develop a more nuanced description of the ITC experiments. The model is based on the McMillan-Mayer framework for dilute multicomponent mixtures(*198*). Assuming that the solvent molality is roughly constant in dilute solutions, the excess enthalpy of mixing for solutes can be expressed in this framework by a polynomial expansion in terms of the concentrations of solutes(*199*). For purposes of describing interactions among solutes, we consider four types of solutes: monomers of C8G1, monomers of CTAB, C8G1 in micellar form, and CTAB in micellar form. Other forms of dilution model were considered but this was found to provide the best match to the experimental data. If $h_i^x$ is the coefficient describing excess enthalpic interactions between solute *i* in form *x* (*x* = *m* for monomers and *mic* for micelles) and water, and $h_{ij}^x$ is the coefficient describing excess enthalpic interactions between solute *i* and solute *j* in form *x* with water as solvent, to second order, the heat of dilution can be expressed as:

$$\begin{aligned} Q_{dil} = {} & h_1^m C_1^m + h_2^m C_2^m + h_1^{mic} C_1^{mic} + h_2^{mic} C_2^{mic} + h_{11}^m (C_1^m)^2 \\ & + h_{22}^m (C_2^m)^2 + h_{12}^m (C_1^m * C_2^m) + h_{11}^{mic} (C_1^{mic})^2 \\ & + h_{22}^{mic} (C_2^{mic})^2 + h_{12}^{mic} \left(C_1^{mic} * C_2^{mic}\right) \end{aligned} \tag{3.13}$$

Initial attempts to fit the entire data set using a single set of interaction parameters was not successful, so two sets were used – one to fit low-concentration experiments (total surfactant concentration < 12 mM) and one to fit high-concentration experiments.

### 3.4.1 Fitting the model

Non-linear regression was used to simultaneously fit the data for all ITC experiments to obtain one set of parameters for the model outlined above. Fitting of the model to the ITC heat curves was accomplished by using the Levenberg-Marquardt algorithm to minimize the sum of squares of the errors (SSE) between the data and the model, as implemented in Excel's Solver. The parameters used to fit the entire data set include the enthalpy of demicellization for pure surfactants, cmc values for the pure surfactants, thermodynamic interaction parameter β, and parameters associated with enthalpy of dilution of the micelles and monomers.

To fit the data initially the mole fractions at each step was iteratively calculated using equation 3.8 providing experimental cmc values. All the data obtained was simultaneously fit using equation 3.12, by substituting enthalpy of dilution from equation 3.13. Square errors were calculated and a weighted square error term was summed to calculate SSE. A higher weighting was applied to the data from the mixed surfactant (multiplier of 1) experiments compared to pure surfactants (multiplier of 0.5) to ensure that they were well fit. Error analysis on the parameters obtained from fits was performed using solver statistics module in Excel(*200*).

## 3.5. Results and Discussion

Surfactant mixtures as well as pure surfactants were studied using ITC. The enthalpy versus concentration diagrams for the pure surfactants CTAB and C8G1 are presented in Figure 3.2. Traditional techniques can be used to determine both the cmc and the

enthalpy of demicellization for CTAB and C8G1. In both experiments, a high concentration solution (approximately five times the cmc) is added from the syringe in small steps into a thermodynamically isolated ampoule at 25 ˚C. As we add the micellar solution into the ampoule, initially a very dilute monomeric solution is formed due to demicellization. ITC records the heat associated with this process. As more and more surfactant is added in to the ampoule, we approach the cmc. As we cross cmc, a sharp change is observed in the enthalpy associated with the process. After the cmc, the process mainly involves adding a micellar solution from the syringe to an already existing micellar solution in the ampoule. Once stable micellar solution are present in both the ampoule and the syringe, high concentration plateau is obtained with a small enthalpy per injection, although a residual enthalpy can still be observed. This enthalpy results from dilution effects associated with injecting a high-concentration solution from the syringe into a low-concentration solution in the ampoule. To determine the enthalpy of demicellization, lines are fit to the plateaus above and below the inflection and extended beyond the inflection. A line is drawn perpendicular to the x axis at the cmc, and the enthalpy of demicellization is measured from the length of the segment connecting the lines. The process is represented in figure A.1 in appendix A. To determine the cmc by this direct analysis of the heat curves, the first derivative of enthalpy with respect to concentration is plotted against concentration and the cmc is estimated from the extremum in the plot, since this represents an inflection in the heat vs. concentration curve. The enthalpy of demicellization and cmc determined by this procedure will be termed ‘differential’ values based on the cmc estimation method.

Using this technique, the differential cmc for CTAB was determined to be 0.97 mM while for C8G1 it was determined to be 25.6 mM. These cmc values are comparable to values reported previously(*68, 201*). Based on differential analysis, the enthalpy of micellization for CTAB at 25 ˚C was estimated to be -6.6 kJ/mol, which differs somewhat from the value of -10.2 kJ/mol reported in the literature(*202*). The enthalpy of micellization of C8G1 at 25 ˚C was found to be 6.0 kJ/mol which is close to the value reported in literature(*35*).

The enthalpy vs concentration diagrams for mixed surfactant systems are presented in Figure 3.3. Unlike single surfactant demicellization experiments, for mixed surfactant systems, curves are seen to deviate from the sharp sigmoidal shape usually associated with demicellization. The curves broad transitions after the onset of a micellar transition is observed. This trend is most apparent in solutions with higher mole fraction of C8G1 compared to CTAB. The broad transition region is attributed to shifting concentration of surfactant in the micelle, which leads to a gradual phase change over a range of concentration. As more and more surfactant is added into the ampoule from the syringe, the micelles start reorganizing from micelles which have higher CTAB mole fraction to micelles which have higher C8G1 mole fraction. This change causes a long tail like transition region until a point where the mole fraction change in the micelles in the ampoule start to reach a plateau. At this point, a high-concentration plateau is observed indicating the end of the curve.

A clear change can be observed in enthalpies of demicellization as well. The mixed micelles dominated by higher mole fraction of CTAB in the bulk have endothermic enthalpies of demicellization. As the bulk mole fraction of C8G1 increases, the micelles

formed in the ampoule after titration gradually become dominated by C8G1. As the mole fraction of C8G1 in the bulk solutions increases, the enthalpy of demicellization shifts from endothermic to exothermic.

The obtained experimental data from demicellization experiments performed using ITC was fit using two variants of the model outlined above. The first variant (Model 1) includes all parameters in the dilution term and the best-fit curves are shown in Figure 3.5. The second variant (Model 2) does not include first-order terms in the enthalpy of dilution model, and the best-fit curves are shown in Figure 3.6. Using the models, single unified values were obtained for enthalpies of demicellization, cmc values of pure surfactants and thermodynamic interaction parameter (β).

Model 1 was developed using all terms in equation 3.13 for enthalpy of dilution and calculating the modeled enthalpy using equation 3.12. It can be observed from Figure 3.5 that Model 1 fit the data for mixed systems quite well. However, good fits were not be obtained for the demicellization curves of CTAB and C8G1 alone. This may be in part because the pure surfactant ITC curves were weighted less during regression, to provide the best opportunity for the mixed micellar system to be fit. This naturally may have led to more noticeable deviations of model curves for single surfactants. The parameters obtained by regression along with the associated standard deviations are presented in Table 3.3. It was observed with Model 1 that cmc values and β could be estimated with good standard deviations, but that the uncertainty associated with the enthalpies of demicellization were unacceptably high. This appears to be related to large uncertainties observed in the first-order terms for the McMillan-Mayer dilution model (Table 3.3). The reason for the large uncertainties in all of these parameters is that they are all related

to the relative positions of the plateaus before and after the micellization inflection. Because multiple parameters affect these plateau positions, they are coupled and therefore cannot be estimated accurately. However, removing selected sets of the first-order dilution terms from the model significantly reduced the quality of the fit without decreasing the uncertainty in the parameters. It was found that removing all first-order terms was the only way to reduce uncertainties in the estimates of enthalpies of demicellization in the model.

In Model 2, all first order terms were eliminated to obtain another fit for the data. In other words, the dilution enthalpy for this model was calculated using equation 3.14 while keeping the rest of the model fixed.

$$Q_{dil} = h_{11}^{m}(C_1^m)^2 + h_{22}^{m}(C_2^m)^2 + h_{12}^{m}(C_1^m * C_2^m) + h_{11}^{mic}(C_1^{mic})^2 + h_{22}^{mic}(C_2^{mic})^2 + h_{12}^{mic}\left(C_1^{mic} * C_2^{mic}\right) \quad (3.14)$$

The fits for Model 2 are shown in Figure 3.6. Eliminating first order dilution terms produced good fits for experiments performed at low total concentration (pure CTAB, 3:1 and 1:1 CTAB:C8G1) while the model fits at high concentration regions for mixtures of 1:3 and 1:5 CTAB:C8G1 were unable to match the initial monomeric regions of the curves. Despite this problem, the total residual error obtained for Model 2 was found to be lower than that obtained for Model 1. Through error analysis it was observed that uncertainties in all parameters used to fit Model 2 were very low, although the value of β providing the best fit was found to be -1.9 which differed from values reported in literature (-2.5(*192*)). The values of all parameters associated with the Model are shown along with uncertainties in Table 3.3. Due to strong coupling observed between first

order dilution terms and enthalpies of demicellization of CTAB and C8G1, the model was also changed to fix the enthalpy of demicellization based on differential enthalpy calculations while using equation 3.13 for dilution (Model 3). Large uncertainties were obtained for first order dilution terms in Model 3 and the results are discussed in Appendix A.

Table 3.1 compares the values of fitting parameters obtained for C8G1 and CTAB using Models 1 and 2 and those obtained through differential enthalpy analysis. The cmc values of CTAB and C8G1 estimated using Models 1 and 2 are slightly higher than that estimated using the differential enthalpy analysis. However, this is not unexpected given possible differences in how the cmc is defined (see next paragraph). Enthalpy of demicellization values for both CTAB and C8G1 also differ from those obtained through differential enthalpy analysis. During fitting more weight was given to the error associated with mixed surfactant experiments while the weight on single surfactant experiments was reduced, which may have led to deviations from the experimentally obtained values. Another reason for the differences may be that enthalpy of dilution plays a significant role in the net heat observed in this system. For instance, for CTAB, at the cmc the heat recorded at the concentration used (8 mM CTAB in the syringe) is close to 2 kJ/mol, whereas in the report of Blandamer et al. (for 15.4 mM CTAB in the syringe), the heat of injection is almost zero immediately following the cmc(*201*). By taking into account both dilution and the thermodynamics of demicillization and demixing, Model 1 predicts enthalpy of demicillization values (9.5 kJ/mol for CTAB) closer to previously reported values (10.2 kJ/mol (*201*)) than direct differential analysis.

Table 3.2 compares the cmc values for mixed systems found fitting the full set of ITC data using Model 1 and Model 2 with cmc values estimated by differential analysis (described above), or by estimating the onset of micellization from the intersection of lines extrapolated from the ITC data near the initial change in slope in the heat curves. The values are plotted along with theoretical predictions for ideal mixtures ($\beta=0$) and with $\beta$ parameters from Models 1 and 2 in Figure 3.7. Despite the difference in $\beta$, the values predicted by both models are very close to each other and match the cmc of mixtures estimated from the *onset* of the micellization process. This makes sense given that the models also define the cmc based on the onset of the micellization process. However, the values of cmcs obtained through differential analysis are much larger than those determined from the onset of micellization, and in some cases are larger than the ideal cmc. The difference is caused by the broad transition associated with mixtures of surfactants where once micelles start forming, continuous changes in the micellar mole fraction cause a gradual change in the excess enthalpy of mixing which broadens the transition from simple demicellization to micelle dilution as concentration increases. The value of $\beta$ found using the full models are consistent with values of $\beta$ estimated by methods based only on the cmc values of mixed surfactant systems, which suggests that the onset of the transition should be used for comparison to other experimental methods of cmc determination.

Due to large number of parameters in the dilution equation, another attempt at fitting the data was also undertaken in an effort to reduce the number of adjustable parameters even beyond that in Model 2. This was accomplished by fixing the enthalpies of demicellization and the cmcs of the pure surfactants found using the differential enthalpy

approach (the values are summarized in Table 3.1). The parameters associated with dilution obtained from the fitting by this approach for both Model 1 and Model 2 dilution equations are shown in Table A.2 in the appendix A. Fixing the enthalpies of demicellization and cmcs of pure surfactants provides the benefit of giving certain parameters with a limited, simpler set of experiments. Unfortunately, this approach did not improve the fits obtained ($R^2$ = 0.967 for Model 1 and $R^2$ = 0.955 for Model 2), and perhaps more importantly, several of the relative uncertainties associated with the dilution parameters increased. The increase in uncertainty is most likely because the enthalpies observed in the ITC experiments are a sum of enthalpy of dilution and enthalpy of demicellization. When the values are fixed for enthalpies of demicellization based on the differential approach, the apparent enthalpy of demicellization should be equivalent to the result of addition of demicellization and several terms related to dilution of monomers and micelles before and after the cmc. Hence setting the enthalpy of demicellization to the apparent value from differential analysis is the most likely cause of an increase in overall error for some dilution enthalpy parameters, where now the equation also has to accommodate for the error created by misappropriating the value of demicellization enthalpy. Overall, while this would appear to be a beneficial approach, fixing demicellization enthalpy and cmc to values found by differential analysis of pure surfactants does not allow for separation of observed enthalpy in the experiment into dilution and demicellization. Because fitting Models 1 and 2 with all parameters allowed to vary does allow dilution contributions to be separated from demicelliation, it seems that this actually is the preferred approach. In the future, it would be worth further

investigation of methods of estimating and confirming individual dilution terms, as a way of accounting for their contribution to the observed apparent demicellization enthalpy.

To further explore the reason for the broad transition observed in some systems, especially those with a large mole fraction of C8G1, Figure 3.8 shows the calculated mole fraction of C8G1 in the micelle as a function of the total concentration of surfactant in the ampoule using the values of cmc and β obtained from Model 2. The mole fractions are calculated using Eq. 3.8 with the overall mole fraction of C8G1, cmc values of pure surfactants and β specified and varying C, the total surfactant concentration. At the onset of the micellization process, a small number of micelles is at equilibrium with a larger set of monomers whose composition equals the bulk value. The composition of these initial micelles is much different than the bulk composition – in all cases they contain less C8G1 and the difference is accentuated as the bulk mole fraction increases. As the concentration in the ampoule increases, the micellar mole fraction shifted towards micelles having higher C8G1 at each injection step, approaching the bulk mole fraction as the concentration of micelles increases. The solutions with the greatest mole fraction of C8G1 exhibit the broadest micelle transitions both because of the larger range of $x_1$ values seen and because the concentration range used in the experiments is greater. This is because they have larger cmc values, so the concentration in the syringe must be significantly greater for these mixtures so that the cmc can be crossed over the course of the ITC experiments. In addition to causing a continuous change in the population of monomers and micelles after the cmc in mixed systems, the trends in Figure 3.8 also imply that the excess enthalpy of mixing in the micelles changes as a function of

concentration. This change is captured in Models 1 and 2, and is part of the reason that that are abe to match most features of the experimental heat curves.

## 3.6. Conclusion

ITC was utilized to obtain continuous thermodynamic data for demicellization of cetyltrimethylammonium bromide (CTAB), n-octyl-β-D-glucopyranoside (C8G1) and mixtures of CTAB and C8G1. Broad transitions were observed for mixed surfactant systems, especially for mixtures with higher bulk mole fractions of C8G1, which precluded straightforward analysis of the data using differential analysis of heat vs. concentration curves. The expected sigmoidal curves with sharp transitions at the cmc were obtained for both CTAB and C8G1 individually, but significant dilution effects are apparent in the data of these systems which also complicates the direct differential analysis of the data.

To overcome the limitations in the direct analysis of ITC data in this mixed nonideal surfactant system, a thermodynamic framework was developed using a pseudo-phase separation approximation and regular solution theory to model the demicellization curves of CTAB, C8G1 and CTAB/C8G1 mixtures. Due to the complex nature of this non-ideal system, the enthalpy of dilution associated with the process was described using an extension of the McMillan-Mayer approach with second order terms for the dilution enthalpy of surfactants in monomers and micelles.

Surfactant demicellization curves for mixtures could be fit very well using Model 1, which included all dilution terms, but the behavior of individual surfactant demicellization for CTAB and C8G1 could not be matched well. In Model 1, a strong coupling between first order terms in the dilution model and the enthalpy of demicellization values was observed, leading to unacceptably high uncertainties in these

parameters. Therefore, Model 2 was developed by eliminating the first order terms in the dilution enthalpy model. Model 2 fit the set of experimental data better overall and acceptable uncertainties for all parameters were found. The cmc values found in model 2 matched prior literature quite well although the enthalpy of demicellization values were significantly different (-8.6 kJ/mol for C8G1 and 8.3 kJ/mol for CTAB, compared to -6.0(*35*) and 10.2 kJ/mol(*202*) in the literature). The value of β found using Model 2 (-1.9) was slightly smaller in magnitude than literature values reported based only on cmc values (-2.5)(*192*) but the predicted cmc values are relatively insensitive to the β value in the C8G1/CTAB system.

In addition to these quantitative conclusions, several qualitative suggestions emerge from this study regarding the use of ITC to study non-ideal surfactant mixtures. First, broad micellization transitions are expected in these systems and can be explained based on the shifting composition of the micelles relative to the bulk concentration as concentration increases in these experiments. Second, when comparing to other methods of cmc estimation, the *onset* of the micellization transition observed in ITC should be used. The ITC method provides significantly more information regarding the evolution of the system during micellization, but it appears from this study that other methods of cmc estimation are most sensitive to the initial point at which micelles form. Finally, when interpreting ITC curves, it is important to consider the effects of dilution enthalpy on the observed heats. It seems logical and consistent to use the difference in heat evolution at estimated cmc point on the ITC curve to estimate enthalpy of (de)micellization, for instance, but significant dilution effects may contribute to the process at this point. We hope that this work will inspire more research into models for

both activity coefficient models of mixed surfactant systems and dilution thermodynamics of aggregation colloids.

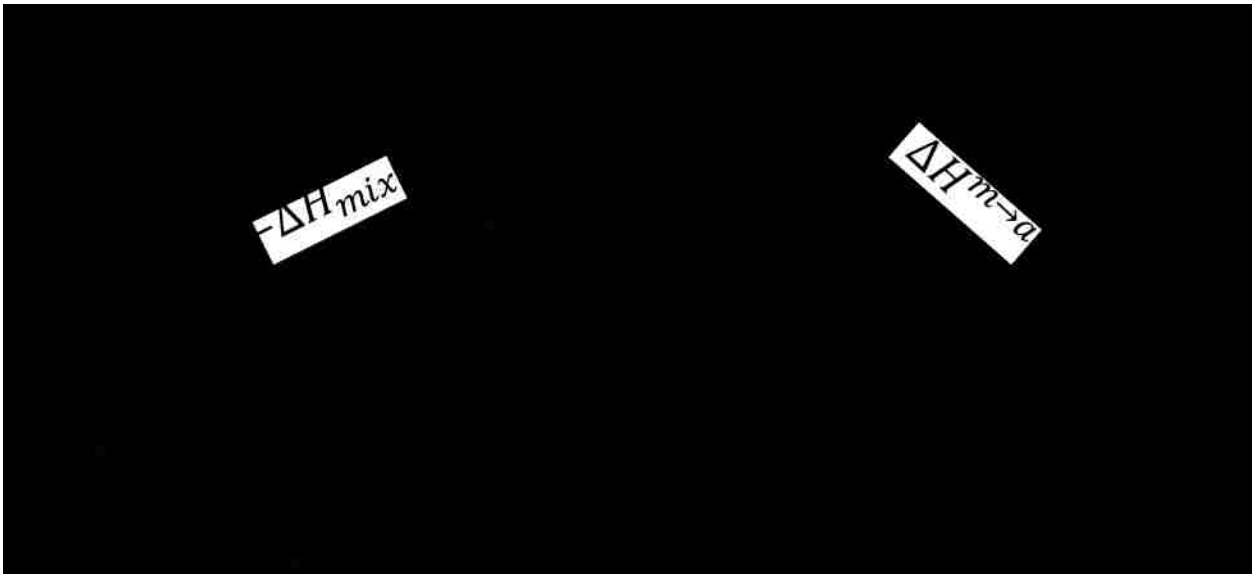


**Figure 3.1.** Representation of thermodynamic cycle used to represent demicellization of a non-ideal mixed micelle when the concentration of the system after injection of an aliquot is below the cmc of the mixture.

**Figure 3.2.** Representation of thermodynamic cycle for demicallization of a non-ideal mixed micelle when the concentration in the ampoule is above cmc of the mixture.

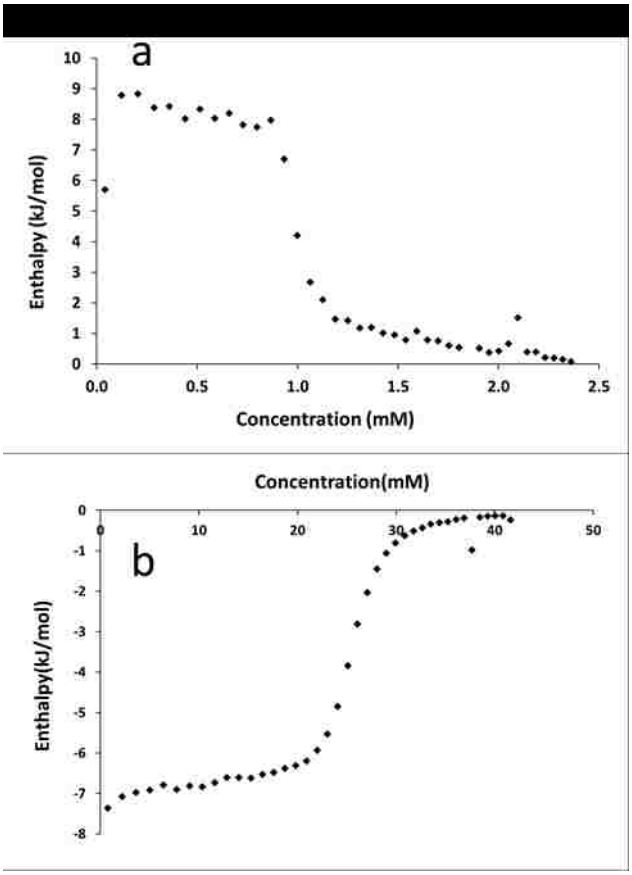


**Figure 3.3.** (a) Enthalpy vs. concentration diagram for (a) CTAB injected from a syringe containing 8 mM CTAB into an ampoule containing water and (b) C8G1injected from a syringe containing142 mM C8G1 into an ampoule containing water.

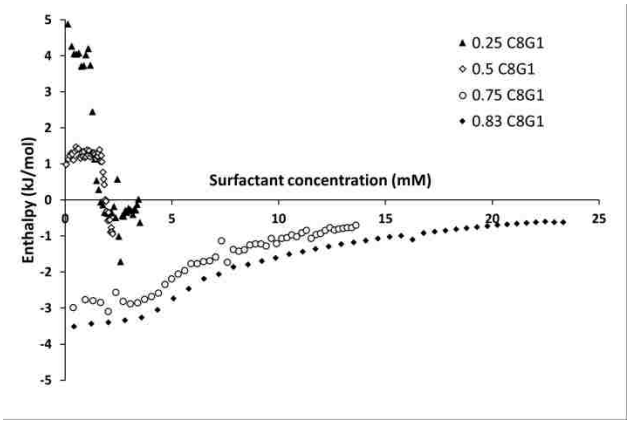


**Figure 3.4.** Enthalpy vs. concentration diagrams for demicellization experiments measured using ITC for 0.25, 0.5, 0.75, 0.83 bulk mole fraction of C8G1 in C8G1/CTAB mixed surfactant solutions. The total concentrations of surfactants in the syringe used for these experiments were 12 mM, 8 mM, 60 mM and 80 mM, respectively.

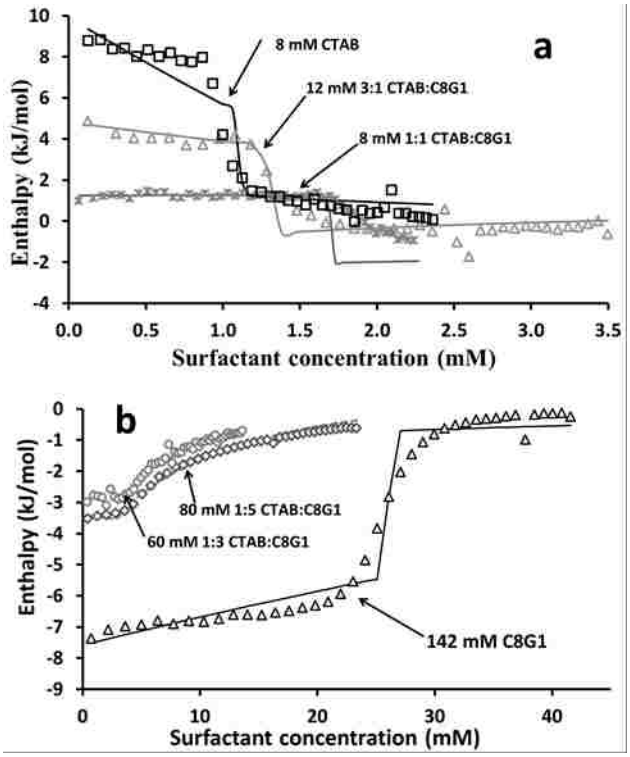


**Figure 3.5.** Experimental and best-fit enthalpy vs concentration diagrams obtained by fitting Model 1, in which enthalpy of dilution was modeled using all terms in equation 3.13. The plots are divided into (a) low concentration experiments with 8 mM CTAB, 12 mM 3:1 CTAB:C8G1 and 8 mM 1:1 CTAB:C8G1 and (b) high concentration experiments with 60 mM 1:3 CTAB:C8G1, 80 mM 1:5 CTAB:C8G1 and 142 mM C8G1.

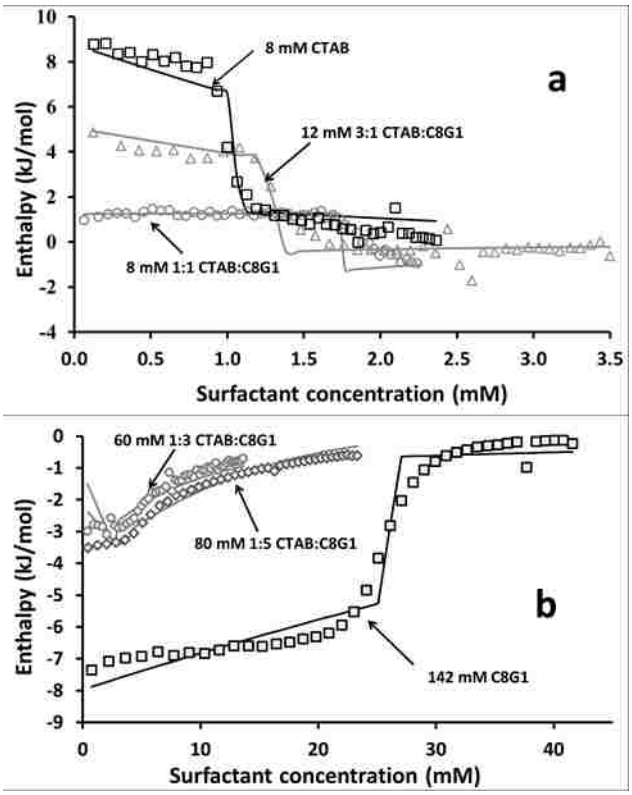


**Figure 3.6.** Experimental and best-fit enthalpy vs concentration diagrams obtained by fitting Model 2, in which enthalpy of dilution was modeled using all terms in equation 3.14. The plots are divided into (a) low concentration experiments with 8 mM CTAB, 12 mM 3:1 CTAB:C8G1 and 8 mM 1:1 CTAB:C8G1 and (b) high concentration experiments with 60 mM 1:3 CTAB:C8G1, 80 mM 1:5 CTAB:C8G1 and 142 mM C8G1.

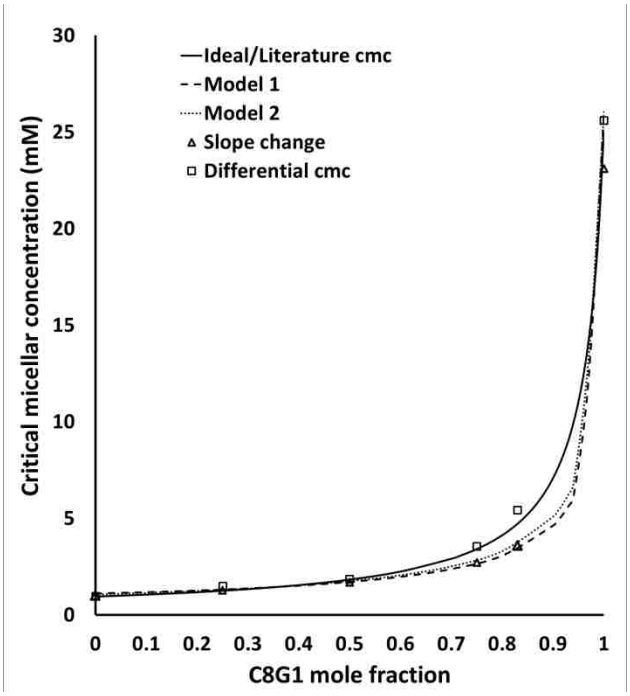


**Figure 3.7.** Critical micellar concentrations plotted against C8G1 mole fraction in the bulk mixture. The ideal/literature curve refers to cmc values obtained for pure surfactants from literature along with an ideal model ($\beta$=0) for cmcs of mixed surfactants. Models 1 and 2 are curves plotted using the best-fit parameters from the two models. The points labeled "onset" are calculated based on the slope change in the ITC curve corresponding to the onset of micellization and the points labeled "differential" are calculated from the extremum in the derivative of heat with respect to concentration in the ITC curves.

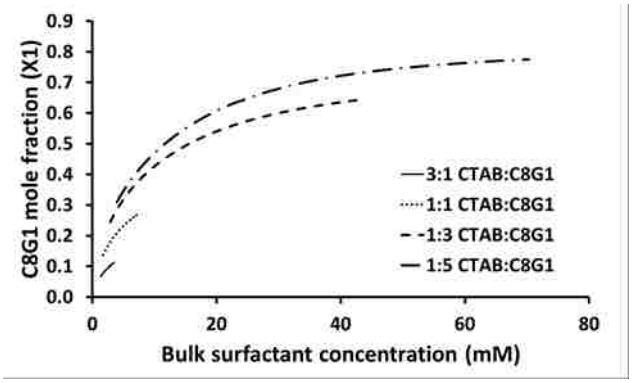


**Figure 3.8.** Calculated mole fraction of C8G1 in the micelle as a function of total bulk surfactant concentration for surfactant solutions at each injection step for mixtures containing 3:1, 1:1, 1:3 and 1:5 CTAB:C8G1. Curves are plotted using (a) best-fit Model 1 parameters and (b) best-fit Model 2 parameters.

**Table 3.1.** Properties obtained for single surfactant demicellization obtained from fitting the model to the data and from experiments.

| Obtained from ↓ | cmc (C8G1) | cmc (CTAB) | $\Delta H_{m\rightarrow aq}$ (C8G1) | $\Delta H_{m\rightarrow aq}$ (CTAB) | β |
|---|---|---|---|---|---|
| **Model 1** | 26.0 ± 0.14 | 1.11 ± 0.01 | -6.3 ± $2.85\times10^5$ | 9.5 ± $3.26\times10^5$ | -2.42 ± 0.065 |
| **Model 2** | 26.1 ± 0.11 | 1.05 ± 0.006 | -8.6 ± 0.28 | 8.3 ± 0.32 | -1.89 ± 0.059 |
| **Differential*** | 25.6 | 0.97 | -6.0 | 6.6 | -2.53 |

* Differential refers to property listed in the table calculated by plotting first differential of enthalpy against concentration. The cmc is determined as the concentration at which a maximum occurs while the enthalpy of demicellization was calculated as the distance between regression lines for high and low concentration plateaus, parallel to y axis at the cmc.

**Table 3.2.** Comparison of cmc of C8G1/CTAB mixtures calculated using best-fit parameters from the models, from the onset of micellization in the ITC curves, from differential analysis of the ITC data, and ideal values based on literature cmc values of C8G1 and CTAB.

| Mole fraction C8G1 | cmc from Model 1 (mM) | cmc from Model 2 (mM) | cmc from onset (mM) | Differential analysis (mM) | Ideal /literature (mM) |
|---|---|---|---|---|---|
| 0 | 1.11 | 1.05 | 1.00 | 0.97 | 0.95(*202*) |
| 0.25 | 1.31 | 1.30 | 1.13 | 1.51 | 1.25 |
| 0.5 | 1.70 | 1.75 | 1.62 | 1.86 | 1.86 |
| 0.75 | 2.70 | 2.84 | 2.70 | 3.55 | 3.41 |
| 0.83 | 3.42 | 3.71 | 3.63 | 5.43 | 4.72 |
| 1 | 26.0 | 26.1 | 23.1 | 25.6 | 25.24(*68*) |

**Table 3.3.** Summary of dilution parameters providing best fits for Models 1 and 2.

| | **Model 1** | **Model 2** |
|---|---|---|
| **Parameters**[a] | **Best fit value ± std dev** | **Best fit value ± std dev** |
| $h_{11}^{mic}$ (kJ $l^2$/mmol$^2$mol) | -4.7 ± 1.4 | -1.3 ± 0.24 |
| $h_{11}^{m}$ (kJ $l^2$/mmol$^2$mol) | -2.8 ± 1.3 | 1.4 ± 0.49 |
| $h_{12}^{m}$ (kJ $l^2$/mmol$^2$mol) | 5.1 ± 1.4 | -0.14 ± 0.55 |
| $h_{22}^{mic}$ (kJ $l^2$/mmol$^2$mol) | -0.20 ± 2.7x10$^{-2}$ | -0.23 ± 0.02 |
| $h_{22}^{m}$ (kJ $l^2$/mmol$^2$mol) | -2.2 ± 0.31 | -1.1 ± 0.25 |
| $h_{12}^{mic}$ (kJ $l^2$/mmol$^2$mol) | 1.9 ± 0.27 | 1.1 ± 0.13 |
| $h_{1}^{m}$ (kJ l/mmol mol) | -7.0 ± 6.4x10$^5$ | --- |
| $h_{2}^{m}$ (kJ l/mmol mol) | 2.3 ± 1.7x10$^5$ | --- |
| $h_{2}^{mic}$ (kJ l/mmol mol) | 5.4 ± 6.4x10$^5$ | --- |
| $h_{2}^{mic}$ (kJ l/mmol mol) | 2.2 ± 2.5x10$^5$ | --- |
| $h_{11}^{mic}$ **(H)** (kJ $l^2$/mmol$^2$mol) | 0.01 ± 0.002 | 6.9x10$^{-3}$ ± 1.43x10$^{-3}$ |
| $h_{11}^{m}$ **(H)** (kJ $l^2$/mmol$^2$mol) | 0.05 ± 0.01 | 0.058 ± 7.8x10$^{-3}$ |
| $h_{12}^{m}$ **(H)** (kJ $l^2$/mmol$^2$mol) | -1.3 ± 0.920 | -0.59 ± 0.62 |
| $h_{22}^{mic}$ **(H)** (kJ $l^2$/mmol$^2$mol) | 0.28 ± 0.17 | 0.24 ± 0.13 |
| $h_{22}^{m}$ **(H)** (kJ $l^2$/mmol$^2$mol) | 4.4 ± 3.7 | -5.80 ± 1.5 |
| $h_{12}^{mic}$ **(H)** (kJ $l^2$/mmol$^2$mol) | -0.28 ± 0.036 | -0.30 ± 2.6x10$^{-2}$ |
| $h_{1}^{m}$ **(H)** (kJ l/mmol mol) | -0.84 ± 2.3x10$^5$ | --- |
| $h_{2}^{m}$ **(H)** (kJ l/mmol mol) | -6.8 ± 1.2x10$^6$ | --- |
| $h_{2}^{mic}$**(H)** (kJ l/mmol mol) | 0.98 ± 3.2x10$^5$ | --- |
| $h_{2}^{mic}$**(H)** (kJ l/mmol mol) | 3.03 ± 1.1x10$^6$ | --- |
| $R^2$ | 0.956 | 0.973 |

[a] **(H)** in Table A.1 indicates dilution parameters associated with the high concentration region.

Copyright © Suvid Joshi 2014

# CHAPTER FOUR

# 4. INTERFACIAL MOLECULAR IMPRINTING OF STÖBER PARTICLE SURFACES: A SIMPLE APPROACH TO TARGETED SACCHARIDE ADSORPTION

## 4.1 Summary

The use of surfactant headgroups for interfacial imprinting is established as a simple and tunable approach to create molecularly imprinted silica nanoparticles based on a modification of the Stöber method. Adsorption of D-glucose and D-xylose (initial concentrations ranging from 0.139 to 1.67 mol/L) was measured on silica nanoparticles created by the addition of a glucose-based surfactant (n-octyl-β-D-glucopyranoside (C8G1)) or surfactant mixtures (C8G1 and cetyltrimethylammonium bromide (CTAB)) to Stöber particles shortly after their precipitation. Silica particles synthesized in the presence of C8G1 as an imprinting surfactant have a significantly higher affinity for glucose over xylose (as much as 3.25 times greater at 0.25 M saccharide), and an enhanced affinity for glucose relative to nonimprinted silica particles (as much as 4 times greater at 0.25 M), which adsorb glucose and xylose similarly. Glucose imprinting is significantly enhanced using a surfactant mixture of 1:1 C8G1 / CTAB. The interfacial activity of the nonionic imprinting surfactant at the silica surface is suggested to be improved by the presence of interfacial cationic CTAB, which is driven to the silica surface through electrostatic interactions. The concept of imprinting through the interaction of surfactant head groups with the soft surface of silica particles is supported by the importance of the time of addition of the surfactants. The greatest enhancement in glucose adsorption is observed when the surfactants are added 1 minute after precursor addition (at the onset of aggregated particle formation, as indicated by solution turbidity) and the silica affinity for glucose decreases with the time of surfactant addition. The

versatility of the surfactant imprinting of Stöber particles is demonstrated by the enhanced adsorption of xylose relative to glucose on particles imprinted using a 1:1 mixture of n-octyl-β-D-xylopyranoside and CTAB, suggesting that the process can be customized to selectively adsorb target molecules of interest.

## 4.2 Introduction

Molecularly imprinted silica materials have been of growing interest recently for applications requiring a high degree of substrate selectivity including catalysis and separations.(*17-19, 80, 106*) Molecularly imprinted silica has been synthesized successfully but complex techniques have been required such as covalent imprinting using custom precursors(*81, 203*) or microemulsion-based synthesis.(*106*) Here, we propose a simple alternative method based on the Stöber method(*22*) to synthesize molecularly imprinted silica particles using surfactants for interfacial imprinting. We hypothesize that addition of surfactants to the Stöber particles shortly after they precipitate to their final aggregated size (at which point they are still soft) facilitates imprinting the surface of these particles with sites complementary to a target molecule which is also present as the headgroup of one of the surfactants, as illustrated in Scheme 1.

The Stöber method was first reported in 1968 as a method for making uniform spherical silica particles.(*22*) Since then several mechanisms have been proposed for the synthesis process, initially based on nucleation and growth(*204*) and later including controlled aggregation.(*205*),(*206*) TEM investigations of the formation of Stöber particles and surfactant-templated mesoporous particles suggest that uniformly sized, soft droplets / particles of silica precursors form by aggregation shortly after the onset of turbidity in these solutions, and subsequently react to form solid nanoparticles.(*151, 207,*

*208*) Primary particles < 10 nm in diameter have also been observed by several techniques in Stöber particle and zeolite synthesis solutions(*209-211*), and have properties consistent with either low-crosslink density polymers(*207, 209*) or micellar aggregates(*210, 212-215*) rather than fully condensed particles. This suggests that shortly after they form, the particles are susceptible to modification by noncovalent interactions at their surface. As the particles age and become more rigid, they would be expected to be less amenable to imprinting.

Many modifications of the Stöber method have been developed to functionalize them – e.g. with dye molecules, (*142, 216*) magnetite(*217*) and biomolecules(*143*). Strategies have also been described based on modifying fully cured Stöber particles with functional groups or polymer layers to create selective adsorption sites, but none of these methods targets the silica surface itself.(*203, 218-221*) On the other hand, many examples of molecular imprinting (MI) of bulk sol-gel silica have been reported(*19*); in fact, silica gel was initially used by Dickey as the matrix to demonstrate noncovalent MI with alkyl orange dyes,(*222, 223*) although subsequent studies suggested that residual entrapped dye interfered with those experiments.(*224, 225*) More recent evidence for MI of silica has been presented, although elaborate template removal procedures are sometimes required.(*80, 226*) One successful MI strategy is covalent imprinting, which involves attaching a molecular template directly to the silica precursor, and thus requires synthesis of a custom silane for each target molecule.(*80, 227, 228*) Successful non-covalent MI of the surfaces of silica particles has also been reported by Markowitz et al. using reverse water-in-oil microemulsion synthesis.(*105-107*) This approach requires that a surfactant whose headgroup imprints for the target molecule of interest be incorporated into a stable

reverse microemulsion, which while successful may not be flexible or facile enough for some targets.

Because it only depends on weak intermolecular forces such as hydrogen bonding and van der Waals interactions, non-covalent imprinting is expected to be a flexible, facile approach to MI if conditions are found to prevent interference from solvents and other species. This approach has been explored for silica,(*80, 229*) but can result in insufficiently selective imprinting(*230, 231*) and interference from nonspecific binding of polar compounds(*232, 233*). Here we propose non-covalent imprinting by adsorption of surfactants at the surface of freshly aggregated Stöber particles. The amphiphilic nature of the surfactants is expected to drive them to the particle surface where their headgroups (which are derivatives of the target molecule) can interact with silicates to facilitate imprinting. In addition, several studies have indicated that water may be excluded from the solid-liquid interface by surfactant monolayers,(*234-237*) which may contribute to MI if it occurs at the Stöber particle-solution interface.

N-octyl-β-D-glucopyranoside (C8G1) will be used as the primary imprinting molecule to target adsorption of D-glucose (referred to simply as glucose here) on silica. This choice is motivated by the need to separate (D-)xylose (a five carbon sugar) and glucose (a six carbon sugar) in mixtures derived by saccharification of lignocellulosic biomass in a biorefinery.(*238*) This separation also offers a challenging proof of concept for saccharide separations, as these sugars differ by one hydroxymethyl group and otherwise have identical stereochemistry. Cetyltrimethylammonium bromide (CTAB) will serve as a co-surfactant expected to bind strongly to the particle surface by electrostatic interactions. Mixing cationic surfactants with nonionic sugar-based

surfactants has previously been shown to enhance their adsorption to solid silica surfaces.(*79, 235*) C8G1 and CTAB have also been shown to be compatible with silica-based materials synthesis (although the goal in that case was unrelated to the present study).(*6*) The suggested technique for MI is inexpensive, requires no custom silane precursors for imprinting or surface modification, and is easily scalable(*239*). Because it is based on the general phenomenon of surfactant adsorption, the technique can be easily tailored for various target molecules, and uniformly sized spherical Stöber particles provide tunable size as well as favorable flow and transport properties for adsorption and chromatography.(*240*)

To demonstrate the concept of surface MI, the adsorption of glucose and xylose will first be compared using four materials: Stöber silica prepared without surfactants and with only CTAB, only C8G1, or a 1:1 mixture CTAB and C8G1. Enhancement of glucose adsorption over xylose in particles prepared with C8G1 will be interpreted using a two-site Langmuir isotherm with sites specific for glucose. Once the concept is established, a series of samples prepared with varying CTAB:C8G1 ratios (1:3, 1:1 and 3:1) will be used to determine the optimal surfactant mixture for enhancing glucose adsorption. To test the hypothesis that MI results from interactions of the surfactants with the soft surface of freshly precipitated particles, a series of samples will be discussed in which a 1:1 CTAB / C8G1 surfactant mixture is added at times varying from 1 min to 4 h after initiating Stöber particle formation. Finally, to demonstrate the versatility of the process, octyl-β-D-xyloside (C8X1) will be used in place of C8G1 to imprint the particles for enhanced adsorption of xylose.

## 4.3 Experimental Section

### 4.3.1 Materials

Cetyltrimethylammonium bromide (CTAB) (99.9%) and deionized ultrafiltered (DIUF) water were purchased from Fisher Scientific; tetraethyl orthosilicate (TEOS), concentrated ammonium hydroxide (~29% w/v) and D-xylose (>99%) from Acros Organics; absolute ethanol from Deacon Labs; octyl-β-D-glucopyranoside (C8G1, 99.9%) from Affymetrix; and D-glucose (>99.5%) from Sigma. All chemicals were used as received without further purification.

### 4.3.2 Octyl-β-D-xylopyranoside synthesis (C8X1)

C8X1 was synthesized from D-xylose by first converting it to peracetylated β-D-xylose using acetic anhydride in pyridine to protect hydroxyl groups. HBr was then used to brominate the carbon neighboring oxygen in the furan ring. The brominated ring was esterified by 1-octanol in presence of $Ag_2CO_3$ and $CaSO_4$. Sodium methoxide in methanol was used for deprotection of acetylated hydroxyl groups to obtain the final product C8X1, which was purified by recrystallization. The full procedure is described by Xu et al.(*241*)

### 4.3.3 Particle synthesis

Unless otherwise indicated, all silica materials were synthesized by the same room temperature procedure. 58.2 g of anhydrous ethanol, 9.8 ml of ammonia solution and 10.8 g of DIUF water were first mixed and stirred for 15 min. Particle formation was initiated by adding 5.26 g of TEOS under vigorous stirring. If surfactants were used, they were added a set time after TEOS addition. The quantity and types of surfactants will be described below. The default time was 1 min after TEOS addition, at which point the reaction mixture had begun turning turbid. All particle solutions were stirred for 24 h

after surfactant addition (or after TEOS addition if no surfactant was used) at room temperature to allow for solidification of the silica. The particles were then centrifuged at 5500 rpm for 5 min, the supernatant was discarded, and the particles were dried and aged at 50 °C for 24 h.

Initial studies of differences in the adsorption of glucose and xylose caused by the addition of surfactants were performed using a set of four samples. They were prepared with an ammonia reagent containing ~15% w/v $NH_4OH$ and varying additives: either no surfactant (sample **1**), 20 mg of CTAB only (sample **2**), 20 mg of C8G1 only (sample **3**), or 10 mg CTAB + 10 mg C8G1 (sample **4**). The total amount of surfactant (20 mg) was estimated to be enough to provide approximately a monolayer of surfactant at the surface of the particles.

For the rest of the materials (samples **5-14**), saturated aqueous ammonia (~29% w/v $NH_4OH$) was used to give larger, easier to handle particles (see below for characterization). The first two series of these particles were prepared to observe the effects of key process parameters on surfactant incorporation and subsequent glucose adsorption. The first (samples **6-8**) was prepared with varying ratios of CTAB: C8G1. For comparison with these materials, sample **5** was prepared with no surfactant. Particles with ratios of 1:3, 3:1, and 1:1 were prepared by adding 5 mg CTAB + 15 mg C8G1, 15 mg CTAB + 5 mg C8G1, or 10 mg CTAB + 10 mg C8G1 to samples **6-8**, respectively. Surfactant was added 1 min after introducing TEOS for samples **6-8**. The second series was prepared with a constant ratio of 1:1 CTAB to C8G1 (10 mg CTAB + 10 mg C8G1) but with varying time of addition. Samples **8-12** were prepared with surfactant addition 1

min, 2.5 min, 5 min, 1 h or 4 h after introducing TEOS, respectively. Sample **5** also serves as the control sample without surfactant for comparison to this series.

Versatility of the imprinting technique was demonstrated by using another saccharide surfactant in place of C8G1. C8X1 imprinted particles (sample **13**) were prepared by first mixing 56.64 g of anhydrous ethanol, 9.8 ml of saturated aqueous ammonia and 10.8 ml of DIUF water in a conical flask, and stirring the mixture in a water bath maintained at 50 ˚C for 15 min. Because of the limited solubility of C8X1 in water, a mixture of 10 mg CTAB and 10 mg C8X1 was prepared in 2 ml of ethanol (rather than using dry surfactants as in all other particles in this study). The mixture was heated to 50 ˚C for 5 minutes in a tightly closed vial to prevent evaporation of ethanol. 5.26 g of TEOS was then added to the conical flask containing ethanol, ammonia and water. 50 sec after TEOS addition, the surfactant solution was added to the conical flask, the conical flask was stirred at 50 ˚C for another minute, and then it was removed from the water bath and stirred at room temperature for 24 h. Particles without surfactant (sample **14**) were also synthesized under the same conditions as sample **13** except that 50 sec after TEOS addition, 2 ml of ethanol (without surfactants) was added to the conical flask. To recover and wash the particles, the same procedure was used as for C8G1 imprinted particles.

*Washing particles:* After aging, all particles (on average 1.3 g of particles per batch) were washed with 12-13 ml of ethanol in 15 ml centrifuge tubes to remove the surfactant from the silica surface. Three washing cyles with ethanol were performed (with sonication to disperse the particles each time), and the particles were subsequently washed several times with DIUF water using sonication and centrifugation until the pH

of the supernatant was found to be approximately 7 using pH paper. The particles were finally recovered by centrifugation and dried at 50 °C for 24 h.

### 4.3.4 Particle characterization

Nitrogen adsorption was performed using a Micromeritics Tristar 3000 automatic gas adsorption instrument. The particles were degassed under flowing nitrogen for 5 h at 140 °C prior to analysis. Surface areas were determined using the multilayer adsorption isotherm of Brunauer, Emmett and Teller (BET)(*164*). A Beckman Coulter *Delsa Nano C* particle size analyzer was used to determine particle size and zeta potential in solution. Particles were dispersed in DIUF water for DLS using a sonication bath until a uniform colloidal suspension was obtained. The suspension was allowed to sit in a microcentrifuge tube for 30 minutes to allow settling of any aggregates that were present. A Hitachi S-4300 scanning electron microscope (SEM) was used to visualize the particles. The samples were prepared for SEM by adding a small amount of particles on carbon tape placed on a sample holder. Excess particles were blown off using pressurized air. Particles were sputtered with a conductive Au / Pd layer using an Emscope SC400 before analysis. FTIR spectra of the solid samples were measured using a ThermoElectron Nexus 470 instrument using samples pressed into KBr pellets at an approximate concentration of 1 wt%. KBr pellets were prepared using a benchtop press.

### 4.3.5 Saccharide Adsorption Measurements:

The dried particles were used to measure the adsorption of glucose and xylose from aqueous solutions. For detailed analysis (samples **1-4**), the initial concentrations of the saccharide solutions ranged from 0.139 mol/l to 1.67 mol/L in increments of 0.139 mol/L. For truncated analysis (used in samples **5-12**), three initial glucose concentrations

of 0.139, 0.694 and 1.39 mol/l were used. For xylose-imprinted materials (samples **13** and **14**), the initial concentrations were 0.15, 0.75 and 1.5 mol/L. For each adsorption measurements, 50 mg of particles were initially wetted by suspending them in 1 mL of DIUF water and stirring for 24 h in a 5 mL vial. The wetted particles were then centrifuged and the particles were transferred to the original vials along with 1 ml of a saccharide solution of known concentration. The solutions were stirred vigorously for 24 h at room temperature, centrifuged, and the supernatant was analyzed to determine the final saccharide concentration.

### 4.3.6 Saccharide Analysis

Saccharide concentrations in solution were quantified using attenuated total reflection (ATR) FTIR analysis of the solutions in a horizontal trough ATR accessory (from Pike Technologies) with a ZnSe ATR element. The spectrum of pure DIUF water was subtracted from each spectrum prior to analysis and the area under the curve from 900 to 1200 $cm^{-1}$ was used to quantify the concentration of each saccharide(*242*). Linear calibration curves (Appendix B Figure B.1) were measured for standard solutions with $R^2$ = 0.997 (for glucose) and 0.999 (for xylose). The amount of saccharide adsorption was determined by solution depletion, where the concentrations of saccharide before and after adsorption as measured by ATR-FTIR were subtracted and the amount of saccharide per mass of adsorbent was calculated by a mass balance. Adsorption measurements were performed in triplicate to determine mean and standard deviation values for all samples.

## 4.4. Results and Discussion

As noted above, four samples were first prepared to investigate the effects of the addition of surfactants early in the synthesis process on the adsorption of glucose and

xylose from aqueous solutions. These two sugars were selected because they are the most abundant saccharides found in biomass hydrolyzates, but they also are a pair of saccharides differing by a single hydroxymethyl group. Samples were prepared using no surfactant (sample **1**); or with CTAB (**2**), C8G1 (**3**), or a 1:1 mixture of CTAB and C8G1 (**4**) added 1 minute after TEOS addition. One minute is the point at which solutions become turbid after TEOS addition.

Infrared spectroscopy was used to show the inclusion of surfactants in the as-prepared samples, and their removal following washing. Removal of the templates from molecularly imprinted materials is essential to avoid potential misinterpretation of the effects observed in subsequent binding experiments, as has been pointed out for Dickey's original studies of molecular imprinting of silica gels(*225*). Figure 4.1 shows FTIR spectra of unwashed and washed silica particles as well as the solid surfactant reagents. Figure 4.1A shows the region containing bands associated with $CH_2$ stretching in the surfactants (near 2900 $cm^{-1}$, highlighted in grey). The bands are observed for CTAB, C8G1 and in all particles prepared with surfactants, which suggests that even after centrifugation the surfactants are associated with the surface of the particles. This is consistent with MI occurring on the particle surface. Fig. 4.1A also shows that the washing procedure completely removes surfactants from the particles, as indicated by the absence of $CH_2$ stretching bands in the washed particles. Figure 4.1B shows the region containing the siloxane stretching bands from ca. 1100 to 1300 $cm^{-1}$ for the Stöber particles. These bands indicate that the silica particles are well cured and that there is no harmful effect of washing on the particles. Silanol bands are present before and after

extraction (the bands at ~950 $cm^{-1}$ and within the broad OH stretching band centered near 3400 $cm^{-1}$) but no obvious differences among the bands can be discerned.

Figure 4.2 shows a representative SEM micrograph for the 1:1 CTAB/C8G1 sample (sample **4**); all samples have similar smooth, monodisperse particles with no evidence of surface features even at higher magnification (Appendix B Figure B.2). Nitrogen adsorption measurements show that all of the particle samples are nonporous, as indicated by the absence of capillary condensation in the adsorption isotherms (Appendix B Figure B.3). The surface areas of the particles from the BET isotherm are estimated to be on the order of 9-12 $m^2/g$ (Table 4.1), which is similar to the surface area calculated using the average particle size from the SEM images and assuming a silica density of 1.8 ($g/cm^3$)(*243*). The diameters of the particles from SEM all fall in the range from 310 to 350 nm (consistent with the correlation of Bogush et al. for a reagent containing ~ 15 w/v% ammonia) and no systematic trend is observed regarding the relationship between surfactant used and particle size although sample **4** (prepared with a 1:1 CTAB/C8G1 mixture) has the greatest particle size and smallest surface area. The hydrodynamic diameters from DLS agree well but are slightly larger than the diameters of the particles in SEM because of water adsorbed to the particle surfaces and concentration effects in the DLS measurement. Zeta potential measurements indicate that the particles prepared without surfactants (**1**) and imprinted with non-ionic C8G1 (**3**) are the least negative, while using CTAB during synthesis gives particles with a higher negative surface charge (samples **2** and **4**). CTAB may induce the formation of particles with a higher density of hydroxyl groups at the particle surfaces, or more acidic hydroxyl groups. Despite small differences among samples **1**-**4**, the characteristics summarized in Table 1 show that the

surfactants do not create porosity, or significant changes in particle structure. This is consistent with the surfactants remaining at the surface of the particles during synthesis.

Adsorption isotherms for aqueous glucose and xylose solutions on samples **1-4** are presented in Figure 4.3. These isotherms confirm the hypothesis that synthesis of silica particles in the presence of C8G1 leads to higher affinity, capacity, and selectivity for glucose. Particles imprinted with a 1:1 mixture of CTAB and C8G1 (sample **4**) show the highest glucose adsorption affinity and capacity followed by those imprinted with only C8G1 (sample **3**). Particles imprinted with CTAB (sample **2**) also show enhanced adsorption of glucose compared to the particles made without surfactants (sample **1**), but the adsorption seems to be non-specific, as a high level of adsorption begins to be seen even at low concentrations, and xylose adsorption levels are comparable to glucose. Enhanced non-specific adsorption in sample **2** may be the result of the increased density or acidity of the silanol groups implied by its large negative zeta potential (Table 4.1). The xylose adsorption isotherms for all particles are shown in Fig. 4.3 as well, and while the results show significant levels of nonspecific binding, they are comparable across all samples, and are consistent with C8G1 creating specific adsorption sites for glucose.

The curves plotted in Figure 4.3 are fits of a one- (4.1) or two- (4.2) site Langmuir isotherm to the data.

$$[S]_{ads} = \frac{C_{NS}K_{NS}[S]}{1 + K_{NS}[S]} \tag{4.1}$$

$$[S]_{ads} = \frac{C_{NS}K_{NS}[S]}{1 + K_{NS}[S]} + \frac{C_S K_S[S]}{1 + K_S[S]} \tag{4.2}$$

In the equations, $[S]_{ads}$ = the concentration of saccharide adsorbed per unit of area, $C_{NS}$ = the non-specific capacity of the adsorbent, $C_S$ is specific capacity of the adsorbent, $K_{NS}$ = the non-specific equilibrium coefficient for binding, $K_S$ = the specific equilibrium coefficient for binding, and $[S]$ = the aqueous saccharide concentration. The coefficients found by nonlinear regression are summarized in Table 4.2. For both xylose and glucose, the set of adsorption parameters was simultaneously fit to all four isotherms while keeping $K_{NS}$ constant among all adsorbents but allowing $C_{NS}$, $K_S$ and $C_S$ values to vary among samples. The square of the difference between measured adsorbed glucose concentrations and the model concentrations were weighted using the inverse of the standard deviation in the measurement, and minimization of the sum of the squared residuals (SSR) was performed using the Levenberg-Marquardt algorithm.(*244*)

A single-site model (Equation 4.1) was used whenever possible, and was found to provide an adequate fit for glucose adsorption onto the samples prepared without surfactants or with only CTAB (samples **1** and **2**). Equation 1 was also used for all xylose adsorption isotherms. The two-site Langmuir adsorption isotherm was only used for adsorption of glucose onto the samples made with C8G1 (**3**) and the 1:1 C8G1/CTAB mixture (**4**). This model gave a significantly superior fit for these samples, mainly because it is able to model a more rapid increase in adsorbed glucose at low concentrations than the single-site Langmuir model. The $R^2$ values for the best-fit glucose adsorption curves in Fig. 4.6 are 0.973, 0.885, 0.975 and 0.975 for samples **1-4**, respectively (Table 4.2). When a one-site model was used for all adsorbents, the corresponding $R^2$ values were significantly less: 0.791, 0.753, 0.968 and 0.836, respectively (see Appenix B Figure B.4). Attempting to use the two-site model for

xylose adsorption led to one best-fit adsorption capacity ($C_S$ or $C_{NS}$) being estimated as zero, which suggests that a one-site model was sufficient. Using a two-site model for glucose adsorption on the samples prepared without surfactant and with CTAB (**1** and **2**) led to the same conclusion. Also, fitting individual adsorption isotherms by linear or nonlinear regression was explored but the global nonlinear regression procedure employed here led to much smaller uncertainties in the optimized parameters.

Comparison of the coefficients in Table 4.2 helps to interpret the differences among isotherms in Fig. 4.3. First, we note that the capacity for non-specific binding ($C_{NS}$) changes only slightly upon going from no surfactant (0.000593±5.5% mol/m$^2$) to C8G1 (0.000554±6.4% mol/m$^2$) and the 1:1 mixture of C8G1 and CTAB (0.000595±8.2% mol/m$^2$). At the same time, the capacity for specific binding of glucose increases to a maximum of 0.000330±4.5% mol/m$^2$ for the 1:1 C8G1/CTAB mixture. This is consistent with C8G1 reorganizing some of the hydroxyl groups at the surface of the Stöber particles to create sites specific towards glucose (perhaps at the expense of some of the nonspecific surface). The total capacity of these adsorbents is on the order of 0.008 mol glucose/m$^2$, which corresponds to roughly 0.21 Å$^2$/molecule. This molecular area is much less than the molecular area that estimated from the structure of glucose (51 Å$^2$)(*245*), from the monolayer capacity estimated by molecular dynamics simulations of glucose adsorption in silica pores (44 Å$^2$)(*245*), or from the monolayer capacity of glucose dispersed on silica in the solid state (12 Å$^2$)(*246*). The high levels of adsorption found here indicate that glucose adsorbs to silica in multilayer fashion, or in clusters that nucleate at the silica surface, as observed in molecular dynamics simulations of glucose adsorption in silica channels(*247*). The amounts of glucose adsorbed during our

experiments, although high (some exceeding 1 g glucose / g particles), are consistent with a previous report of Kuhn et al., who reported a linear isotherm up to 0.8 g glucose / g celite at 30 °C over a concentration range up to 1 mol/L of glucose(*248*). CTAB increases adsorption capacity (to 0.000861±5.2% mol/$m^2$) but not adsorption specificity in sample **2**, which suggests that the effect of CTAB is to increase the density of accessible hydroxyl groups on the silica surface (consistent with its large negative zeta potential).

The nonspecific glucose adsorption equilibrium coefficient for unimprinted Stöber silica (Table 4.2) is estimated to be $K_{NS}$ = 0.862±8.6% l/mol. This value compares favorably with the order of magnitude estimated by molecular dynamics by Ziemys et al. (0.67 l/mol(*249*)), and the product $K_{NS}C_{NS}$ is equal to $6.4\times10^{-3}$ l/g, which compares favorably to the slope of the linear isotherm reported for glucose adsorption on celite at 30 °C by Kuhn et al., $3.75\times10^{-3}$ l/g(*248*). The greatest advantage offered by the 1:1 mixture of CTAB and C8G1 (sample **4**) is that it increases the equilibrium coefficient ($K_S$) for specific adsorption significantly compared to nonspecific adsorption (to $K_S$ = 42±57% l/mol). The material made with only C8G1 imprinting (**3**) shows a smaller, but still significant increase in $K_S$ compared to $K_{NS}$. The difference in affinity for glucose between samples **3** and **4** is hypothesized to be due to the relatively strong electrostatic interaction between CTAB and silica, which helps to more effectively draw C8G1 into a mixed monolayer on the Stöber particle surface during synthesis compared to hydrogen bonding interactions with C8G1 alone. The xylose adsorption parameters indicate less affinity for silica ($K_{NS}$ = 0.56±14% l/mol) and capacities that remain near 0.0008 mol/$m^2$ for all adsorbents. Overall, the Langmuir model parameters suggest that imprinting with

C8G1 creates a fraction of adsorption sites with greater affinity for glucose, even though nonspecific binding still plays a prominent role. Using only CTAB increases the capacity for both saccharides. The greatest enhancement and specificity for glucose adsorption are observed in sample **4.** This effect is most pronounced at low saccharide concentrations; for instance at 0.25 M saccharide, sample **4** adsorbs roughly *4 times as much glucose* as the sample made without surfactants (sample**1**), and roughly *3.25 times as much glucose as xylose*.

Samples **1-4** provide saccharide adsorption results consistent with MI, but additional experiments were performed to show that their synthesis conditions are optimal and consistent with the proposed mechanism. First, to determine whether a 1:1 ratio of cationic and saccharide surfactants is optimal, samples **5-8** were prepared with varying ratios of CTAB to C8G1 (summarized in Table 4.3). Uniform spherical, nonporous particles (Appendix B Figures B.5 and B.6 show SEM and nitrogen adsorption results) were obtained in all cases. All particles in this series are between 500 and 550 nm in diameter, which is consistent with the particle size predicted by the correlation of Bogush et al.(*243*) for Stöber silica under the conditions used. Other physical characteristics of the particles are summarized in Table 4.3. The particle size of these samples is greater than for samples **1-4** (Table 4.1) because samples **5-8** were prepared with fresh concentrated ammonia (~15 w/v% ammonia), while samples **1-4** were prepared with less concentrated ammonia (~15 w/v% ammonia). The larger particle size was used for ease of centrifugation and handling, but amounts of saccharide adsorbed by the two types of samples are comparable when expressed as glucose adsorbed per unit area of the particles (a direct comparison is shown for samples **4** and **8** in Figure B.7 of the Appendix B).

Similar to other surfactant-templated materials (Fig. 4.1), samples **6-8** have FTIR spectra (Appendix B Figure B.8) indicating surfactant incorporation in unwashed samples (by $CH_2$ stretching bands) and complete surfactant removal after washing. Zeta potential values for all samples prepared with mixed CTAB and C8G1 (samples **4** and **6-8**) are comparable and slightly more negative than for particles prepared without surfactant.

The glucose adsorption data for samples **5-8** are shown in Figure 4.4. Because the form of the isotherms and selectivity towards xylose was established in samples **1-4**, measurements were performed at only three initial glucose concentrations as indicators of imprinting for glucose. The data show statistically significant enhancement in the amount of glucose adsorbed for all surfactant-containing samples relative to the particles with no surfactant (sample **5**). At the higher glucose concentrations, a significant increase was also observed for the 1:1 (sample **8**) imprinted materials relative to the 1:3 and 3:1 CTAB:C8G1 imprinted materials (samples **6** and **7**). However, no statistically significant difference in the amounts of glucose adsorbed on the 1:3 and 3:1 imprinted materials was observed. This series of samples shows that enhanced glucose adsorption occurs due to the use of mixed surfactant that include C8G1, and that a 1:1 CTAB:C8G1 weight ratio appears to be optimal for imprinting for glucose.

To demonstrate that the enhanced glucose adsorption is consistent with the hypothesized mechanism of imprinting at the surface of freshly-precipitated soft silica, the time of addition of a 1:1 CTAB/C8G1 surfactant mixture after TEOS introduction was varied in samples **8-12**. It was speculated based on existing literature(*151*, *207*) that the best time to add surfactants is at the onset of turbidity in the solution (around 1 min after addition of TEOS). At that point in the synthesis, the particles are expected to have reached their

final size, but to be soft enough to allow interactions with surfactant head groups to imprint the particle surface.(*151, 207*) Polycondensation of the silica would be expected to reduce the efficacy of imprinting over time by reducing the ability of headgroups to form complementary binding sites at the particle surface.

All particles in samples **8-12** were uniformly spherical, with diameters in the range of 500-550 nm (Appendix B Figure B.9, nitrogen adsorption results in Figure B.6). No noticeable effect of surfactant addition time on particle size was detected, consistent with the concept that the particle formation process is mostly finished by the earliest time we selected for surfactant addition (1 min). FTIR spectra are reported in Figure 4.5 for as-prepared (unwashed) particles with surfactant addition times of 1 min (**8**), 2.5 min (**9**), 5 min (**10**), 1 h (**11**) and 4 h (**12**). The intensity of the $CH_2$ stretching bands near 2900 $cm^{-1}$ reduces as the time surfactant addition increases, suggesting weaker interactions of surfactants with the Stöber particles. When the surfactants were added 4 h after TEOS addition (sample **12**), no evidence of surfactant incorporation in the unwashed particles could be seen. These observations are consistent with decreasing potential for imprinting as the silica particles solidify while aging. Zeta potentials (Table 4.3) for samples with early surfactant addition (**8-10)** are similar and more negative than for samples **11** and **12**, which have zeta potentials similar to the particles prepared with no surfactants (sample **5**). This is consistent with the surfactants added early in the Stöber process interacting more strongly with the soft particle surface to give a higher density of hydroxyl groups.

Direct evidence for improved imprinting with early surfactant addition is found in the enhancement of glucose adsorption, which is shown in Figure 4.6. Prior to conducting these adsorption experiments, the particles were washed and the complete surfactant

removal confirmed by FTIR (data not shown). Because time of addition is the independent variable of interest in this series, the data in Fig. 4.6 are represented as the amount of glucose adsorbed per unit of particle area as a function of surfactant addition time, for three different initial concentrations of glucose. The final concentrations vary for these experiments, but a sample that adsorbs more glucose will also reach a lower final concentration in solution, which is consistent with shifting the isotherm upwards, towards greater levels of glucose adsorption. From Fig. 4.6 it is clear that as the time of surfactant addition increases, the amount of glucose adsorbed decreases, especially for the higher two concentration of glucose. By a surfactant addition time of one hour, the amount of glucose adsorbed appears to be level, and nearly the same as the amount of adsorption observed without surfactants (for sample **5**, shown at the rightmost part of Fig. 4.6). This observation confirms the hypothesis that the observed enhancement of glucose adsorption in the particles prepared with a 1:1 mixture of CTAB and C8G1 (samples **4** and **8**) is due to the interaction of the surfactants with the soft surface of freshly aggregated silica particles. These particles are present at the onset of turbidity, but as time progresses, the particles solidify, leading to less opportunity for molecular imprinting. Thus, as the age of the particles in solution increases, we see not only decreased incorporation of surfactants at the particle surface (Fig. 4.5), but also less enhancement of glucose adsorption due to imprinting (Fig. 4.6).

As a final test of the generality of this imprinting concept, particles were prepared using the xylose-based surfactant octyl β-D-xylopyranoside (C8X1) along with CTAB (sample **13**). If the concept of molecular imprinting by a carbohydrate surfactant is broadly applicable, C8X1 is expected to impart selectivity for xylose. Through DSC

experiments, the Krafft temperature of C8X1 was determined to be 46.3 ˚C (Figure B.10 in Appendix B). Therefore, to ensure that the surfactant was soluble during synthesis, the synthesis was carried out at an initial temperature of 50 ˚C. To minimize the impact of high temperature synthesis the particles were stirred at 50 ˚C for only 50 sec after surfactant addition, by which time the particle formation (indicated by the onset of turbidity) is thought to be complete. As in other surfactant-templated particles, FTIR spectra of sample **13** prepared using a 1:1 mixture of C8X1 and CTAB (Figure 4.7**)** show $CH_2$ stretching bands associated with surfactants before washing and elimination of these bands after washing, with no change in the siloxane stretching bands near 1200 $cm^{-1}$.

SEM images of particles synthesized at 50 °C with and without CTAB/C8X1 surfactants (samples **13** and **14**) are shown in Appendix B Figure B.11. No drastic effect is seen on particle size (330-360 nm) or particle shape due to use of higher temperature. The nitrogen adsorption isotherm (Appendix B Figure B.12) shows no evidence for porosity. However, the zeta potentials of both samples prepared at 50 °C are significantly less negative than for samples prepared at room temperature (Table 4.3).

The adsorption of glucose and xylose (initial concentrations of 0.15, 0.75 and 1.5 M) on the particles synthesized from 1:1 CTAB:C8X1 and non-imprinted particles are compared in Figure 4.8. The imprinted particles (sample **13**) adsorb significantly more xylose than the non-imprinted particles (sample **14**). The greatest enhancement is observed at the lowest initial saccharide concentration, where the xylose adsorption is increases by *5.5 times*. Glucose adsorption on the sample made with 1:1 CTAB and C8X1 (**13**) is only slightly greater than for the comparable sample made without surfactants (**14**), which exhibits the same amount of non-specific adsorption of both

glucose and xylose. These results demonstrate that the enhancement of adsorption is specific to the target molecule that is present in the headgroup of the surfactant used for particle preparation. Particles with affinity for either glucose or xylose can be prepared by simply using a saccharide surfactant whose headgroup is the saccharide of interest. Closely related saccharides (such as glucose in Fig. 4.8) show similar levels of adsorption on both non-imprinted particles and particles imprinted to target a different saccharide (xylose in Fig. 4.8).

Overall, the xylose imprinting by C8X1 appears to be somewhat more effective than glucose imprinting by C8G1. Imprinting with a 1:1 CTAB/C8G1 mixture gives at most a 4-fold increase in glucose adsorption (at 0.25 M saccharide, Fig. 4.3) compared with a 5.5-fold increase in xylose adsorption for imprinting with a 1:1 CTAB/C8X1 mixture (at ~0.15 M saccharide, Fig. 4.8). The effect of particle synthesis temperature (room temperature for glucose imprinted materials and 50 °C for xylose imprinted materials), necessitated by differences in the solubility of C8G1 and C8X1, may accentuate the imprinting effect of C8X1. Non-specific adsorption of both glucose and xylose to these non-imprinted materials was significantly reduced for particles synthesized at 50 °C relative to room temperature synthesis. For instance, the sample prepared without surfactants at room temperature (**5**) adsorbs 0.00034 mol glucose/$m^2$ at 1.3 mol glucose/L in solution, while the sample precipitated without surfactants at 50 °C (sample **14**) adsorbs 0.0001 mol glucose/$m^2$ at 1.5 mol glucose/L in solution. We speculate that this may be because the higher synthesis temperature leads to a lower hydroxyl density on the final particle surface (consistent with the reduced magnitude of zeta potential of these particles), and hence less functional groups for saccharide interactions. Regardless of the

source of reduced nonspecific binding, however, the increased hydrophobicity of the xylopyranoside headgroup of C8X1 relative to C8G1 would be expected to help to drive the surfactant to the particle surface during synthesis, thus leading to the improved efficacy of imprinting. This observation suggests that tuning the surface forces that drive surfactant templates to the surface of freshly precipitated Stöber silica particles should be a way to further improve molecular imprinting by this approach.

## 4.5. Conclusions

In conclusion, evidence was presented consistent with molecular imprinting of freshly precipitated Stöber silica particles by headgroups of saccharide surfactants to impart selective enhancement in adsorption of the corresponding target saccharide. Cationic surfactant CTAB was added to improve imprinting by providing strong electrostatic interactions in the mixed surfactant adlayers.(*79, 235*) Of the surfactant compositions tested, a 1:1 mixture of CTAB and the saccharide surfactant was found to give the greatest enhancement in saccharide adsorption. Detailed analysis of saccharide adsorption isotherms showed that the glucose-based surfactant C8G1 imprints the silica with sites that have a significantly greater affinity for glucose than non-imprinted silica. The effect was greatest for the sample prepared with a 1:1 mixture of CTAB and C8G1 (sample **12**), which showed roughly 4 times more glucose adsorption than non-imprinted particles and 3.25 times more glucose adsorption than xylose, both at saccharide concentrations in solution of 0.25 M. The time of surfactant addition was also varied, and FTIR showed that the greatest amount of surfactant was incorporated for the earliest surfactant addition time tested, at the onset of turbidity of the solution 1 min after silica precursor addition. Consistent with molecular imprinting of freshly precipitated silica

particle surfaces, glucose adsorption was also most strongly enhanced for the earliest surfactant addition.

This approach to molecular imprinting is novel but simple, and can be generalized to other target molecules because no modification of the particle synthesis procedure is required. This point was demonstrated by preparing imprinted particles with the xylose-based surfactant C8X1 that selectively adsorb xylose compared to glucose. These results suggest that a wide variety of target compounds can be used as long as surfactant imprinting molecules are available, and further modification to add complementary functionality or to block nonspecific binding are possible ways to further enhance the effectiveness of this approach.

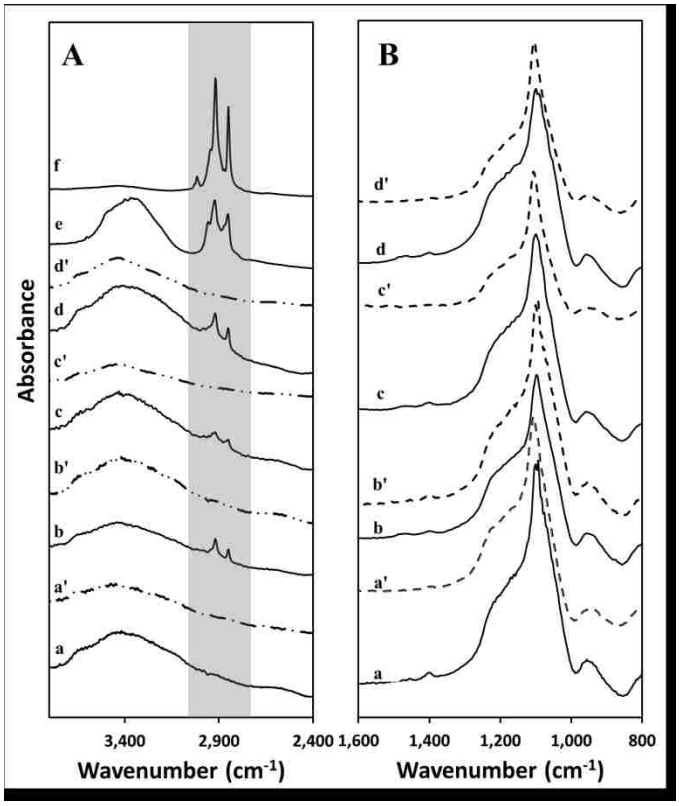


**Figure 4.1.** (A) High wavenumber and (B) low wavenumber regions of the FTIR spectra of imprinted Stöber particles, showing the presence of surfactant on the particles before washing and its removal upon washing. Spectra are shown for (a) sample 1, non-imprinted silica, (b) sample 2, prepared with CTAB, (c) sample 3, prepared with C8G1, (d) sample 4, prepared with a 1:1 CTAB / C8G1 mixture, (e) crystalline C8G1 and (f) crystalline CTAB. Spectra labeled with primes (a' through d') are the spectra of washed samples 1-4, respectively.

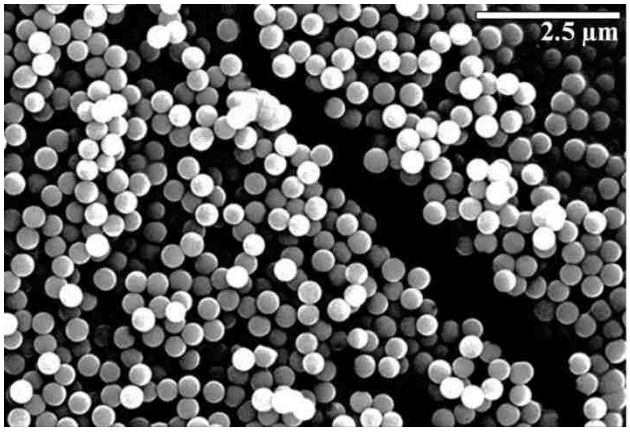


**Figure 4.2.** Representative SEM micrograph of monodisperse nonporous silica particles synthesized using the Stöber process, with imprinting using a 1:1 mixture of CTAB and C8G1 by weight (sample **4**). SEM micrographs of all other samples are qualitatively similar, and included in the Supplemental Information.

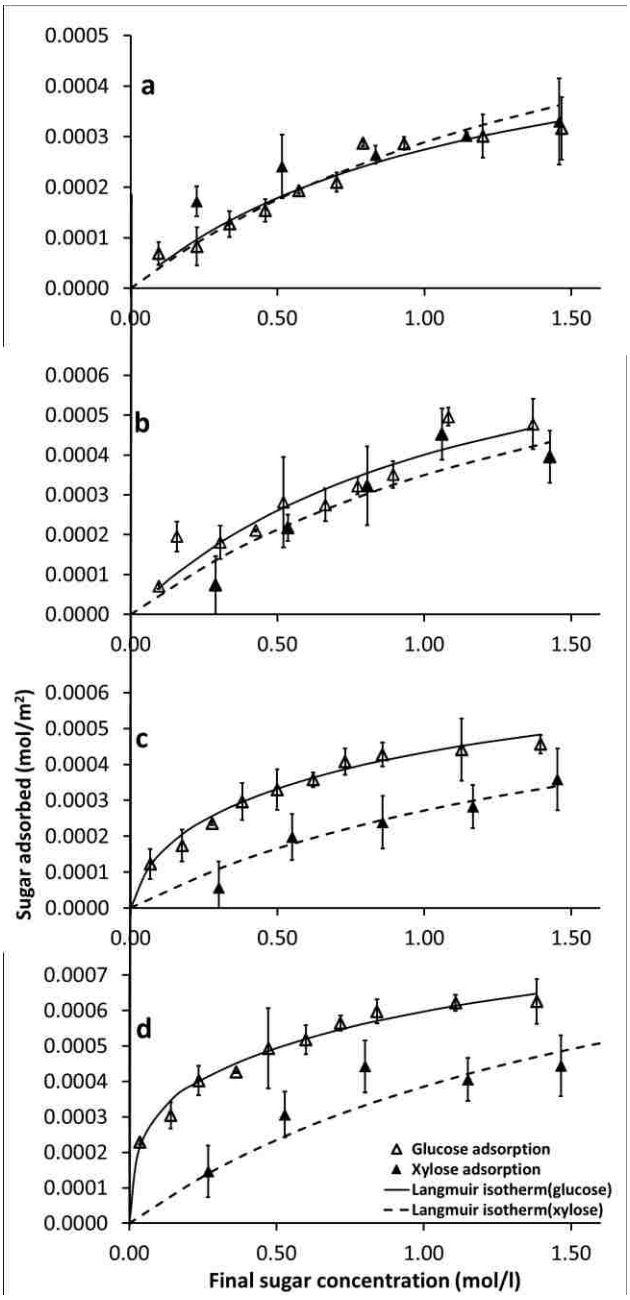


**Figure 4.3.** Comparison of adsorption isotherms for D-glucose and D-xylose adsorbing from aqueous solution onto (a) sample **1**, non-imprinted particles, (b) , sample **2**, prepared with CTAB, (c) sample **3**, prepared with C8G1, and (d) sample **4**, prepared with a 1:1 mixture of CTAB and C8G1. The vertical axis represents moles of saccharide adsorbed per $m^2$ of silica particle area, and the horizontal axis represents the final moles of sugar per liter of solution. Curves are best-fit Langmuir isotherms found by globally optimizing adsorption parameters for all adsorbents (see text for further explanation).

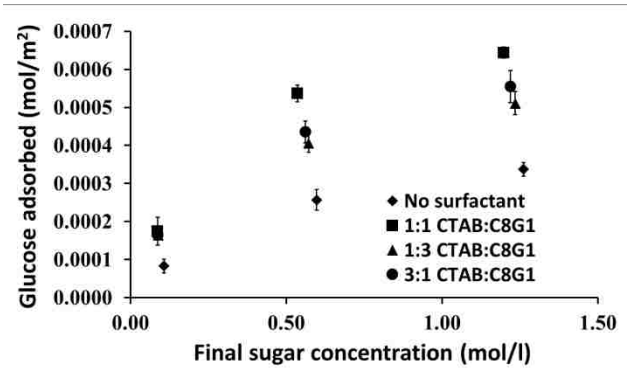


**Figure 4.4.** Adsorption isotherms for adsorption of glucose onto particles prepared with different ratios of surfactants (samples **5-8**), expressed as moles of glucose per $m^2$ of particle surface vs. moles of glucose remaining per liter of aqueous solution.

**Figure 4.5.** FTIR absorbance curves for unwashed Stöber particles in KBr pellets. All samples (numbers **8-12**) were imprinted with a 1:1 mixture of CTAB and C8G1 by addition of the surfactant at the indicated times after addition of TEOS. The $CH_2$ stretching bands between 2800 and 3000 $cm^{-1}$ indicate surfactant incorporation in the particles.

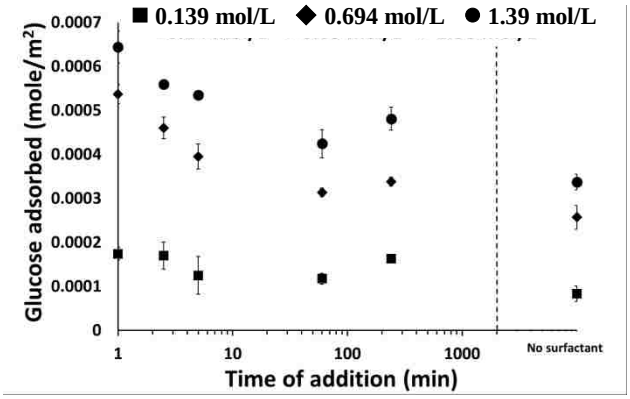


**Figure 4.6.** Moles of sugar adsorbed per area as a function of the time of addition of surfactant during the particle synthesis (for samples **8-12**). Results are shown for three different initial glucose concentrations, indicated in the legend. The rightmost set of points is for sample **5**, prepared without any surfactant added.

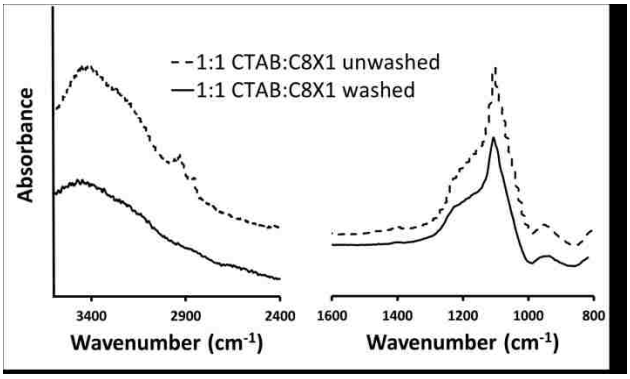


**Figure 4.7** FTIR absorbance spectra for 1:1 CTAB / C8X1 imprinted Stöber particles (sample **13**) before and after washing to remove the template. The siloxane stretching band is visible between 1000 and 1300 $cm^{-1}$, and the $CH_2$ stretching band (indicating the presence of surfactants) is visible between 2800 and 3000 $cm^{-1}$ in the unwashed sample.

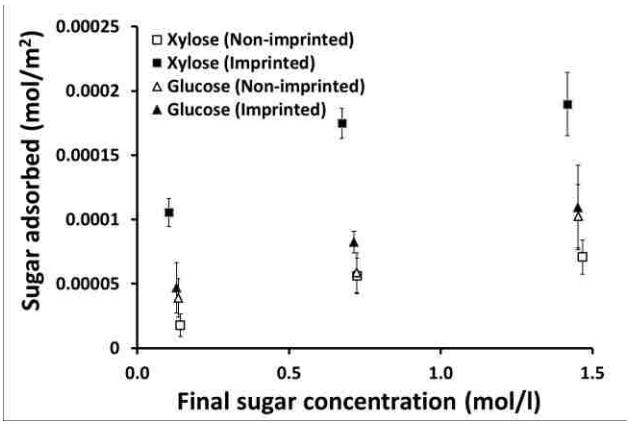


**Figure 4.8.** Adsorption isotherms for xylose and glucose on comparable particles imprinted with a 1:1 mixture of C8X1 and CTAB (sample **13**) or prepared without surfactant (non-imprinted, sample **14**).

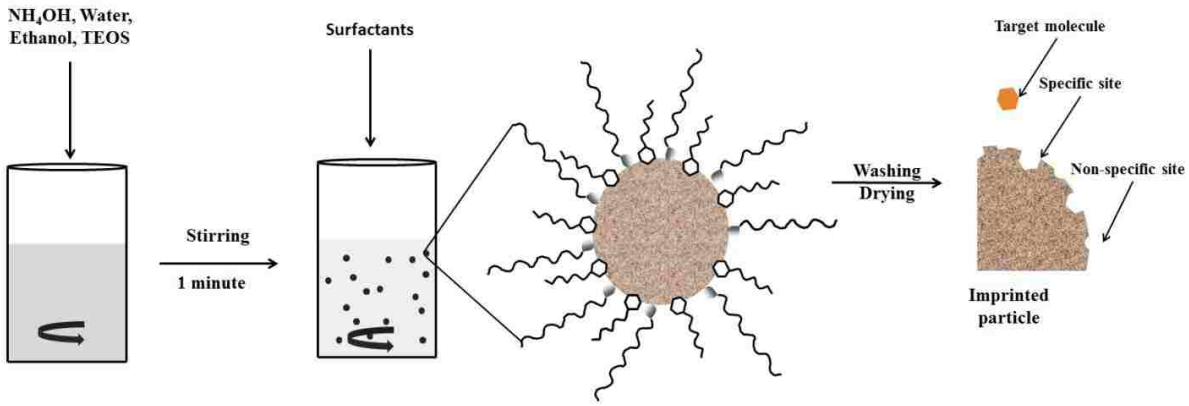


**Scheme** Error! No text of specified style in document.**-1 .** Synthesis procedure for Stöber particles and schematic of the proposed surfactant-based molecular imprinting mechanism.

**Table 4.1.** Physical characteristics of particles synthesized with low-concentration ammonia with and without various surfactants, determined using nitrogen adsorption, SEM and DLS.

| Sample | Surfactant | BET surface area ($m^2/g$) | SEM surface area[a] ($m^2/g$) | SEM particle dia.[b] (nm) | DLS hydrodynamic dia.[c] (nm) | Zeta potential (mV)[d] |
|---|---|---|---|---|---|---|
| **1** | No surfactant | 12.5 | 10.6 | 312±15 | 420.7(0.13) | -48.57±0.10 |
| **2** | CTAB | 12.3 | 9.6 | 346±12 | 410.2(0.05) | -56.43±0.29 |
| **3** | C8G1 | 11.8 | 9.9 | 335±10 | 386(0.11) | -48.03±0.16 |
| **4** | 1:1 CTAB:C8G1 | 9.0 | 9.5 | 349±23 | 413.9(0.12) | -52.09±0.18 |

[a] Calculated from the mean particle diameter assuming a silica density of 1.8 ($g/cm^3$) (*243*). [b] Mean particle diameter ± standard deviation calculated using 10 different particles. [c] Hydrodynamic radius with polydispersity index indicated in parentheses. [d] Mean zeta potential ± the range from two repeated measurements.

**Table 4.2.** Langmuir isotherm parameters found by nonlinear regression for D-glucose and for D-xylose adsorbed to all silica samples. The curves corresponding to these parameters are shown in Figure 4.2.[a]

| **Surfactant (sample)** | **K (l/mol)** | | | **C (moles sugar/$m^2$ silica)** | | | **$R^2$** | |
|---|---|---|---|---|---|---|---|---|
| | *Glucose* $K_{NS}$[b] | *Glucose* $K_S$ | *Xylose* $K_{NS}$[b] | *Glucose* $C_{NS}$ | *Glucose* $C_S$ | *Xylose* $C_{NS}$ | *Glucose* | *Xylose* |
| No surfactant (**1**) | | N/A | | $5.93*10^{-4}$ ±5.5% | N/A | $8.00*10^{-4}$ ±17% | 0.973 | 0.641 |
| CTAB **(2)** | | N/A | | $8.61*10^{-4}$ ±5.2% | N/A | $9.75*10^{-4}$ ±25% | 0.885 | 0.891 |
| C8G1 **(3)** | 0.862±4.9% | 13±33% | 0.56±14% | $5.54*10^{-4}$ ±6.5% | $1.91*10^{-4}$ ±6.4% | $7.63*10^{-4}$ ±12% | 0.975 | 0.943 |
| 1:1 CTAB:C8G1 **(4)** | | 42±57% | | $5.95*10^{-4}$ ±8.2% | $3.30*10^{-4}$ ±4.5% | $1.01*10^{-3}$ ±17% | 0.975 | 0.800 |

[a] The uncertainties indicated for all values are 95% confidence intervals calculated using Fisher's F distribution as described by Kemmer and Keller(*250*). For glucose, 9 parameters were used for regression and 39 data points. For xylose, 5 parameters were used for regression and 24 data points.

[b] One value of $K_{NS}$ was used to fit the entire glucose adsorption data set, and another single value for the entire xylose adsorption data set.

**Table 4.3.** Synthesis conditions for particles prepared with fresh, saturated ammonia and varying ratios of surfactants, time of surfactant addition and temperature, and their physical characteristics determined using nitrogen adsorption, SEM and DLS.

| Sample | Surfactant | Temperature | Time of addition | BET surface area ($m^2/g$) | SEM surface area[a] ($m^2/g$) | Zeta potential (mV) |
|---|---|---|---|---|---|---|
| **5** | No surfactant | RT | n/a | 7.47 | 5.4 | -47.49±0.39 |
| **6** | 5 mg CTAB, 15 mg C8G1 | RT | 1 min | 5.97 | 6.2 | -51.71±0.36 |
| **7** | 15 mg CTAB, 5 mg C8G1 | RT | 1 min | 6.05 | 5.9 | -55.83±0.48 |
| **8** | 10 mg CTAB, 10 mg C8G1 | RT | 1 min | 5.87 | 6.1 | -51.87±0.36 |
| **9** | 10 mg CTAB, 10 mg C8G1 | RT | 2.5 min | 5.92 | 6.1 | -54.50±0.53 |
| **10** | 10 mg CTAB, 10 mg C8G1 | RT | 5 min | 5.94 | 5.9 | -50.26±0.75 |
| **11** | 10 mg CTAB, 10 mg C8G1 | RT | 1 h | 6.48 | 6.1 | -47.42±0.81 |
| **12** | 10 mg CTAB, 10 mg C8G1 | RT | 4 h | 5.85 | 6.1 | -48.00±0.30 |
| **13** | No surfactant | 50 ˚C | 50 s | 9.4 | 9.1 | -37.57±0.47 |
| **14** | 10 mg CTAB, 10 mg C8X1 | 50 ˚C | 50 s | 8.7 | 10.3 | -41.81±0.98 |

[a] Calculated from the mean particle diameter assuming a silica density of (1.8 $g/cm^3$) (*243*).

Copyright © Suvid Joshi 2014

# CHAPTER FIVE
# 5. IMPRINTING OF STÖBER PARTICLES TO TARGET MONOSACCHARIDES AND DISACCHARIDES FOR APPLICATION IN CHIRAL SEPARATION

## 5.1 Summary

A simple, inexpensive and tunable imprinting technique to produce nonporous particles for chiral adsorption of saccharides has been developed. It is based on adding sugar-based surfactants early in the Stöber silica particle synthesis process (around 1 minute after silica precursor addition) to create molecularly imprinted sites on the surface of silica particles which are sensitive to the chirality of carbohydrate adsorbates. Mixtures of hexadecyltrimethylammonium bromide (CTAB) and n-octyl-β-D-glucopyranoside (C8G1) or n-dodecyl-β-D-maltopyranoside (C12G2) are employed to target adsorption of D-glucose or D-maltose, respectively. It is observed that the adsorption of D-glucose on these imprinted materials is enhanced when compared to adsorption of other hexoses like D-mannose and D-galactose which differ by a change at only one chiral center (by approximately 1.5 times) and even more (>3 times) when compared to the enantiomer L-glucose. Materials imprinted to target D-maltose showed nearly 5 times enhancement in adsorption of D-maltose over cellobiose at the lowest tested concentration. This is significant because both of these saccharides are dimers of D-glucose that differ only in the linkage between the saccharides. Thus, this study shows that a straightforward molecular imprinting approach of the surface of freshly prepared, soft silica particles can yield particles that exhibit preferential adsorption for a chiral target over similar molecules differing by one or more chiral centers, or by the anomeric attachment between polysaccharides.

## 5.2 Introduction

Many examples are available in the literature reporting the synthesis of molecularly imprinted silica materials for applications like catalysis, sensing and separations(*18, 80, 251-254*). Although such materials have been successfully synthesized for a long time, the methods used for imprinting, such as covalent imprinting(*81, 255, 256*) and microemulsion-based approaches(*105, 107, 257, 258*), are complex and sometimes require extensive techniques for template removal. In this paper we utilize a simple technique recently discovered in our group to non-covalently imprint silica particles. The hypothesis underlying the approach is that adding a surfactant with a head group similar to the target molecule early in the Stöber silica particle synthesis(*22*) (when the particles have just precipitated) will imprint the silica surface with sites selective towards the target molecule.

The Stöber process is a well-known method to synthesize monodisperse spherical silica particles by precipitation in basic medium(*22*). Several mechanisms have been proposed for the synthesis process, initially based on nucleation and growth(*204*) and later including controlled aggregation.(*205*),(*206*) TEM investigations of the formation of Stöber particles and surfactant-templated mesoporous particles suggest that uniformly sized, soft droplets / particles of silica precursors form by aggregation shortly after the onset of turbidity in these solutions, and subsequently react to form solid nanoparticles.(*151, 207, 259*) Primary particles < 10 nm in diameter have also been observed by several techniques in Stöber particle and zeolite synthesis solutions(*209-211*), and have properties consistent with either low-crosslink density polymers(*207, 209*) or micellar aggregates(*210, 212-215*) rather than fully condensed particles. This suggests that shortly after they form, the particles are susceptible to modification by non-covalent

interactions at their surface. As the particles age and become more rigid, they would be expected to be less amenable to imprinting. In Chapter 4, imprinting of Stöber particles has been demonstrated for selectivity towards targeted sugars with different molecular weights, but selectivity towards sugars with the same molecular weights (chiral separations) has not been demonstrated yet.

Chiral separations are of immense importance(*260*) in biochemistry and in the pharmaceutical industry due to significant differences in activity of enantiomeric pairs of active ingredients. This is especially important because there are multiple examples where one enantiomer displays desired pharmacological activity while the other enantiomer is toxic.(*261*) Chiral separations have broader applications in determining food quality(*262*), and in determining enantiomeric excess in applications such as archaeology(*263*) and astronomy(*264*). Several reviews have been published detailing methods currently available for separation of enantiomers using techniques including capillary electrophoresis, capillary chromatography, gas chromatography, and nano-liquid chromatography.(*261, 265-267*) While all of these techniques have been successfully utilized for separations, none of these techniques directly targets differences in the 3D structure of the molecules to be separated. Molecular imprinting can potentially be used to more directly target structural differences to bind specific chiral molecules.

Molecular imprinting is an established technique for targeting specific molecules in applications requiring a high degree of specificity(*18, 82, 268, 269*). Molecular imprinting has been demonstrated on various materials including carbon, molecular sieves, polymers and silica surfaces(*16-19, 80, 228, 270*). Silica molecular imprinting was one of the first systems explored for molecular imprinting by Dickey,(*222, 223*),

although Haldeman and Emmett(*86*) questioned whether incomplete template removal was responsible for the enhanced adsorption of the target. Since then, both covalent and non-covalent imprinting have been conclusively demonstrated on silica.(*16, 80*) While covalent imprinting provides more control over the arrangement of functional groups (since they are initially bound to the template), non-covalent imprinting is a viable approach based on weak forces between a template and complementary materials precursor, which is widely used due to its simplicity. A comparison of both approaches to imprinting has been unable to conclusively prove if one of the techniques is better.(*16, 271*) For chiral recognition, molecular imprinting has been recognized for some time as a potential low-cost, high selectivity method to create separation media,(*260*) although heterogeneity of binding sites may provide some limitations(*272*).

Various reviews have summarized the use of molecular imprinting for chiral separations(*18, 82, 269, 270, 273*). Most of the existing work on molecular imprinting for chiral separation employs organic polymers; only a few reports on imprinting of inorganic materials are available, and they focus on amino acid separations(*274-277*). Paik et al(*275*) synthesized chiral mesoporous silica (CMS) using the approach of Che et al.(*278*) with a chiral block copolymer (CBC) containing poly(L-glutamic acid). They reported that CMS imprinted with L-CBC adsorbed 5 times as much L-valine compared to D-valine. Yokoi et al(*276*) synthesized chiral mesoporous silica using molecular imprinting and reported targeted asymmetric separation of L-N-trifluoroacetylalanine ethyl ester ($CF_3CO$-Ala-OEt) from a racemic mixture. Silica materials have also been functionalized for chiral separations. Teicoplanin grafting(*279*) on the surface of magnetic silica nanoparticles was used to separate five different racemates, and

functionalization with oligosaccharides was used to form mesoporous SBA-15 silica that demonstrates enantioselective adsorption(*280*). Chiral catalysis on imprinted nonporous silica particles was observed by Markowitz et al(*105*). They observed that particles imprinted with N-α-decyl- L-phenylalanine-2-aminopyridine displayed a rate of hydrolysis of D-BAPNA 39 times higher than L-BAPNA. It was suggested that molecular structure of the substrates affected the packing at molecularly imprinted sites, causing the difference in rates.

In carbohydrates, chiral variations play rich and complex roles in their structure and function. Not only are there multiple chiral centers present in (poly)saccharides, but also variation in the anomeric form of linkages that are utilized for signaling and molecular recognition.(*281*) Separation of hexoses without imprinting has been demonstrated in the past using both cation and anion exchange resins(*282-285*). Khym and Zill(*284*) demonstrated enhanced separation of various hexoses and pentoses on borate modified anion exchange resins. Hydrophilic interaction liquid chromatography, where a hydrophilic stationary phase is used with organic mobile phase followed by elution with water, has also been demonstrated to be successful in separation of monosaccharides, disaccharides and oligosaccharides(*286-288*). These techniques succeed because of differences in the arrangement of functional groups on the saccharides, but they are not designed to target specific sugars. Non-covalent molecular imprinting is a viable approach to molecular recognition of saccharides that has been demonstrated with several organic polymer systems(*289-301*). Non-covalent imprinting of metal oxides for chiral separation of saccharides is a newer approach.

Imprinting of metal oxide surfaces for saccharides has been reported rarely, but should have advantages related to their chemical, thermal and mechanical robustness.(*252*) Yang et al. reported the preparation of sol-gel titania imprinted with D-glucose coatings on mercaptoethanol modified QCM electrode for sensing of D-glucose(*302*). The imprinted thin films had higher adsorption of D-glucose over D-fructose, D-galactose and D-mannose, and FTIR was used for qualitative assessment of adsorption and desorption of D-glucose over multiple cycles. Despite the success of this approach, the imprinting of oxides such as silica for chiral separation of monosaccharides and disaccharides has not yet been reported. This work will demonstrate a flexible technique to synthesize tunable molecularly imprinted nonporous silica particles with uniform size and shape (advantageous for packing in columns) which are imprinted with surfactant mixtures for chiral selectivity towards imprinted carbohydrate targets.

Here, a new direction is presented for direct molecular imprinting of Stöber particle surfaces for chirally resolved adsorption of saccharides. It will be demonstrated that adding the surfactant at the time of precipitation of Stöber particles from reaction mixture leads to chirally selective adsorption sites. Specifically, D-glucose will be targeted using the template n-octyl-β-D-glucopyranoside (C8G1), and adsorption of D-glucose onto these materials will be compared to D-mannose, D-galactose (both of which differ by only one chiral center) and L-glucose (which is the enantiomer of D-glucose). It will also be shown that the imprinting technique used here is versatile by using the same approach to imprint for D-maltose using n-dodecyl-β-D-maltopyranoside. The effect of the chirality of the anomeric linkage in disaccharides of D-glucose is tested, by comparing the adsorption of D-maltose (which has an α-1,4-glycosidic linkage) and D-cellobiose

(which has a β-1,4-glycosidic linkage). This work will not only provide further evidence that molecular imprinting of soft Stöber particles can occur by the hypothesized mechanism, but will also demonstrate that chirally preferential adsorption can be achieved in the resulting materials.

## 5.3 Materials and methods

### 5.3.1 Materials

Cetyltrimethylammonium bromide (CTAB) (99.9%), D-maltose monohydrate (>99%), cellobiose (>99%) and deionized ultrafiltered (DIUF) water were purchased from Fisher Scientific; tetraethyl orthosilicate (TEOS), concentrated 29.8% w/v ammonium hydroxide, D-mannose (99%), D-galactose(99%) and L-glucose(99%) from Acros Organics; absolute ethanol from Deacon Labs; n-octyl-β-D-glucopyranoside (C8G1, 99.9%) and n-dodecyl-β-D-maltopyranoside (C12G2, 99%) from Affymetrix; and D-glucose (>99.5%) from Sigma. All chemicals were used as received without further purification.

### 5.3.2. Particle synthesis

Particles were prepared by first mixing 58.2 g of ethanol, 9.8 ml of concentrated ammonia and 10.8 g of DIUF water. The solution was stirred for fifteen minutes and 5.26 g of TEOS was added under vigorous stirring. All particle solutions were stirred for 24 hours to allow for solidification of the silica. Particles imprinted for D-glucose were prepared by following the same particle synthesis procedure but adding a solid mixture of 10 mg CTAB and 10 mg C8G1 exactly one minute after the addition of TEOS (at which point the solutions were already turbid due to particle precipitation). To imprint for D-maltose, a solution containing 10 mg CTAB and 10 mg C12G2 was prepared in 2 ml ethanol to compensate for slower dissolution of C12G2. This solution was then added 1

minute after addition of TEOS. The volume of ethanol used for synthesis sol preparation was adjusted to account for this volume (i.e. 56.6 g of ethanol were used rather than 58.2 g). The surfactant amounts were calculated based on the surface area of the non-imprinted particles and were sufficient to form a theoretical monolayer on the particle surface. In all cases, the mixture was stirred at room temperature for 24 hours before the particles were recovered by centrifugation and aged in an oven at 50 °C for 24 h to allow for additional solidification and interactions with surfactants to occur. All particles were subsequently washed with ethanol to remove the surfactant from the silica surface through three cycles of sonication and centrifugation. The particles were subsequently washed several times with DIUF water using sonication and centrifugation until the pH of the supernatant was found to be neutral using pH paper. The particles were finally dried at 50 °C for 24 h to obtain clean particles.

### 5.3.3. Particle characterization

Nitrogen adsorption was performed using a Micromeritics Tristar 3000 instrument. The particles were degassed prior to analysis under flowing nitrogen for 5 hours at 140 °C. Surface areas were determined using the multilayer adsorption isotherm of Brunauer, Emmett and Teller (BET)(*164*). A Beckman Coulter Delsa Nano C particle size analyzer was used to determine particle size and zeta potential in solution. Particles were dispersed in DIUF water for DLS using a sonication bath until a uniform colloidal suspension was obtained. Before analysis, suspensions were allowed to sit in a microcentrifuge tube for 30 minutes to allow settling of any aggregates that were present. A Hitachi S-4300 scanning electron microscope (SEM) was used to visualize the particles. The samples were prepared by dispersing a small amount of particles in ethanol by sonication and

placing few drops of suspension onto carbon tape placed on a sample holder. The samples were dried in a fume hood and excess particles were blown off using pressurized air. Particles were coated with a conductive layer before analysis. FTIR sspectra of the solid samples were also recorded using a ThermoElectron Nexus 470 instrument for samples pressed into KBr pellets at an approximate concentration of 1 wt%.

### 5.3.4. Saccharide Adsorption Measurements

The washed, dried particles were used to measure the adsorption of hexoses from aqueous solutions onto particles imprinted for D-glucose and non-imprinted particles, while adsorption of disaccharides from aqueous solution was measured on particles imprinted for D-maltose. The initial concentrations of the saccharide solutions ranged from 0.14 mol/L to 1.4 mol/L for hexoses while D-maltose solutions ranged from 0.073 mol/L to 0.73 mol/L and D-cellobiose solutions from 0.073 mol/L to 0.365 mol/L due to limited solubility at room temperature. For each adsorption measurement, 50 mg of particles was suspended in 1 mL of DIUF water and stirred for 24 h in a 5 mL vial to wet the particles. The wetted particles were then centrifuged and the particles were transferred to the original vials along with 1 ml of a saccharide solution of known concentration. The solutions were stirred vigorously for 24 h at room temperature, centrifuged, and the supernatant was analyzed to determine the final saccharide concentration.

### 5.3.5. Saccharide Analysis

Calibration curves were prepared using standard saccharide solutions. Concentration was quantified using attenuated total reflection (ATR) FTIR analysis of the solutions with concentrations from 0.14 mol/L to 1.66 mol/L in a horizontal trough ATR accessory

(from Pike Technologies) with a ZnSe ATR element. The spectrum of pure DIUF water was subtracted from each spectrum prior to analysis and the area under the curve from 900 to 1200 $cm^{-1}$ was used to quantify the concentration of each saccharide. Linear calibration curves (Appendix C Figures C.1 and C.2) were obtained for all hexoses used in the study as well as the disaccharides. High $R^2$ values (at least 0.994) were obtained for all of the calibration curves. To determine the amount adsorbed, the concentrations of saccharide in the supernatants after adsorption as measured by ATR-FTIR were subtracted from the measured initial concentration and the amount of saccharide per mass of adsorbent was determined by a material balance. Adsorption measurements were performed in triplicate to determine the mean and standard deviation values for all measurements.

## 5.4 Results and Discussion

The first set of experiments performed as part of this study were based on imprinting using a 1:1 mixture of CTAB and C8G1. The objective is to determine whether imprinting with the β-D-glucopyranoside headgroup leads to enhanced adsorption of D-glucose in comparison to related hexoses, whose 3-D structures are illustrated in Figure 5.1. As Fig. 5.1a illustrates, D-glucose has a relatively flat conformation, with all of the hydroxyl groups arranged equatorially around the pyranose ring. Making one chiral change, either at the 4-carbon (in D-galactose, Fig. 1b) or the 2-carbon (in D-mannose, Fig. 1d) moves that hydroxyl group out of the equatorial position to point axially, which is a subtle but potentially significant difference. Changing all of the chiral centers in the enantiomer L-glucose (Fig. 1c) leads to a large change in the 3D structure, where the hydroxyl groups are split axially between the two sides of the pyranose ring. These

differences in structure due to changes in chiral centers are hypothesized to lead to preferential adsorption in the D-glucose imprinted silica materials.

Prior to saccharide adsorption measurements, nitrogen adsorption, SEM and dynamic light scattering were performed on the imprinted (prepared with 1:1 CTAB/C8G1) and non-imprinted (prepared without surfactant) samples used for hexose adsorption. The surface areas of the non-imprinted and imprinted particles were comparable (7.9 $m^2/g$ and 8.1 $m^2/g$, respectively). Nitrogen adsorption isotherms for both particles (Appendix C Figure C.3) indicate no porosity. The average particle sizes in the SEM images (Figure 5.2) are also comparable (456 nm for non-imprinted and 464 nm for imprinted particles). The surface areas estimated based on the SEM diameter of the particles averaged over at least 20 particles and the density of silica (1.8 $g/cm^3$) were similar to (but systematically smaller than) the BET surface areas. The imprinted particles had a somewhat more negative zeta potential (-51.7 mV) compared to materials which were prepared without imprinting (-48.1 mV). This may be because of the presence of a larger density of hydroxyl groups on the silica particle surface due to interaction with ionic surfactants used for imprinting. The physical characteristics of the particles are summarized in Table 1. The overall similarity in characteristics of the particles is consistent with the surfactants interacting only with the surface of the particles, without significantly changing their physical characteristics or introducing porosity.

FTIR spectra (Figure 5.3) for imprinted and non-imprinted particles pressed in KBr pellets were measured before washing to confirm the incorporation of surfactants, and after washing to confirm their removal by the washing process. Complete removal of templates after the imprinting process is essential to avoid their influence on subsequent

adsorption experiments. Before washing, $CH_2$ stretching bands are clearly present between 2800 and 3000 $cm^{-1}$, indicating that surfactants are incorporated at the particle surface during synthesis. After washing, these peaks are completely absent, which shows that the washing procedure effectively removes the adsorbed surfactant from the surface of the particles. FTIR spectra in the range from 800 to 1600 $cm^{-1}$ (the right-hand side of Fig. 3) show mainly Si-O-Si stretching bands from 1000 to 1200 $cm^{-1}$ and a Si-OH band near 960 $cm^{-1}$. The peaks are similar before and after washing, suggesting that the particles are stable during washing.

Liquid-phase adsorption experiments were performed to compare the preferential adsorption of D-glucose (the target saccharide); D-mannose and D-galactose (both differing by one chiral center); and L-glucose (the enantiomer of D-glucose). The structural differences in the 3D structure of this series of molecules (Fig. 5.1) provides an excellent opportunity to observe how preferential is the molecular imprinting by C8G1 at the Stöber particle surface. The small structural differences of D-mannose and D-galactose compared with D-glucose are expected to be a sensitive test of preferential adsorption. Figure 5.4 presents adsorption results for each of the saccharides from aqueous solution onto imprinted and non-imprinted particles. The D-glucose adsorption results are included in each figure so that a consistent comparison can be made among the saccharides. Fig. 5.4A compares the adsorption of D-glucose and L-glucose. The adsorption of L-glucose on both imprinted and non-imprinted surfaces is less than the adsorption of D-glucose on the non-imprinted silica surface. This is not surprising given that all 5 hydroxyl groups of D-glucose are oriented equatorially (and thus might allow for multiple interactions with the silica surface and with other D-glucose molecules)

while the hydroxyls are split on two sides of the molecule in L-glucose (see Fig. 5.1). While the amount of L-glucose on the imprinted particles is identical to what was observed on non-imprinted particles, significantly more D-glucose adsorption is observed on imprinted particles (roughly twice the amount observed on non-imprinted particles at high concentration). The results show that molecular imprinting using a surfactant derived from D-glucose has a clear and significant effect on the adsorption of D-glucose, but that the enhanced adsorption is highly preferential towards D-glucose compared to its enantiomer. The largest enhancement of D-glucose adsorption compared to L-glucose was roughly 5 times and it was observed at the lowest initial concentration of 0.14 mol/L. The ratios of D-glucose adsorption over other hexose studied here are documented in supplemental information Table C.1.

A comparison is made to sugars with smaller chiral differences from D-glucose in Figs. 5.4B and 5.4C. Both D-galactose and D-mannose show a slight decrease in adsorption to the non-imprinted silica surface compared with D-glucose, but not as dramatic a difference as L-glucose (Fig. 5.4A). The slight decrease is most likely because one hydroxyl group in each of the sugars is oriented axially (Figs. 5.1b and 5.1d), thus reducing the number of hydroxyl groups available for simultaneous hydrogen bonding with silica. Also, because the structural differences are subtle, both D-galactose (Fig. 5.4B) and D-mannose (Fig. 5.4C) show some enhancement in adsorption on the imprinted particles. However, the amount adsorbed for the middle and highest saccharide concentrations (0.69 and 1.4 mol/L) are roughly the same for D-galactose and D-mannose, while adsorption continues to increase for D-glucose. Overall, the adsorption results in Fig. 5.4 suggest that molecularly imprinted materials which target D-glucose

show preferential adsorption for D-glucose over the closely related hexose sugars D-galactose and D-mannose. This suggests that the D-glucose imprinted particles may have a larger adsorption capacity for D-glucose than for saccharides with one differing chiral center. However, because the structural changes induced by changing one chiral center are small, the preference is less pronounced than what was observed when comparing D-glucose and L-glucose. It was observed that the enhancement in absorption of D-glucose was close to 1.5 times when compared to D-galactose or D-mannose. No specific trend in the enhanced selectivity was observed with increasing initial concentration of sugars in the solution. This shows the potential power of this molecular imprinting strategy to prepare materials selective towards one of several related chiral compounds.

As an additional test of the ability of this imprinting strategy to make chiral distinctions in adsorption of saccharides, a pair of di-hexose sugars with identical building blocks (D-glucose) and 1-4 linkages were selected, that differ in the chirality of the point of attachment. These are α-D-glucopyranosyl (1→4) D-glucopyranose (maltose) and β-D-glucopyranosyl (1→4) D-glucopyranose (cellobiose). Figure 5.5 highlights the 3D structural differences that the linker induces by showing structures where the left D-glucopyranose units are aligned in roughly the same orientation. The two D-glucopyranose units of cellobiose (Fig. 5.5b) are found in about the same plane, but with one twisted relative to the other. In maltose (Fig. 5.5b), the D-glucopyranose units are twisted in the opposite direction, and the α(1→4) linkage causes a bend in the molecule so that monomers do not lie in the same plane. These conformation are consistent with recent molecular dynamics simulations that show that disaccharides, while flexible, have a narrow range of configurations that they tend to explore(*303*).

Because of the structural differences between these two, it is hypothesized that molecular imprinting with a surfactant with a D-maltose headgroup should lead to preferential adsorption of only D-maltose.

Before discussing the disaccharide adsorption, we again discuss the characteristics of the particles. Nitrogen adsorption (Appendix C Figure C.3) showed that the particles imprinted with a 1:1 mixture of CTAB and C12G2 had a surface area (7.1 $m^2/g$) comparable to non-imprinted particles (Table 5.1). SEM images of the CTAB/C12G2 imprinted particles (Figure 5.6) shows that they are highly monodisperse and spherical in nature and have particles averaging 510 nm in diameter (averaged for 21 particles), comparable to the non-imprinted and CTAB/C8G1 imprinted particles. FTIR spectra for CTAB/C12G2 imprinted particles (Figure 5.7) show that, like the CTAB/C8G1 imprinted particles, $CH_2$ stretching bands are present in the unwashed materials, and that the surfactant is completely removed by washing. The region of the spectra from 800 to 1200 $cm^{-1}$ shows no significant change upon washing, consistent with stable CTAB/C12G2 imprinted particles.

When conducting adsorption experiments, it was necessary to limit the concentration range of cellobiose due to its limited solubility in water at room temperature (~0.36 mol/L)(*304*). The adsorption of D-maltose and cellobiose onto both CTAB/C12G2 imprinted and non-imprinted particles is presented in Figure 5.8. As anticipated based on a molecular imprinting mechanism, the D-maltose imprinted particles show enhanced adsorption of D-maltose relative to non-imprinted particles. The greatest enhancement was roughly twice the amount of D-maltose adsorbed on non-imprinted particles at a solution concentration of 0.277 mol/L. On the other hand, cellobiose adsorption is about

the same as D-maltose on the non-imprinted particles, and enhanced only slightly (by at most ~50% at 0.277 mol/L in solution). Thus, a similar preferential adsorption caused by molecular imprinting is observed for the maltose / cellobiose pair as was observed for the hexose series. At the lowest initial concentration studied (0.069 mol/L), the greatest difference in adsorption of maltose and cellobiose can be seen for imprinted particles, where almost 5 times as much maltose ($2.9x10^{-4}$ mol/g) as cellobiose ($6x10^{-5}$ mol/g) is adsorbed. However, the difference is not as great at higher concentrations, where at 0.138 mol/L initial sugar concentration maltose to cellobiose adsorption ratio was 1.6 and at 0.277 mol/L initial sugar concentration the ratio was 1.4. This would be consistent with C12G2 creating a small set of adsorption sites that are selective towards D-maltose (and that are saturated at low concentration) while nonselective binding occurs across the range of saccharide concentrations. The difference in adsorption of D-maltose and cellobiose suggests that, just like for hexoses, imprinting Stöber particles using the D-maltose based surfactant C12G2 creates specific adsorption sites which lead to enhanced adsorption of D-maltose.

One interesting observation about Fig. 5.8 compared to Fig. 5.4 is that the amount of disaccharides adsorbed is much smaller than for the monosaccharides. One of the reason for this is the size of the disaccharides – if they lay flat on the surface, they are expected to occupy roughly twice the area of a monosaccharide (so the capacity should be roughly half of what was observed for monosaccharides). This does not completely explain the difference. The molecular area occupied by D-maltose was calculated from the amount adsorbed at the highest initial concentration to be 0.265 $nm^2$/molecule. Based on molecular dynamics the surface area of maltose has been reported to be 0.651

$nm^2$/molecule(*305*). The area per molecule at saturation is smaller than the surface area of maltose, which suggests that multilayer adsorption of maltose occurs. The adsorption may take place in cluster form as has been shown through molecular dynamics for adsorption of glucose on solid surfaces(*247*). The observed difference between monolayer capacity and theoretical area is much smaller for D-maltose compared to that observed for D-glucose (Chapter 4), which may be caused by the ability of D-maltose to form more hydrogen bonds due to polymerization in head group.

At the lowest concentration the selectivity towards adsorption of target molecule was close to 5 times for both D-maltose (compared to cellobiose) and D-glucose (compared to L-glucose). However at higher initial concentrations studied, because of the large number of hydroxyl groups available for interaction with silica, the enhancement is not as great as the difference observed between D-glucose and L-glucose (the largest difference in adsorption found in this study). The 3D arrangement of hydroxyl groups in L-glucose compared to D-glucose may also play an important role in such a large difference in enhancement of adsorption.

## 5.5 Conclusion

This study has shown that molecular imprinting by a simple modification of the Stöber silica synthesis process leads to chirally resolved preferential adsorption of target saccharides. Silica particles imprinted with a 1:1 mixture by weight of CTAB with n-octyl-β-D-glucopyranoside (C8G1) or n-dodecyl-β-D-maltoside (C12G2) were prepared. It was shown for both types of imprinted particles that the surfactants are incorporated at the surface of the particles without inducing significant changes in the structure, size or surface area of the particles. As expected based on the principle of molecular imprinting of the surface of soft, freshly precipitated particles, the particles

imprinted with a CTAB/C8G1 mixture showed enhanced, preferential adsorption of D-glucose. Some, but significantly less (nearly 1.5 times enhancement), enhanced adsorption of D-mannose and D-galactose (which differ from D-glucose by only one chiral center each) was observed on the CTAB/C8G1 imprinted particles. The greatest enhancement in the adsorption of D-glucose compared to D-glucose (greater than 3 times at all concentrations) was found in the CTAB/C8G1 imprinted particles, which is consistent with the greater structural difference between L-glucose and D-glucose.

The technique of imprinting with a mixture of cationic surfactant and saccharide surfactant was extended to a mixture of CTAB and C12G2 with a slight change in synthesis procedure. The resultant particles showed enhancement in adsorption of D-maltose compared to non-imprinted particles. The imprinted particles were also found to preferential adsorption of D-maltose over cellobiose (nearly 5 times enhancement at 0.0069 mol/L initial saccharide concentration). This preferential adsorption is significant because both molecules are disaccharides of D-glucose, but they differ in the chirality of the 1,4 glycosidic linkage. This small change is enough to allow molecular imprinting and preferential adsorption to occur.

By showing that this imprinting strategy can target saccharides based on subtle chiral structural differences, this study suggests that "soft imprinting" of freshly precipitated particles may be a general strategy to preparing selective adsorbents and chromatography packings. The technique is inexpensive, simple and tunable to a desired target molecule. The particles are nonporous and uniformly sized, which gives them beneficial flow characteristics as packing materials for separations. The developed technique serves as a first example in chirally targeted adsorption of chirally differentiated sugars through

molecular imprinting on the external surface of nonporous materials, and can be extended to pharmaceuticals or amino acids by using surfactant derivatives of those compounds.

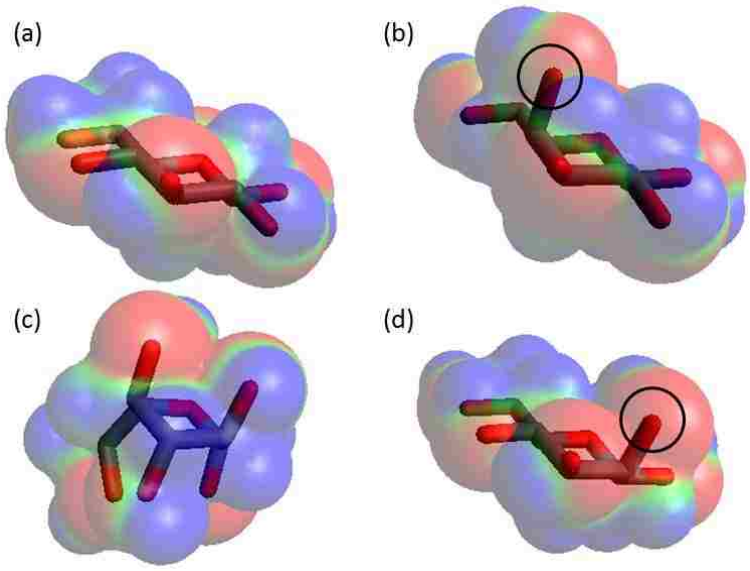


**Figure 5.1.** Projections of the 3D geometry of the monosaccharides investigated in this study: (a) D-glucose, (b) D-galactose, (c) L-glucose and (d) D-mannose. The structures are all optimized using the Universal Force Field (UFF) as implemented in Avogadro, and the translucent surfaces are van der Waals surfaces colored by electrostatic potential. Hydrogen atoms were used for geometry optimization and to generate the surfaces, but are not depicted in the stick geometries shown. The circled atoms in (b) and (d) are the oxygen atoms with different chirality from D-glucose

.

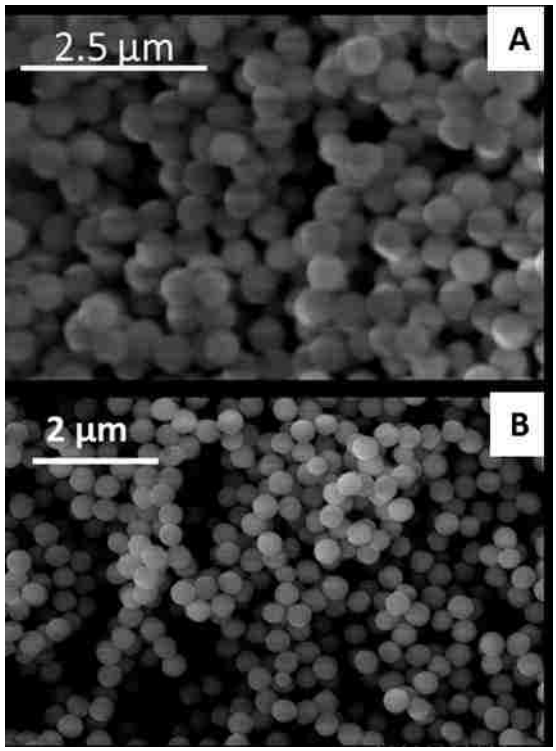


**Figure 5.2.** SEM images after washing and drying of particles made A) without addition of surfactants and B) particles prepared with addition of 1:1 mixture of CTAB and C8G1.

**Figure 5.3.** FTIR spectra of Stöber particles in KBr pellets. (a) Washed non-imprinted Stöber particles, (a') As synthesized Stöber particles without surfactant addition, (b) Washed Stöber particles imprinted with 1:1 CTAB/C8G1 mixture, (b') As synthesized Stöber particles imprinted with 1:1 CTAB/C8G1 mixture by adding surfactant at 1 minute after TEOS addition.

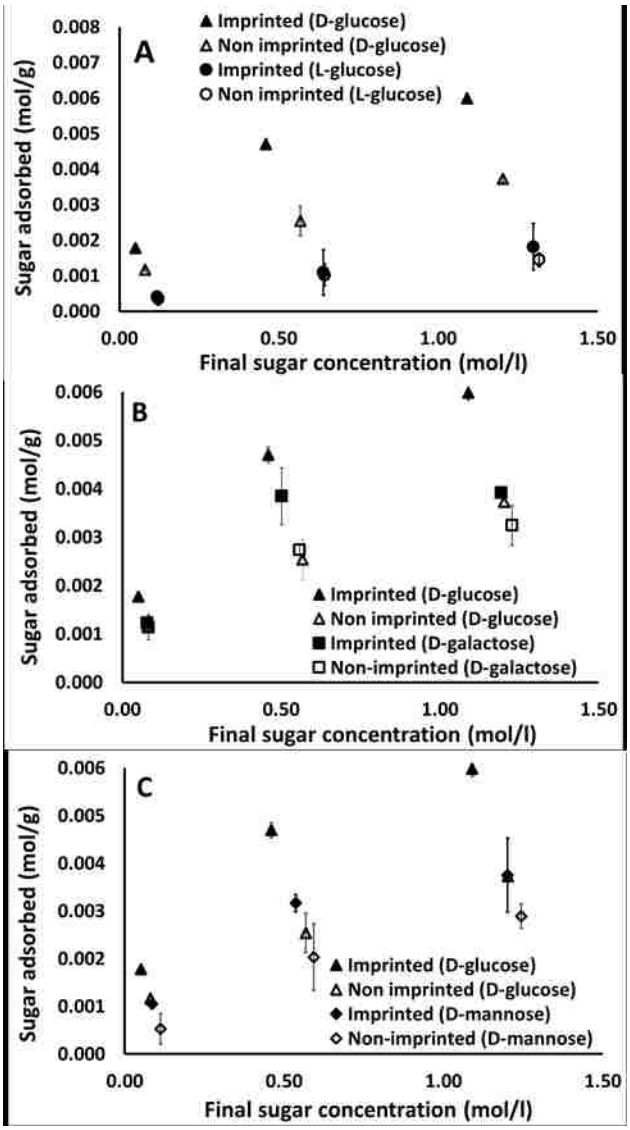


**Figure 5.4.** Comparison of the results of adsorption from aqueous solution of D-glucose and (A) L-glucose, (B) D-galactose and (C) D-mannose. The figures show that there is a higher preference for adsorption of D-glucose on C8G1 imprinted materials compared to other hexoses, while no significant difference is observed for adsorption of hexoses on non-imprinted Stöber particles.

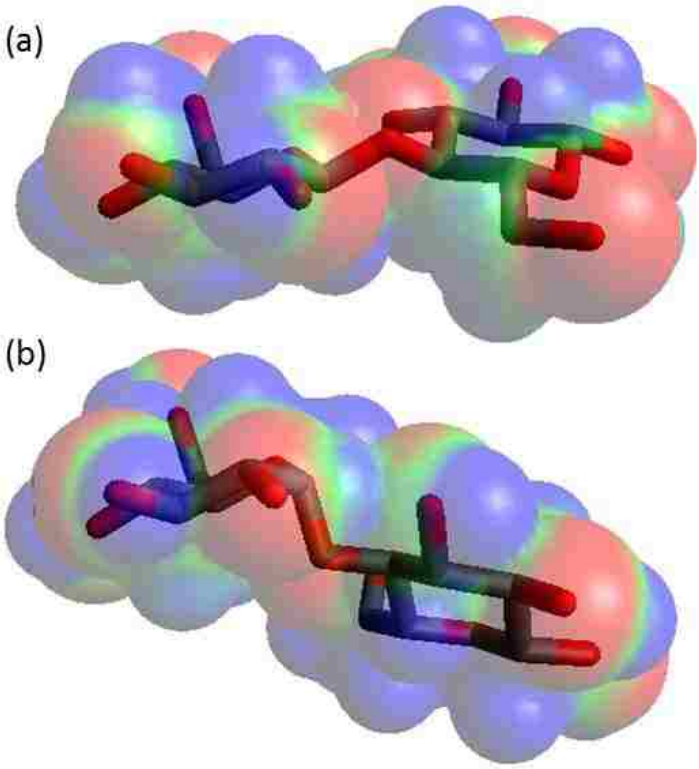


**Figure 5.5.** 3D structures of (a) cellobiose and (b) maltose obtained by starting with the experimental coordinates and performing geometry optimization with the UFF potential. The translucent surfaces are van der Waals surfaces colored by electrostatic potential using Avogadro. Note that the left glucopyranose units are oriented in roughly the same way in both molecules.

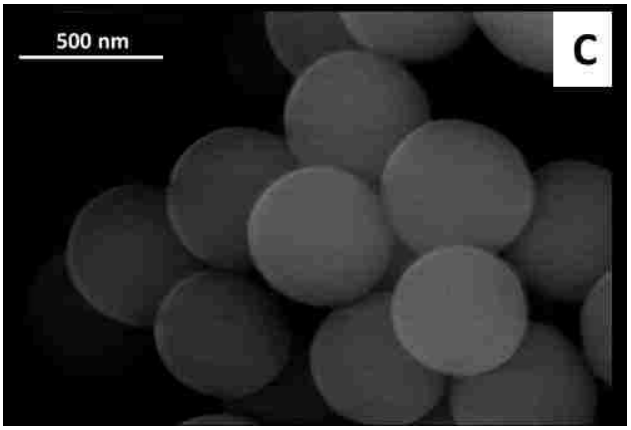


**Figure 5.6.** SEM images of C) 1to1 CTAB and C12G2 imprinted nanoparticles.

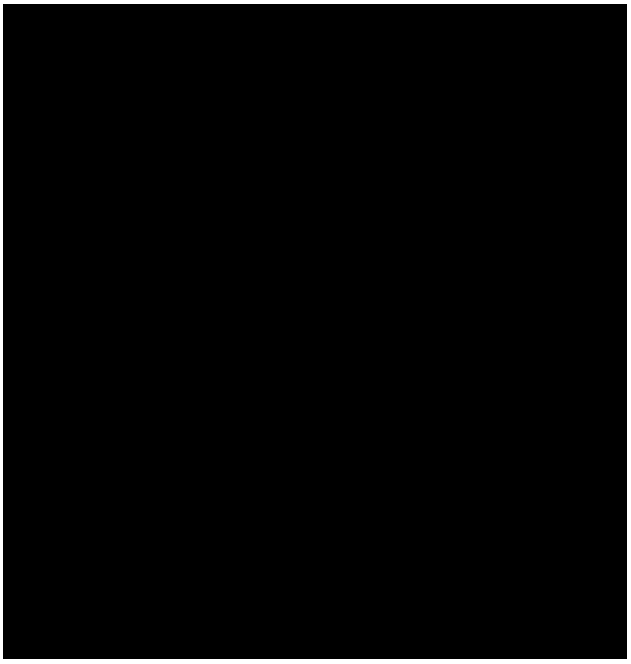

**Figure 5.7.** FTIR curves for particles imprinted with 1:1 mixture of CTAB and C12G2 before and after washing. $CH_2$ stretching bands can be seen between 3000 and 2800 $cm^{-1}$ before washing which are absent after washing.

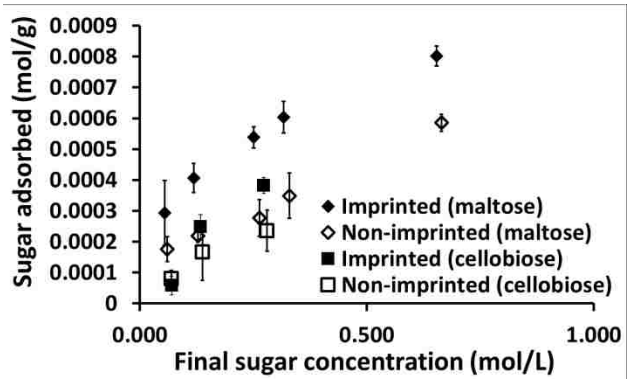


**Figure 5.8.** Adsorption of maltose and cellobiose on maltose imprinted Stöber particles and non-imprinted Stöber particles

**Table 5.1.** Physical characteristics of particles prepared without surfactant, with a 1:1 mixture of CTAB and C8G1 and with a 1:1 mixture of CTAB and C12G2.

| Suractant(s) | BET surface area ($m^2/g$) | SEM particle diameter (nm) | SEM surface area ($m^2/g$) | Zeta potential (mV) |
|---|---|---|---|---|
| No surfactant | 7.9 | 464±9 | 7.2 | -48.1 ± 0.39 |
| CTAB/C8G1 | 8.1 | 456±10 | 7.3 | -51.7 ± 0.90 |
| CTAB/C12G2 | 7.1 | 510±18 | 6.5 | -52.1 ± 0.63 |

Copyright © Suvid Joshi 2014

# CHAPTER SIX

# 6. INCORPORATION OF TITANIUM IN SILICA STRUCTURES USING SACCHARIDE SURFACTANTS TO STABILIZE AND LOCALIZE TITANIUM PRECURSORS

## 6.1. Summary

This chapter discusses work addressing the incorporation of titania in silica frameworks. Titanium sites dispersed in silica frameworks provide opportunities for oxidation catalysis and photocatalysis. Titanium is also known to bind strongly to biomolecules and this property could be exploited to create highly selective materials for adsorption. Ligand assisted stabilization of a titania precursor has been exploited in this work using a sugar based surfactant to help stabilize and disperse titania in the mesostructure. Titanosilicate mesoporous thin films have been synthesized to confirm the prior study of Rahman that showed that it is possible to homogeneously incorporate increasing amounts of titanium in the silica framework by increasing the amount of sugar surfactant based on the ternary phase diagram of n-dodecyl-β-D-maltopyranoside (C12G2), hexadecyltrimethylammonium bromide (CTAB) and water. The same surfactant mixture was utilized to synthesize titanosilicate bulk materials containing variable amounts of titania. The catalytic performance of the bulk materials was tested in our group for epoxidation of styrene. The catalytic testing provided evidence that the titania sites dispersed in silica structure were tetra-coordinated, which are known to be responsible for epoxidation catalysis. Catalytic activity of titanosilicates was compared to TS-1 and it was found that the catalytic activity for mesoporous titanosilicate with the lowest titania content had higher turnover frequency compared to TS-1. Catalytic activity and selectivity of mesoporous titanosilicates reduced with increasing titania content.

Synthesis of nonporous Stöber silica particles with titania incorporation by surfactant complexation has also been demonstrated. Evidence was found that the sugar surfactant binds very strongly with titania, and calcination at high temperatures was necessary to remove the surfactant from the materials. Such nonporous titanosilicates could potentially be used as stationary phases in adsorptive separations.

## 6.2. Introduction

Supported titania has been used over the past two decades for various catalytic applications like photocatalysis, acid catalysis and oxidation catalysis. These applications of the titanosilicates is a result of two main factors, generation of new acid sites and silica being a strong support due to its thermal and mechanical stability(*306*). The other advantages silica provides include photoinertness, high surface area and chemical stability(*307, 308*).

Since the discovery of TS-1,(*126*) materials with titania substituted for silica have been used for various oxidation catalysis in the presence of $H_2O_2$(*309*). Literature provides many novel synthesis methods to prepare both crystalline and amorphous titananosilicate materials for epoxidation catalysis(*132, 310-313*). For epoxidation, isolated titanium sites which are tetracoordinated (Ti(IV)) have been shown to be the active sites(*132*). Many examples of titanosilicate zeolites have been reported in the literature, including TS-1 and TS-2, for use in epoxidation catalysis(*314, 315*), but due to the limited pore size (around 0.5 nm) the number of substrates that can undergo catalysis are limited. An alternative to overcome the limitations of zeolites is the synthesis of mesoporous titanosilicates. Multiple examples of mesoporous titanosilicates have been presented in the literature with different types of pore geometry such as Ti MCM-41(*129, 315*), Ti MCM-48(*128, 316*), Ti SBA-1,(*317, 318*) and Ti SBA-15(*319*).

Various methods to synthesize titanosilicate mixed oxides have been mentioned in the literature using grafting, sol-gel hydrolysis(*320, 321*), co-precipitation(*322-325*) and flame hydrolysis(*306, 326*) out of which sol-gel hydrolysis and co-precipitation are the most common. The sol-gel synthesis method has been used commonly to introduce transition metals into silica structures. The sol-gel method provides a high degree of control over the structural properties of the material like shape and size of the pores as well as the distribution of transition metal sites in the structure(*327-329*). During nano-casting, surfactant self-assembly occurs and interactions between the surfactants and silica precursors in their hydrolyzed form leads to formation of ordered mesoporous structure. The cooperative interaction between inorganic species and the hydrophilic ends of the surfactant micelles leads to formation of metal oxide walls with ordered arrays of micelles.

Two types of sol-gel methods have been used commonly to incorporate metal oxides into silica structures: co-condensation and post-synthesis grafting. Co-condensation provides better control over dispersion and composition of metals in the silica structure, while pore blocking can be avoided by control of the reactions. Transition metal precursors have higher reactivity compared to silica precursors(*330*) which may lead to metal oxide rich domains in the materials and poor dispersion of metal atoms. In titania silica mixed oxides, $TiO_2$ could be present as isolated species or it could be part of the mixed oxide structure through Ti-O-Si linkages. The ratio of these species in the material is dependent on synthesis method and chemical composition(*132, 331*). Several ways have been suggested to avoid formation of metal oxide rich domains in silica metal oxide mixed structures including: prehydrolysis of the silica precursor with a substoichiometric

amount of water(*133*), synthesis of special precursors with both transition metal and silicon(*332, 333*), ligand assisted methods to reduce reactivity of transition metal precursors(*134, 334*) and nonhydrolytic sol-gel methods(*135, 335, 336*).

To develop well-defined ordered mesoporous mixed oxides, surfactants can be simultaneously used both as structure directing agents and transition metal precursor stabilizing agents. Work has been done on using various block copolymers to synthesize ordered materials using ligand assisted templating. Celik and Dag reported the use of this technique in synthesizing liquid crystals of cubic and hexagonal geometry by complexing poly(ethylene oxide) with transition metal salts(*337*). Huesing(*338*) et al. used this concept to synthesize Si-Ti mixed oxide thin films based on lyotropic liquid crystalline phases of oligo(ethylene oxide) surfactants. The metal oxide complexed with the surfactant, and the silica precursor was prehydrolyzed separately to prevent segregation and formation of metal oxide rich domains(*338, 339*).

In this work, the use of a saccharide surfactant is demonstrated for stabilization of a titania precursor. Transition metal complexes with have been well studied in the past in carbohydrate chemistry and biology(*340-342*). Studies have also shown that naturally occurring saccharides and saccharide derivatives act as ligands for transition metal complexation(*343, 344*). Morosanova and co-workers have also studied interactions of silica-titania xerogels with ascorbic acids and various phenolic compounds (which bear some structural similarity to monosaccharides) and demonstrated the formation of silica-titania complexes with these compounds(*345, 346*). In this work we will demonstrate forming stable ordered titanosilicate films, based on work of Rahman(*347*), which are of potential interest due to their photocatalytic activity(*338, 339*). Surfactants selected for

the purpose of this study are n-dodecyl-β-D-maltopyranoside (C12G2) and hexadecyltrimethylammonium bromide (CTAB). C12G2 will serve in stabilizing the titania precursor through bidentate binding and will also act as a structure directing agent. C12G2 will also help in uniformly dispersing titania throughout silica structure due to its complexation with the titania precursor. CTAB will be used to provide structural stability during formation of the mixed oxide materials. The same concept has been extended to synthesize titanosilicate bulk materials. Strong interaction of saccharide surfactants with a titania precursor has also been exploited to synthesize nonporous, spherical titanosilicate particles based on modification of Stöber(*22*) method.

In this chapter we verify the production of stable titanosilicate thin films to show that it is possible to incorporate a greater amount of titania into silica mesostructures than previously demonstrated(*348*) while maintaining the stability of structure using FTIR. The same synthesis concept of ligand assisted templating method has been used to synthesize bulk powders of titanosilicates according to the procedures of Rahman(*347*), and the bulk materials have been characterized using nitrogen adsorption, X-ray diffraction, UV-visible spectroscopy and FTIR. The bulk powders have been utilized to catalyze the epoxidation of styrene in presence of hydrogen peroxide. Beck et al(*131*) found that a mixture of tetracoordinated isolated titanium sites were responsible for epoxidation. Beck et al(*131*) also reported that for epoxidation of of 2-cyclohexene-1-ol in presence of titania silica mixed oxides, increasing the amount of incorporated titania promoted side reactions like oligomerization and Brönstead acid sites led to dimerization instead of epoxidation. Catalysis provides further proof that the synthesis method using a mixture of cationic and nonionic surfactants generates tetracoordinated Ti(IV) sites.

Comparison between mesoporous titanosilicates and TS-1 shows that the mesoporous materials with less titanium incorporation than TS-1 have higher selectivity for styrene and nearly 2.5 times the activity per Ti site.

The property of transition metal complexation with saccharide and saccharide derivatives(*341*, *343*, *344*) has also been used to synthesize modified Stöber particles(*22*) incorporating titania. Synthesis of titania coated silica particles which are monodisperse has been demonstrated previously(*349*). In this work, it will be demonstrated that it is possible to incorporate titania into Stöber particles through minor process modifications to the Stöber synthesis process. C8G1 will be used to stabilize titania precursor and addition of complexed titania along with CTAB at the point of turbidity is expected to incorporate titania sites into the particle structure. It is also hypothesized that complexation will provide imprinted sites for specific saccharide adsorption. Tani et al(*350*) previously studied retention of monosaccharides and disaccharides on titania which clearly showed that sugars can be retained on the surface of titania. Through molecular imprinting it may be possible to preserve sites selective for a particular saccharide and may help in separation of the targeted saccharides from other molecules. Such materials may also find utility in asymmetric oxidation catalysis if the sites are able to differentiate between enantiomers as previously demonstrated for imprinted silica Stöber particles in Chapter 5. The synthesis of such particles reduces the diffusion resistance which would be encountered by porous materials and may prove advantageous for catalysis of large molecules. FTIR characterization of these materials will show that the titania is incorporated in to the structure but it is hard to remove the complexed surfactant.

## 6.3 Experimental Section

### 6.3.1 Materials

All of the reagents utilized in this work were used as obtained without any further purification. N-dodecyl-β-D-maltopyranoside (C12G2, >99%) and n-octyl-β-D-glucopyranoside (C8G1, >99%) were obtained from Affymetrix. Ammonium hydroxide ($NH_4OH$, 30% V/V), tetraethyl orthosilicate (TEOS, > 98%) and titanium isopropoxide (TIP, > 98%) were received from Acros organics. 1N hydrochloric acid, DIUF water, hexadcyltrimethylammonium bromide (CTAB, > 99% pure), concentrated sulfuric acid and NoChromix were purchased from Fisher scientific. 200 proof ethanol was obtained from Deacon labs. 200 µm silicon wafers were obtained from University Wafers.

### 6.3.2 Synthesis

***Synthesis of titanosilicate thin films***

The synthesis described here is for a 41:5:54 ratio of CTAB:C12G2:$H_2O$ as described by Rahman and Rankin(*5*). The synthesis was done on a 0.8 g total weight basis of water, CTAB and C12G2 (the quantity of lyotropic liquid crystal hypothesized to have the same structure as the surfactant / silica composite). To synthesize titanosilicate thin films, C12G2 was initially dried overnight at 50 ˚C in a vacuum oven under high vacuum. 39.4 mg C12G2 was then dissolved in 1.83 g ethanol in a bottle which was pre-flushed with nitrogen to keep the vial dry. The vial was placed in a nitrogen glove bag and 23 µL of TIP was added to the vial under vigorous stirring such that the TIP:C12G2 molar ratio was 1:1. The mixture was stirred vigorously for 3 hours in the glove bag to promote complexation of TIP and C12G2. TEOS hydrolysis was carried out in a separate vial. The amount of TEOS was calculated by replacing the amount of water from the ternary phase

diagram between CTAB, C12G2 and water by fully hydrolyzed equivalent amount of silica precursor(*5, 351*). 1.38 g of TEOS was added to a vial along with 0.76 g of ethanol, 0.186 mL water and 0.292 mL 0.1 N HCl. The ratio of the TEOS, water and ethanol was 1:4:2.5 while the added HCl brought the pH of the mixture to 2. The silica was prehydrolyzed for one hour. The prehydrolyzed silica sol was then added to the vial containing mixture of TIP and C12G2, drop by drop under vigorous stirring. After addition of sol 0.12 g of water was added along with 0.763 g of ethanol. An ethanolic solution of CTAB containing 0.32 g of CTAB dissolved in 2.75 g of ethanol was added to the mixture and it was stirred further for 1 hour under nitrogen atmosphere. To increase titania incorporation the ratio of C12G2:CTAB was varied.

To prepare the dip coated samples, silicon wafers were immersed in NoChromix solution for at least three hours. The wafers were then rinsed with DIUF water followed by a rinse with acetone. The wafers were suspended in an oven at 50 ˚C for 5 minutes to dry. The dried wafers were dip-coated at 12.5 cm/min. Wafers were aged at 50 ˚C for at least 24 hours before further analysis.

***Synthesis of titanosilicate bulk materials***

To synthesize the bulk titanosilicate samples, C12G2 was dried under continuous vacuum for 24 hours at 50 $^{0}$C. 100 mg of dried surfactant was then added to a vial which was heated above 100 $^{0}$C to avoid moisture. C12G2 was dissolved in 4.7 g of 200 proof ethanol. The vial was closed and immediately placed in a nitrogen glove bag to avoid contact with moisture. The glove bag was purged with nitrogen and 59.4 µl TIP was added under vigorous stirring to give a 1:1 molar ratio of TIP:C12G2. The mixture was stirred for 3 hours under nitrogen. Tetraethyl orthosilicate (TEOS) was pre-hydrolyzed

for 1 hour by adding 1.57 g 200 proof ethanol, 0.7 ml of 0.1 N HCl and 0.53 ml of water and stirring the mixture vigorously. The amount of TEOS was calculated based on ternary phase diagram for C12G2, CTAB and water by replacing the volume of water in the ternary phase diagram with volume of silica and water of hydrolysis based on work by Alberius et al(*351*), while the HCl was added to bring the pH of the reaction mixture to 2. Water was added to provide four moles of water per mole of TEOS necessary for hydrolysis. The final molar ratio was TEOS: ethanol: (water + HCl) = 1:2:4. The pre-hydrolyzed TEOS mixture was added drop by drop with a syringe to the reaction mixture in a nitrogen filled glove bag under stirring, followed by addition of 0.82 g CTAB. The mixture was then stirred for 60 minutes and spread thinly in 6 cm diameter petri dishes. Alcohol was removed from the mixture in a desiccator under vacuum until a thick viscous sol was obtained. The viscous sol was aged at 50 $^{0}$C in air for at least 2 days. Transparent flakes obtained after aging were crushed and calcined in a tubular furnace. The finely crushed material was spread thinly in a quartz calcination boat and the tubular furnace was sealed to avoid air leakage. A temperature ramp of 1 $^{0}$C/min was used to reach a final temperature of 550 $^{0}$C. Dried air was used at 1 L/min flow rate under back pressure. The material was held at 550 $^{0}$C for 3 hours and then allowed to cool in the furnace to room temperature. Calcined material was stored in a desiccator under vacuum. Materials with higher titanium content were prepared by changing the amount of sugar surfactant added while keeping the total surfactant content (CTAB+C12G2) constant during synthesis. The materials with 1.14%, 2.9%, 5.35% and 7.4% titanium will be referred to as S-1, S-2, S-3 and S-4 respectively for the purpose of this work. A silicate

was also synthesized using the same procedure and ratio of surfactants used for S-1, but no titania precursor was added.

For comparison of catalytic activity, TS-1 was prepared using the method reported by Thangaraj et al(*352*) and mesoporus titania was prepared using the method of Peng et al(*353*). Both of these materials were prepared by Dr. Janet Mohandas, a postdoctoral researcher at the University of Kentucky.

***Synthesis of titania-containing Stöber particles***

Titania-containing Stöber particles were prepared using a modification of the Stöber process utilized previously to synthesize particles with imprinted silica surfaces (Chapters 4, 5). To synthesize the particles, C8G1 was dried at 50 ˚C for 24 hours under vacuum. 40 mg of C8G1 was then added to a vial which was heated at 100 ˚C for 2 hours to keep the vial dry. The added C8G1 was then dissolved in 2 mL of 200 proof ethanol and the vial was placed in a glove bag under nitrogen atmosphere. In the glove bag, 41 µL of TIP was added to the vial under vigorous stirring. The molar ratio of C8G1 to TIP was 1:1. Complexation of C8G1 and TIP was allowed to proceed for 3 hours. Based on the work done by Bogush et al(*136*) a recipe to synthesize 200 nm particles was utilized. In a separate conical flask, 67.8 g of 200 proof ethanol, 3.15 mL of 30% w/w ammonium hydroxide and 4.32 g of water were mixed and stirred slowly for 5 minutes after which 6.32 g of TEOS was added to the synthesis mixture. 20 minutes after addition of TEOS, at which point solution starts showing signs of turbidity, the complexed mixture of C8G1 and TIP was added to the synthesis mixture along with 40 mg of CTAB. The synthesis solution was stirred for 24 hours and then centrifuged to recover the particles. The

particles were then aged at 50 ˚C for 24 hours to promote interaction of surfactant with particles.

At the end of aging cycle the particles were put through three different cleaning treatments to observe the effect of cleaning cycles on the stronger bond between titania and saccharide surfactant. In the first method the particles were washed for three cycles with ethanol, centrifuged to remove surfactant-containing solution and sonicated to suspend particles for three cycles followed by the same treatment with DIUF water to bring the pH of the synthesis mixture to neutral. The particles were then dried at 50 ˚C for 24 hours. In the second method the particles were calcined at 550 ˚C for 4 hours with a ramp rate of 35 ˚C/min. In the third method, Soxhlet extraction was carried out in 200 proof ethanol before the particles were dried at 50 ˚C.

### 6.3.3 Catalytic testing

Catalytic activity measurements for the titanosilicate bulk materials was carried out by Janet Mohandas. The reaction equipment consisted of 25 mL round bottom flask with a magnetic stirrer, connected to a reflux condenser. Temperature was controlled using a heated oil bath with a thermostat. A thermometer was also placed in the flask to measure reaction temperature. The reaction was carried out on the basis of 0.5 mL styrene. A 1:5 ratio of catalyst to styrene by weight was used and a 2:1 ratio of styrene to hydrogen peroxide by volume was used for oxidation. Sodium hydroxide (1 mL, 0.1 N) was used in some reactions to neutralize the acidic surface of the catalysts. The epoxidation reaction was carried out at 85 ˚C for 5 hours. Acetonitrile was used as the solvent and the analysis of products was carried out using GC with a flame ionization detector and a capillary column.

### 6.3.4 Material characterization

For FTIR analysis, thin films prepared by coating sol onto 200 μm silicon wafers were analyzed. A background spectrum was collected for each silicon wafer before coating with the titanosilicate sol. FTIR of thin films was performed using a ThermoNicolet Nexus 470 with a liquid nitrogen-cooled MCT detector. FTIR analysis was done in approximately the same region on the silicon wafer before and after coating to avoid noise due to variation in thickness of the oxide layer on the wafer.

Analysis of bulk titanosilicates was carried out using a ThermoNicolet Nexus 470 with a DTGS detector. The pellets were prepared by mixing approximately 1% by weight of titanosilicates with dried KBr and were pressed to give translucent to transparent pellets. To analyze the presence of surfactant on titania-containing Stöber particles, the same FTIR procedure as above was used, although in some cases instead of a DTGS detector, a MCT detector was used to obtain better signal. Analysis of some of the Stöber particle samples was also carried out using an attenuated total reflectance (ATR) accessory on a Varian 700e FTIR instrument, where the samples were directly placed in contact with the internal reflection element for analysis.

Nitrogen adsorption for the titanosilicate bulk materials was carried out using a Micromeritics Tristar 3000 nitrogen adsorption instrument. Before nitrogen adsorption measurements, the samples were degassed at 120 ˚C for 4 hours. XRD patterns for titanosilicate bulk materials were collected using a Bruker D8 Advance diffractometer using Ni-filtered Cu $K_\alpha$ radiation ($\lambda$ = 1.5406 Å) at a scan rate of 0.2 ˚/min for 2θ values between 1.8 degrees and 6.5 degrees.

## 6.4. Results and discussion

### 6.4.1 Titanosilicate thin films

FTIR analysis of titanosilicate thin films was carried to support work previously reported by Rahman(*347*) regarding the synthesis of ordered mesoporous titanosilicate thin films. It was observed that with increasing amount of titania precursor used in the synthesis, incorporation of tiania in the thin films increased. The FTIR spectra of the thin films after processing are shown in Figure 6.1. The relative intensity of the peak associated with Ti-O-Si bond vibrations(*354*) (960 $cm^{-1}$) increases with respect to the peak associated with Si-O-Si bond vibration (1050 $cm^{-1}$), suggesting that titania is actually incorporated in the structure of the thin films. The materials have been characterized using XRD, UV-vis spectroscopy, STEM and nitrogen adsorption to show that the thin films have hexagonal mesoporous structure with long range order(*347*). The results were consistent with the observations of Rahman(*347*), which showed that in films prepared by pre-complexing the TIP with C12G2, the titanium in the final material is present mainly as isolated tetracoordinated sites, irrespective of the amount of titanium incorporated. NMR experiments were also performed to show the binding sites of C12G2 with titania precursor during complexation step are bidentate(*355*). The bidentate interaction helps in stabilizing and dispersing Ti in the mesostructure of the silica. Further work with titanosilicate powders has been shown below for styrene epoxidation which demonstrates that the incorporated titania is tetracoordinated and works as an epoxidation catalyst.

### 6.4.2 Titanosilicate bulk materials

Physical characteristics for all the bulk materials are presented in Table 6.1. Nitrogen adsorption isotherms for mesoporous titanosilicates are shown in Figure 6.2. The BET

surface areas of the materials are presented in Table 6.1. All of the titanosilicates exhibit Type-IV nitrogen adsorption isotherms although the capillary condensation step is not well pronounced in the plot. Capillary condensation at low relative pressure is observed when the pore sizes are close to transition region from the microporous to mesoporous region(*167, 356*). No hysteresis was observed for the nitrogen adsorption isotherms, which suggests that the pores are uniformly sized. The maximum volume of nitrogen adsorbed also decreases as the amount of titanium incorporated is increased. This shows that the pore volume decreases, which suggests that the stability of the ordered porous titanosilicates decreases as we increase the amount of titanium incorporated. The reduction in nitrogen volume adsorbed may correspond to collapse of pores due to instability. However, a similar loss in pore volume has been observed upon increasing the C12G2 content in mesoporous silica prepared using CTAB/C12G2 mixtures, so this may simply be an effect of the surfactant templates(*5*). Sample S1, which incorporates 1% titanium has a comparable nitrogen adsorption isotherm to the silicate synthesized using the same method. With increasing amount of titanium content the surface area decreases. Negligible micropore volume is observed for S1 and the pure silica material, while very small micropore volume was observed S2 and S3. S4 shows a large micropore volume which is comparable to mesopore volume. The total pore volumes are documented in Table 6.1.

Pore diameters were calculated using method of Barrett, Joyner and Halenda(*166*) with corrections to the equation implemented by Kruk, Jaroniec and Sayari (KJS)(*357*). Pore diameters for titanosilicates and silicate are shown in Figure 6.3. Pore diameters are above 2 nm in diameter for mesoporous silica as well as S1 to S3 titanosilicates. For S4

the maximum pore size appears to lie below the capabilities of the pressure transducers to accurately measure. This is consistent with shrinkage or collapse of mesopores as more titania (and more C12G2) is employed.z With increasing amount of incorporated titanium the pore diameter reduces slightly. The diameter for all the titanosilicates was larger than TS-1. It was also observed that the pore volume increased from S1 to S2 but was gradually lesser thereafter. The increase in pore volume may be a result of larger number of pores in microporous region with increasing incorporation of titania, while for S4 the high amount of titania may have led to collapse of pores due to structural instability and hence very low pore volumes were obtained. Larger pore diameter provides smaller diffusion resistance to substrate molecules, which may provide higher efficiency for epoxidation reactions.

Low angle X-ray diffraction patterns were collected for titanosilicates between 1.8 to 6.5 degrees (Figure 6.4). Only one peak could be observed in XRD patterns for silicates and titanosilicates suggesting that the materials are ordered but do not have long range order. It can be observed that with an increase in titanium content the intensity of the (100) reflection reduces, until S4 (containing 7.4 % titanium) which has no detectable reflections. Increasing the amount of sugar surfactant during synthesis leads to a decrease in structural stability. Replacing the tetra coordinated silicon with tetracoordinated titanium ion while increasing titanium incorporation may also have led to loss of order in materials(*130*). The $d_{100}$ spacing calculated using Bragg's law for silicate, S1, S2 and S3 were found to be similar and had values of 2.88 nm, 2.74 nm, 2.63 nm and 2.87 nm respectively. For S4 no strong peak could be observed and hence d spacing could not be calculated.

FTIR spectra collected for the titanosilicates are shown in Figure 6.5. The spectra presented were normalized with respect to the Si-O-Si bond vibration intensity around 1050 $cm^{-1}$. A peak can also be observed at 960 $cm^{-1}$ for silicate prepared without titania incorporation (6.5b). This peak is associated with the silanol group bond stretching vibration. A band in the same region is also observed for asymmetric Si-O-Ti bond stretching vibration(*354*). The band increases in intensity with incorporation of higher amount of titania in the materials. A band is also observed in all the materials for symmetric Si-O stretching at 800 $cm^{-1}$. A ratio of intensity of peaks at 960 $cm^{-1}$ and 800 $cm^{-1}$ was plotted against the nominal percentage of incorporated titania (Figure 6.6) to show an almost linear relationship, which is consistent with titanium incorporation into the structure according to the amount provided in the synthesis mixture.

Diffuse reflectance UV-visible spectroscopy was performed to determine the coordination state of titania in the materials. For the mesoporous titanosilicates a shoulder was observed between 250 and 270 nm wavelengths suggesting a possible mixture of tetra-coordinated and higher coordination (pentacoordinated or hexacoordinated) sites. The UV visible spectrum is shown in Figure 6.7. The spectrum is also shown for TS-1 which is a microporous zeolite used for epoxidation, and it has a shoulder at 210 nm.

The results of catalytic testing for mesoporous titanosilicates (S1 to S4), TS-1, porous titania and mesoporous silica are summarized in Table 6.2. Except for the titanium-free mesoporous silica, all of the samples provided 100% conversion of $H_2O_2$, which suggests that the isolated titania sites may be responsible for peroxide binding leading to epoxidation. It was observed that for epoxidation of styrene carried out in the presence of 1 mL of 0.1 N NaOH, the conversion was similar for S1, S2 and S3 while a significant

drop was seen for S4. The highest turnover frequency per titania site was observed for S1 and it was seen under similar reaction conditions that the turnover frequency of S1 was more than twice the turnover frequency of TS-1 for styrene epoxidation. The reduction in turnover frequency for samples containing more titanium may be a result of smaller surface area, and lower pore accessibility due to collapse of pores. It was observed that the selectivity of titanosilicates towards styrene oxide formation reduced with increasing titania content. Formation of titania clusters may have led to complete cleavage of the carbon carbon double bond in styrene leading to formation of by-products like benzaldehyde instead of the expected epoxide, thus leading to lower selectivity towards styrene epoxide. Titanosilicates S1 and S2 showed appreciably higher selectivity towards styrene epoxidation compared to other examples in the literature(*312, 313*). The conversion and selectivity towards styrene oxide for different mole percentage of titania in the materials has been plotted in Figure 6.8. It can be seen that with increasing titania incorporation the selectivity towards styrene epoxide reduces, which may be a result of formation of higher coordination titania sites catalyzing complete oxidation. The conversion of styrene was observed to be similar from S1 to S3 but fell sharply for S4. The sudden decrease in conversion results from collapse of mesopores which makes the titania sites in the materials less accessible and thus shows low conversion.

### 6.4.3. Titania incorporated Stöber particles

FTIR was performed on the Stöber particles prepared with incorporated titania. Figure 6.9 shows unwashed titania-containing Stöber particles in comparison to calcined titanosilicate Stöber particles. It can be observed from Fig. 6.9(A) that the uncalcined particles showed a broad peak between 3400 and 3800 $cm^{-1}$ which is associated with

hydroxyl stretching. The peak may have resulted from water retained on the particle surface after aging or hydroxyl groups. For the calcined particles no such peaks were obtained which may have resulted from high temperature used in calcination. Between 2900 and 3100 $cm^{-1}$, peaks associated with $CH_2$ stretching were visible for uncalcined particles. The presence of these peaks suggests surfactant incorporation on the particle surface during synthesis. The peaks were not observed after the material was calcined at 550 ˚C. Figure 6.9(B) also shows FTIR spectra in the range from 700 to 1700 $cm^{-1}$. A strong peak associated with siloxane stretching is observed with maximum absorbance at 1050 $cm^{-1}$. Peaks in the spectra are also observed for both calcined and uncalcined materials at 960 $cm^{-1}$ and 800 $cm^{-1}$. The peak at 960 $cm^{-1}$ has been reported in literature to be associated with Ti-O-Si stretching. Peaks associated with uncondensed hydroxyl groups have also been reported near 960 $cm^{-1}$. The intensity of peak at 960 $cm^{-1}$ was very high for uncalcined materials, but reduced after calcination. Ratio of area under the curve for peak at 960 cm-1 associated with Si-OH stretching and Ti-O-Si vibrations was obtained with respect to silioxane stretching band. The ratio of the peaks was compared for calcined and uncalcined Stöber particles as well as calcined and uncalcined titania containing Stöber particles. It was observed that uncalcined silicate Stober particles and titania containing Stöber particles had a ratio of 0.0584 and 0.0634 respectively. But, it was observed that after calcination at 550 ˚C the ratio dropped to 0 for silicate Stöber particles, as no intensity could be observed at 960 cm-1. Titania containing Stöber particles on the other hand had a residual ratio of 0.0196 even after calcination. Calcination at high temperature may have led to disappearance of intensity associated

with surface hydroxyl groups and the residual intensity associated with Ti incorporated may have resulted in the weak peak observed at 960 $cm^{-1}$ for calcined materials.

A comparison of titania-incorporated Stöber particles and silica Stöber particles has been shown in Appendix D Figure D.1. After calcination at 300 ˚C the Si-OH stretching bands for silica Stöber particles at 960 $cm^{-1}$ were eliminated while a peak at 960 $cm^{-1}$ could still be observed for titania incorporated Stöber particles which suggests incorporation of titania in the synthesized particles. It was determined that none of the techniques utilized for removal of surfactant complexed with titania worked except for calcination of materials at 550 ˚C. FTIR spectra for titani- incorporated Stöber particles which were washed with ethanol and water or that were Soxhlet extracted are shown in Appendix D Figure D.2. The peaks associated with $CH_2$ stretching between 2800 and 3000 $cm^{-1}$ are present for both particles cleaned with Soxhlet extraction and which were washed. This could have occurred due to two possibilities: 1) the complexed titania could have been incorporated inside the structure of particles which would have resulted in C12G2 being inaccessible to washing and unresponsive to calcination, or 2) the bond between titania and C12G2 may have been strong enough to withstand all the treatments used for surfactant removal. Calcination was the only technique which was demonstrated to remove the surfactant. This was a problem that made it difficult to pursue the testing of these materials as imprinted particles for saccharide adsorption, but in the future this strong bonding may be useful for tuning the nonselective binding to the remainder of the surface of the particles.

## 6.5. Conclusion

Titanosilicate thin films and bulk materials were synthesized using ligand assisted titania incorporation with C12G2 used to stabilize titania precursor and disperse titania in the

silica mesostructure. FTIR was used to show increasing amount of titanium incorporation in the synthesized thin films. All bulk materials except the one synthesized with highest titania content had pore sizes larger than 2 nm. High surface area was obtained for all of the mesoporous silicates, although the surface area and pore size reduced with increasing titania incorporation. A single intense XRD peak was observed for the mesoporous titanosilicates and silicate. The $d_{100}$ spacing calculated using Bragg's law for silicate, S1, S2 and S3 were found to be similar and had values of 2.88 nm, 2.74 nm, 2.63 nm and 2.87 nm respectively. The single peak suggested that the pore structure of these materials had order but long range order was found to be absent due to absence of higher order reflections. The intensity of XRD peak reduced with increasing titania incorporation suggesting disordering. For highest titania containing material almost no intensity was observed, which may be result of total disordering or collapse of pores. Catalytic testing on titanosilicates showed reducing selectivity for styrene epoxide with increasing titania incorporation. S1, S2, S3 had similar conversions while conversion dropped for S4. This may have happened due to collapse of pores for S4. Activity per titania site for S-1 was more than twice of TS-1, which may have been a result of better pore accessibility for mesoporous titanosilicates. Nonporous titanosilicate particles were synthesized. Using FTIR it was shown that titania could be incorporated in the particles, but it was difficult to remove surfactant from particle most likely due to strong complexation between C12G2 and titanium. It was shown that calcination at 550 ˚C was able to remove surfactant.

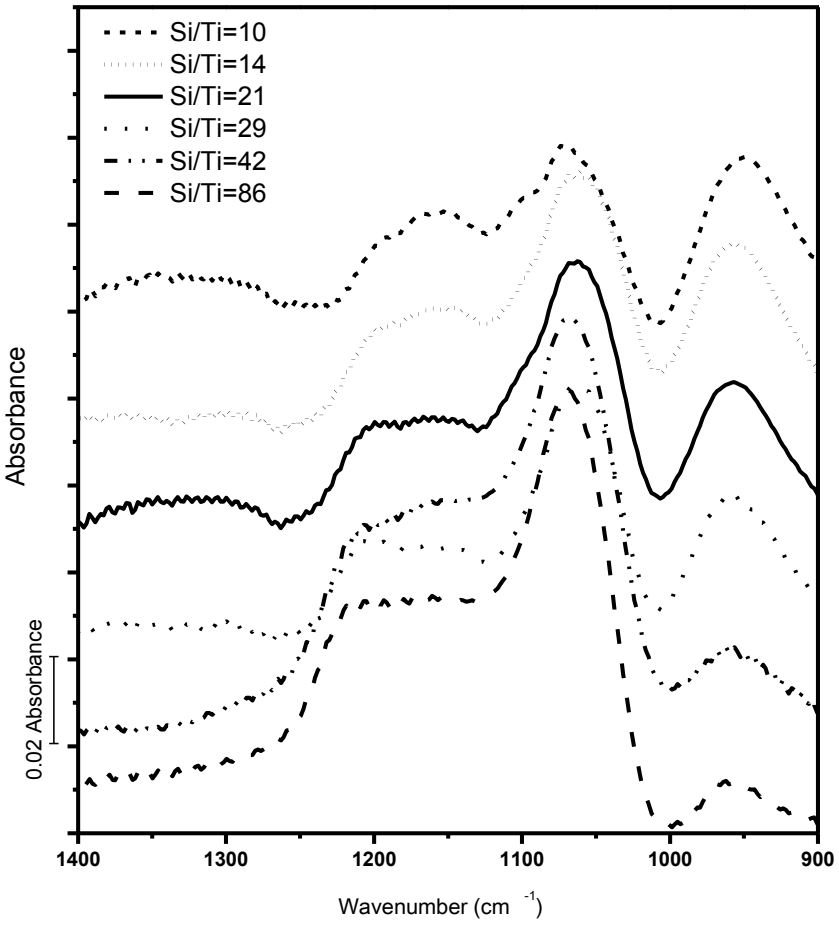


**Figure 6.1.** FTIR for titanosilicate thin films with increasing amount of titania incorporation from bottom to top. The figure shows increase in the intensity of the peak at 960 $cm^{-1}$ as the amount of incorporated titanium increases.

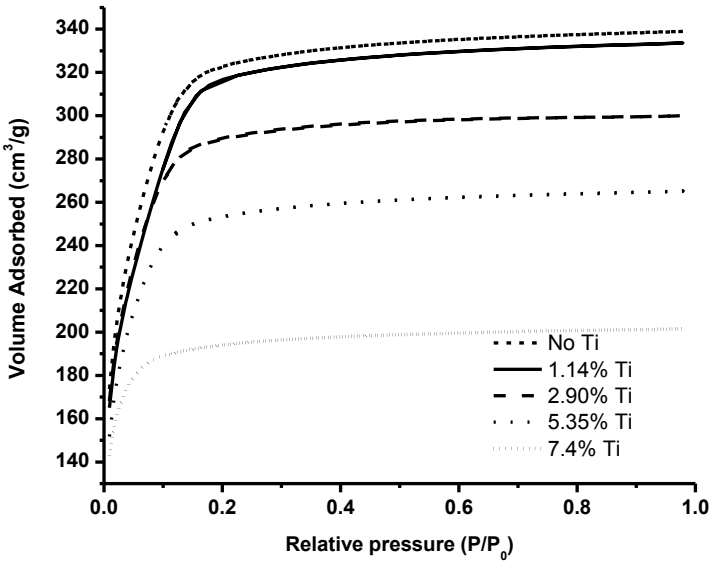


**Figure 6.2.** Nitrogen adsorption isotherms for mesoporous titanosilicates

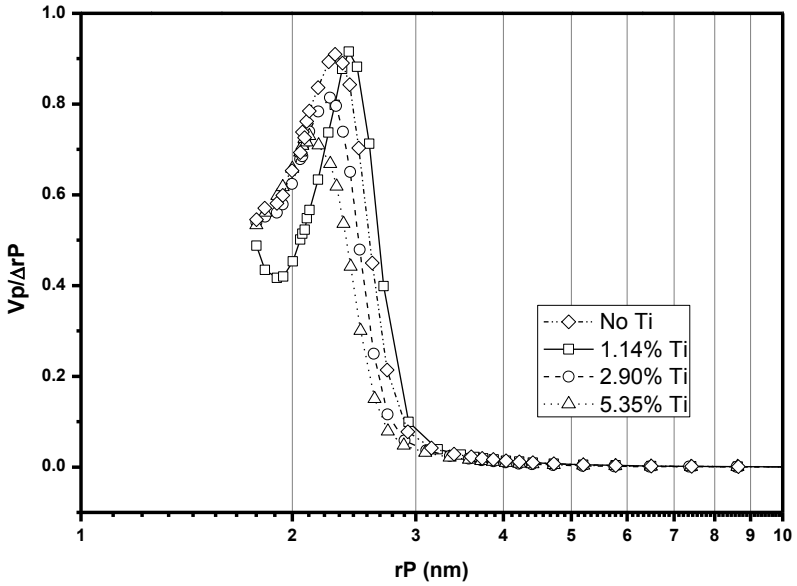


**Figure 6.3**. Pore size distribution for mesoporous titanosilicates estimated using the KJS method

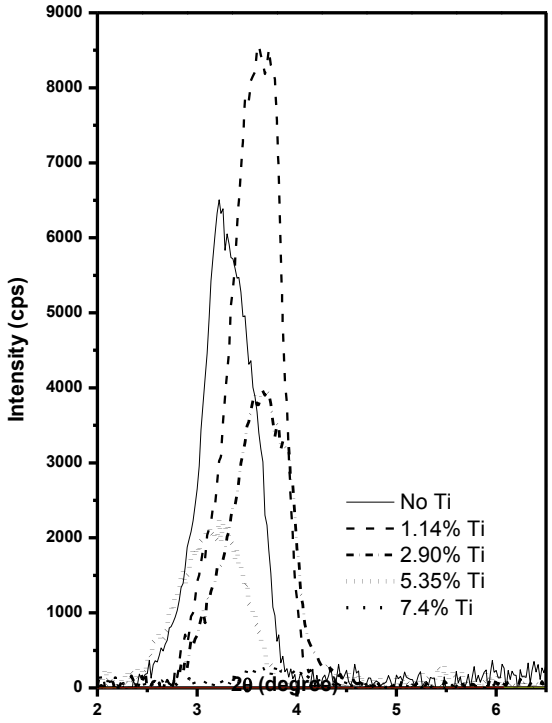


**Figure 6.4.** Low angle X-ray diffraction pattern for mesoporous titanosilicates and pure mesoporous silica.

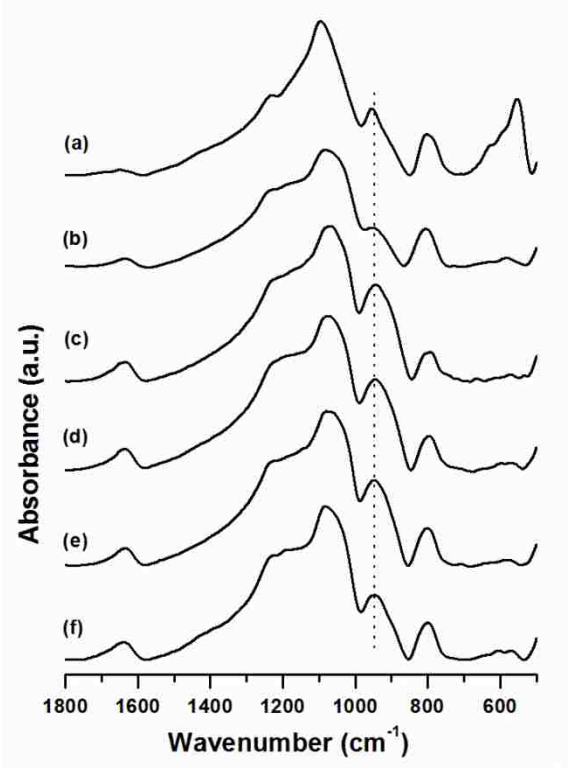


**Figure 6.5.** FT-IR absorbance spectra of titano silicates with varying Ti content (a) TS-1 (Ti ~2.9 %) and mesoporous titanosilicates with Ti content corresponding to (b) no Ti (c) Ti ~7.4 % (d) Ti ~5.35 % (e) Ti ~3.29% and (f) Ti~1.14%

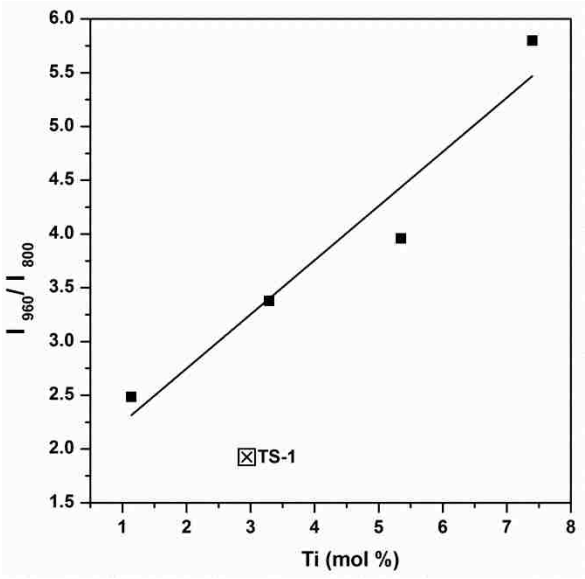


**Figure 6.6.** Ratio of the integrated areas of the 960 and 800 $cm^{-1}$ IR bands with respect to the framework titanium content in different bulk titanosilicate powders.

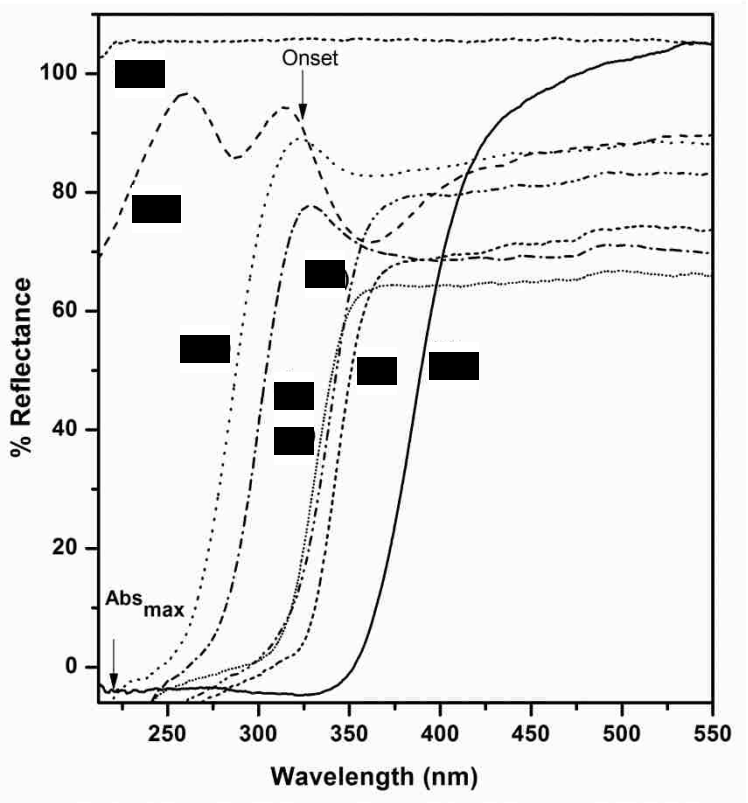


**Figure 6.7.** Diffuse reflectance UV-visible spectra of samples (a) $BaSO_4$ as background (b) $SiO_2$ (Ti~ 0 %) (c) TS1 (Ti ~2.9 %) (d) S-3 (Ti ~5.35%) (e) S-1 (Ti~1.14%) (f) S-2 (Ti ~3.29%) (g) S-4 (Ti ~7.4%) and (h) $TiO_2$ (Ti ~100%).

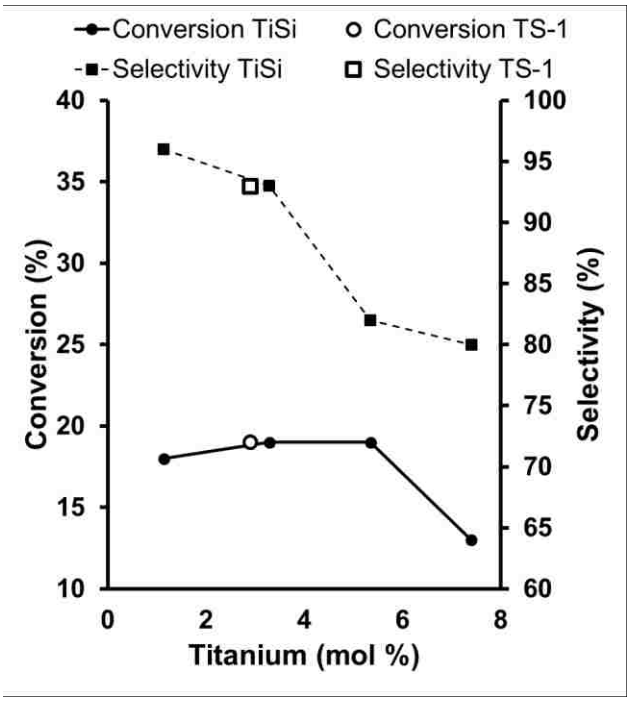


**Figure 6.8.** Conversion and selectivity of various titanosilicate samples with respect to Ti content. With increasing mol percentage the samples go from S1 (1.29% titanium) to S4 (7.1 % titanium).

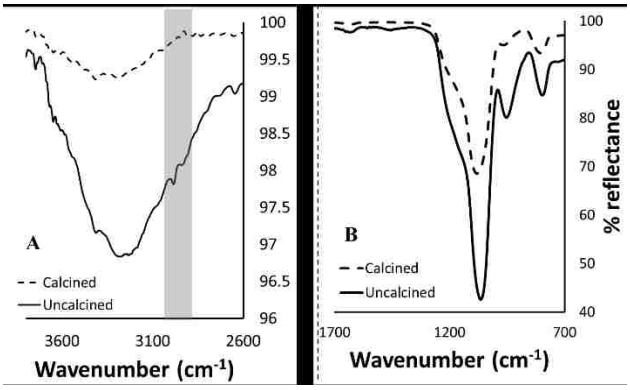


**Figure 6.9.** Reflectance spectra of calcined and uncalcined titanosilicate Stöber particles collected using ATR. A) Spectra between 2600 and 3000 $cm^{-1}$ wavenumber, showing peaks between 2900 $cm^{-1}$ and 3000 $cm^{-1}$ associated with $CH_2$ stretching before calcination and disappearance of such peaks after calcination. B) Spectra between 700 and 1700 cm-1 shows siloxane stretching band with peak at 1050 cm-1 and a peak at at 960 cm-1 due to Si-O-Ti vibrations and Si-OH bond vibrations. After calcination the intensity at 960 cm-1 reduces due to removal of surface hydroxyl groups and residual intensity as a result of Si-O-Ti vibrations is observed.

**Table 6.1.** Textural and surface properties of titanosilicates

| Sample ID | Si/Ti ratio | Nominal Ti content (mol %) | Acidity (mmol/ g) | Surface area ($m^2$/g) | Porevolume ($cm^3$/g) | Pore diameter[a] (nm) |
|---|---|---|---|---|---|---|
| S1 | 86 | 1.14 | 0.246 | 947 | 0.678 | 2.4 |
| S2 | 28 | 3.29 | 0.458 | 856 | 0.790 | 2.3 |
| S3 | 16 | 5.35 | 0.515 | 745 | 0.730 | 2.1 |
| S4 | 10 | 7.4 | 0.620 | 556 | 0.513 | --- |
| TS-1 | 33 | 2.9 | 0.241 | 360 | 0.117 | 0.5[b] |
| $SiO_2$ | -- | 0 | 0.147 | 960 | 0.664 | 2.3 |
| $TiO_2$ | -- | 100 | 0.011 | 125 | 0.191 | 3.9 |

a: Maximum in pore size distribution obtained using KJS method.
b: This could not be accurately measured using the Tristar 3000 but this is a typical pore diameter for TS-1(*352*).

**Table 6.2.** Catalytic activity of titanosilicates with varying titanium content

| Sample ID | Ti content (mol %) | Acidity (mmol/g) | $H_2O_2$ Conversion (%) | Conversion (%) | Selectivity (%) | | Turn over frequency ($h^{-1}$) |
|---|---|---|---|---|---|---|---|
| | | | | | Styrene oxide | Benzaldehyde | |
| S1 | 1.14 | 0.246 | 100 | 18 | 96 | 4 | 10.14 |
| S2 | 3.29 | 0.458 | 100 | 19 | 93 | 7 | 3.72 |
| S3 | 5.35 | 0.515 | 100 | 19 | 82 | 18 | 2.29 |
| S4 | 7.4 | 0.620 | 100 | 13 | 80 | 20 | 1.08 |
| TS-1 | 2.9 | 0.241 | 100 | 19 | 93 | 7 | 4.23 |
| *$SiO_2$ | 0 | 0.147 | 40 | 28 | 2 | < 1 | --- |
| *$TiO_2$ | 100 | 0.011 | 100 | 12 | 4 | 0 | 0.09 |

Styrene: 0.5 ml; $H_2O_2$: 0.25 ml; Solvent: Acetonitrile = 4.8 ml; Internal standard: 1, 2- Dichlorobenzene = 0.4 ml NaOH: 1 ml, 0.1 N; Sample wt.:20 wt% of the substrate (Styrene); Temperature: 85 °C; Reaction time: 5 h.
*Resulted in polymerization

Copyright © Suvid Joshi 2014

# CHAPTER 7
# 7. CONCLUSIONS AND FUTURE WORK

## 7.1. Conclusions

Sugar based surfactants are important in the industry due to their biodegradability and possibility of production from renewable resources. Sugar surfactants can be produced at industrial scale and direct applications of surfactants are as detergents, as anti-foaming agents, in cosmetics, for biochemical separations, in biomimetic science and in synthesis of templated materials. In this dissertation, various mixtures of saccharide surfactants with a cationic surfactant (cetyltrimethylammonium bromide, CTAB) have been explored from a thermodynamic point of view and applications of such mixtures for synthesis of catalysts and adsorbents has been explored.

In chapter 3, the thermodynamics of demicellization of a mixture of CTAB and C8G1 were studied. Isothermal titration calorimetry (ITC) was employed as a relatively novel approach to measuring micellar thermodynamics in this type of mixed system. ITC provides the opportunity to directly study thermodynamic behavior of a surfactant mixture by introducing surfactants in solution in small steps to generate heat vs. concentration diagrams. Rubingh's model(*12*) of nonideal surfactant micellization is typically used to determine thermodynamics of surfactant mixtures from measurements that do not provide direct thermodynamic information, (e.g. critical micelle concentration (cmc) values from surface tension measurements). However, this model is based on a regular solution theory activity coefficient model, and this approach was used to develop a model for heat vs. concentration data obtained using ITC. Two models were developed and the models were fit to a set of ITC curves for systems with varying surfactant composition to estimate the enthalpy of demicellization of each surfactant, cmc values of

each surfactant, the thermodynamic interaction parameter (β) and a set of dilution parameters used to improve the match to the data before and after the cmc. It was observed that Model 1 in Chapter 3 matched the demicellization curves very well, but a large uncertainty was observed in parameters associated with first order terms in enthalpy of dilution (equation 3.13) and enthalpy of demicellization of pure surfactants was observed. The value of β was found to be very close to the values commonly reported in the literature for mixtures of n-octyl-β-D-glucopyranoside (C8G1) and CTAB. Model 2 was also used to fit the data and it differed from Model 1 based on the enthalpy of dilution equation. The enthalpy of dilution equation for Model 2 eliminated first order terms associated with enthalpy of dilution. Very small uncertainties were observed for all the parameters in Model 2, but the value of β was different than the value of β commonly reported in literature. It was also observed that Model 2 could not fit the data below cmc for high concentration of surfactants in mixed system. Model 1 and Model 2 predicted mixed surfactant cmcs which matched well with cmc taken as point of departure from low concentration plateau. The models extend the work of Tsamaloukas et al(*74*) (which was applicable only to ideal mixtures of surfactants) to ITC of non-ideal surfactant mixtures.

The remainder of the dissertation was focused on the use of saccharide surfactants to create imprinted sites on metal oxide surface for specific adsorption and catalysis. In Chapter 4 a modification to the Stöber silica particle synthesis process is described to synthesize imprinted nonporous particles for selective adsorption of D-glucose or D-xylose in comparison to the other sugar. Early addition of surfactant around the time at which Stöber particles start precipitating was demonstrated to be the best point for

surfactant addition. It was shown using FTIR that surfactants were present on the surface of freshly prepared, unwashed particles and that it was also possible to completely remove surfactants from the particle surface by washing with ethanol and water. The preferential adsorption of particles imprinted using CTAB, C8G1, 1:1 CTAB:C8G1 mixture was studied and it was found that the particles imprinted with a mixture of CTAB and C8G1 had the greatest enhancement in adsorption of D-glucose relative to D-xylose. Though CTAB was found to increase adsorption capacity, no preference for D-glucose or D-xylose was observed for such materials. When a CTAB / C8G1 mixture was used to imprint the silica surface, CTAB adsorbed strongly by electrostatic interactions with the negatively charged silica surface, which enhanced the ability of nonionic C8G1 to interact with the surface, thus leading to better imprinting and selectivity greater preference for glucose.

To support the hypothesis of early time of addition (around 1 minute) for better surfactant interaction with silica surface, time of addition of surfactants was varied after silica precursor (TEOS) addition. As the time of addition of surfactant mixture was increased the $CH_2$ stretching bands in as-prepared particles progressively became weaker until they disappeared when surfactant was added at 1 hour after TEOS addition, suggesting that little imprinting occurred. It was shown that the particles prepared by adding surfactant 1 minute after TEOS addition adsorbed the highest amount of glucose, and that the adsorption of glucose gradually reduced with surfactant addition time until reaching the point that particles with surfactant addition 1 hour or 4 hours after precursor addition had similar adsorption to non-imprinted Stöber particles. The ratio of CTAB

and C8G1 was also varied and the best ratio of surfactants for glucose adsorption was found to be a 1:1 ratio by weight of CTAB and C8G1.

A two-site Langmuir adsorption isotherm with specific and non-specific adsorption sites was applied to model the adsorption of glucose and xylose on particles imprinted for glucose. It was assumed that sites which were non-specific had the same adsorption equilibrium constant for all particles. The model was able to fit the adsorption behavior of both glucose and xylose on non-imprinted and CTAB imprinted particles with only non-specific adsorption sites. A one-site, non-specific Langmuir model was also able to fit xylose adsorption isotherms on C8G1 and CTAB/C8G1 imprinted particles. However, the full two site model was needed to fit the experimental adsorption isotherm of glucose on C8G1 and CTAB/C8G1imprinted particles. In addition to separate adsorption measurements for glucose and xylose, mixed sugar adsorption from biomass hydrolyzates on the CTAB/C8G1 imprinted particles was measured by a collaborator, Alcia Modenbach, which showed selective adsorption of glucose from a mixture(*358*).

Flexibility of the imprinting technique was demonstrated by modifying the method to imprint the silica particles for xylose using a mixture of CTAB and n-octyl-b-D-xylopyranoside (C8X1). Although minor modifications to the synthesis were required to dissolve C8X1, it was possible to obtain imprinted silica particles which showed a preference for adsorption of xylose compared to glucose. These nonporous particles, which were synthesized at 50 ˚C to ensure that all surfactants were soluble, had less non-specific adsorption than particles synthesized at room temperature. Thus, the imprinting approach based on adding surfactants to freshly precipitated Stöber particles could be

tuned to tuned to target different molecules with minor changes in the synthetic procedure.

In chapter 5, the concept of preference of D-glucose imprinted Stöber particle surfaces was tested in comparison to chiral homologues of D-glucose. Adsorption of particles imprinted with a CTAB/C8G1 mixture for D-glucose was compared with adsorption of D-mannose, D-galactose and L-glucose. It was observed that the largest difference in adsorption was observed between D-glcuose and L-glucose. L-glucose is the enantiomer of D-glucose (so all chiral centers are opposite in L-glucose), and therefore a large difference in structure may have resulted in very low adsorption of L-glucose. Structure of L-glucose obtained after free energy minimization also showed that the hydroxyl group on L-glucose responsible for hydrogen bonding with hydroxyl groups on silica, are out of the plane of the ring, which may explain the reduced adsorption of L-glucose on both imprinted and non-imprinted particles. D-glucose adsorption was as large as three times greater than L-glucose adsorption on particles imprinted for D-glucose. It was found that D-mannose and D-galactose, which differed from D-glucose at just one chiral center, also showed significant differences in adsorption on particles imprinted for D-glucose. D-glucose adsorption was nearly 1.5 times the adsorption of either D-galactose or D-mannose. The difference in selectivity supports the molecular imprinting mechanism and shows that technique developed in chapter 4 also provides an opportunity for developing chirally selective materials. The molecular imprinting technique was also extended to synthesize materials selective towards a disaccharide, D-maltose, using a mixture of CTAB and n-dodecyl-β-D-maltoside (C12G2) for imprinting. The imprinted materials demonstrated higher adsorption of D-maltose when compared with D-

cellobiose. D-maltose and D-cellobiose differ from each other only in the anomeric form of the linkage between two D-glucose units. Despite this seemingly subtle difference, the materials imprinted for D-maltose showed more than 5 times as much adsorption (at low concentration) of D-maltose compared with D-cellobiose. The ability to create preferential adsorption sites for D-maltose supported the molecular imprinting mechanism and also showed the possibility of imprinting the surface for selective adsorption of larger molecules.

As a final demonstration of the use of sugar surfactants in materials synthesis, saccharide surfactant complexation with transition metal oxide precursors was explored to incorporate titania in mesoporous silica structure and on the surface of nonporous silica particles. The mesoporous materials were processed in both thin film and bulk material forms. Thin films were synthesized based on the ternary diagram of CTAB, C12G2 and water developed by Rahman and Rankin(*5*). The thin films confirmed the procedure of Rahman(*347*) to create isolated tetracoordinated titanium sites by stabilizing the titania precursor by complexation with the headgroup of C12G2 during synthesis of the materials. The same concept of use of saccharide surfactants to stabilize titania precursor while simultaneously acting as a structure directing agent was used to synthesize bulk mesoporous titanosilicates using the process developed by Rahman(*347*). High surface areas were obtained for all the titanosilicates synthesized, although it decreased with increasing titania content due to a loss in long-range order in the materials. The bulk materials had pore sizes above 2 nm, but the pore size decreased with increasing titania content, as observed by Rahman(*347*). Diffuse reflectance UV-visible spectroscopy showed that a mixture consisting of primarily tetra-coordinated titania sites

and some higher coordination sites was present in the titanosilicates. The tetra-coordinated sites are known to be responsible for catalyzing the epoxidation reactions of alkenes. The catalytic activity of the titanosilicates synthesized was measured by a collaborator, Dr. Janet Mohandas, and compared with the titania-containing zeolite TS-1 for styrene epoxidation. It was found that the titanosilicates showed decreasing selectivity towards the epoxidized product with increasing titania content. This may have occurred due to formation of titania sites with higher coordinated states, which catalyze complete oxidation or polymerization. The conversion after 5 hours of reaction dropped significantly for the highest amount of titania (~7.4 mol%) while remaining almost the same at lower titania contents. The sudden drop may have resulted from collapse of mesostructure leading to smaller accessibility of the titania sites. It was found that titanosilicate containing the least (1.14 mol%) titania had more than twice the turnover number per titania site compared to TS-1 containing 2.9 mol% titanium. The higher turnover number may have resulted from highly accessible large pores in mesoporous materials as well as the larger surface area (nearly three times) of the mesoporous materials compared with TS-1. The selectivity for styrene epoxide was found to be similar to TS-1, with the mesoporous titanosilicate with the lowest titanium content showing 3% higher selectivity.

The concept of sugar surfactant complexation with titania precursor was extended further with an aim to synthesize nonporous spherical, uniformly sized particles with titania incorporation at their surface. It was found that through surfactant complexation, titania could be incorporated in the particle structure in a one pot synthesis procedure. However, the titania/C8G1 complex formed during synthesis appeared to be very strong,

and calcination at 550 ˚C was necessary to remove the surfactant from the titania sites. Such nonporous particles could potentially serve as adsorbents for sugar separations, or as highly accessible catalysts. Some of the potential applications of the work demonstrated in the dissertation are discussed in the next section.

## 7.2. Future work

Chapter 3 discussed a thermodynamic model for non-ideal mixing of surfactants which could be applied to ITC data of mixed surfactants. The applicability of such a model lies in the prediction of mixed cmcs and thermodynamic mixing behavior based on calorimetric data. It is possible to refine the model further by developing a better model for enthalpy of dilution. It may be possible to develop and test a model for micellar surfactant dilution that is better parameterized and better understood. It is also necessary to study the universal applicability of the model by collecting more data on various binary surfactant mixtures and utilizing the model to fit the data. The model could also be used in the future to develop new ITC protocols to most efficiently measure nonideal mixing in surfactant mixtures. The model should be applicable to both ideal and non-ideal systems.

In chapter 4 a new and versatile method to imprint Stöber particle surfaces using surfactants was discussed. It was observed during the study that adding surfactants just around the time when silica particles start precipitating gives the best imprinting effectiveness. Various saccharide surfactants were used to imprint the Stöber particles to demonstrate versatility of the process. Non-specific adsorption of molecules which were not targeted was also observed. A future project to determine the possibility of blocking

non-specific adsorption sites may be necessary and useful to enhance the selectivity of the materials towards the target compound, for instance for sensing applications.

In chapter 5 it was shown that the imprinted particles also demonstrate chiral selectivity. The materials were imprinted for a monosaccharide (D-glucose) and disaccharide (D-maltose). Through imprinting of Stöber particles not only chiral selectivity was demonstrated, but also the versatility of the process to use bulkier molecules for imprinting was seen. Use of still bulkier molecules (such as polysaccharides and polypeptides) could be explored using this molecular imprinting approach, and it may be possible to imprint Stöber particles for proteins. Chiral selectivity may also help in separation of amino acids and peptides with small structural differences for use in the pharmaceutical separations industry. The effectiveness of such materials could also be improved by blocking non-specific adsorption sites.

In chapter 6, the use of saccharide surfactants was demonstrated for stabilizing and dispersing titania at the surface of a mesoporous silica framework. It was shown that ligand assisted titania stabilization could be utilized to synthesize porous thin films, porous bulk materials and titania incorporated Stöber particles. As suggested by Rahman(*347*) there is possibility of utilizing the ligand assisted stabilization to incorporate other transition metals incluing vanadium, zirconium etc. for applications in catalysis and electronics. It was also shown in chapter 6 that it was possible to incorporate titania on the surface of Stöber particles by adding surfactant complexed titania precursor around the time of precipitation of the particles. It was observed that it was difficult to remove complexed surfactant through washing and Soxhlet extraction. Difficulty in surfactant removal may prove advantageous in this case, where the non-

specific hydroxyl groups on silica surface could be blocked. Harsher extraction methods then could be utilized to remove complexed surfactant. It was also observed that when calcined, FTIR peak associated with hydroxyl groups on silica surface reduced in intensity leaving behind some residual intensity associated with Ti-O-Si vibrations. A study on the effects of titania incorporation in particles on adsorption and selectivity of saccharides could be conducted and the results could be compared with imprinted Stöber particles. A study on chiral selectivity of titania sites also needs to be conducted. Titania sites if found to be chirally selective could be used for asymmetric catalysis. The titania incorporated particles are nonporous and hence low diffusion resistance encountered could be useful in catalysis of large molecules.

Copyright © Suvid Joshi 2014

**APPENDIX A**
**SUPPLEMENTAL INFORMATION CHAPTER 3**

## A.1. Visual basic code to estimate micellar mole fraction

```
Public Function Frxn1(beta, cmc1, cmc2, alpha, C)
x1 = 0 'Lower bound
x2 = 1 'Upper bound
xacc = 0.00001 'Accuracy of x  value
x = alpha * 0.2 'initial guess
fl = fofx(x1, beta, cmc1, cmc2, alpha, C)
fh = fofx(x2, beta, cmc1, cmc2, alpha, C)
If ((fl > 0 And fh > 0) Or (fl < 0 And fh < 0)) Then
   Frxn1 = -2
   Exit Function
ElseIf (fl = 0) Then
   Frxn1 = x1
   Exit Function
ElseIf (fh = 0) Then
   Frxn1 = x2
   Exit Function
ElseIf (fl < 0) Then
   xl = x1
   xh = x2
Else
   xh = x1
   xl = x2
End If
rtsafe = 0.5 * (x1 + x2) 'Value to return to if necessary
dxold = Abs(x2 - x1)
dx = dxold
f = fofx(rtsafe, beta, cmc1, cmc2, alpha, C)
df = dfdx(rtsafe, beta, cmc1, cmc2, alpha, C)

For i = 1 To 2000
' f = fofx(x, beta, cmc1, cmc2, alpha, C)
' df = dfdx(x, beta, cmc1, cmc2, alpha, C)
' xguess = x - f / df
If (((rtsafe - xh) * df - f) * ((rtsafe - x1) * df - f) >= 0 Or Abs(2 * f) > Abs(dxold * df))
Then
   dxold = dx
   dx = 0.5 * (xh - xl)
   rtsafe = xl + dx
   If (xl = rtsafe) Then
     Frxn1 = xl
     Exit Function
   End If
```

```
Else
  dxold = dx
  dx = f / df
  temp = rtsafe
  rtsafe = rtsafe - dx
  If (temp = rtsafe) Then
    Frxn1 = temp
    Exit Function
  End If
End If
If Abs(dx) < xacc Then
  Frxn1 = rtsafe
  Exit Function
End If
f = fofx(rtsafe, beta, cmc1, cmc2, alpha, C)
df = dfdx(rtsafe, beta, cmc1, cmc2, alpha, C)
If (f < 0) Then
  xl = rtsafe
Else
  xh = rtsafe
End If
' If (Abs((x - xguess) / x) < 1 * 10 ^ -6) Then
' Frxn1 = xguess
' Exit Function
' End If
' x = xguess
Next i
Frxn1 = -2
End Function

Public Function fofx(x, beta, cmc1, cmc2, alpha, C)
fofx = x ^ 2 * (cmc2 * Exp(beta * x ^ 2) - cmc1 * Exp(beta * (1 - x) ^ 2)) + x * (C +
cmc1 * Exp(beta * (1 - x) ^ 2) - cmc2 * Exp(beta * x ^ 2)) - alpha * C
End Function

Public Function dfdx(x, beta, cmc1, cmc2, alpha, C)
dfdx = 2 * x * cmc2 * Exp(beta * (x ^ 2)) - 2 * x * cmc1 * Exp(beta * (1 - x) ^ 2) + 2 *
beta * x ^ 3 * cmc2 * Exp(beta * (x ^ 2)) + 2 * beta * x ^ 2 * cmc1 * Exp(beta * (1 - x) ^
2) - 2 * beta * x ^ 3 * cmc1 * Exp(beta * (1 - x) ^ 2) + C + cmc1 * Exp(beta * (1 - x) ^ 2)
- cmc2 * Exp(beta * (x ^ 2)) - 2 * beta * x * cmc1 * Exp(beta * (1 - x) ^ 2) + 2 * beta * x
^ 2 * Exp(beta * (1 - x) ^ 2) - 2 * beta * x ^ 2 * cmc2 * Exp(beta * (x ^ 2))
End Function
Public Function Frxn2(beta, cmc1, cmc2, alpha)
x = alpha * 0.1 'initial guess

For i = 1 To 1000
```

```
f = -(beta * (x ^ 2) * ((1 - x) ^ 2)) + (((1 - x) ^ 2) * Log(((1 - alpha) * x * cmc1 *
Exp(beta * ((1 - x) ^ 2))) / (alpha * (1 - x) * cmc2)))
df = -((2 * beta * x * ((1 - x) ^ 2)) - (2 * (1 - x) * beta * (x ^ 2))) - 2 * (1 - x) * Log((1 -
alpha) * x * cmc1 * Exp(beta * (1 - x) ^ 2)) + (((1 - x) ^ 3 * alpha * cmc2) / ((1 - alpha) *
x * cmc1 * Exp(beta * (1 - x) ^ 2))) * ((((1 - alpha) * cmc1 * Exp(beta * (1 - x) ^ 2) -
Exp(beta * (1 - x) ^ 2) * 2 * (1 - x)) / (alpha * (1 - x) * cmc2)) + ((1 - alpha) * x * cmc1 *
Exp(beta * (1 - x) ^ 2)) / (alpha * (1 - x) ^ 2 * cmc2))

xguess = x - f / df
If (Abs((x - xguess) / x) < 1 * 10 ^ -6) Then
Frxn2 = xguess
Exit Function
End If
x = xguess
Next i

End Function
```

## A.2 Supplemental information

Due to coupling effect observed between enthalpy of demicellization and first order terms in enthalpy of dilution, a third model (Model 3) was tried which had fixed values of enthalpy of demicellization for the pure surfactants CTAB and C8G1. The obtained figures for fitting are shown below in Figure A.2. While it was observed that the obtained fit matched the data well, large variability was seen for first order parameters associated with enthalpy of dilution. A regression value higher than Model 1 and comparable to Model 2 for the curves was obtained, β was found to deviate even more from literature reported values compared to β obtained from Model 2. The obtained parameters for enthalpy of dilution, cmcs and enthalpies of demicellization for pure surfactants along with their variability are shown in Table A.1.

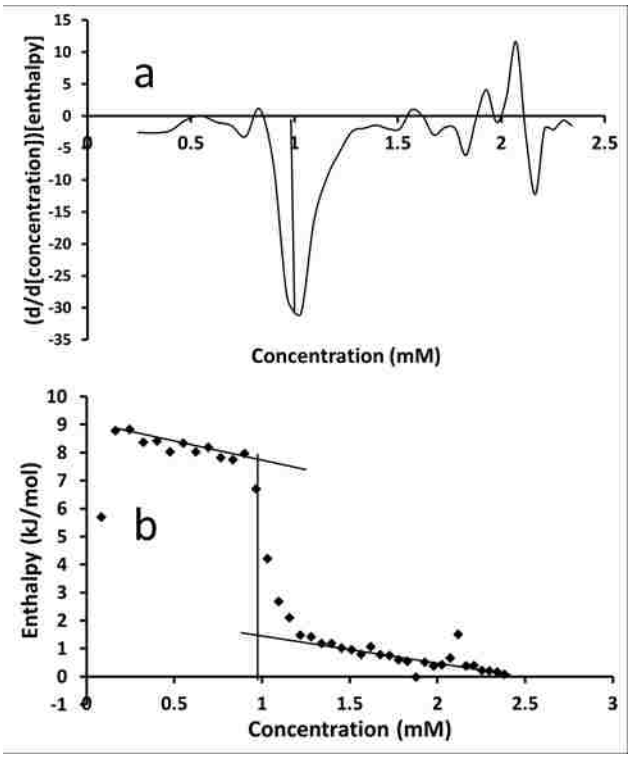


**Figure A.1.** Differential enthalpy analysis for 8.1 mM CTAB demicellization experiment in water. Figure A.1 a) shows the first order differential of enthalpy calculated using central difference method plotted against the concentration. The line perpendicular to concentration axis marks the cmc at extremum. Figure A.1 b) shows an enthalpy versus concentration diagram for 8.1 mM CTAB, where the enthalpy of demicellization is determined as the value between intersection of line at cmc (perpendicular to concentration axis) and the regression lines for low and high concentration plateaus.

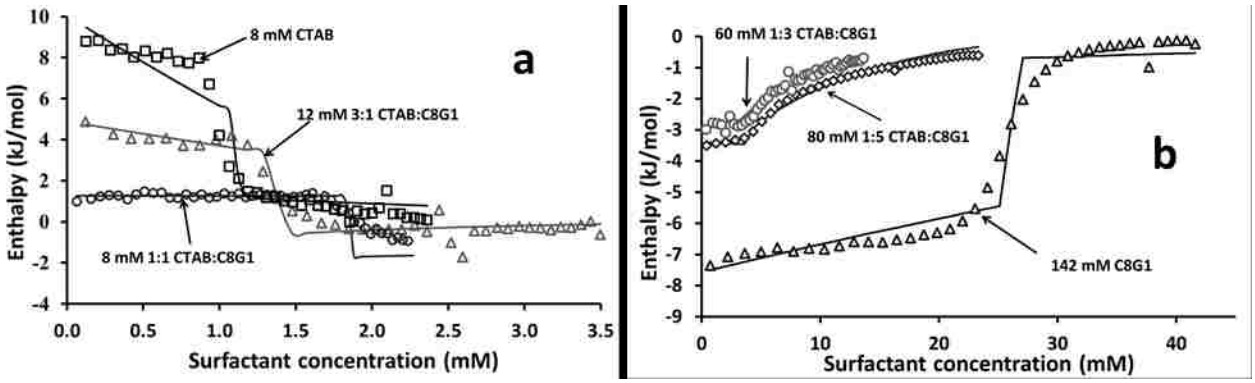


**Figure A.2.** Experimental and modeled enthalpy vs concentration diagrams obtained using fitting with Model 3 where enthalpy of demicellization is fixed and enthalpy of dilution was modeled using equation 3.13. Figure A.2 a) shows the low concentration region with 8 mM CTAB, 12mM 3:1 CTAB:C8G1, 8 mM 1:1 CTAB:C8G1 and Figure A.2 b) shows the high concentration region with 60 mM 1:3 CTAB:C8G1, 80mM 1:5 CTAB:C8G1.

**TableA.1.** Comparison of parameters and their variability for Models 1,2 and 3

| Parameters | Model 1<br>Best fit value ± std dev | Model 2<br>Best fit value ± std dev | Model 3<br>Best fit value ± std dev |
|---|---|---|---|
| $C_1$ (mM) | 26.0 ± 0.14 | 26.1 ± 0.11 | 26.04 ± 0.11 |
| $C_2$ (mM) | 1.11± 0.01 | 1.05 ± 0.006 | 1.11 ± 8x$10^{-3}$ |
| $\Delta H_1^{m\rightarrow aq}$ (kJ/mol) | -6.31± 2.85×$10^5$ | -8.60 ± 0.28 | --- |
| $\Delta H_2^{m\rightarrow aq}$ (kJ/mol) | 9.54 ± 3.26×$10^5$ | 8.28 ± 0.32 | --- |
| β | -2.43± 0.065 | -1.89 ± 0.059 | -1.8 ± 0.06 |
| $h_{11}^{mic}$ (kJ $l^2/mmol^2 mol$) | -4.7 ± 1.4 | -1.3 ± 0.24 | -5.1 ± 1.3 |
| $h_{11}^{m}$ (kJ $l^2/mmol^2 mol$) | -2.8 ± 1.3 | 1.4 ± 0.49 | -2.1 ± 0.94 |
| $h_{12}^{m}$ (kJ $l^2/mmol^2 mol$) | 5.1 ± 1.4 | -0.14 ± 0.55 | 4.42 ± 1.01 |
| $h_{22}^{mic}$ (kJ $l^2/mmol^2 mol$) | -0.20 ± 2.7x$10^{-2}$ | -0.23 ± 0.02 | -0.19 ± 0.02 |
| $h_{22}^{m}$ (kJ $l^2/mmol^2 mol$) | -2.2 ± 0.31 | -1.1 ± 0.25 | -2.3 ± 0.23 |
| $h_{12}^{mic}$ (kJ $l^2/mmol^2 mol$) | 1.9 ± 0.27 | 1.1 ± 0.13 | 1.2 ± 0.14 |
| $h_1^{m}$ (kJ l/mmol mol) | -7.0 ± 6.4x$10^5$ | --- | -8.7 ± 3.5x$10^5$ |
| $h_2^{m}$ (kJ l/mmol mol) | 2.3 ± 1.7x$10^5$ | --- | 3.93 ± 6.7x$10^4$ |
| $h_2^{mic}$ (kJ l/mmol mol) | 5.4 ± 6.4x$10^5$ | --- | 6.36 ± 3.5x$10^5$ |
| $h_2^{mic}$ (kJ l/mmol mol) | 2.2 ± 2.5x$10^5$ | --- | 0.74 ± 6.7x$10^4$ |
| $h_{11}^{mic}$ **(H)** (kJ $l^2/mmol^2 mol$) | 0.01 ± 0.002 | 6.9x$10^{-3}$ ± 1.43x$10^{-3}$ | 0.01 ± 1x$10^{-3}$ |
| $h_{11}^{m}$ **(H)** (kJ $l^2/mmol^2 mol$) | 0.05 ± 0.01 | 0.058 ± 7.8x$10^{-3}$ | 0.05 ± 8x$10^{-3}$ |
| $h_{12}^{m}$ **(H)** (kJ $l^2/mmol^2 mol$) | -1.3 ± 0.920 | -0.59 ± 0.62 | -0.92 ± 0.62 |
| $h_{22}^{mic}$ **(H)** (kJ $l^2/mmol^2 mol$) | 0.28 ± 0.17 | 0.24 ± 0.13 | 0.13 ± 0.14 |
| $h_{22}^{m}$ **(H)** (kJ $l^2/mmol^2 mol$) | 4.4 ± 3.7 | -5.80 ± 1.5 | 3.03 ± 2.5 |

| | | | |
|---|---|---|---|
| $h_{12}^{mic}$ **(H)** (kJ $l^2/mmol^2 mol$) | -0.28 ± 0.036 | -0.30 ± 2.6x10$^{-2}$ | -0.28 ± 0.027 |
| $h_1^m$ **(H)** (kJ l/mmol mol) | -0.84 ± 2.3x10$^5$ | --- | -0.71 ± 1.5x10$^5$ |
| $h_2^m$ **(H)** (kJ l/mmol mol) | -6.8 ± 1.2x10$^6$ | --- | -4.62 ± 1.0x10$^6$ |
| $h_2^{mic}$**(H)** (kJ l/mmol mol) | 0.98 ± 3.2x10$^5$ | --- | 0.81 ± 1.5x10$^6$ |
| $h_2^{mic}$**(H)** (kJ l/mmol mol) | 3.03 ± 1.1x10$^6$ | --- | 2.59 ± 1.0x10$^6$ |
| $R^2$ | 0.956 | 0.973 | 0.973 ± |

**(H)** in Table A.1 indicates dilution parameters associated with the high concentration region.

**Table A.2.** Comparison of parameters obtained for dilution models 1 and 2 after fixing pure surfactant cmcs and enthalpies of demicellization to apparent enthalpy recorded using ITC.

| | **Model 1** | **Model 2** |
|---|---|---|
| **Parameters**[a] | **Best fit value ± std dev** | **Best fit value ± std dev** |
| $h_{11}^{mic}$ (kJ $l^2/mmol^2 mol$) | -1.54 ± 1.52 | -1.29 ± 0.22 |
| $h_{11}^m$ (kJ $l^2/mmol^2 mol$) | 0.87 ± 0.98 | 0.69 ± 0.51 |
| $h_{12}^m$ (kJ $l^2/mmol^2 mol$) | -0.14 ± 1.11 | -0.66 ± 0.70 |
| $h_{22}^{mic}$ (kJ $l^2/mmol^2 mol$) | -0.28 ± 0.02 | -0.29 ± 0.02 |
| $h_{22}^m$ (kJ $l^2/mmol^2 mol$) | -0.74 ± 0.31 | -0.01 ± 0.2 |
| $h_{12}^{mic}$ (kJ $l^2/mmol^2 mol$) | 0.98 ± 0.12 | 1.13 ± 0.14 |
| $h_1^m$ (kJ l/mmol mol) | -0.99 ± 3.9x10$^5$ | --- |
| $h_2^m$ (kJ l/mmol mol) | 0.47 ± 1.4x10$^5$ | --- |
| $h_2^{mic}$ (kJ l/mmol mol) | 0.98 ± 3.9x10$^5$ | --- |
| $h_2^{mic}$ (kJ l/mmol mol) | -0.48 ± 1.45x10$^5$ | --- |
| $h_{11}^{mic}$ **(H)** (kJ $l^2/mmol^2 mol$) | 0.01 ± 1.5x10$^{-3}$ | 0.01 ± 1.4x10$^{-3}$ |
| $h_{11}^m$ **(H)** (kJ $l^2/mmol^2 mol$) | 0.05 ± 9x10$^{-3}$ | 0.02 ± 7.2x10$^{-3}$ |
| $h_{12}^m$ **(H)** (kJ $l^2/mmol^2 mol$) | -1.14 ± 0.72 | -1.61 ± 0.78 |
| $h_{22}^{mic}$ **(H)** (kJ $l^2/mmol^2 mol$) | 0.06 ± 0.16 | 0.34 ± 0.16 |
| $h_{22}^m$ **(H)** (kJ $l^2/mmol^2 mol$) | 3.41 ± 2.9 | -3.66 ± 1.89 |
| $h_{12}^{mic}$ **(H)** (kJ $l^2/mmol^2 mol$) | -0.27 ± 0.03 | -0.29 ± 3.3x10$^{-2}$ |
| $h_1^m$ **(H)** (kJ l/mmol | -0.56 ± 1.01x10$^5$ | --- |

| | | |
|---|---|---|
| mol) | | |
| $h_2^m$ **(H)** (kJ l/mmol mol) | -3.67 ± 1.08x$10^5$ | --- |
| $h_2^{mic}$**(H)** (kJ l/mmol mol) | 0.56 ± 1.01x$10^5$ | --- |
| $h_2^{mic}$**(H)** (kJ l/mmol mol) | 3.59 ± 1.07x$10^5$ | --- |

[a] **(H)** in Table A.2 indicates dilution parameters associated with the high concentration region.

**APPENDIX B**
**SUPPLEMENTAL INFORMATION (CHAPTER 4)**

## B.1. Calibration curves for xylose and glucose

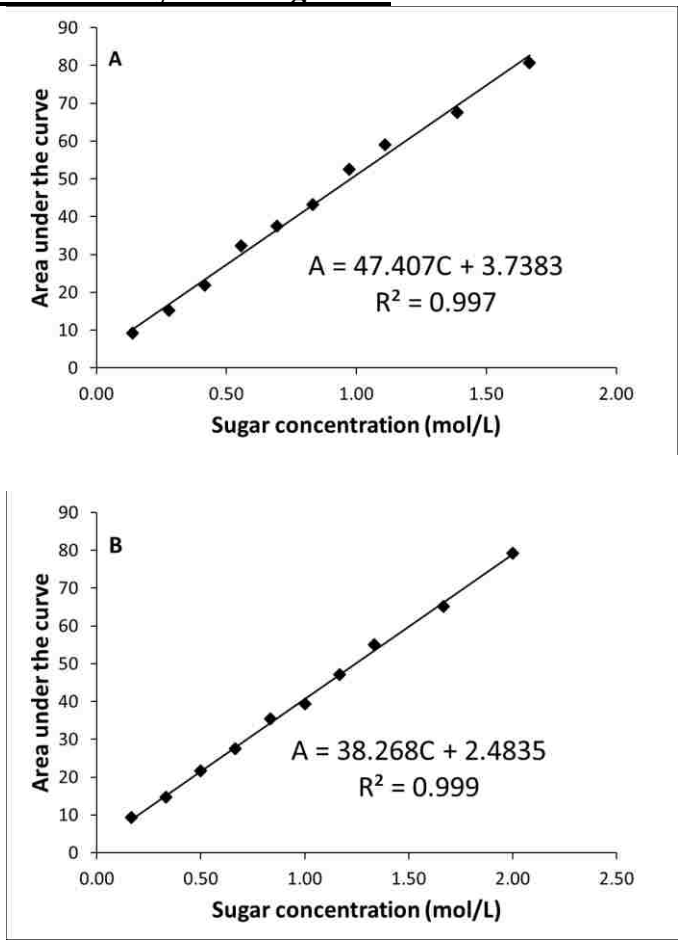


**Figure B.1.** A) Calibration curve for glucose solutions using FTIR-ATR B) FTIR-ATR calibration curve for xylose

A calibration curve for the analysis of glucose solutions was created by making standard solutions of glucose and xylose in DIUF water. The spectrum of DIUF water was subtracted from spectrum of standard sugar solutions generated using ATR-FTIR. The subtracted spectra was analyzed for area under the curve between 900 and 1200 $cm^{-1}$

was measured for each substrates spectrum. Linear regression was used to generate calibration curves shown for each sugar. The supernatant sugar solutions collected after adsorption were analyzed using the same ATR-FTIR technique. Sugar solutions were transferred to the ATR accessory until the surface of the zinc selenide crystal was covered completely with the solution. The solutions were then analyzed from 700 $cm^{-1}$ to 4000 $cm^{-1}$. The FTIR spectrum of DIUF water was collected and subtracted from each sugar solution absorption data in the same wave number region. The area under the curve from 900 to 1200 $cm^{-1}$ was used to determine the concentration of the sugar from the calibration curves in Figure S-1.

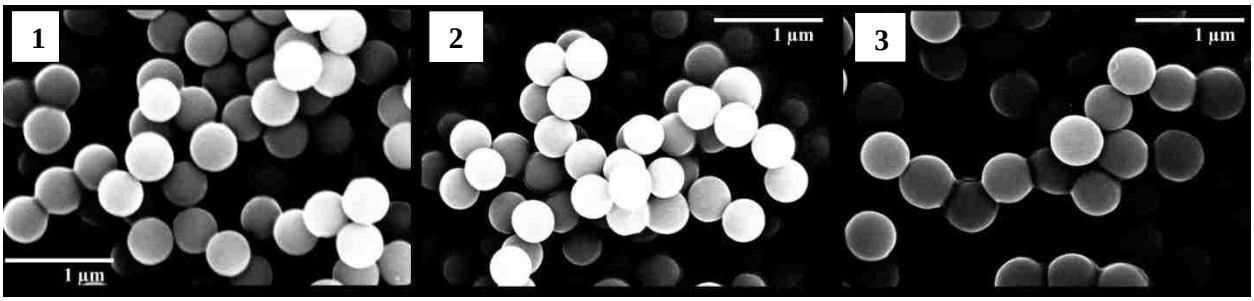


**Figure B.2.** SEM micrograph of Stöber particles with dilute ammonia and no surfactant (**1**), prepared with only CTAB (**2**), prepared with only C8G1 (**3**). All the micrographs displayed here show uniformly sized particles with spherical shape. The particles are homogenous. All the micrographs have been obtained at a magnification of 45000x.

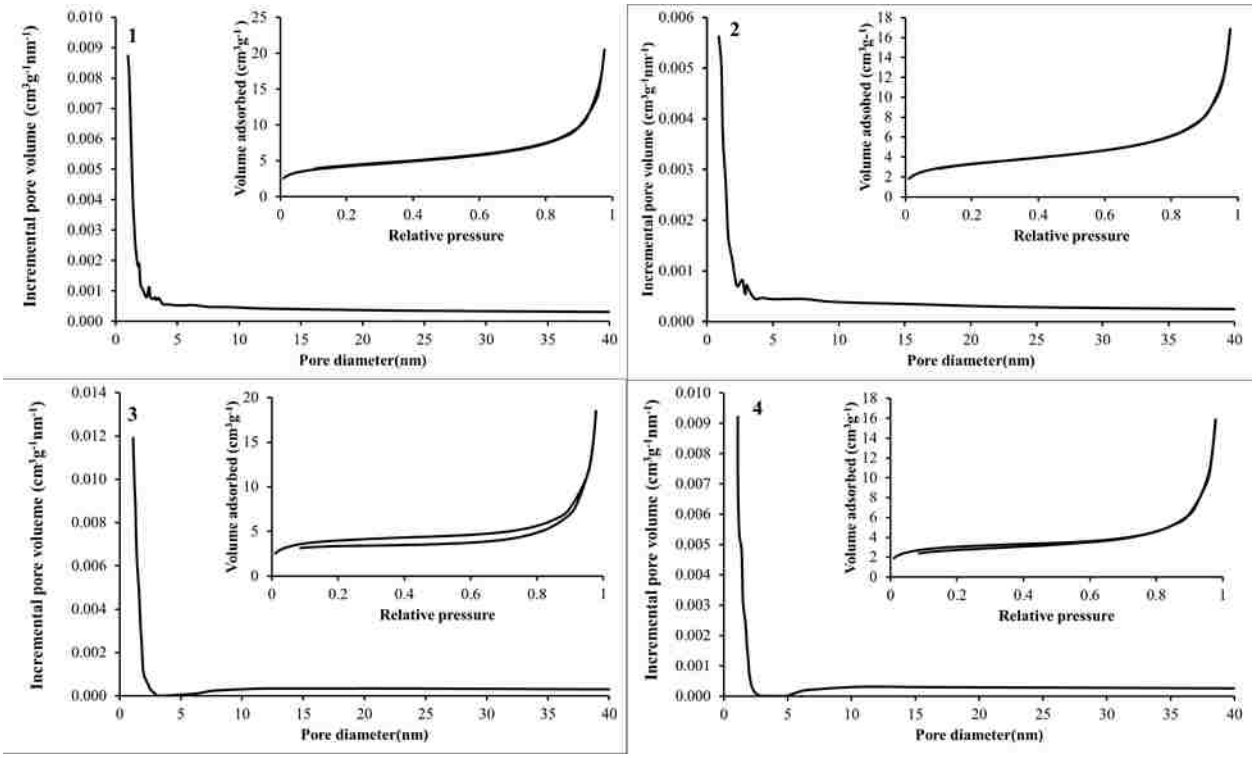


**Figure B.3.** Pore size distribution in laid with nitrogen adsorption isotherms obtained at 78 K for (1) Non-imprinted particles, (2) CTAB imprinted particles, (3) C8G1 imprinted particles, and (4) 1:1 CTAB:C8G1 imprinted particles

## B.2. Sugar adsorption

Adsorption isotherms for glucose and xylose obtained using a single coefficient Langmuir adsorption model are shown in Figure S-4. As can be seen, the model seems to fit all the data well except for the adsorption isotherms for C8G1 imprinted materials and 1:1 CTAB:C8G1 imprinted materials. The low-concentration points (circled) are the least well fit by this model. Having a separate equilibrium coefficient for imprinted and non-imprinted sites as well as different saturation capacities in a 2-site Langmuir model provides significantly better fits, as shown in the main text.

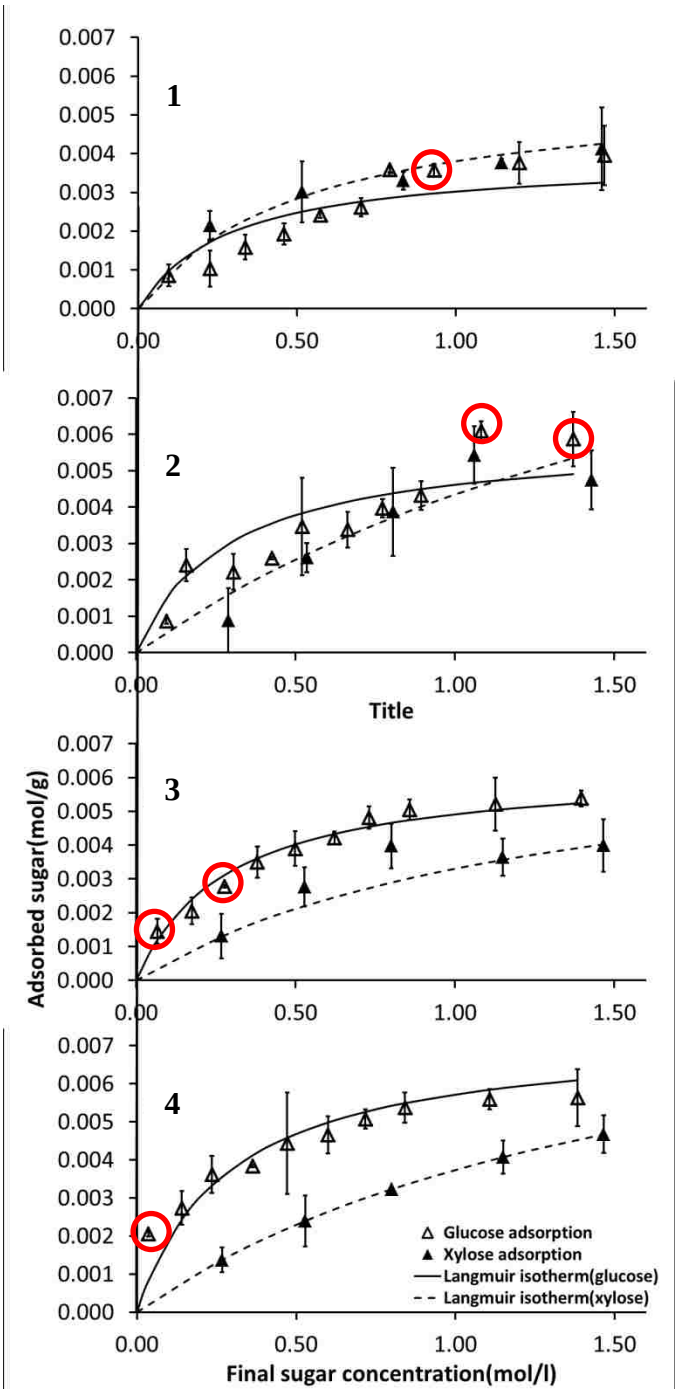


**Figure B.4.** Comparison of adsorption isotherms for D-glucose and D-xylose adsorbing from aqueous solution onto (**1**) non-imprinted particles, (**2**) particles prepared with CTAB, (**3**) particles prepared with C8G1, and (**4**) particles prepared with a 1:1 mixture of CTAB:C8G1. The points which do not fit using a one-site Langmuir isotherm are circled.

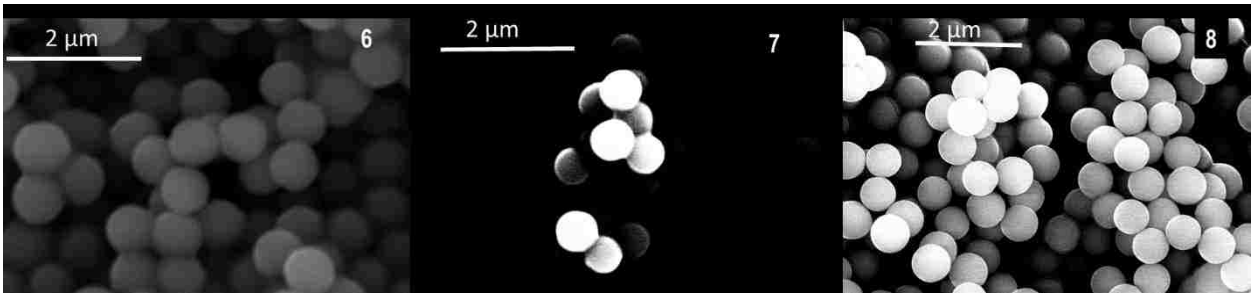


**Figure B.5.** SEM micrographs of washed samples prepared by addition of different ratios of surfactants 1 minute after TEOS addition. The sample numbers are indicated on the micrograph: 6) 1:3 CTAB:C8G1, 7) 3:1 CTAB:C8G1 and 8) 1:1 CTAB:C8G1.

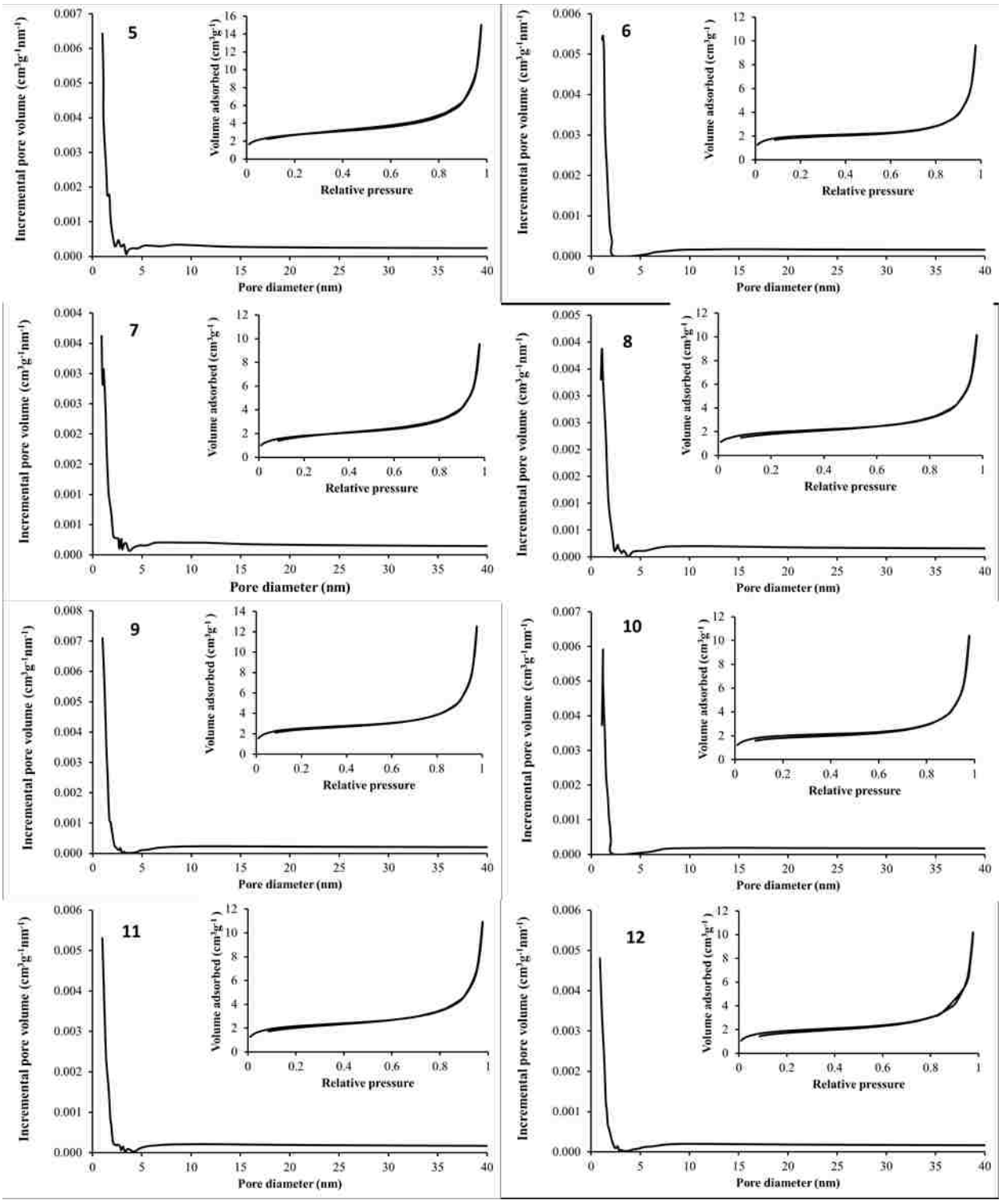


**Figure B.6**. Nitrogen adsorption isotherms and pore size distribution curves for samples synthesized to study effects of ratio and time of addition of surfactants. 5) Sample prepared with no surfactant. 6) 1:3 CTAB:C8G1 added at 1 minute after TEOS addition. 7) 3:1 CTAB:C8G1 added 1 minute after TEOS addition. 8) 1:1 CTAB:C8G1 added 1 minute after TEOS addition. 9) 1:1 CTAB:C8G1 added 2.5 minute after TEOS addition.

10) 1:1 CTAB:C8G1 added 5 minute after TEOS addition. 11) 1:1 CTAB:C8G1 added 1 hour after TEOS addition. 12) 1:1 CTAB:C8G1 added 4 hours after TEOS addition.

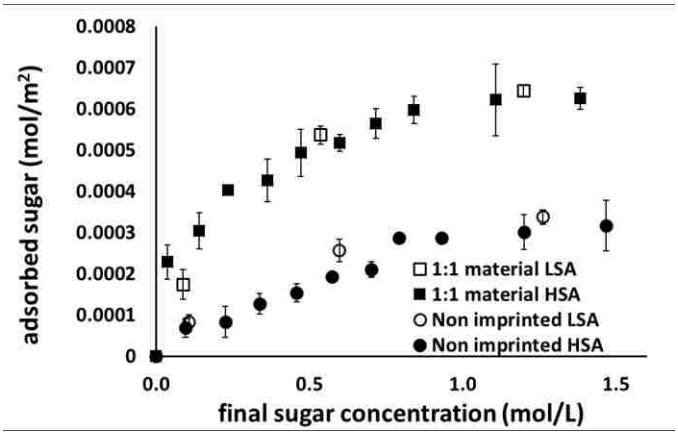


**Figure B.7.** Comparison of glucose adsorption on the silica surface as a function of the concentration in solution for samples with different surface area. LSA stands for low surface area (samples **5** and **8**) while HSA stands for high surface area (samples **1** and **4**) sample. Comparison of both 1:1 CTAB:C8G1 imprinted and non-imprinted materials has been presented. It is observed that when the glucose adsorption is normalized with respect to particle surface area similar amounts of glucose adsorption are observed.

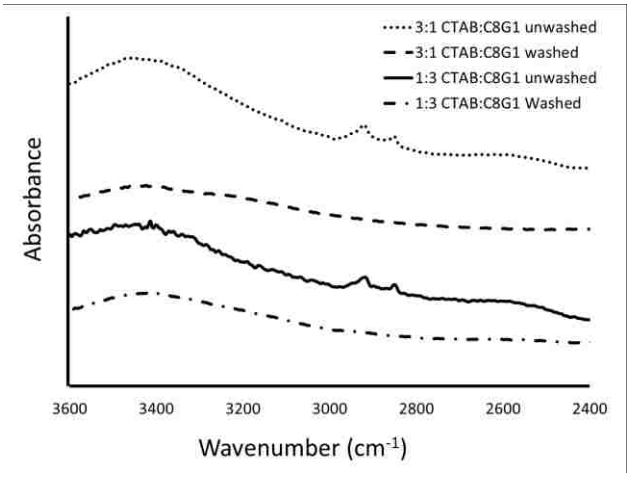


**Figure B.8.** FTIR spectra for samples prepared with 1:3 CTAB:C8G1 (**6**) and 3:1 CTAB:C8G1 (**7**) showing the presence of $CH_2$ stretching bands between 2800 and 3000 $cm^{-1}$. The spectra are shown before and after washing the particles. The spectra suggest that it is possible to completely remove surfactant on the surface by washing the particles.

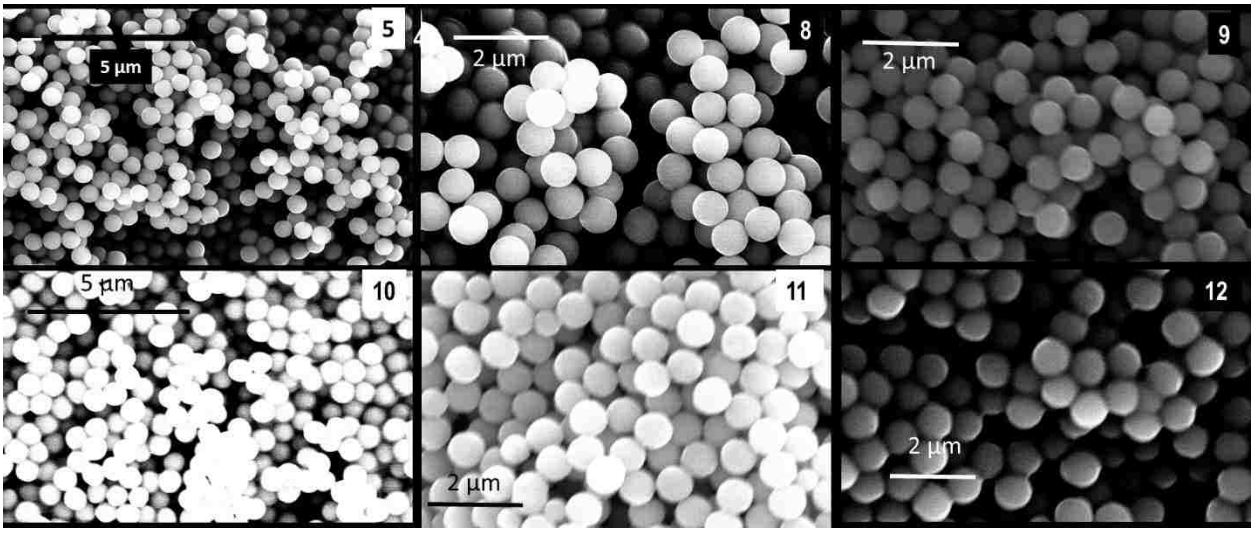


**Figure B.0.9.** SEM micrographs for particles made made with same surfactant ratio (1:1 CTAB:C8G1) but with varying times of addition. All of the particles are washed and made by imprinting the surface of particles with surfactant addition at different times after TEOS addition. (**5**) was prepared without addition of any surfactant, (**8**) with surfactant addition at 1 min after TEOS addition, (**9**) surfactant added at 2.5 min, (**10**) with surfactant added at 5 min, (**11**) with surfactant added at 1 hour, and (**12**) with surfactant added at 4 hours. Micrographs are labeled according to sample numbers.

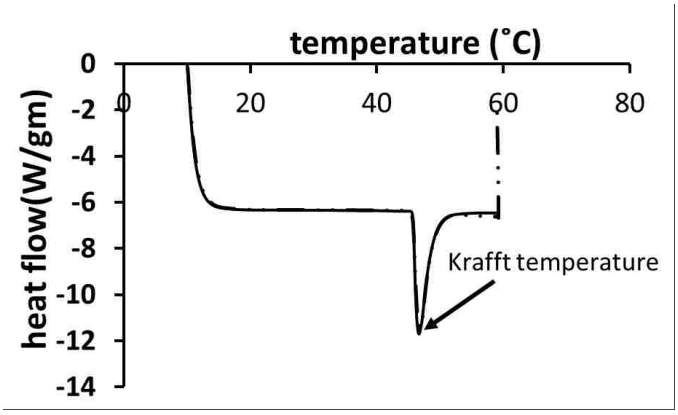


**Figure B.10.** Differential scanning calorimetry of 0.17 mg octyl xyloside in 20 mg of water obtained using DSC to determine Krafft temperature of C8X1 in water. The exothermic peak obtained at 46.5 ˚C indicates the Krafft temperature for the surfactant.

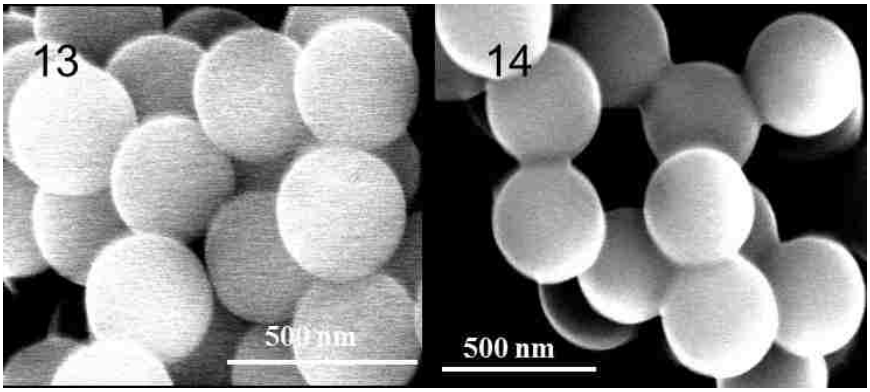


Figure B.0.11. SEM micrographs for control particles prepared by following Stöber synthesis procedure without adding surfactant at 50 ˚C (**13**) and by adding 1:1 mixture of CTAB and C8X1 at 50 ˚C (**13**).

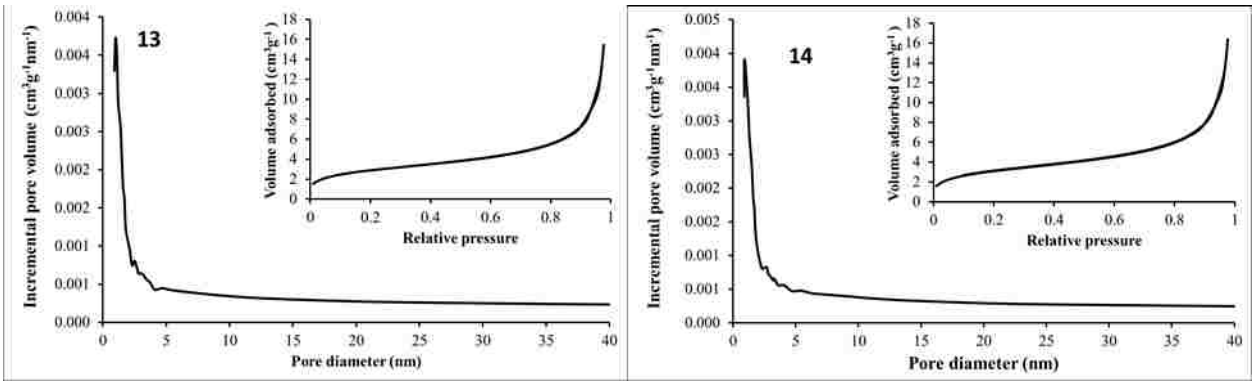


**Figure B.12.** Nitrogen adsorption isotherms and pore size distribution for samples prepared at 50 ˚C. **13**) Sample prepared without adding any surfactant by stirring solution at 50 ˚C for 2 minutes. **14**) Prepared by adding a 1:1 CTAB:C8X1 mixture at 50 s after TEOS addition at 50 s and stirring for 1 addition minute at 50 ˚C.

**APPENDIX C**
**SUPPLEMENTAL INFORMATION (CHAPTER FIVE)**

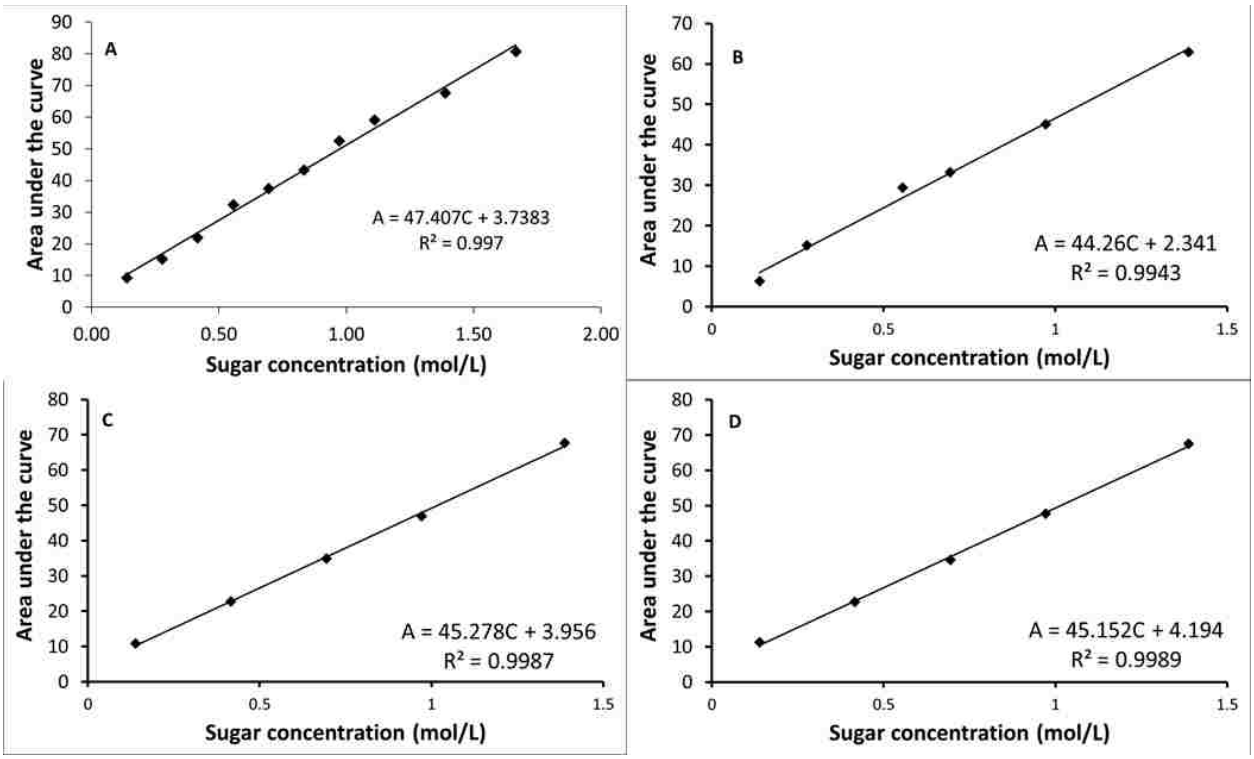


**Figure C.1.** Calibration curves obtained for hexose's using FTIR-ATR by plotting area under the curve between 900 and 1200 $cm^{-1}$ against the concentration of sugars in mol/L. A) D-Glucose, B) L-Glucose, C) D-Mannose, D) D-Galactose. The plotted points represent average value of two measurements.

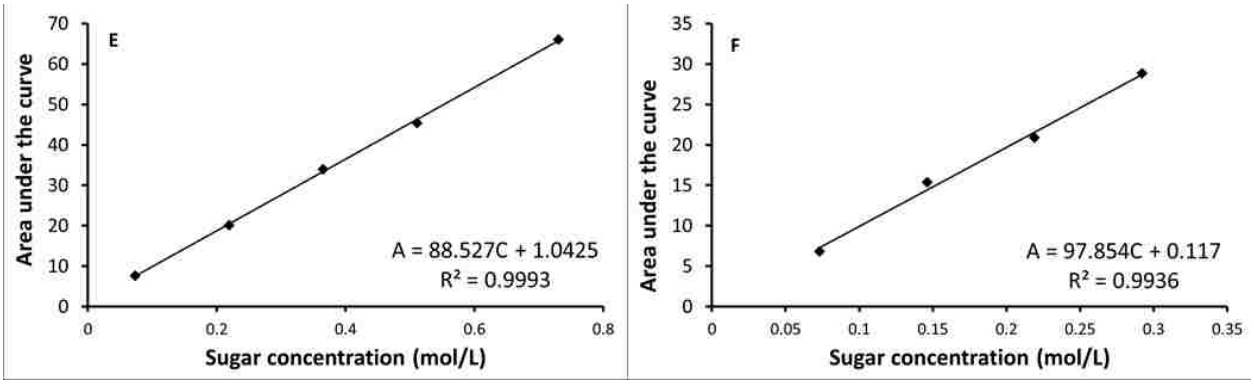


**Figure C.2.** Calibration curves for disaccharides using FTIR-ATR by plotting the area under the curve between 900 and 1200 cm-1 against the concentration of disaccharides in mol/L. E) D-Maltose, F) D-cellobiose. The plotted points in each case represent average value of two measurements.

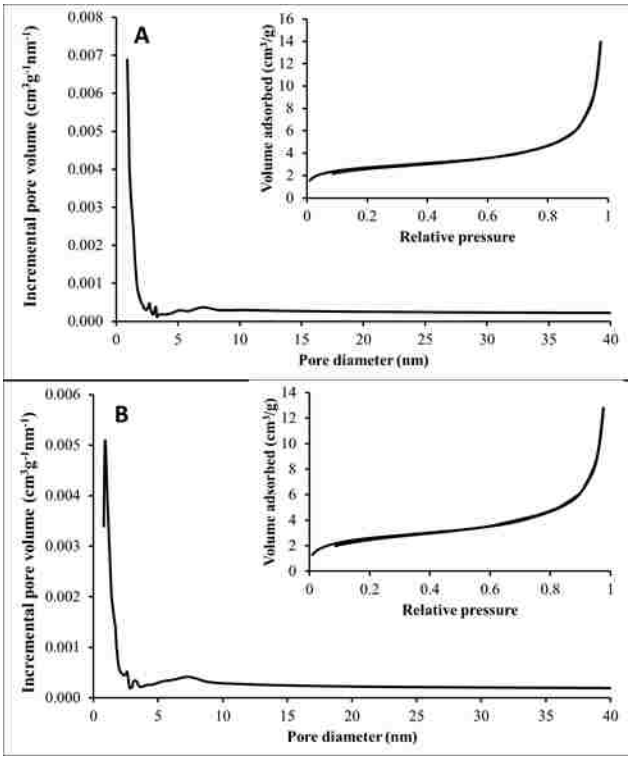


**Figure C.3.** Nitrogen adsorption isotherms and pore size distribution for Stöber particles with A) no surfactant added and B) particles imprinted with 1:1 mixture of CTAB and C8G1.

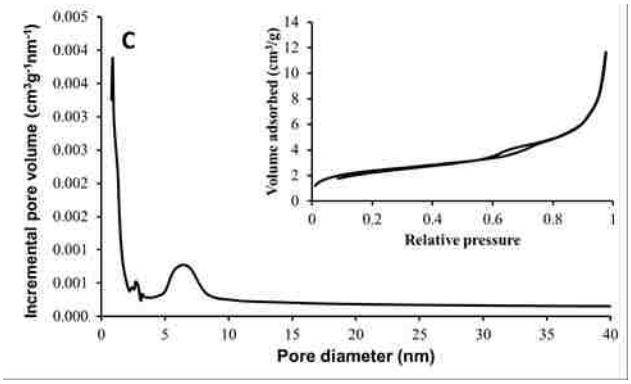


**Figure C.4.** Nitrogen adsorption isotherm and pore size distribution for Stöber particles synthesized by adding 1:1 mixture of CTAB and C12G2.

**Table C.1.** Ratio of target molecule adsorption compared to other saccharides at different initial concentrations of saccharides in solution. The ratios here are indicated for imprinted particles.

| Target molecule/ Saccharide adsorption ratio | Initial concentration (mol/L) | | |
|---|---|---|---|
| | **0.138** | **0.694** | **1.389** |
| **D-glucose/L-glucose** | 5.1 | 4.3 | 3.3 |
| **D-glucose/D-galactose** | 1.4 | 1.2 | 1.5 |
| **D-glucose/D-mannose** | 1.7 | 1.5 | 1.6 |

| Target molecule/ Saccharide adsorption ratio | Initial concentration (mol/L) | | |
|---|---|---|---|
| | **0.069** | **0.138** | **0.277** |
| **Maltose/Cellobiose** | 4.8 | 1.6 | 1.4 |

**APPENDIX D**
**SUPPLEMENTAL INFORMATION (CHAPTER SIX)**

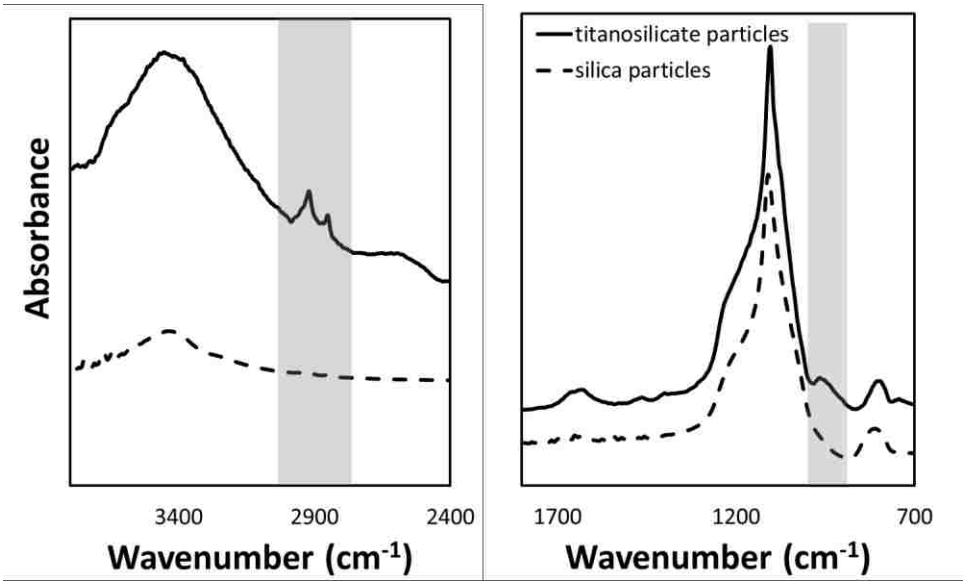


**Figure D.1.** Stöber silica particles and titanosilicate Stöber particles calcined at 300 ˚C. Band at 960 $cm^{-1}$ is visible after calcination for titanosilicates but is absent in case of silicates. $CH_2$ stretching bands are clearly visible for titanosilicate particles between 2800 and 3000 $cm^{-1}$ while are absent for calcined silica particles.

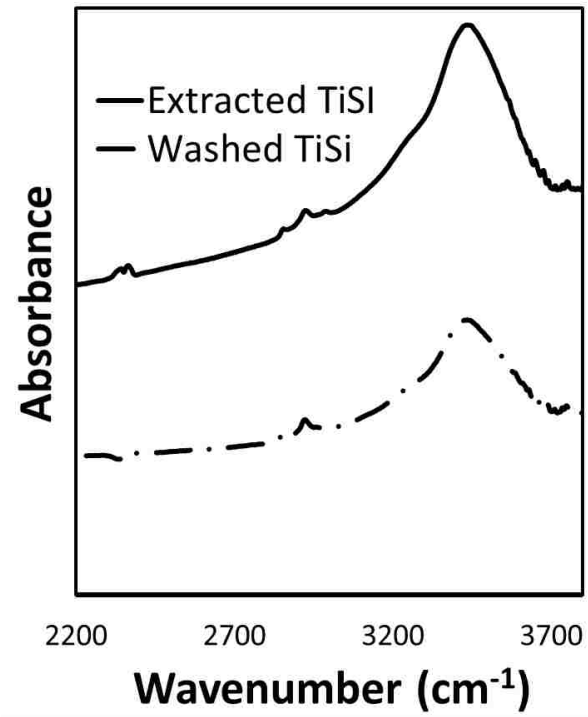


**Figure D.2.** Spectra of soxhlet 'extracted' titanosilicate particles and titanosilicate particles 'washed' with three cycles with ethanol and three cycles with water till the pH was 7. The spectra shows $CH_2$ stretching bands between 2800 and 3000 $cm^{-1}$.

## REFERENCES


(1) Desai, T. R., and Dixit, S. G. (1996) Interaction and viscous properties of aqueous solutions of mixed cationic and nonionic surfactants. *Journal of Colloid and Interface Science 177*, 471-477.

(2) Carnero Ruiz, C. (2008) Micellar properties and molecular interactions in binary surfactant systems containing a sugar-based surfactant, in *Sugar-based surfactants* pp 413-467, CRC Press, New-york.

(3) Kronberg, B. (1997) Surfactant mixtures. *Current Opinion in Colloid & Interface Science 2*, 456-463.

(4) Shiloach, A., and Blankschtein, D. (1998) Predicting micellar solution properties of binary surfactant mixtures. *Langmuir 14*, 1618-1636.

(5) Rahman, M. S., and Rankin, S. E. (2010) Predictive synthesis of ordered mesoporous silica with maltoside and cationic surfactants based on aqueous lyotropic phase behavior. *Journal of Colloid and Interface Science 342*, 33-42.

(6) Xing, R., and Rankin, S. E. (2007) Use of the ternary phase diagram of a mixed cationic/glucopyranoside surfactant system to predict mesostructured silica synthesis. *Journal of Colloid and Interface Science 316*, 930-938.

(7) Hines, J. D. (2001) Theoretical aspects of micellisation in surfactant mixtures. *Current opinion in colloid & interface science 6*, 350-356.

(8) Carale, T. R., and Blankschtein, D. (1992) Theoretical and experimental determinations of the crossover from dilute to semidilute regimes of micellar solutions. *Journal of Physical Chemistry 96*, 459-467.

(9) Puvvada, S., and Blankschtein, D. (1990) Molecular-thermodynamic approach to predict micellization, phase behavior and phase separation of micellar solutions. I. Application to nonionic surfactants. *The Journal of chemical physics 92*, 3710.

(10) Puvvada, S., and Blankschtein, D. (1992) Theoretical and experimental investigations of micellar properties of aqueous-solutions containing binary-mixtures of nonionic surfactants. *Journal of Physical Chemistry 96*, 5579-5592.

(11) Nagarajan, R. (1985) Molecular theory for mixed micelles. *Langmuir 1*, 331-341.

(12) Holland, P. M., and Rubingh, D. N. (1983) Nonideal Multicomponent Mixed Micelle Model. *Journal of Physical Chemistry 87*, 1984-1990.

(13) Hoffmann, H., and Poessnecker, G. (1994) The Mixing Behavior of Surfactants. *Langmuir 10*, 381-389.

(14) Dickey, F. H. (1949) The preparation of specific adsorbents. *Proceedings of the National Academy of Sciences of the United States of America 35*, 227.

(15) Mosbach, K. (1994) Molecular imprinting. *Trends in biochemical sciences 19*, 9-14.

(16) Alexander, C., Andersson, H. S., Andersson, L. I., Ansell, R. J., Kirsch, N., Nicholls, I. A., O'Mahony, J., and Whitcombe, M. J. (2006) Molecular imprinting science and technology: a survey of the literature for the years up to and including 2003. *Journal of Molecular Recognition 19*, 106-180.

(17) Wulff, G. (1995) Molecular Imprinting in Cross-Linked Materials with the Aid of Molecular Templates— A Way towards Artificial Antibodies. *Angewandte Chemie International Edition in English 34*, 1812-1832.

(18) Wulff, G. (2001) Enzyme-like Catalysis by Molecularly Imprinted Polymers. *Chemical Reviews 102*, 1-28.

(19) Díaz-García, M. E., and Laínño, R. B. (2005) Molecular Imprinting in Sol-Gel Materials: Recent Developments and Applications. *Microchimica Acta 149*, 19-36.

(20) Tanev, P. T., Chibwe, M., and Pinnavaia, T. J. (1994) Titanium-containing mesoporous molecular sieves for catalytic oxidation of aromatic compounds. *Nature 368*, 321-323.

(21) Corma, A., Navarro, M. T., and Pariente, J. P. (1994) Synthesis of an ultralarge pore titanium silicate isomorphous to MCM-41 and its application as a catalyst for selective oxidation of hydrocarbons. *Journal of the Chemical Society, Chemical Communications*, 147-148.

(22) Stöber, W., Fink, A., and Bohn, E. (1968) Controlled growth of monodisperse silica spheres in the micron size range. *Journal of Colloid and Interface Science 26*, 62-69.

(23) Ruiz, C. C. (2008) *Sugar-based surfactants: fundamentals and applications*, Vol. 143, CRC.

(24) Fischer, E. (1893) Ueber die Glucoside der Alkohole. *Berichte der deutschen chemischen Gesellschaft 26*, 2400-2412.

(25) Nieendick, C., and Schmid, K.-H. (1995) Alkyl polyglycosides: a new generation of surfactants for the use in manual dishwashing agents. *Chimica oggi 13*, 42-45.

(26) Marinova, K. G., and Denkov, N. D. (2001) Foam destruction by mixed solid-liquid antifoams in solutions of alkyl glucoside: Electrostatic interactions and dynamic effects. *Langmuir 17*, 2426-2436.

(27) Štangar, U. L., and Hüsing, N. (2003) Alkyl-glycoside surfactants in the synthesis of mesoporous silica films. *Silicon Chemistry 2*, 157-165.

(28) Suzuki, K., Ando, T., Susaki, H., Mimori, K., Nakabayashi, S., and Sugiyama, Y. (1999) Structural requirements for alkylglycoside-type renal targeting vector. *Pharmaceutical research 16*, 1026-1034.

(29) Okada, T., Takeda, K., and Kouyama, T. (1998) Highly selective separation of rhodopsin from bovine rod outer segment membranes using combination of divalent cation and alkyl (thio) glucoside. *Photochemistry and photobiology 67*, 495-499.

(30) Shinoda, K., and Hutchinson, E. (1962) Pseudo-phase separation model for thermodynamic calculations on micellar solutions. *The Journal of Physical Chemistry 66*, 577-582.

(31) Mukerjee, P., Mysels, K., and Kapauan, P. (1967) Counterion specificity in the formation of ionic micelles-size, hydration, and hydrophobic bonding effects. *The Journal of Physical Chemistry 71*, 4166-4175.

(32) Boyd, B. J., Drummond, C. J., Krodkiewska, I., Weerawardena, A., Furlong, D. N., and Grieser, F. (2001) Alkyl chain positional isomers of dodecyl β-D-glucoside: Thermotropic and lyotropic phase behavior and detergency. *Langmuir 17*, 6100-6107.

(33) Bocker, T., and Thiem, J. (1989) Synthesis and properties for nonionic surfactants. *Tenside Surf Det 26*, 318-323.

(34) Thiem, J., and Böcker, T. (1992) pp 123, Royal Society of Chemistry: Cambridge.

(35) Fukada, K., Kawasaki, M., Seimiya, T., Abe, Y., Fujiwara, M., and Ohbu, K. (2000) Stereochemical aspects of micellar properties of esterified glucoside surfactants in water: apparent molar volume, adiabatic compressibility, and aggregation number. *Colloid and Polymer Science 278*, 576-580.

(36) Garofalakis, G., Murray, B. S., and Sarney, D. B. (2000) Surface activity and critical aggregation concentration of pure sugar esters with different sugar headgroups. *Journal of colloid and interface science 229*, 391-398.

(37) Aveyard, R., Binks, B., Chen, J., Esquena, J., Fletcher, P., Buscall, R., and Davies, S. (1998) Surface and colloid chemistry of systems containing pure sugar surfactant. *Langmuir 14*, 4699-4709.

(38) Nilsson, F., Söderman, O., and Johansson, I. (1998) Four Different $C_8G_1$Alkylglucosides. Anomeric Effects and the Influence of Straight vs Branched Hydrocarbon Chains. *Journal of colloid and interface science 203*, 131-139.

(39) Focher, B., Savelli, G., Torri, G., Vecchio, G., McKenzie, D., Nicoli, D., and Bunton, C. (1989) Micelles of 1-alkyl glucoside and maltoside: Anomeric effects on structure and induced chirality. *Chemical Physics Letters 158*, 491-494.

(40) Hoffmann, B., and Platz, G. (2001) Phase and aggregation behaviour of alkylglycosides. *Current opinion in colloid & interface science 6*, 171-177.

(41) Holtzer, A., and Holtzer, M. F. (1974) Use of the van't Hoff relation in determination of the enthalpy of micelle formation. *The Journal of Physical Chemistry 78*, 1442-1443.

(42) Emerson, M. F., and Holtzer, A. (1967) Hydrophobic bond in micellar systems. Effects of various additives on the stability of micelles of sodium dodecyl sulfate and of n-dodecyltrimethylammonium bromide. *The Journal of Physical Chemistry 71*, 3320-3330.

(43) Nilsson, F., Söderman, O., Hansson, P., and Johansson, I. (1998) Physical−Chemical Properties of C9G1 and C10G1 β-Alkylglucosides. Phase Diagrams and Aggregate Size/Structure. *Langmuir 14*, 4050-4058.

(44) Nilsson, F., Söderman, O., and Johansson, I. (1996) Physical−Chemical Properties of the n-Octyl β-d-Glucoside/Water System. A Phase Diagram, Self-Diffusion NMR, and SAXS Study. *Langmuir 12*, 902-908.

(45) Boyd, B. J., Drummond, C. J., Krodkiewska, I., and Grieser, F. (2000) How Chain Length, Headgroup Polymerization, and Anomeric Configuration Govern the Thermotropic and Lyotropic Liquid Crystalline Phase Behavior and the Air−Water Interfacial Adsorption of Glucose-Based Surfactants. *Langmuir 16*, 7359-7367.

(46) Platz, G., Poelike, J., Thunig, C., Hofmann, R., Nickel, D., and von Rybinski, W. (1995) Phase Behavior, Lyotropic Phases, and Flow Properties of Alkyl Glycosides in Aqueous Solution. *Langmuir 11*, 4250-4255.

(47) Zhang, L., Somasundaran, P., and Maltesh, C. (1997) Adsorption of< i> n</i>-Dodecyl-β-d-maltoside on Solids. *Journal of colloid and interface science 191*, 202-208.

(48) Giles, C. H., Smith, D., and Huitson, A. (1974) A general treatment and classification of the solute adsorption isotherm. I. Theoretical. *Journal of Colloid and Interface Science 47*, 755-765.

(49) Somasundaran, P., and Fuerstenau, D. W. (1966) Mechanisms of Alkyl Sulfonate Adsorption at the Alumina-Water Interface1. *The Journal of Physical Chemistry 70*, 90-96.

(50) Lu, S., Bian, Y., Zhang, L., and Somasundaran, P. (2007) pH dependence of adsorption of n-dodecyl-β-d-maltoside on solids. *Journal of Colloid and Interface Science 316*, 310-316.

(51) Jakobs, B., Sottmann, T., Strey, R., Allgaier, J., Willner, L., and Richter, D. (1999) Amphiphilic block copolymers as efficiency boosters for microemulsions. *Langmuir 15*, 6707-6711.

(52) Kjellin, M., and Johansson, I. (2010) *Surfactants from renewable resources*, John Wiley & Sons.

(53) Urbanski, R., Draye, M., Cote, G., and Szymanowski, J. (2000) Removal of bisphenol A from aqueous streams by micellar extraction and ultrafiltration. *Solvent Extraction and Ion Exchange 18*, 533-550.

(54) Stubenrauch, C. (2001) Sugar surfactants—aggregation, interfacial, and adsorption phenomena. *Current opinion in colloid & interface science 6*, 160-170.

(55) Ogino, K., and Abe, M. (1993) *Mixed surfactant systems*, Vol. 46, CRC Press.

(56) Holmberg, K. (2004) Surfactant-templated nanomaterials synthesis. *Journal of Colloid and Interface Science 274*, 355-364.

(57) Antonietti, M. (2001) Surfactants for novel templating applications. *Current opinion in colloid & interface science 6*, 244-248.

(58) Nishikido, N. (1993) Thermodynamic models for mixed micellization, in *Mixed surfactant systems* (Ogino, K., and Abe, M., Eds.), CRC Press, New York.

(59) Puvvada, S., and Blankschtein, D. (1992) Thermodynamic description of micellization, phase-behavior, and phase-separation of aqueous-solutions of surfactant mixtures. *Journal of Physical Chemistry 96*, 5567-5579.

(60) Maeda, H. (2005) A thermodynamic analysis of charged mixed micelles in water. *Journal of Physical Chemistry B 109*, 15933-15940.

(61) Motomura, K., Yamanaka, M., and Aratono, M. (1984) Thermodynamic consideration of the mixed micelle of surfactants. *Colloid and Polymer Science 262*, 948-955.

(62) Clint, J. H. (1975) Micellization of Mixed Nonionic Surface-Active Agents. *Journal of the Chemical Society-Faraday Transactions I 71*, 1327-1334.

(63) Liljekvist, P., and Kronberg, B. (2000) Comparing Decyl-β-maltoside and Octaethyleneglycol Mono< i> n</i>-Decyl Ether in Mixed Micelles with Dodecyl Benzenesulfonate: 1. Formation of Mixed Micelles. *Journal of colloid and interface science 222*, 159-164.

(64) Bergström, M., Jonsson, P., Persson, M., and Eriksson, J. C. (2003) A model-independent evaluation of experimental data, and comparison with theory, of

synergistic effects in mixtures of an ionic and a nonionic surfactant. *Langmuir 19*, 10719-10725.

(65) Hierrezuelo, J., Aguiar, J., and Carnero Ruiz, C. (2005) Micellar properties of a mixed surfactant system constituted by< i> n</i>-octyl-β-d-thioglucopyranoside and sodium dodecyl sulphate. *Colloids and Surfaces A: Physicochemical and Engineering Aspects 264*, 29-36.

(66) Kameyama, K., Muroya, A., and Takagi, T. (1997) Properties of a mixed micellar system of sodium dodecyl sulfate and octylglucoside. *Journal of colloid and interface science 196*, 48-52.

(67) Sierra, M., and Svensson, M. (1999) Mixed micelles containing alkylglycosides: effect of the chain length and the polar head group. *Langmuir 15*, 2301-2306.

(68) Lainez, A., del Burgo, P., Junquera, E., and Aicart, E. (2004) Mixed micelles formed by n-octyl-beta-D-glucopyranoside and tetradecyltrimethylammonium bromide in aqueous media. *Langmuir 20*, 5745-5752.

(69) del Burgo, P., Junquera, E., and Aicart, E. (2004) Mixed micellization of a nonionic-cationic surfactant system constituted by n-octyl-β-D-glucopyranoside/dodecyltrimethylammonium bromide/H2O. An electrochemical, thermodynamic, and spectroscopic study. *Langmuir 20*, 1587-1596.

(70) Kakehashi, R., Shizuma, M., Yamamura, S., and Takeda, T. (2004) Mixed micelles containing sodium oleate: the effect of the chain length and the polar head group. *Journal of Colloid and Interface Science 279*, 253-258.

(71) Wydro, P. (2007) The influence of the size of the hydrophilic group on the miscibility of zwitterionic and nonionic surfactants in mixed monolayers and micelles. *Journal of colloid and interface science 316*, 107-113.

(72) Jarek, E., Wydro, P., Warszyński, P., and Paluch, M. (2006) Surface properties of mixtures of surface-active sugar derivatives with ionic surfactants: Theoretical and experimental investigations. *Journal of colloid and interface science 293*, 194-202.

(73) Zhang, R., and Somasundaran, P. (2006) Advances in adsorption of surfactants and their mixtures at solid/solution interfaces. *Advances in colloid and interface science 123*, 213-229.

(74) Tsamaloukas, A. D., Beck, A., and Heerklotz, H. (2009) Modeling the Micellization Behavior of Mixed and Pure n-Alkyl-Maltosides. *Langmuir 25*, 4393-4401.

(75) Xu, Q., Vasudevan, T., and Somasundaran, P. (1991) Adsorption of anionic—nonionic and cationic—nonionic surfactant mixtures on kaolinite. *Journal of colloid and interface science 142*, 528-534.

(76) Huang, L., Maltesh, C., and Somasundaran, P. (1996) Adsorption behavior of cationic and nonionic surfactant mixtures at the alumina–water interface. *Journal of colloid and interface science 177*, 222-228.

(77) Matsson, M. K., Kronberg, B., and Claesson, P. M. (2005) Enhanced adsorption of alkyl glucosides on the silica/water interface by addition of amine oxides. *Langmuir 21*, 2766-2772.

(78) Somasundaran, P., Fu, E., and Xu, Q. (1992) Coadsorption of anionic and nonionic surfactant mixtures at the alumina-water interface. *Langmuir 8*, 1065-1069.

(79) Zhang, L., Zhang, R., and Somasundaran, P. (2006) Adsorption of mixtures of nonionic sugar-based surfactants with other surfactants at solid/liquid interfaces: II. Adsorption of n-dodecyl-β-d-maltoside with a cationic surfactant and a nonionic ethoxylated surfactant on solids. *J. Colloid Interface Sci. 302*, 25-31.

(80) Collinson, M. M. (2010) Imprinted Functionalized Silica, in *The Supramolecular Chemistry of Organic-Inorganic Hybrid Materials* pp 581-598, John Wiley & Sons, Inc.

(81) Katz, A., and Davis, M. E. (2000) Molecular imprinting of bulk, microporous silica. *Nature 403*, 286-289.

(82) Kempe, M., and Mosbach, K. (1995) Molecular imprinting used for chiral separations. *J Chromatogr A 694*, 3-13.

(83) Sellergren, B. (2000) *Molecularly imprinted polymers: man-made mimics of antibodies and their application in analytical chemistry*, Vol. 23, Access Online via Elsevier.

(84) Sellergren, B., and Allender, C. J. (2005) Molecularly imprinted polymers: A bridge to advanced drug delivery. *Advanced drug delivery reviews 57*, 1733-1741.

(85) Polyakov, M. (1931) Adsorption properties and structure of silica gel. *Zhur Fiz Khim 2*, 799-805.

(86) Haldeman, R., and Emmett, P. (1955) Specific Adsorption of Alkyl Orange Dyes on Silica Gel. *The Journal of Physical Chemistry 59*, 1039-1043.

(87) Curti, R., and Colombo, U. (1952) Chromatography of stereoisomers with “tailor made” compounds. *J. Am. Chem. Soc. 74*, 3961-3961.

(88) Takagishi, T., and Klotz, I. M. (1972) Macromolecule-small molecule interactions; introduction of additional binding sites in polyethyleneimine by disulfide cross–linkages. *Biopolymers 11*, 483-491.

(89) Wulff, G., and Sarhan, A. (1972) Use of polymers with enzyme-analogous structures for the resolution of racemates. *Angew. Chem. Int. Ed. Engl 11*, 341-342.

(90) Damen, J., and Neckers, D. C. (1980) Memory of synthesized vinyl polymers for their origins. *The Journal of Organic Chemistry 45*, 1382-1387.

(91) Wulff, G., Sarhan, A., and Zabrocki, K. (1973) Enzyme-analogue built polymers and their use for the resolution of racemates. *Tetrahedron Letters 14*, 4329-4332.

(92) Shea, K. J., Stoddard, G., Shavelle, D., Wakui, F., and Choate, R. (1990) Synthesis and characterization of highly crosslinked poly (acrylamides) and poly (methacrylamides). A new class of macroporous polyamides. *Macromolecules 23*, 4497-4507.

(93) Marty, J.-D., Tizra, M., Mauzac, M., Rico-Lattes, I., and Lattes, A. (1999) New molecular imprinting materials: liquid crystalline networks. *Macromolecules 32*, 8674-8677.

(94) Wulff, G., and Haarer, J. (1991) Enzyme-analogue built polymers, 29. The preparation of defined chiral cavities for the racemic resolution of free sugars. *Die Makromolekulare Chemie 192*, 1329-1338.

(95) Wulff, G., and Poll, H. G. (1987) Enzyme-analogue built polymers, 23. Influence of the structure of the binding sites on the selectivity for racemic resolution. *Die Makromolekulare Chemie 188*, 741-748.

(96) Wulff, G., and Schauhoff, S. (1991) Racemic resolution of free sugars with macroporous polymers prepared by molecular imprinting. Selectivity dependence on the arrangement of functional groups versus spatial requirements. *Journal of organic chemistry 56*, 395-400.

(97) Arshady, R., and Mosbach, K. (1981) Synthesis of substrate-selective polymers by host-guest polymerization. *Die Makromolekulare Chemie 182*, 687-692.

(98) Makote, R., and Collinson, M. M. (1998) Template recognition in inorganic-organic hybrid films prepared by the sol-gel process. *Chemistry of materials 10*, 2440-2445.

(99) Makote, R., and M Collinson, M. (1999) Organically modified silicate films for stable pH sensors. *Analytica chimica acta 394*, 195-200.

(100) Wulff, G., and Biffis, A. (2000) Molecular imprinting with covalent or stoichiometric non-covalent interactions. *Techniques and Instrumentation in Analytical Chemistry 23*, 71-111.

(101) Whitcombe, M. J., Rodriguez, M. E., Villar, P., and Vulfson, E. N. (1995) A new method for the introduction of recognition site functionality into polymers prepared by molecular imprinting: synthesis and characterization of polymeric receptors for cholesterol. *J. Am. Chem. Soc. 117*, 7105-7111.

(102) Komiyama, M., Takeuchi, T., Mukawa, T., and Asanuma, H. (2003) *Front Matter*, Wiley Online Library.

(103) Dai, S., Shin, Y., Barnes, C., and Toth, L. (1997) Enhancement of uranyl adsorption capacity and selectivity on silica sol-gel glasses via molecular imprinting. *Chemistry of materials 9*, 2521-2525.

(104) Morihara, K., Kurokawa, M., Kamata, Y., and Shimada, T. (1992) Enzyme-like enantioselective catalysis over chiral 'molecular footprint'cavities on a silica (alumina) gel surface. *J. Chem. Soc., Chem. Commun.*, 358-360.

(105) Markowitz, M. A., Deng, G., and Gaber, B. P. (2000) Effects of added organosilanes on the formation and adsorption properties of silicates surface-imprinted with an organophosphonate. *Langmuir 16*, 6148-6155.

(106) Markowitz, M. A., Kust, P. R., Deng, G., Schoen, P. E., Dordick, J. S., Clark, D. S., and Gaber, B. P. (1999) Catalytic Silica Particles via Template-Directed Molecular Imprinting. *Langmuir 16*, 1759-1765.

(107) Markowitz, M. A., Kust, P. R., Klaehn, J., Deng, G., and Gaber, B. P. (2001) Surface-imprinted silica particles: the effects of added organosilanes on catalytic activity. *Analytica Chimica Acta 435*, 177-185.

(108) Xie, C., Liu, B., Wang, Z., Gao, D., Guan, G., and Zhang, Z. (2008) Molecular imprinting at walls of silica nanotubes for TNT recognition. *Analytical chemistry 80*, 437-443.

(109) Dickert, F., and Hayden, O. (2002) Bioimprinting of polymers and sol-gel phases. Selective detection of yeasts with imprinted polymers. *Analytical chemistry 74*, 1302-1306.

(110) Lulka, M. F., Iqbal, S. S., Chambers, J. P., Valdes, E. R., Thompson, R. G., Goode, M. T., and Valdes, J. J. (2000) Molecular imprinting of Ricin and its A

and B chains to organic silanes: fluorescence detection. *Materials Science and Engineering: C 11*, 101-105.

(111) Iqbal, S. S., Lulka, M. F., Chambers, J. P., Thompson, R. G., and Valdes, J. J. (2000) Artificial receptors: molecular imprints discern closely related toxins. *Materials Science and Engineering: C 7*, 77-81.

(112) Hench, L. L., and West, J. K. (1990) The sol-gel process. *Chemical Reviews 90*, 33-72.

(113) Reed, J. S. (1995) *Principles of ceramics processing*, Wiley New York.

(114) Inagaki, S., Guan, S., Fukushima, Y., Ohsuna, T., and Terasaki, O. (1999) Novel mesoporous materials with a uniform distribution of organic groups and inorganic oxide in their frameworks. *J. Am. Chem. Soc. 121*, 9611-9614.

(115) Yanagisawa, T., Shimizu, T., Kuroda, K., and Kato, C. (1990) The preparation of alkyltrimethylammonium-kanemite complexes and their conversion to microporous materials. *Bull. Chem. Soc. Jpn 63*, 988-992.

(116) Chen, C.-Y., Xiao, S.-Q., and Davis, M. E. (1995) Studies on ordered mesoporous materials III. Comparison of MCM-41 to mesoporous materials derived from kanemite. *Microporous Mater 4*, 1-20.

(117) Huo, Q., Margolese, D. I., Ciesla, U., Demuth, D. G., Feng, P., Gier, T. E., Sieger, P., Firouzi, A., and Chmelka, B. F. (1994) Organization of organic molecules with inorganic molecular species into nanocomposite biphase arrays. *Chemistry of Materials 6*, 1176-1191.

(118) Firouzi, A., Kumar, D., Bull, L., Besier, T., Sieger, P., Huo, Q., Walker, S., Zasadzinski, J., Glinka, C., and Nicol, J. (1995) Cooperative organization of inorganic-surfactant and biomimetic assemblies. *Science 267*, 1138-1143.

(119) Firouzi, A., Schaefer, D. J., Tolbert, S. H., Stucky, G. D., and Chmelka, B. F. (1997) Magnetic-Field-Induced Orientational Ordering of Alkaline Lyotropic Silicate−Surfactant Liquid Crystals. *J. Am. Chem. Soc. 119*, 9466-9477.

(120) Bagshaw, S. A., Prouzet, E., and Pinnavaia, T. J. (1995) Templating of mesoporous molecular sieves by nonionic polyethylene oxide surfactants. *Science 269*, 1242-1244.

(121) Tanev, P. T., and Pinnavaia, T. J. (1995) A neutral templating route to mesoporous molecular sieves. *Science 267*, 865-867.

(122) Wan, Y., and Zhao, D. (2007) On the controllable soft-templating approach to mesoporous silicates. *Chemical reviews 107*, 2821-2860.

(123) Attard, G. S., Glyde, J. C., and Göltner, C. G. (1995) Liquid-crystalline phases as templates for the synthesis of mesoporous silica. *Nature 378*, 366-368.

(124) Ogawa, M. (1994) Formation of novel oriented transparent films of layered silica-surfactant nanocomposites. *J. Am. Chem. Soc. 116*, 7941-7942.

(125) He, X., and Antonelli, D. (2002) Recent advances in synthesis and applications of transition metal containing mesoporous molecular sieves. *Angewandte Chemie International Edition 41*, 214-229.

(126) Taramasso, M., Perego, G., and Notari, B. (1983), Google Patents.

(127) Sudhakar Reddy, J., and Kumar, R. (1991) Synthesis, characterization, and catalytic properties of a titanium silicate, TS-2, with MEL structure. *Journal of Catalysis 130*, 440-446.

(128) Corma, A., and Kan, Q. (1998) Synthesis of Si and Ti-Si-MCM-48 mesoporous materials with controlled pore sizes in the absence of polar organic additives and alkali metal ions. *Chem. Commun.*, 579-580.

(129) Zhang, W., Fröba, M., Wang, J., Tanev, P. T., Wong, J., and Pinnavaia, T. J. (1996) Mesoporous Titanosilicate Molecular Sieves Prepared at Ambient Temperature by Electrostatic (S+ I-, S+ X-I+) and Neutral (S° I°) Assembly Pathways: A Comparison of Physical Properties and Catalytic Activity for Peroxide Oxidations. *J. Am. Chem. Soc. 118*, 9164-9171.

(130) Alba, M. D., Luan, Z., and Klinowski, J. (1996) Titanosilicate mesoporous molecular sieve MCM-41: synthesis and characterization. *The Journal of Physical Chemistry 100*, 2178-2182.

(131) Beck, C., Mallat, T., Bürgi, T., and Baiker, A. (2001) Nature of Active Sites in Sol–Gel TiO2–SiO2 Epoxidation Catalysts. *Journal of Catalysis 204*, 428-439.

(132) Hutter, R., Mallat, T., and Baiker, A. (1995) Titania Silica Mixed Oxides: II. Catalytic Behavior in Olefin Epoxidation. *Journal of Catalysis 153*, 177-189.

(133) Holland, M. A., Pickup, D. M., Mountjoy, G., Tsang, E. S., Wallidge, G. W., Newport, R. J., and Smith, M. E. (2000) Synthesis, characterisation and performance of (TiO2) 0.18 (SiO2) 0.82 xerogel catalysts. *J Mater Chem 10*, 2495-2501.

(134) Doeuff, S., Henry, M., Sanchez, C., and Livage, J. (1987) Hydrolysis of titanium alkoxides: Modification of the molecular precursor by acetic acid. *Journal of Non-crystalline solids 89*, 206-216.

(135) Lafond, V., Mutin, P., and Vioux, A. (2004) Control of the texture of titania-silica mixed oxides prepared by nonhydrolytic sol-gel. *Chemistry of materials 16*, 5380-5386.

(136) Bogush, G., Tracy, M., and Zukoski, C. (1988) Preparation of monodisperse silica particles: control of size and mass fraction. *Journal of Non-Crystalline Solids 104*, 95-106.

(137) Wang, X.-D., Shen, Z.-X., Sang, T., Cheng, X.-B., Li, M.-F., Chen, L.-Y., and Wang, Z.-S. (2010) Preparation of spherical silica particles by Stöber process with high concentration of tetra-ethyl-orthosilicate. *Journal of Colloid and Interface Science 341*, 23-29.

(138) Branda, F., Silvestri, B., Luciani, G., and Costantini, A. (2007) The effect of mixing alkoxides on the Stöber particles size. *Colloids and Surfaces A: Physicochemical and Engineering Aspects 299*, 252-255.

(139) Li, J. H., Zheng, Z. J., Fu, S. P., and Zhu, J. B. (2012) Preparation and Characterization of Paclitaxel Imprinted Silica Nanoparticles. *Advanced Materials Research 399*, 1894-1897.

(140) Wu, X., You, L., Di, B., Hao, W., Su, M., Gu, Y., and Shen, L. (2013) Novel chiral core–shell silica microspheres with trans-(1R,2R)-diaminocyclohexane bridged in the mesoporous shell: Synthesis, characterization and application in high performance liquid chromatography. *J Chromatogr A 1299*, 78-84.

(141) Gao, D., Zhang, Z., Wu, M., Xie, C., Guan, G., and Wang, D. (2007) A Surface Functional Monomer-Directing Strategy for Highly Dense Imprinting of TNT at Surface of Silica Nanoparticles. *J. Am. Chem. Soc. 129*, 7859-7866.

(142) Ow, H., Larson, D. R., Srivastava, M., Baird, B. A., Webb, W. W., and Wiesner, U. (2004) Bright and Stable Core−Shell Fluorescent Silica Nanoparticles. *Nano Letters 5*, 113-117.

(143) Luckarift, H. R., Dickerson, M. B., Sandhage, K. H., and Spain, J. C. (2006) Rapid, Room-Temperature Synthesis of Antibacterial Bionanocomposites of Lysozyme with Amorphous Silica or Titania. *Small 2*, 640-643.

(144) LaMer, V. K., and Dinegar, R. H. (1950) Theory, production and mechanism of formation of monodispersed hydrosols. *J. Am. Chem. Soc. 72*, 4847-4854.

(145) Matsoukas, T., and Gulari, E. (1988) Dynamics of growth of silica particles from ammonia-catalyzed hydrolysis of tetra-ethyl-orthosilicate. *Journal of colloid and interface science 124*, 252-261.

(146) Matsoukas, T., and Gulari, E. (1989) Monomer-addition growth with a slow initiation step: A growth model for silica particles from alkoxides. *Journal of Colloid and Interface Science 132*, 13-21.

(147) Feeney, P. J., Napper, D. H., and Gilbert, R. G. (1984) Coagulative nucleation and particle size distributions in emulsion polymerization. *Macromolecules 17*, 2520-2529.

(148) Hochberg, A., Tanaka, T., and Nicoli, D. (1979) Spinodal line and critical point of an acrylamide gel. *Physical Review Letters 43*, 217.

(149) Bogush, G., and Zukoski, C. (1991) Studies of the kinetics of the precipitation of uniform silica particles through the hydrolysis and condensation of silicon alkoxides. *Journal of Colloid and Interface Science 142*, 1-18.

(150) Kim, S., and Zukoski, C. F. (1990) A model of growth by hetero-coagulation in seeded colloidal dispersions. *Journal of Colloid and Interface Science 139*, 198-212.

(151) Tan, B., and Rankin, S. E. (2004) Interfacial Alignment Mechanism of Forming Spherical Silica with Radially Oriented Nanopores. *The Journal of Physical Chemistry B 108*, 20122-20129.

(152) Bailey, J., and Mecartney, M. (1992) Formation of colloidal silica particles from alkoxides. *Colloids and Surfaces 63*, 151-161.

(153) Freyer, M. W., and Lewis, E. A. (2008) Isothermal titration calorimetry: experimental design, data analysis, and probing macromolecule/ligand binding and kinetic interactions. *Methods in cell biology 84*, 79-113.

(154) Grime, J. K. (1985) *Chemical Analysis: A Series of Monographs on Analytical Chemistry and Its Applications*, Vol. 79, John Wiley & Sons.

(155) Robinson, J. W., Frame, E. M. S., and Frame II, G. M. (2004) *Undergraduate instrumental analysis*, CRC Press.

(156) Guidotti, M., Ravasio, N., Psaro, R., Ferraris, G., and Moretti, G. (2003) Epoxidation on titanium-containing silicates: do structural features really affect the catalytic performance? *Journal of catalysis 214*, 242-250.

(157) Hind, A., Bhargava, S., and Grocott, S. (1997) Attenuated total reflection fourier transform infrared spectroscopic investigation of the solid/aqueous interface of

low surface area, water-soluble solids in high ionic strength, highly alkaline, aqueous media. *Langmuir 13*, 3483-3487.

(158) Smith, F. (1999) *Industrial applications of X-ray diffraction*, CRC Press.

(159) Heiney, P. A.

(160) Goldstein, J., Newbury, D. E., Joy, D. C., Lyman, C. E., Echlin, P., Lifshin, E., Sawyer, L., and Michael, J. R. (2003) *Scanning electron microscopy and X-ray microanalysis*, Springer.

(161) Everhart, T., and Thornley, R. (1960) Wide-band detector for micro-microampere low-energy electron currents. *Journal of scientific instruments 37*, 246.

(162) Sing, K., Sing, K., Everett, D., Haul, R., Moscou, L., Pierotti, R., Rouquerol, J., and Siemieniewska, T. (1982) Reporting physisorption data for gas/solid systems. *Pure and Appl Chem 54*, 2201.

(163) Manocha, S. M. (2003) Porous carbons. *Sadhana 28*, 335-348.

(164) Brunauer, S., Emmett, P. H., and Teller, E. (1938) Adsorption of gases in multimolecular layers. *J. Am. Chem. Soc. 60*, 309-319.

(165) Sing, K. (2001) The use of nitrogen adsorption for the characterisation of porous materials. *Colloids and Surfaces A: Physicochemical and Engineering Aspects 187*, 3-9.

(166) Barrett, E. P., Joyner, L. G., and Halenda, P. P. (1951) The determination of pore volume and area distributions in porous substances. I. Computations from nitrogen isotherms. *J. Am. Chem. Soc. 73*, 373-380.

(167) Kruk, M., Jaroniec, M., and Sayari, A. (1997) Adsorption study of surface and structural properties of MCM-41 materials of different pore sizes. *The Journal of Physical Chemistry B 101*, 583-589.

(168) Kruk, M., and Jaroniec, M. (2001) Gas adsorption characterization of ordered organic-inorganic nanocomposite materials. *Chemistry of Materials 13*, 3169-3183.

(169) Schártl, W. (2007) *Light scattering from polymer solutions and nanoparticle dispersions*, Springer.

(170) Manual, Z. N. S. U. (2003) Malvern Instruments Ltd. *Manual Version IM 100*, 1.23-1.26.

(171) Sing, K. S. W., Everett, D. H., Haul, R. A. W., Moscou, L., Pierotti, R. A., Rouquerol, J., and Siemieniewska, T. (1985) Reporting physisorption data for gas solid systems with special reference to the determination of surface-area and porosity (recommendations 1984). *Pure Appl. Chem. 57*, 603-619.

(172) Paula, S., Sues, W., Tuchtenhagen, J., and Blume, A. (1995) Thermodynamics of micelle formation as a function of temperature: a high sensitivity titration calorimetry study. *The Journal of Physical Chemistry 99*, 11742-11751.

(173) Holmberg, K., Jönsson, B., Kronberg, B., and Lindman, B. (2003) *Surfactants and polymers in aqueous solution*, Vol. 2, John Wiley & Sons Chichester.

(174) Opatowski, E., Kozlov, M. M., Pinchuk, I., and Lichtenberg, D. (2002) Heat Evolution of Micelle Formation, Dependence of Enthalpy, and Heat Capacity on the Surfactant Chain Length and Head Group. *Journal of Colloid and Interface Science 246*, 380-386.

(175) Dupuy, C., Auvray, X., Petipas, C., Rico-Lattes, I., and Lattes, A. (1997) Anomeric effects on the structure of micelles of alkyl maltosides in water. *Langmuir 13*, 3965-3967.

(176) Rosen, M. J., and Dahanayake, M., AOCS Press.

(177) Zhao, X., Su, F., Yan, Q., Guo, W., Bao, X. Y., Lv, L., and Zhou, Z. (2006) Templating methods for preparation of porous structures. *J Mater Chem 16*, 637-648.

(178) Berggren, A., Palmqvist, A. E., and Holmberg, K. (2005) Surfactant-templated mesostructured materials from inorganic silica. *Soft Matter 1*, 219-226.

(179) Wan, Y., and Zhao. (2007) On the Controllable Soft-Templating Approach to Mesoporous Silicates. *Chemical Reviews 107*, 2821-2860.

(180) Moulik, S. P., Haque, M. E., Jana, P. K., and Das, A. R. (1996) Micellar properties of cationic surfactants in pure and mixed states. *Journal of Physical Chemistry 100*, 701-708.

(181) Udugamasooriya, D. G., and Spaller, M. R. (2008) Conformational constraint in protein ligand design and the inconsistency of binding entropy. *Biopolymers 89*, 653-667.

(182) Fan, Y. R., Li, Y. J., Cao, M. W., Wang, J. B., Wang, Y. L., and Thomas, R. K. (2007) Micellization of dissymmetric cationic gemini surfactants and their interaction with Dimyristoylphosphatidylcholine vesicles. *Langmuir 23*, 11458-11464.

(183) Ababou, A., and Ladbury, J. E. (2005) Survey of the year 2004: literature on applications of isothermal titration calorimetry. *Journal of Molecular Recognition 19*, 79-89.

(184) Ababou, A., and Ladbury, J. E. (2006) Survey of the year 2005: literature on applications of isothermal titration calorimetry. *Journal of Molecular Recognition 20*, 4-14.

(185) Cliff, M. J., and Ladbury, J. E. (2003) A survey of the year 2002 literature on applications of isothermal titration calorimetry. *Journal of Molecular Recognition 16*, 383-391.

(186) Falconer, R. J., and Collins, B. M. (2011) Survey of the year 2009: applications of isothermal titration calorimetry. *Journal of Molecular Recognition 24*, 1-16.

(187) Freiburger, L. A., Auclair, K., and Mittermaier, A. K. (2009) Elucidating Protein Binding Mechanisms by Variable-c ITC. *ChemBioChem 10*, 2871-2873.

(188) Norvaišas, P., Petrauskas, V., and Matulis, D. (2012) Thermodynamics of Cationic and Anionic Surfactant Interaction. *The Journal of Physical Chemistry B 116*, 2138-2144.

(189) Olofsson, G., and Loh, W. (2009) On the use of titration calorimetry to study the association of surfactants in aqueous solutions. *Journal of the Brazilian Chemical Society 20*, 577-593.

(190) Bouchemal, K., Agnely, F., Koffi, A., Djabourov, M., and Ponchel, G. (2010) What can isothermal titration microcalorimetry experiments tell us about the self-organization of surfactants into micelles? *Journal of Molecular Recognition 23*, 335-342.

(191) Holland, P. M. (1992) Modeling Mixed Surfactant Systems - Basic Introduction. *Acs Symposium Series 501*, 31-44.

(192) Bakshi, M. S., and Kaur, G. (2005) Mixed micelles of series of monomeric and dimeric cationic, zwitterionic, and unequal twin-tail cationic surfactants with sugar surfactants: A fluorescence study. *Journal of Colloid and Interface Science 289*, 551-559.

(193) Garidel, P., and Hildebrand, A. (2005) Thermodynamic properties of association colloids. *Journal of Thermal Analysis and Calorimetry 82*, 483-489.

(194) Hill, K., and Catherine, L.-F. (2008) Sugar-based surfactants for consumer and technical applications, in *Sugar-Based Surfactants Fundamentals and Applications* (Carnero Ruiz, C., Ed.) pp 1-20, CRC Press.

(195) Heerklotz, H., and Seelig, J. (2000) Correlation of membrane/water partition coefficients of detergents with the critical micelle concentration. *Biophys J 78*, 2435-40.

(196) Huang, L., and Somasundaran, P. (1997) Theoretical Model and Phase Behavior for Binary Surfactant Mixtures. *Langmuir 13*, 6683-6688.

(197) Thibaut, A., Misselyn-Bauduin, A.-M., Grandjean, J., Broze, G., and Jérôme, R. (2000) Adsorption of an aqueous mixture of surfactants on silica. *Langmuir 16*, 9192-9198.

(198) McMillan Jr, W. G., and Mayer, J. E. (1945) The statistical thermodynamics of multicomponent systems. *The Journal of Chemical Physics 13*, 276.

(199) Franks, F., Pedley, M., and Reid, D. S. (1976) Solute interactions in dilute aqueous solutions. Part 1.-Microcalorimetric study of the hydrophobic interaction.

*Journal of the Chemical Society, Faraday Transactions 1: Physical Chemistry in Condensed Phases 72*, 359-367.

(200) Billo, E. J. (2007) *Excel for Scientists and Engineers: Numerical Methods*, Wiley. com.

(201) Blandamer, M. J., Cullis, P. M., and Engberts, J. B. F. N. (1998) Titration microcalorimetry. *Journal of the Chemical Society-Faraday Transactions 94*, 2261-2267.

(202) Blandamer, M. J., Cullis, P. M., and Engberts, J. B. F. N. (1995) Differential scanning and titration calorimetric studies of macromolecules in aqueous solution. *Journal of Thermal Analysis 45*, 599-613.

(203) Xie, C., Li, H., Li, S., and Gao, S. (2011) Surface molecular imprinting for chemiluminescence detection of the organophosphate pesticide chlorpyrifos. *Microchimica Acta 174*, 311-320.

(204) Mer, V. K. L. (1952) Nucleation in Phase Transitions. *Industrial & Engineering Chemistry 44*, 1270-1277.

(205) Lee, K., Look, J.-L., Harris, M. T., and McCormick, A. V. (1997) Assessing Extreme Models of the Stöber Synthesis Using Transients under a Range of Initial Composition. *Journal of Colloid and Interface Science 194*, 78-88.

(206) Harris, M. T., Brunson, R. R., and Byers, C. H. (1990) The base-catalyzed hydrolysis and condensation reactions of dilute and concentrated TEOS solutions. *Journal of Non-Crystalline Solids 121*, 397-403.

(207) Bailey, J. K., and Mecartney, M. L. (1992) Formation of colloidal silica particles from alkoxides. *Colloids and Surfaces 63*, 151-161.

(208) Burneau, A., and Humbert, B. (1993) AGGREGATIVE GROWTH OF SILICA FROM AN ALKOXYSILANE IN A CONCENTRATED-SOLUTION OF AMMONIA. *Colloid Surf. A-Physicochem. Eng. Asp. 75*, 111-121.

(209) Green, D. L., Lin, J. S., Lam, Y. F., Hu, M. Z. C., Schaefer, D. W., and Harris, M. T. (2003) Size, volume fraction, and nucleation of Stober silica nanoparticles. *Journal of Colloid and Interface Science 266*, 346-358.

(210) Tleugabulova, D., Duft, A. M., Zhang, Z., Chen, Y., Brook, M. A., and Brennan, J. D. (2004) Evaluating formation and growth mechanisms of silica particles using fluorescence anisotropy decay analysis. *Langmuir 20*, 5924-5932.

(211) Schoeman, B. J., and Regev, O. (1996) A study of the initial stage in the crystallization of TPA-silicalite-1. *Zeolites 17*, 447-456.

(212) Rimer, J. D., Fedeyko, J. M., Vlachos, D. G., and Lobo, R. F. (2006) Silica self-assembly and the synthesis of microporous and mesoporous silicates. *Chem.-Eur. J. 12*, 2926-2934.

(213) Rimer, J. D., Trofymluk, O., Navrotsky, A., Lobo, R. F., and Vlachos, D. G. (2007) Kinetic and thermodynamic studies of silica nanoparticle dissolution. *Chemistry of Materials 19*, 4189-4197.

(214) Rimer, J. D., Trofymluk, O., Lobo, R. F., Navrotsky, A., and Vlachos, D. G. (2008) Thermodynamics of silica nanoparticle self-assembly in basic solutions of monovalent cations. *J Phys Chem C 112*, 14754-14761.

(215) Rimer, J. D., Lobo, R. F., and Vlachos, D. G. (2005) Physical basis for the formation and stability of silica nanoparticles in basic solutions of monovalent cations. *Langmuir 21*, 8960-8971.

(216) van Blaaderen, A., and Vrij, A. (1993) Synthesis and Characterization of Monodisperse Colloidal Organo-silica Spheres. *Journal of Colloid and Interface Science 156*, 1-18.

(217) Kobayashi, Y., Yoshida, M., Nagao, D., Ando, Y., Miyazaki, T., and Konno, M. (2006) Synthesis of SiO2-Coated Magnetite Nanoparticles and Immobilization of Proteins on Them, in *Characterization and Control of Interfaces for High Quality Advanced Materials II* pp 135-141, John Wiley & Sons, Inc.

(218) He, H., Fu, G., Wang, Y., Chai, Z., Jiang, Y., and Chen, Z. (2010) Imprinting of protein over silica nanoparticles via surface graft copolymerization using low monomer concentration. *Biosensors and Bioelectronics 26*, 760-765.

(219) Peng, Y., Xie, Y., Luo, J., Nie, L., Chen, Y., Chen, L., Du, S., and Zhang, Z. (2010) Molecularly imprinted polymer layer-coated silica nanoparticles toward dispersive solid-phase extraction of trace sulfonylurea herbicides from soil and crop samples. *Analytica Chimica Acta 674*, 190-200.

(220) Zhao, W., Sheng, N., Zhu, R., Wei, F., Cai, Z., Zhai, M., Du, S., and Hu, Q. (2010) Preparation of dummy template imprinted polymers at surface of silica microparticles for the selective extraction of trace bisphenol A from water samples. *Journal of Hazardous Materials 179*, 223-229.

(221) Gauczinski, J., Liu, Z., Zhang, X., and Schönhoff, M. (2012) Surface Molecular Imprinting in Layer-by-Layer films on Silica Particles. *Langmuir*.

(222) Dickey, F. H. (1949) The Preparation of Specific Adsorbents. *Proceedings of the National Academy of Sciences of the United States of America 35*, 227-229.

(223) Dickey, F. H. (1955) Specific adsorption. *Journal of Physical Chemistry 59*, 695-707.

(224) Haldeman, R. G., and Emmett, P. H. (1955) Specific Adsorption of Alkyl Orange Dyes on Silica Gel. *Journal of Physical Chemistry 59*, 1039-1043.

(225) Morrison, J. L., Worsley, M., Shaw, D. R., and Hodgson, G. W. (1959) The nature of the specificity of adsorption of alkyl orange dyes on silica gel. *Canadian Journal of Chemistry-Revue Canadienne De Chimie 37*, 1986-1995.

(226) Ye, L., and Mosbach, K. (2008) Molecular Imprinting: Synthetic Materials As Substitutes for Biological Antibodies and Receptors†. *Chemistry of Materials 20*, 859-868.

(227) Hwang, C.-C., and Lee, W.-C. (2002) Chromatographic characteristics of cholesterol-imprinted polymers prepared by covalent and non-covalent imprinting methods. *J Chromatogr A 962*, 69-78.

(228) Chen, L., Xu, S., and Li, J. (2011) Recent advances in molecular imprinting technology: current status, challenges and highlighted applications. *Chemical Society Reviews 40*.

(229) Turner, N. W., Jeans, C. W., Brain, K. R., Allender, C. J., Hlady, V., and Britt, D. W. (2006) From 3D to 2D: A Review of the Molecular Imprinting of Proteins. *Biotechnology Progress 22*, 1474-1489.

(230) Hunnius, M., Rufinska, A., and Maier, W. F. (1999) Selective surface adsorption versus imprinting in amorphous micoporous silicas. *Micropor. Mesopor. Mater. 29*, 389-403.

(231) Katz, A., and Davis, M. E. (2000) Molecular imprinting of bulk, microporous silica. *Nature 403*, 286-289.

(232) Cummins, W., Duggan, P., and McLoughlin, P. (2005) A comparative study of the potential of acrylic and sol-gel polymers for molecular imprinting. *Anal. Chim. Act. 542*, 52-60.

(233) Marx, S., and Liron, Z. (2001) Molecular Imprinting in Thin Films of Organic-Inorganic Hybrid Sol-Gel and Acrylic Polymers. *Chem. Mater. 13*, 3624-3630.

(234) Luderitz, L. A. C., and von Klitzing, R. (2013) Interaction forces between silica surfaces in cationic surfactant solutions: An atomic force microscopy study. *J. Colloid Interface Sci. 402*, 19-26.

(235) Zhou, Q., and Somasundaran, P. (2009) Synergistic adsorption of mixtures of cationic gemini and nonionic sugar-based surfactant on silica. *Journal of Colloid and Interface Science 331*, 288-294.

(236) Macakova, L., Blomberg, E., and Claesson, P. M. (2007) Effect of adsorbed layer surface roughness on the QCM-D response: Focus on trapped water. *Langmuir 23*, 12436-12444.

(237) Gutig, C., Grady, B. P., and Striolo, A. (2008) Experimental studies on the adsorption of two surfactants on solid-aqueous interfaces: Adsorption isotherms and kinetics. *Langmuir 24*, 4806-4816.

(238) Ragauskas, A. J., Williams, C. K., Davison, B. H., Britovsek, G., Cairney, J., Eckert, C. A., Frederick, W. J., Hallett, J. P., Leak, D. J., Liotta, C. L., Mielenz, J. R., Murphy, R., Templer, R., and Tschaplinski, T. (2006) The Path Forward for Biofuels and Biomaterials. *Science 311*, 484-489.

(239) Giesche, H. (1994) SYNTHESIS OF MONODISPERSED SILICA POWDERS .2. CONTROLLED GROWTH REACTION AND CONTINUOUS PRODUCTION PROCESS. *J. European Ceram. Soc. 14*, 205-214.

(240) Netrabukkana, R., Lourvanij, K., and Rorrer, G. L. (1996) Diffusion of Glucose and Glucitol in Microporous and Mesoporous Silicate/Aluminosilicate Catalysts. *Ind Eng Chem Res 35*, 458-464.

(241) Xu, W., Osei-Prempeh, G., Lema, C., Davis Oldham, E., Aguilera, R. J., Parkin, S., Rankin, S. E., Knutson, B. L., and Lehmler, H.-J. (2012) Synthesis, thermal properties, and cytotoxicity evaluation of hydrocarbon and fluorocarbon alkyl β-d-xylopyranoside surfactants. *Carbohydrate Research 349*, 12-23.

(242) Bartl, F., Delgadillo, I., Davies, A. N., Huvenne, J. P., Meurens, M., Volka, K., and Wilson, R. H. (1996) An interlaboratory comparison of sample presentation methods for the analysis of aqueous solutions using fourier transform infrared spectroscopy. *Fresenius' Journal of Analytical Chemistry 354*, 1-5.

(243) Bogush, G. H., Tracy, M. A., and Zukoski, C. F. (1988) PREPARATION OF MONODISPERSE SILICA PARTICLES - CONTROL OF SIZE AND MASS FRACTION. *Journal of Non-Crystalline Solids 104*, 95-106.

(244) Levenberg, K. (1944) A Method for the Solution of Certain Non-Linear Problems in Least Squares. *Quarterly of Applied Mathematics 2*, 164-168.

(245) Ziemys, A., Grattoni, A., Fine, D., Hussain, F., and Ferrari, M. (2010) Confinement effects on monosaccharide transport in nanochannels. *The Journal of Physical Chemistry B 114*, 11117-11126.

(246) Wang, Y., Lin, L., Zhu, B. S., Zhu, Y. X., and Xie, Y. C. (2008) Different dispersion behavior of glucose and sucrose on alumina and silica surfaces. *Appl. Surf. Sci. 254*, 6560-6567.

(247) Lerbret, A., Lelong, G., Mason, P. E., Saboungi, M. L., and Brady, J. W. (2011) Molecular Dynamics and Neutron Scattering Study of Glucose Solutions Confined in MCM-41. *Journal of Physical Chemistry B 115*, 910-918.

(248) Kuhn, R. C., and Maugeri, F. (2010) Selection of Adsorbents and Determination of Parameters for the Separation of Glucose, Fructose, Sucrose and Fructooligosaccharides. *International Journal of Food Engineering 6*.

(249) Ziemys, A., Grattoni, A., Fine, D., Hussain, F., and Ferrari, M. (2010) Confinement Effects on Monosaccharide Transport in Nanochannels. *Journal of Physical Chemistry B 114*, 11117-11126.

(250) Kemmer, G., and Keller, S. (2010) Nonlinear least-squares data fitting in Excel spreadsheets. *Nature Protocols 5*, 267-281.

(251) Kriz, D., Ramström, O., and Mosbach, K. (1997) Peer Reviewed: Molecular Imprinting: New Possibilities for Sensor Technology. *Analytical Chemistry 69*, 345A-349A.

(252) Díaz-García, M. E., and Laíño, R. B. (2005) Molecular Imprinting in Sol-Gel Materials: Recent Developments and Applications. *Microchim. Acta 149*, 19-36.

(253) Holthoff, E. L., and Bright, F. V. (2007) Molecularly imprinted xerogels as platforms for sensing. *Accounts Chem. Res. 40*, 756-767.

(254) Mujahid, A., Lieberzeit, P. A., and Dickert, F. L. (2010) Chemical Sensors Based on Molecularly Imprinted Sol-Gel Materials. *Materials 3*, 2196-2217.

(255) Bass, J. D., and Katz, A. (2006) Bifunctional surface imprinting of silica: Thermolytic synthesis and characterization of discrete thiol-amine functional group pairs. *Chemistry of Materials 18*, 1611-1620.

(256) Do Ki, C., Oh, C., Oh, S. G., and Chang, J. Y. (2002) The use of a thermally reversible bond for molecular imprinting of silica spheres. *J. Am. Chem. Soc. 124*, 14838-14839.

(257) Jayasundera, S., Zeinali, M., Miller, J. B., Velea, L. M., Gaber, B. P., and Markowitz, M. A. (2006) Investigation of surface interactions in molecular recognition of phosphonate imprinted organosilicates and the role of water. *Journal of Physical Chemistry B 110*, 18121-18125.

(258) Markowitz, M. A., Kust, P. R., Deng, G., Schoen, P. E., Dordick, J. S., Clark, D. S., and Gaber, B. P. (2000) Catalytic silica particles via template-directed molecular imprinting. *Langmuir 16*, 1759-1765.

(259) Burneau, A., and Humbert, B. (1993) Aggregative growth of silica from an alkoxysilane in a concentrated solution of ammonia. *Colloid Surf. A-Physicochem. Eng. Asp. 75*, 111-121.

(260) Maier, N. M., Franco, P., and Lindner, W. (2001) Separation of enantiomers: needs, challenges, perspectives. *J Chromatogr A 906*, 3-33.

(261) Fanali, S. (1996) Identification of chiral drug isomers by capillary electrophoresis. *J Chromatogr A 735*, 77-121.

(262) Blanch, G. P., Caja, M. d. M., Ruiz del Castillo, M. L., and Herraiz, M. (1998) Comparison of different methods for the evaluation of the authenticity of olive oil and hazelnut oil. *Journal of agricultural and food chemistry 46*, 3153-3157.

(263) Meyer, V., and Ahuja, S. (1991) in *ACS Symposium Series, American Chemical Society, Washington DC* pp 217-227.

(264) Cronin, J. R., and Pizzarello, S. (1997) Enantiomeric excesses in meteoritic amino acids. *Science 275*, 951-955.

(265) Fanali, S. (2000) Enantioselective determination by capillary electrophoresis with cyclodextrins as chiral selectors. *J Chromatogr A 875*, 89-122.

(266) Rocco, A., Maruška, A., and Fanali, S. (2013) Enantiomeric separations by means of nano-LC. *Journal of separation science 36*, 421-444.

(267) Ward, T. J., and Ward, K. D. (2010) Chiral separations: fundamental review 2010. *Analytical chemistry 82*, 4712-4722.

(268) Maier, N. M., and Lindner, W. (2007) Chiral recognition applications of molecularly imprinted polymers: a critical review. *Analytical and bioanalytical chemistry 389*, 377-397.

(269) Ramström, O., and Ansell, R. J. (1998) Molecular imprinting technology: challenges and prospects for the future. *Chirality 10*, 195-209.

(270) Maier, N., and Lindner, W. (2007) Chiral recognition applications of molecularly imprinted polymers: a critical review. *Analytical and Bioanalytical Chemistry 389*, 377-397.

(271) Kugimiya, A., Matsui, J., Abe, H., Aburatani, M., and Takeuchi, T. (1998) Synthesis of castasterone selective polymers prepared by molecular imprinting. *Analytica Chimica Acta 365*, 75-79.

(272) Sellergren, B., and Shea, K. J. (1995) Origin of peak asymmetry and the effect of temperature on solute retention in enantiomer separations on imprinted chiral stationary phases. *J Chromatogr A 690*, 29-39.

(273) Zhang, H., Ye, L., and Mosbach, K. (2006) Non-covalent molecular imprinting with emphasis on its application in separation and drug development. *Journal of Molecular Recognition 19*, 248-259.

(274) Di, B., Cheng, L., Jiang, Q., Su, M., and Hao, W. (2013) Anionic surfactant templated chiral nanospheres and their enantioselective adsorption. *New Journal of Chemistry 37*, 1603-1609.

(275) Paik, P., Mastai, Y., Kityk, I., Rakus, P., and Gedanken, A. (2012) Synthesis of amino acid block-copolymer imprinted chiral mesoporous silica and its acoustically-induced optical Kerr effects. *Journal of Solid State Chemistry 192*, 127-131.

(276) Yokoi, T., Sato, S., Ara, Y., Lu, D., Kubota, Y., and Tatsumi, T. (2010) Synthesis of chiral mesoporous silica and its potential application to asymmetric separation. *Adsorption 16*, 577-586.

(277) Paik, P., Gedanken, A., and Mastai, Y. (2010) Chiral separation abilities: Aspartic acid block copolymer-imprinted mesoporous silica. *Microporous and Mesoporous Materials 129*, 82-89.

(278) Che, S., Liu, Z., Ohsuna, T., Sakamoto, K., Terasaki, O., and Tatsumi, T. (2004) Synthesis and characterization of chiral mesoporous silica. *Nature 429*, 281-284.

(279) Wu, J., Su, P., Huang, J., Wang, S., and Yang, Y. (2013) Synthesis of teicoplanin-modified hybrid magnetic mesoporous silica nanoparticles and their application in chiral separation of racemic compounds. *Journal of colloid and interface science*.

(280) Vega, E., Marzabadi, C., Kazakevich, Y., and Fadeev, A. Y. (2011) Synthesis of chiral mesoporous silicas with oligo (saccharide) surfaces and their use in separation of stereoisomers. *Journal of colloid and interface science 359,* 542-544.

(281) Seeberger, P. H. (2009) Chemical glycobiology: why now? *Nature Chemical Biology 5,* 368-72.

(282) Jandera, P., and Churáček, J. (1974) Gradient elution in liquid chromatography : I. The influence of the composition of the mobile phase on the capacity ratio (retention volume, band width, and resolution) in isocratic elution — theoretical considerations. *J Chromatogr A 91,* 207-221.

(283) Goulding, R. W. (1975) Liquid chromatography of sugars and related polyhydric alcohols on cation exchangers : The effect of cation variation. *J Chromatogr A 103*, 229-239.

(284) Khym, J. X., and Zill, L. P. (1951) THE SEPARATION OF MONOSACCHARIDES BY ION EXCHANGE. *J. Am. Chem. Soc. 73,* 2399-2400.

(285) Jones, J., and Wall, R. (1960) THE SEPARATION OF SUGARS ON ION-EXCHANGE RESINS: PART II. SEPARATION OF MONOSACCHARIDES. *Canadian Journal of Chemistry 38,* 2290-2294.

(286) Karlsson, G., Winge, S., and Sandberg, H. (2005) Separation of monosaccharides by hydrophilic interaction chromatography with evaporative light scattering detection. *J Chromatogr A 1092*, 246-249.

(287) Kakita, H., Kamishima, H., Komiya, K., and Kato, Y. (2002) Simultaneous analysis of monosaccharides and oligosaccharides by high-performance liquid chromatography with postcolumn fluorescence derivatization. *J Chromatogr A 961*, 77-82.

(288) Alpert, A. J., Shukla, M., Shukla, A. K., Zieske, L. R., Yuen, S. W., Ferguson, M. A. J., Mehlert, A., Pauly, M., and Orlando, R. (1994) Hydrophilic-interaction chromatography of complex carbohydrates. *J Chromatogr A 676*, 191-202.

(289) Schumacher, S., Gruneberger, F., Katterle, M., Hettrich, C., Hall, D. G., Scheller, F. W., and Gajovic-Eichelmann, N. (2011) Molecular imprinting of fructose using a polymerizable benzoboroxole: Effective complexation at pH 7.4. *Polymer 52*, 2485-2491.

(290) Hilt, J. Z., Byrne, M. E., and Peppas, N. A. (2006) Microfabrication of intelligent biomimetic networks for recognition of D-glucose. *Chemistry of Materials 18*, 5869-5875.

(291) Mayes, A. G., Andersson, L. I., and Mosbach, K. (1994) Sugar binding polymers showing high anomeric and epimeric discrimination obtained by noncovalent molecular imprinting. *Anal. Biochem. 222*, 483-488.

(292) Chen, G., Guan, Z., Chen, C.-T., Fu, L., Sundaresan, V., and Arnold, F. H. (1997) A glucose-sensing polymer. *Nat Biotech 15*, 354-357.

(293) Striegler, S. (2001) Investigation of disaccharide recognition by molecularly imprinted polymers. *Bioseparation 10*, 307-314.

(294) Wizeman, W. J., and Kofinas, P. (2001) Molecularly imprinted polymer hydrogels displaying isomerically resolved glucose binding. *Biomaterials 22*, 1485-1491.

(295) Parmpi, P., and Kofinas, P. (2004) Biomimetic glucose recognition using molecularly imprinted polymer hydrogels. *Biomaterials 25*, 1969-1973.

(296) Striegler, S. (2003) Carbohydrate recognition in cross-linked sugar-templated poly(acrylates). *Macromolecules 36*, 1310-1317.

(297) Rajkumar, R., Warsinke, A., Mohwald, H., Scheller, F. W., and Katterle, M. (2008) Analysis of recognition of fructose by imprinted polymers. *Talanta 76*, 1119-1123.

(298) Sineriz, F., Ikeda, Y., Petit, E., Bultel, L., Haupt, K., Kovensky, J., and Papy-Garcia, D. (2007) Toward an alternative for specific recognition of sulfated sugars. Preparation of highly specific molecular imprinted polymers. *Tetrahedron 63*, 1857-1862.

(299) Curcio, P., Zandanel, C., Wagner, A., Mioskowski, C., and Baati, R. (2009) Semi-Covalent Surface Molecular Imprinting of Polymers by One-Stage Mini-emulsion Polymerization: Glucopyranoside as a Model Analyte. *Macromol. Biosci. 9*, 596-604.

(300) Kirk, C., Jensen, M., Kjaer, C. N., Smedskjaer, M. M., Larsen, K. L., Wimmer, R., and Yu, D. H. (2009) Aqueous batch rebinding and selectivity studies on sucrose imprinted polymers. *Biosens. Bioelectron. 25*, 623-628.

(301) Okutucu, B., Onal, S., and Telefoncu, A. (2009) Noncovalently galactose imprinted polymer for the recognition of different saccharides. *Talanta 78,* 1190-1193.

(302) Yang, D.-H., Takahara, N., Lee, S.-W., and Kunitake, T. (2008) Fabrication of glucose-sensitive TiO2 ultrathin films by molecular imprinting and selective detection of monosaccharides. *Sensors and Actuators B: Chemical 130,* 379-385.

(303) Peric-Hassler, L., Hansen, H. S., Baron, R., and Hunenberger, P. H. (2010) Conformational properties of glucose-based disaccharides investigated using molecular dynamics simulations with local elevation umbrella sampling. *Carbohydrate Research 345,* 1781-1801.

(304) Taylor, J. B. (1957) The water solubilities and heats of solution of short chain cellulosic oligosaccharides. *Transactions of the Faraday Society 53,* 1198-1203.

(305) Abel, S. p., Dupradeau, F. o.-Y., Raman, E. P., MacKerell, A. D., and Marchi, M. (2010) Molecular Simulations of Dodecyl-β-maltoside Micelles in Water: Influence of the Headgroup Conformation and Force Field Parameters. *The Journal of Physical Chemistry B 115,* 487-499.

(306) Gao, X., and Wachs, I. E. (1999) Titania–silica as catalysts: molecular structural characteristics and physico-chemical properties. *Catal. Today 51,* 233-254.

(307) Feng, J., and Zhang, H. (2013) Hybrid materials based on lanthanide organic complexes: a review. *Chemical Society Reviews 42,* 387-410.

(308) Pozzo, R. L., Baltanás, M. A., and Cassano, A. E. (1997) Supported titanium oxide as photocatalyst in water decontamination: State of the art. *Catal. Today 39,* 219-231.

(309) Notari, B. (1993) Titanium silicalites. *Catal. Today 18*, 163-172.

(310) Morey, M. S., O'Brien, S., Schwarz, S., and Stucky, G. D. (2000) Hydrothermal and postsynthesis surface modification of cubic, MCM-48, and ultralarge pore SBA-15 mesoporous silica with titanium. *Chemistry of materials 12*, 898-911.

(311) Eimer, G. A., Casuscelli, S. G., Ghione, G. E., Crivello, M. E., and Herrero, E. R. (2006) Synthesis, characterization and selective oxidation properties of Ti-containing mesoporous catalysts. *Applied Catalysis A: General 298*, 232-242.

(312) Chandra, D., and Bhaumik, A. (2006) Highly Active 2D Hexagonal Mesoporous Titanium Silicate Synthesized Using a Cationic−Anionic Mixed-Surfactant Assembly. *Ind Eng Chem Res 45*, 4879-4883.

(313) Chandra, D., Kishor Mal, N., Mukherjee, M., and Bhaumik, A. (2006) Titanium-rich highly ordered mesoporous silica synthesized by using a mixed surfactant system. *Journal of Solid State Chemistry 179*, 1802-1807.

(314) Liu, Z., Crumbaugh, G. M., and Davis, R. J. (1996) Effect of Structure and Composition on Epoxidation of HexeneCatalyzed by Microporous and Mesoporous Ti–Si Mixed Oxides. *Journal of Catalysis 159*, 83-89.

(315) Blasco, T., Corma, A., Navarro, M., and Pariente, J. P. (1995) Synthesis, characterization, and catalytic activity of Ti-MCM-41 structures. *Journal of Catalysis 156*, 65-74.

(316) Pena, M., Dellarocca, V., Rey, F., Corma, A., Coluccia, S., and Marchese, L. (2001) Elucidating the local environment of Ti (IV) active sites in Ti-MCM-48: a comparison between silylated and calcined catalysts. *Microporous and mesoporous materials 44*, 345-356.

(317) Ji, D., Zhao, R., Lv, G., Qian, G., Yan, L., and Suo, J. (2005) Direct synthesis, characterization and catalytic performance of novel Ti-SBA-1 cubic mesoporous molecular sieves. *Applied Catalysis A: General 281*, 39-45.

(318) Ji, D., Ren, T., Yan, L., and Suo, J. (2003) Synthesis of Ti-incorporated SBA-1 cubic mesoporous molecular sieves. *Materials Letters 57*, 4474-4477.

(319) Li, G., and Zhao, X. (2006) Characterization and photocatalytic properties of titanium-containing mesoporous SBA-15. *Ind Eng Chem Res 45*, 3569-3573.

(320) Dagan, G., Sampath, S., and Lev, O. (1995) Preparation and utilization of organically modified silica-titania photocatalysts for decontamination of aquatic environments. *Chemistry of materials 7*, 446-453.

(321) Inoue, H., Matsuyama, T., Liu, B. J., Sakata, T., Mori, H., and Yoneyama, H. (1994) Photocatalytic Activities of TiO, Microcrystals Prepared in Si02 Matrixes Using a Sol-Gel Method for Carbon Dioxide Reduction. *Chem. Lett*, 653-6.

(322) Doolin, P., Alerasool, S., Zalewski, D., and Hoffman, J. (1994) Acidity studies of titania-silica mixed oxides. *Catalysis letters 25*, 209-223.

(323) Fu, X., Clark, L. A., Yang, Q., and Anderson, M. A. (1996) Enhanced photocatalytic performance of titania-based binary metal oxides: TiO2/SiO2 and TiO2/ZrO2. *Environmental science & technology 30*, 647-653.

(324) Itoh, M., Hattori, H., and Tanabe, K. (1974) The acidic properties of TiO< sub> 2</sub>-SiO< sub> 2</sub> and its catalytic activities for the amination of phenol, the hydration of ethylene and the isomerization of butene. *Journal of Catalysis 35*, 225-231.

(325) Nakabayashi, H. (1992) Properties of Acid Sites on TiO 2–SiO 2 and TiO 2–Al 2 O 3 Mixed Oxides Measured by Infrared Spectroscopy. *Bulletin of the Chemical Society of Japan 65*, 914-916.

(326) Mukhopadhayay, S. M., and Garofalini, S. H. (1990) Surface studies of TiO2/SiO2 glasses by X-ray photoelectron spectroscopy. *Journal of non-crystalline solids 126*, 202-208.

(327) Tanev, P. T., Chibwe, M., and Pinnavaia, T. J. (1994) Titanium-containing mesoporous molecular sieves for catalytic oxidation of aromatic compounds.

(328) Solberg, S. M., Kumar, D., and Landry, C. C. (2005) Synthesis, structure, and reactivity of a new Ti-containing microporous/mesoporous material. *The Journal of Physical Chemistry B 109*, 24331-24337.

(329) Klein, S., Thorimbert, S., and Maier, W. (1996) Amorphous microporous titania–silica mixed oxides: preparation, characterization, and catalytic redox properties. *Journal of Catalysis 163*, 476-488.

(330) Livage, J., and Sanchez, C. (1992) Sol-gel chemistry. *Journal of Non-Crystalline Solids 145*, 11-19.

(331) Liu, Z., and Davis, R. J. (1994) Investigation of the structure of microporous Ti-Si mixed oxides by X-ray, UV reflectance, FT-Raman, and FT-IR spectroscopies. *The Journal of Physical Chemistry 98*, 1253-1261.

(332) Choi, K.-M., Wakabayashi, R., Tatsumi, T., Yokoi, T., and Kuroda, K. (2011) Usefulness of alkoxyltitanosiloxane for the preparation of mesoporous silica containing a large amount of isolated titanium. *Journal of colloid and interface science 359*, 240-247.

(333) Jarupatrakorn, J., and Tilley, T. D. (2002) Silica-supported, single-site titanium catalysts for olefin epoxidation. A molecular precursor strategy for control of catalyst structure. *J. Am. Chem. Soc. 124*, 8380-8388.

(334) Guglielmi, M., and Carturan, G. (1988) Precursors for sol-gel preparations. *Journal of Non-Crystalline Solids 100*, 16-30.

(335) Andrianainarivelo, M., Corriu, R., Leclercq, D., Mutin, P. H., and Vioux, A. (1996) Mixed oxides SiO2–ZrO2 and SiO2–TiO2 by a non-hydrolytic sol–gel route. *J Mater Chem 6*, 1665-1671.

(336) Debecker, D. P., and Mutin, P. H. (2012) Non-hydrolytic sol–gel routes to heterogeneous catalysts. *Chemical Society Reviews 41*, 3624-3650.

(337) Çelik, Ö., and Dag, Ö. (2001) A new lyotropic liquid crystalline system: oligo (ethylene oxide) surfactants with [M (H2O) n] Xm transition metal complexes. *Angewandte Chemie 113*, 3915-3919.

(338) Huesing, N., Launay, B., Kickelbick, G., Gross, S., Armelao, L., Bottaro, G., Feth, M. P., Bertagnolli, H., and Kothleitner, G. (2003) Transition metal oxide-doped mesostructured silica films. *Applied Catalysis A: General 254*, 297-310.

(339) Hüsing, N., Launay, B., Doshi, D., and Kickelbick, G. (2002) Mesostructured Silica−Titania Mixed Oxide Thin Films. *Chemistry of Materials 14*, 2429-2432.

(340) Gyurcsik, B., and Nagy, L. (2000) Carbohydrates as ligands: coordination equilibria and structure of the metal complexes. *Coordination chemistry reviews 203*, 81-149.

(341) Saltman, P. (1965) The role of chelation in iron metabolism. *Journal of Chemical Education 42*, 682.

(342) Mukhopadhyay, A., Karkamkar, A., Kolehmainen, E., and Rao, C. P. (1998) Transition metal-saccharide chemistry: synthesis, characterization and solution stability studies of cis-dioxomolybdenum saccharide complexes. *Carbohydrate research 311*, 147-154.

(343) Bandwar, R. P., and Rao, C. P. (1997) Transition metal-saccharide chemistry and biology: An emerging field of multidisciplinary interest. *CURRENT SCIENCE-BANGALORE- 72*, 788-796.

(344) Rao, C. P., Geetha, K., Raghavan, M., Sreedhara, A., Tokunaga, K., Yamaguchi, T., Jadhav, V., Ganesh, K., Krishnamoorthy, T., and VA Ramaiah, K. (2000) Transition metal saccharide chemistry and biology: syntheses, characterization, solution stability and putative bio-relevant studies of iron–saccharide complexes. *Inorganica Chimica Acta 297*, 373-382.

(345) Morosanova, E., Belyakov, M., and Zolotov, Y. A. (2012) Silicon-titanium xerogels: Synthesis and application to the determination of ascorbic acid and polyphenoles. *Journal of Analytical Chemistry 67*, 14-20.

(346) Morosanova, E. I. (2012) Silica and silica-titania sol-gel materials: synthesis and analytical application. *Talanta*.

(347) Rahman, M. S. (2009) Utilizing mixed surfactants for simultaneous pore templating and active site formation in metal oxides.

(348) Hüsing, N., Launay, B., Kickelbick, G., and Hofer, F. (2003) Silica-titania mesostructured films. *Journal of sol-gel science and technology 26*, 615-619.

(349) Fu, X., and Qutubuddin, S. (2001) Synthesis of titania-coated silica nanoparticles using a nonionic water-in-oil microemulsion. *Colloids and Surfaces A: Physicochemical and Engineering Aspects 179*, 65-70.

(350) Tani, K., Kitada, M., Tachibana, M., Koizumi, H., and Kiba, T. (2003) Retention behavior of monosaccharides and disaccharides on titania. *Chromatographia 57*, 409-412.

(351) Alberius, P. C. A., Frindell, K. L., Hayward, R. C., Kramer, E. J., Stucky, G. D., and Chmelka, B. F. (2002) General predictive syntheses of cubic, hexagonal, and lamellar silica and titania mesostructured thin films. *Chemistry of Materials 14*, 3284-3294.

(352) Thangaraj, A., Kumar, R., Mirajkar, S., and Ratnasamy, P. (1991) Catalytic properties of crystalline titanium silicalites I. Synthesis and characterization of titanium-rich zeolites with MFI structure. *Journal of Catalysis 130*, 1-8.

(353) Peng, T., Hasegawa, A., Qiu, J., and Hirao, K. (2003) Fabrication of titania tubules with high surface area and well-developed mesostructural walls by surfactant-mediated templating method. *Chemistry of materials 15*, 2011-2016.

(354) Zeleňák, V., Hornebecq, V., Mornet, S., Schäf, O., and Llewellyn, P. (2006) Mesoporous Silica Modified with Titania: Structure and Thermal Stability. *Chemistry of Materials 18*, 3184-3191.

(355) Ambati, J. (2011) Studies on Silicon NMR Characterization and Kinetic Modeling of the Structural Evolution of Siloxane-based Materials and Their Applications in Drug Delivery and Adsorption.

(356) Qiao, S., Bhatia, S., and Zhao, X. (2003) Prediction of multilayer adsorption and capillary condensation phenomena in cylindrical mesopores. *Microporous and mesoporous materials 65*, 287-298.

(357) Kruk, M., Jaroniec, M., and Sayari, A. (1997) Adsorption study of surface and structural properties of MCM-41 materials of different pore sizes. *Journal of Physical Chemistry B 101*, 583-589.

(358) Modenbach, A. (2013) Sodium hydroxide pretreatment of corn stover and subsequent enzymatic hydrolysis: An investigation of yields, kinetic modeling and glucose recovery.

# VITA

**Place of Birth:**
Pune, India

**Education:**
B. Chem. Engg., Chemical Engineering, Mumbai University Institute of Chemical Technology, Mumbai, India

**Presentations:**
Suvid Joshi, Dr Barbara Knutson, Dr Stephen Rankin. Surfactant imprinting of the surface of silica nanoparticles for selective adsorption of sugars with subtle structural differences. ACS Colloids and Surfaces 2013, Riverside, CA (Podium).

Suvid Joshi, Alex Rao, Dr Barbara Knutson, Dr Stephen Rankin. Imprinted Stöber particles for application in saccharide and chiral separation. AIChE 2012, Pittsburgh, PA (Podium).

Suvid Joshi, Alex Rao, Dr Barbara Knutson, Dr Stephen Rankin. Imprinted nonporous silica nanoparticles for saccharide adsorption without diffusion resistance. ACS 2012, San Diego, CA. (Poster)

Suvid Joshi, Dr Barbara Knutson, Dr Stephen Rankin. Thermodynamic framework based on consistent application of Regular Solution Theory to model ITC data. AIChE 2010. Salt Lake City, UT (Podium).

Suvid Joshi, Dr Chakkamadathil Janet Mohandas, Dr Stephen Rankin. Synthesis and characterization of sugar-imprinted titano-silicate materials prepared by surfactant co-templating. AIChE 2010. Salt Lake City, UT (Podium).

**Publications:**
Md Shahidur Rahman, Jyothirmai Ambati, Suvid Joshi, Dr Stephen Rankin. Incorporation of Isolated Ti Sites into Mesoporous Silica Thin Films by Sugar Surfactant Complexation. In Press. Microporous and Mesoporous Materials

Suvid Joshi, Alex Rao, Dr Hans Lehmler, Dr Barbara Knutson, Dr Stephen Rankin. Interfacial Molecular Imprinting of Stöber Particle Surfaces: A Simple Approach to Targeted Saccharide Adsorption. Under review J. Coll. and Int. Sci.

Suvid Joshi, Dr Barbara Knutson, Dr Stephen Rankin. Direct molecular imprinting of Stöber particles for separation of sugars with subtle structural differences. Under preparation.

Suvid Joshi, Dr Barbara Knutson, Dr Stephen Rankin. Modeling thermodynamics of non-ideal mixtures of sugar based and cationic surfactants based on ITC data. Under Preparation.

Dr Chakkamadathil Janet Mohandas, Suvid Joshi, Dr Stephen Rankin.Synthesis, characterization and catalytic activity studies of mesoporous titano-silicates synthesized by surfactant complexation. Under Preparation.